An Overview of Major Terrestrial, Celestial, and Temporal Coordinate Systems for Target Tracking

DAVID FREDERIC CROUSE

Surveillance Technology Branch
Radar Division

August 10, 2016

REPORT DOCUMENTATION PAGE			Form Approved OMB No. 0704-0188

Public reporting burden for this collection of information is estimated to average 1 hour per response, including the time for reviewing instructions, searching existing data sources, gathering and maintaining the data needed, and completing and reviewing this collection of information. Send comments regarding this burden estimate or any other aspect of this collection of information, including suggestions for reducing this burden to Department of Defense, Washington Headquarters Services, Directorate for Information Operations and Reports (0704-0188), 1215 Jefferson Davis Highway, Suite 1204, Arlington, VA 22202-4302. Respondents should be aware that notwithstanding any other provision of law, no person shall be subject to any penalty for failing to comply with a collection of information if it does not display a currently valid OMB control number. **PLEASE DO NOT RETURN YOUR FORM TO THE ABOVE ADDRESS.**

1. REPORT DATE (DD-MM-YYYY) 10-08-2016	2. REPORT TYPE Formal Report	3. DATES COVERED (From - To)

4. TITLE AND SUBTITLE An Overview of Major Terrestrial, Celestial, and Temporal Coordinate Systems for Target Tracking	5a. CONTRACT NUMBER
	5b. GRANT NUMBER
	5c. PROGRAM ELEMENT NUMBER
6. AUTHOR(S) David Frederic Crouse	5d. PROJECT NUMBER
	5e. TASK NUMBER
	5f. WORK UNIT NUMBER

7. PERFORMING ORGANIZATION NAME(S) AND ADDRESS(ES) Naval Research Laboratory 4555 Overlook Avenue, SW Washington, DC 20375-5320	8. PERFORMING ORGANIZATION REPORT NUMBER NRL/FR/5344--16-10,279

9. SPONSORING / MONITORING AGENCY NAME(S) AND ADDRESS(ES) Office of Naval Research One Liberty Center 875 North Randolph Street Suite 1425 Arlington, VA 22203-1995	10. SPONSOR / MONITOR'S ACRONYM(S) ONR
	11. SPONSOR / MONITOR'S REPORT NUMBER(S)

12. DISTRIBUTION / AVAILABILITY STATEMENT

Approved for public release; distribution is unlimited.

13. SUPPLEMENTARY NOTES

14. ABSTRACT

Coordinate systems useful for those designing target tracking algorithms are discussed. Strict internationally recognized definitions of terrestrial and celestial coordinate systems are addressed, as well as a number of other lesser coordinate systems that arise when dealing with data typically used in target tracking algorithms. International organizations defining standard systems are indicated, as well as where to obtain data. Limitations in the data are demonstrated and methods for determining one's orientation using gravitation and magnetic measurements, as well as using stars, are presented. The report focuses on implementing the coordinate-system standards using freely available data and software but does not provide specific details on the strict definitions of all of the standards. More detailed information sources are provided in an extensive reference list. So readers can better reproduce the results in this report, summaries of the sources of the data and external code used in creating the plots in the report are provided. All online sources in this report were verified as of April 2015 or later. Even if high-precision global coordinate system definitions are not necessary to meet the basic requirements of a tracking network, they can be necessary in evaluating the performance of tracking algorithms in such a network.

15. SUBJECT TERMS

Coordinate systems	Position measurement	Geomagnetism	Time	Gravity	WGS 84
Standards organization	Orientation estimation	Standardization	Tides	IERS	

16. SECURITY CLASSIFICATION OF:			17. LIMITATION OF ABSTRACT	18. NUMBER OF PAGES	19a. NAME OF RESPONSIBLE PERSON David Frederic Crouse
a. REPORT Unclassified Unlimited	b. ABSTRACT Unclassified Unlimited	c. THIS PAGE Unclassified Unlimited	Unclassified Unlimited	180	19b. TELEPHONE NUMBER (include area code) 202-404-8106

Standard Form 298 (Rev. 8-98)
Prescribed by ANSI Std. Z39.18

i

This page
intentionally
left blank

CONTENTS

EXECUTIVE SUMMARY

When tracking targets over long ranges, it is essential that all sensors in a network translate their measurements or tracks into a common global coordinate system. This report addresses how international standards setting organizations and real data are used to define usable realizations of common terrestrial and celestial coordinate systems. It quantifies the magnitudes of errors that arise when establishing a coordinate system due to a number of model limitations and physical effects (other than measurement errors), such as the ground physically moving due to tides. This report brings together concepts across multiple fields to demonstrate how one's orientation can be determined using magnetic, gravitational, and celestial measurements. Links and references where one can find real data and code necessary for simulating and using standard celestial and terrestrial coordinate systems are provided.

This page
intentionally
left blank

AN OVERVIEW OF MAJOR TERRESTRIAL, CELESTIAL, AND TEMPORAL COORDINATE SYSTEMS FOR TARGET TRACKING

1. INTRODUCTION

Three previous tutorials have focused on the use of nonlinear three-dimensional (3D) monostatic and bistatic measurements, in general [55], and in refractive environments [54], as well as the use of arbitrary nonlinear continuous-time dynamic models [57]. However, a prerequisite to performing accurate tracking in a global environment is the establishment of a common coordinate system across sensors. Indeed, compensation for the effects of atmospheric refraction discussed in [54] might be completely useless if the pointing direction of the sensor cannot be determined to a sufficient precision.

This report looks at strict, internationally recognized definitions of terrestrial and celestial coordinate systems as well as a number of other lesser coordinate systems that arise when dealing with data typically used in target tracking algorithms. Section 2 reviews Cartesian celestial and terrestrial coordinate systems, while Section 3 goes over time standards. Differing time standards might initially seem to be a trivial detail when performing target tracking, except for the fact that the temporal standards are intertwined with celestial coordinate systems due to general relativity.

When simply tracking aircraft for air defense purposes, one would assume that celestial coordinate systems are of little importance. However, celestial objects can play a role in establishing the global look directions of each radar in a network to a high precision (networked sensor registration). Additionally, one should be able to identify celestial objects to avoid confusion with true targets. For example, as shown in real weather-radar data in [139], the Sun can increase the clutter background of a radar in a particular direction.[1] Knowing the location of the Sun can be useful in advanced target tracking algorithms that try to account for reduced target detection probabilities of targets near interference sources as in [185, Ch. 7.2, 7.3]. However, to identify the location of the Sun relative to an observer, one might be able to convert between celestial and terrestrial coordinates.

Section 4 provides an overview of basic coordinate systems for determining the location of an observer with respect to the surface of the Earth. This covers geodetic, geocentric, and ellipsoidal harmonic coordinates.[2] Geodetic coordinates are how one typically reports locations on a map in terms of latitude and longitude. However, geodetic coordinates are taken with respect to a reference ellipsoid, whereas many think that it is with respect to a sphere, as is the case with geocentric coordinates. Ellipsoidal harmonic components shall play a role in gravitational models later in the report.

Manuscript Approved July 22 2016.

[1]This is because, as discussed in [98, Ch. 3.1], for wavelengths longer than $0.4\,\mu$m, the spectrum of the Sun is approximately the spectrum of a black body having temperature $5760\,$K, meaning that within the radio bands typically used by radar, solar interference increases with increasing frequency.

[2]Section 4 does not cover different projections that one might use when creating maps, as the different projections tend to be of limited use in target-tracking systems except for the display of data to the user; see [65, 302] for information on basic map projections.

On the other hand, a lot of confusion can arise when making more intelligent tracking algorithms that utilize terrain data. This could be, for example, to determine whether a missile will hit a mountain or go over a mountain, or to determine whether a mountain is obscuring the view of a target. Digital terrain elevation data (DTED) is often given in terms of orthometric heights, whereas one typically expects a height reported to match an elevation reported by a Global Positioning System (GPS) receiver. Section 5 describes different vertical datums that one might encounter when designing a target-tracking system. Such datums are often defined in terms of the Earth's gravitational field, requiring more physics than one would expect. Section 5 also reviews the definition of pressure altitudes, which one must be familiar with when using data from aircraft transponders that report pressure altitude.

One generally wants to have to account for as few physical effects as possible while still meeting any requirements for the accuracy of a system. Sections 5, 6, and 7 consider the effects of the strict definitions of the Earth's gravitational field, the effects of tides, and models for the Earth's magnetic field. At first glance, each of these effects can appear to be insignificant. However, all of them can be significant in certain applications. For example, as discussed in Section 6, tides can move points on the surface of the Earth by tens of centimeters. Some global navigation satellite system (GNSS) receivers try to "correct" for tides, producing coordinates for stationary objects that do not appear to move over time but which will then not represent "true" coordinates in an Earth-centered Earth-fixed (ECEF) coordinate system [264].[3] Depending on the application and level of precision desired in a sensor network, such corrections may or may not be necessary or desirable. For example, for high-precision tracking of orbital debris, such shifts might matter. The magnetic field plays a role when tracking ships using transponder data as ships often report their heading with respect to magnetic North. However, one might be tempted to also use the magnetic field to align radars in a network. Section 7 demonstrates that magnetic field models are not suitable for high-accuracy global direction estimation.

The establishment of a common coordinate system in a sensor network is an ostensibly simple task: One can use a receiver for signals from a global navigation satellite system (GNSS), such as the United States' GPS, whose interface is described in [11], to determine the location of all of the sensors to an accuracy better than 5 cm [113].[4] However, the determining the orientations of the sensors is much more difficult. In the target tracking literature, numerous algorithms for determining the orientation of a sensor in a global coordinate system exist. However, such algorithms generally require an initial estimate of a sensor's orientation. For example, the algorithms presented in [59, 204, 324] and [372] all use linear approximations to deal with small errors in the range, elevation, and azimuth measurements of multiple sensors in three dimensions. Such approximations are useless without an initial estimate. Moreover, if the local vertical of the radar is itself biased, the corrections for the bias cannot be expressed as constant additive or multiplicative modifications to the measured azimuthal angle.[5] The vertical bias problem is worse when considering algorithms such as those in [1, 247, 250, 371] and [373] that try to establish a common two-dimensional (2D) coordinate system among multiple sensors, as might be the case when using multiple radars that are incapable of making elevation measurements. If the radars are designed such that their local verticals align with the local gravitational verticals, then the planes in which their measurements are taken do not coincide

---

[3]For example, the open-source GPS Toolkit (GPStk) [120] includes a class for solid-Earth tides, as documented at `http://www.gpstk.org/doxygen/SolidEarthTides_8hpp.html` .

[4]Some of the highest-precision commercially available receivers can be found by searching for "real-time kinematic GPS receiver" online.

[5]Consider a sensor with the boresight direction along the *z*-axis that is observing a target with zero elevation and azimuthal angle θ. In the extreme case, if the boresight direction is rotated $90°$, the target will have zero azimuthal angle regardless of the original angle θ, since the projection of the vector into the rotated plane is zero.

and it is not possible to establish a common 2D coordinate system among the radars. Over short distances, an *ad hoc* 2D coordinate system can be established, but it will never be of high precision. On the other hand, algorithms for aligning a 2D sensor with 3D sensors do exist [128, 130]. However, the nonlinear bias estimation algorithms of [132, 189] and the linearized algorithms of [129, 284, 321], which explicitly consider biases in the 3D sensor orientation, all require initial orientation estimates.

To fill the gap in the tracking literature for establishing a 3D global coordinate system without any prior information, Section 8 brings together all of the general concepts discussed in this report to present two techniques for determining a sensor's orientation in a global coordinate system. One method utilizes geomagnetic and gravitational measurements, the other uses measurements of stars;[6] both techniques are based on the same underlying algorithm. Section 8 demonstrates how a wide variety of physical effects must be taken into account for high-precision orientation estimation. The problem of sensor localization is not addressed, because one can simply purchase a commercially available GPS receiver.[7]

The report is concluded in Section 9, where specific contributions of the report not already present in the literature are highlighted. Appendix M lists abbreviations and acronyms used in the report.

This report focuses on implementing the coordinate-system standards using freely available data and software and does not provide specific details on the strict definitions of all of the standards. More detailed information can be found in the references in Table 1. So that readers can better reproduce the results in this report, Table 2 summarizes the sources of the data and external code used in creating the plots in this report. All online sources in this report were verified as of April 2015 or later.

Even if high-precision global coordinate system definitions are not necessary to meet the basic requirements of a tracking network, they can be necessary in evaluating the performance of tracking algorithms in such a network. For example, Automatic Dependent Surveillance-Broadcast[8] (ADS-B) signals sent from aircraft or Automatic Identification System[9] (AIS) messages broadcast y ships can be used as "truth" data against which estimation and tracking algorithms can be compared, because such transponders provide identifying numbers and the Global Positioning System (GPS) locations of planes/ ships, among other information. Such data is widely available.[10]

---

[6]Whereas the majority of algorithms for sensor registration for tracking applications focus on the use of common observations of aircraft, the explicit use of observed aircraft is not considered here for the simple reason that such algorithms will not work if very few aircraft are present. For example, after the terrorist attacks in the United States on 11 September 2001, the airspace over the United States and Canada was closed for a few days [201]. Additionally, aircraft and satellites are not point targets. In the radar community, it has long been known that the apparent location of an aircraft can vary significantly depending on its shape and reflectivity [143].

[7]Commercial GPS solutions are often significantly cheaper than designing a GPS receiver from the ground up – a task that is much more complicated than it seems. To design a GPS receiver, a number of possibly time-consuming, *ad hoc* fixes are necessary to correct for poor satellite design, which varies from satellite to satellite. For example, as described in [310], the L5 signal on satellite SVN49 is corrupted with a multipath return because of reflections from an auxiliary port to the satellite's antenna array and its broadcast ephemerides are biased by 150 m. Failure to include satellite-specific corrections will result in degraded performance.

[8]The standards for ADS-B transponders are maintained by the Radio Technical Commission for Aeronautics (RCTA). A list of the documents defining the standard is available at `http://adsb.tc.faa.gov/ADS-B.htm` The documents can be expensive to those who are not members of RCTA. A detailed description of the data (ADS-B and otherwise) broadcast by Mode S transponders, which tend to be the most common internationally, is available (for a price) from the International Civil Aviation Organization (ICAO) [150].

[9]Specifications on AIS transponders are available for free from the International Telecommunication Union (ITU) at [155].

[10]Most modern aircraft are equipped with transponders supporting ADS-B, and all aircraft operating in Class A, B, and C airspace in the United States (generally all commercial aircraft) are required by U.S. law to carry such transponders as of 1 January

Table 1: References for the Definitions of Modern Celestial and Terrestrial Coordinate Systems

Standard	Description	Reference
IERS Conventions 2010	Standard for terrestrial and celestial coordinate systems	http://maia.usno.navy.mil/conv2010/ http://tai.bipm.org/iers/conv2010/
IERS Conventions Updates	Errata and changes since the last conventions release	http://maia.usno.navy.mil/conv2010/convupdt.html http://tai.bipm.org/iers/convupdt/listupdt.html
WGS 84 Standard	Coordinate-system standard for the United States Department of Defense	http://earth-info.nga.mil/GandG/publications/ NGA_STND_0036_1_0_0_WGS84/NGA.STND.0036_1.0.0_WGS84.pdf
Explanatory Supplement to the Astronomical Almanac	Explains the use of the many coordinate systems in detail	Book: [332]
Errata for the Explanatory Supplement		http://aa.usno.navy.mil/publications/docs/exp_supp_errata.pdf
The Astronomical Almanac for the Year 2014	The Navy's astronomical almanac	Book: [70] Associated Sites: http://asa.usno.navy.mil and http://asa.hmnao.com
Errata 2014	Errata for the Astronomical Almanac	http://asa.usno.navy.mil/Errata/Errata_2014.html
Time from Earth Rotation to Atomic Physics	Describes international time standards	Book: [226]

Note that the Explanatory Supplement to the Astronomical Almanac in [332] refers to the 2014 edition of the almanac, not the frequently cited but out-of-date 1992 edition [285].

2020 [89] (similar regulations exist in Europe [81]). Similarly, the International Maritime Organization's (IMO) Safety of Life at Sea (SOLAS) Convention [152] mandates that a transponder supporting AIS be carried by all passenger ships, ships of 300 gross tonnage(Gross tonnage is *not a measure of weight*). Rather, it is a measure of the volume of a ship [151].

Table 2: Sources of the External Data and Code Related to the Plots in this Report

Description	Reference	Uniform Resource Locator (URL)
Gravitational Model Data and Documentation		
EGM2008 Tide-Free and Zero-Tide Spherical-Harmonic Coefficients		http://earth-info.nga.mil/GandG/wgs84/gravitymod/egm2008/first_release.html
EGM2008 Height Anomaly to Geoid Undulation Coefficients		http://earth-info.nga.mil/GandG/wgs84/gravitymod/egm2008/egm08_wgs84.html
Detailed Report on the EGM96 Model (Predecessor to EGM2008)	[198]	http://bowie.gsfc.nasa.gov/697/staff/lemoine/EGM96_NASA-TP-1998-206861.pdf
Document on the Development of the EGM2008 Model & Errata	[252, 253]	
Tide Model Data and Documentation		
FES2004 Ocean Tide Coefficients		ftp://tai.bipm.org/iers/convupdt/chapter6/tidemodels/fes2004_Cnm-Snm.dat http://maia.usno.navy.mil/conv2010/convupdt/chapter6/tidemodels/ fes2004_Cnm-Snm.dat
Document on the Development of FES2004	[209]	ftp://tai.bipm.org/iers/temp/FES2004_tides_Biancale/FES2004.pdf
IERS Subroutines for Tides (Chapter 7), including `step2diu` and `step2lon` with `dehanttideinel`		http://maia.usno.navy.mil/conv2010/software.html ftp://tai.bipm.org/iers/convupdt/chapter7/
IERS Conventions 2010 Tide Model	[257, Ch. 6,7]	http://www.iers.org/IERS/EN/Publications/TechnicalNotes/tn36.html
A Solid Tide Potential Model Simpler than in the IERS Conventions	[332, Ch. 5]	
Earth Magnetic Field Data, Documentation, and Software		
EMM2010 Spherical-Harmonic Magnetic Coefficients		http://www.ngdc.noaa.gov/geomag/EMM/
WMM2010 Spherical-Harmonic Magnetic Coefficients		http://www.ngdc.noaa.gov/geomag/WMM/DoDWMM.shtml
WMM Documentation (Relevant to the EMM too)	[223]	http://www.ngdc.noaa.gov/geomag/WMM/data/WMM2010/WMM2010_Report.pdf
Documentation for a Predecessor to the EMM	[219]	http://citeseerx.ist.psu.edu/viewdoc/ download?doi=10.1.1.380.1319&rep=rep1&type=pdf
Software Created for the Simulations in this Report Performing Spherical-Harmonic Magnetic Field Synthesis (Choose David F. Crouse)		http://www.ngdc.noaa.gov/geomag/WMM/thirdpartycontributions.shtml
Earth Terrain Models and Documentation		
Earth2012 Spherical-Harmonic Terrain Coefficients with Water		http://geodesy.curtin.edu.au/research/models/Earth2012/
Article on Models Used Deriving Earth2012	[135]	http://www.cage.curtin.edu.au/ will/2011JB008878.pdf
DTM2006.0 Spherical-Harmonic Terrain Coefficients		http://earth-info.nga.mil/GandG/wgs84/gravitymod/egm2008/first_release.html
Document on the Development of the DTM2006.0	[251]	http://earth-info.nga.mil/GandG/wgs84/gravitymod/new_egm/EGM08_papers/ NPavlis&al_S8_Revised111606.pdf
Reference Station Positions		
ITRF2008 Station Positions and Velocities		http://itrf.ign.fr/ITRF_solutions/2008/
Open Access Article Describing the ITRF2008	[7]	http://link.springer.com/article/10.1007/s00190-011-0444-4
Description of the Solution (Software/Technique) Independent Exchange (SINEX) Format		http://www.iers.org/IERS/EN/Organization/AnalysisCoordinator/SinexFormat/ sinex_cont.html
Planetary Ephemeris Data, Software, and Documentation		
SPICE Toolkit Software (with Documentation)		http://naif.jpl.nasa.gov/naif/toolkit.html
The DE430 Ephemerides for SPICE		http://naif.jpl.nasa.gov/pub/naif/generic_kernels/spk/planets/
Documentation for the DE430 Ephemerides	[95]	http://naif.jpl.nasa.gov/pub/naif/generic_kernels/spk/planets/ DE430%20and%20DE431.pdf
Star Catalog Data and Documentation		
The Hipparcos Catalog (The New Reduction, I/311)		http://cdsarc.u-strasbg.fr/viz-bin/Cat?cat=I/311
Description of the New Reduction	[346]	http://arxiv.org/abs/astro-ph/0505432
Validation of the Catalog	[347]	http://arxiv.org/abs/0708.1752
Extensive Documentation on the Original Hipparcos Catalog	[82]	http://www.rssd.esa.int/index.php?project=HIPPARCOS&page=Overview
Errata for the Original Hipparcos Catalog		http://cdsarc.u-strasbg.fr/viz-bin/getCatFile_Redirect/?-plus=-%2B&I/239/errata.htx
Earth-Orientation Parameters, Software, and Documentation		
Earth-Orientation Parameter Data According to the IERS Conventions		http://www.iers.org/IERS/EN/DataProducts/EarthOrientationData/eop.html http://www.usno.navy.mil/USNO/earth-orientation http://hpiers.obspm.fr/eop-pc/
The NGA's Earth-Orientation Parameter Predictions (Not used in the Simulations)		http://earth-info.nga.mil/GandG/sathtml/eopp.html
Explanation of IERS Bulletins A and B Parameters		http://hpiers.obspm.fr/eoppc/bul/bulb/explanatory.html
Documentation on the Combined Solution C04	[30]	http://hpiers.obspm.fr/iers/eop/eopc04/C04.guide.pdf
Code to Add Tides when Interpolating EOPs (`interp` and Subroutines)		http://hpiers.obspm.fr/eop-pc/index.php?index=models
General Software for Astronomy and Time Conversions		
The IAU's Standards of Fundamental Astronomy Software	[146]	http://www.iausofa.org
Software for Optimal 2D Assignment		
An overview of 2D assignment algorithms; the appendix in each paper contains Matlab code.	[53, 56]	
Simple Map Data		
The Global, Self-Consistent, Hierarchical, High-Resolution Geography Database (GSHHG) (coasts and political boundaries)	[359]	http://www.soest.hawaii.edu/pwessel/gshhg/
Shape File Format Definition	[79]	http://www.esri.com/library/whitepapers/pdfs/shapefile.pdf
M_Map: Free Software to Read Shapefiles in Matlab (*Cannot be Used in a Commercial Product!*)		http://www2.ocgy.ubc.ca/ rich/map.html

All software and data except for M_Map appear to be usable in commercial products with nothing more than an attribution to the source. However, developers should verify the licensing terms with an attorney before use in any product.

2. CELESTIAL AND TERRESTRIAL COORDINATE SYSTEMS

Due to the complexity of defining global celestial and terrestrial coordinate systems, international standards form the backbone of national standards. For example, since the advent of GPS, one of the most frequently encountered terrestrial coordinate systems is the United States Department of Defense's (U.S. DoD's) World Geodetic System 1984 (WGS 84) [69]. While the WGS 84 standard is developed and maintained by the United States' National Geospatial-Intelligence Agency (NGA),[11] it is in close agreement with international standards. The latest version of the WGS 84 standard used by U.S. DoD agrees with the alignment and location of the axes in the latest (2008) version of the International Terrestrial Reference Frame (ITRF) [66, 68], which is a realization of the International Terrestrial Reference System (ITRS) defined by the International Earth Rotation and Reference Systems Service (IERS). Differences between the WGS 84 and ITRF2008 arise due to differences in points of reference used to implement the standards, as discussed in [136, Ch. 2.11], and both standards are identical within the precision bounds of the ITRF definition.

Other countries maintain similar levels of compliance with international standard. The Russian Federation's GNSS system, GLONASS,[12] whose interface is described in English in [263], uses the Parametry Zemli 1990 (PZ-90) coordinate system [348]. The latest version of the PZ-90 coordinate system (PZ-90.11) is consistent to a centimeter-level precision with the ITRF2008 at epoch 2011 [349]. The GNSS system run by China is the BeiDou Satellite Navigation System (BDS), whose interface is described in [48]. The BDS uses the Chinese Geodetic Coordinate System 2000 (CGCS2000), which is consistent with an older (ITRF97) version of the ITRF [365]. The axes of all GNSS systems coincide with those of the ITRF2008. The Galileo Terrestrial Reference Frame (GTRF), the coordinate system of Europe's GNSS system (the interface is described in [83]) which is still under development, agrees with the ITRF2008 to the millimeter level [6]. Many countries are harmonizing their GNSS systems through participation in groups like the United Nations Office for Outer Space Affairs, International Committee on Global Navigation Satellite Systems.[13] Other countries, such as Japan, with its Quasi-Zenith Satellite System (QZSS) [148], and India, with the GPS-Aided GEO Augmented Navigation (GAGAN) system [180, 267], use GPS augmented with their own satellites.

The ITRF and WGS 84 standards are realizations of ECEF coordinate systems: Their origins coincide with the center of mass of the Earth and their axes rotate with the Earth's crust. The axes are what are termed "geographical axes" in [237] in that they are defined by the relative position and motion of numerous reference stations on the Earth's surface. The ITRF is a realization of the ITRS in that it defines specific points of reference, whereas the ITRS defines the coordinate system in a more abstract manner. According to Chapter 4.1 of the (older) 2003 version of the IERS conventions [225],[14]

> A Terrestrial Reference System (TRS) is a spatial reference system co-rotating with the Earth in its diurnal motion in space. In such a system, positions of points attached to the solid surface of the Earth have coordinates which undergo only small variations with time, due to

---

[11]The NGA was formerly known as the National Imagery and Mapping Agency (NIMA), which itself formed in part from the Defense Mapping Agency (DMA). A brief history of the agency can be found at [246].

[12]In Russian: ГЛОНАСС=ГЛОбáльная НАвигациóнная Спýтниковая Систéма or Global Navigation Satellite System.

[13]The harmonization of satellite navigation systems simplifies the fusion of signals from multiple systems for more robust localization. For example, Apple's iPhone starting with the 4S model uses the United States' GPS jointly with Russia's GLONASS system [273] for improved localization reliability.

[14]The current (2010) version of the IERS conventions [257] does not redefine a TRS and a TRF; it simply does not provide as concise an explanation of the two systems.

geophysical effects (tectonic or tidal deformations). A Terrestrial Reference Frame (TRF) is a set of physical points with precisely determined coordinates in a specific coordinate system (Cartesian, geographic, mapping...) attached to a Terrestrial Reference System. Such a TRF is said to be a realization of the TRS.

On the other hand, the term "WGS 84 standard" refers both to an abstract standard described in [69] and to its implementation. As mentioned in [66], implementations of the WGS 84 in terms of reference points often have names like G1150, where 'G' refers to the use of GPS measurements to obtain coordinates and '1150' is the GPS week number when the coordinates were implemented into the NGA's GPS ephemeris estimation process.

When describing celestial bodies, the U.S. Navy's astronomical almanac uses a realization of the International Celestial Reference System (ICRS) as its primary coordinate system [70, Ch. B, L]. Both the ICRS and ITRS are defined by the IERS in their conventions [257]. The ICRS defines the alignment of the axes of a celestial coordinate system (that does not rotate with the Earth). However, the Geocentric Celestial Reference System (GCRS) and the Barycentric Celestial Reference System (BCRS) place the ICRS axes either at the center of mass of the Earth, for the GCRS, or at the center of mass of the solar system for the BCRS. Both the BCRS and GCRS are defined within a general relativistic framework, which necessitates the definition of specific relativistically consistent timescales. Section 3 maps out the international organizations that play fundamental roles in defining celestial and terrestrial timescales.

When describing the location of objects on or near the Earth, non-Cartesian coordinate systems, such as the familiar geodetic latitude and longitude, are often used. Section 4 describes a number of common coordinate systems for specifying the location of points on or near the Earth and how they relate to the approximate gravitational shape of the Earth. Note, however, that a very large number of alternate, local implementations of terrestrial coordinate systems exist in different countries for legal as well as practical purposes. Countries generally define legal boundaries in terms of geographic landmarks or in terms of geodetic latitude and longitude using their own local datums (manner of defining horizontal and vertical locations) to maintain a consistent set of boundaries in spite of plate tectonics. For example, certain reference stations in Australia moved approximately 2 cm between 1996 and 1998 [329], and if national boundaries were defined solely in terms of coordinates in the ITRF2008, then the western part of France and Spain would be slowly becoming ocean at a rate of centimeters per year while Russia consumes the eastern part of Europe as the Eurasian plate moves East, as can be seen from Fig. 1, which shows the locations and direction vectors of the stations defining the ITRF2008.

Thus, the European Union has the European Terrestrial Reference System (ETRS), a datum defined such that coordinates throughout the European Union do not change much over time. The ETRS is realized through the European Terrestrial Reference Frame 1989 (ETRF89) (see `http://www.epncb.oma.be`), which can be transformed to the ITRF [117]. However, individual countries within the European Union define local coordinates in terms of their own datums. For example, SAPOS[15] provides coordinates within the ETRS for places in Germany [117].

Even in the United States, where the WGS 84 coordinate system is a DoD standard, the National Geodetic Survey (NGS) (see the web site at `http://www.ngs.noaa.gov`) defines the horizontal datum for

---

[15]SAPOS stands for "Satellitenpositionierungsdienst der deutschen Landesvermessung," which means satellite positioning service of the German national survey.
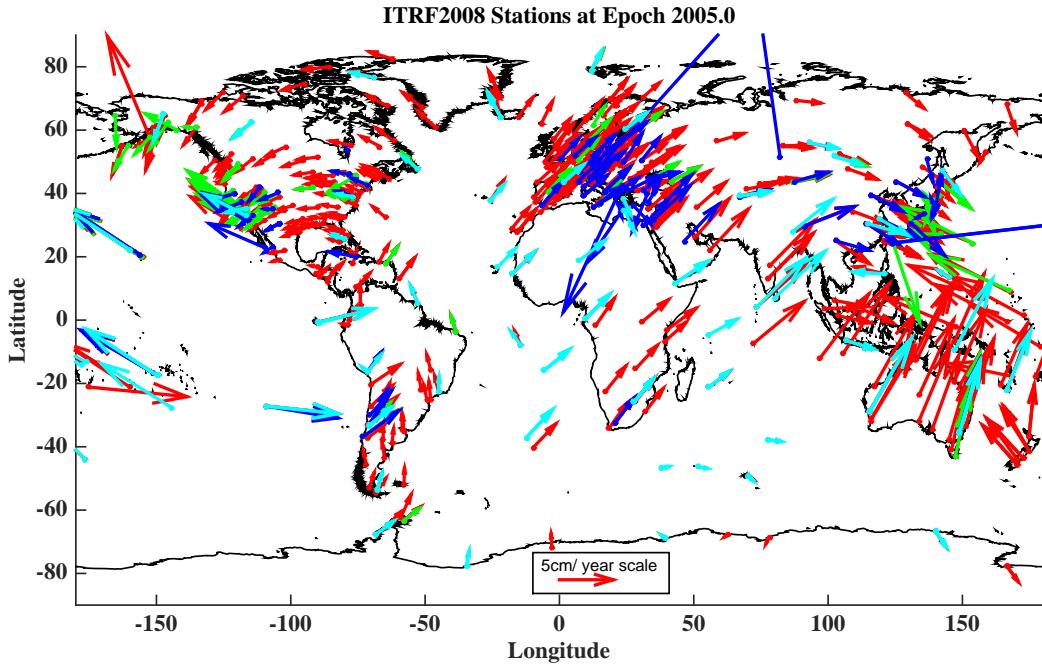
Fig. 1: Location points and direction vectors indicating the relative degree of motion in the local tangent plane (with the vertical defined by the WGS 84 reference ellipsoid) of the stations defining the ITRF2008 at the epoch of the data 2005.0 (the timescale was not specified; presumably TT was used). Red points and arrows refer to GNSS stations, green to very long baseline interferometry (VLBI) stations, dark blue to satellite laser-ranging (SLR) stations and dark blue to Doppler Orbitography and Radiopositioning Integrated by Satellite (DORIS) stations. Station motion is on the order of centimeters per year, presumably a Julian year in terrestrial time ($31,557,600$ seconds per Julian year). The data for the outlines of the continents are from the Global Self-Consistent, Hierarchical, High-Resolution Geography Database (GSHHG) listed in Table 2 along with links to software for reading one type of file format of the data. (The software was tested, but not used to make this plot. Rather, the ASCII version of the data was read directly into Matlab and plotted, with care taken at the $\pm 180°$ boundary.)

the United States to be the North American Datum of 1983 (NAD 83).[16] Consequently, a point in latitude and longitude on the WGS 84 reference ellipsoid (as one might obtain using a GPS receiver) will not align with a point having the same latitude and longitude in the NAD 83 standard [306]. A discussion of the time dependence of datums around the world is in [301]. To convert between a number of different local and global datums as well as many different map projections, one can use the free Mensuration Services Program (MSP) Geographic Translator (GEOTRANS) that is offered with source code in C++ and Java from the NGA at `http://earth-info.nga.mil/GandG/geotrans/` and is documented in [17, 18]. Alternatively, one can perform a number of datum conversions using the function in the NGS Geodetic Tool Kit, which can be downloaded from `http://www.ngs.noaa.gov/TOOLS/` and is described in a number of articles in *Professional Surveyor* starting with [368], which are all available on the NGS web site. Datum conversions are constantly updated and are not described in this report. The European Petroleum Survey Group (EPSG) of the International Association of Oil and Gas Producers (IOGP) maintains an online registry of datums at `http://www.epsg.org` that assigns each datum a spatial reference system identifier

---

[16]The current version is NAD 83(2011).

(SRID). For example, the WGS 84 standard has identifiers 7030, 6326, and 4326, each addressing different aspects of the standard.

The IERS conventions [257] form the basis of the most important Cartesian celestial and terrestrial coordinate systems. A large number of organizations play a role in contributing to the celestial and terrestrial standards set by the IERS, as illustrated in Fig. 2. The centers of the International Gravity Field Service (IGFS) and the IERS Product Centers are all sources of geophysical data. The Commission on International Coordination of Space Techniques for Geodesy and Geodynamics (CSTG) is an example of one of many entities that work to standardize techniques between space geodetic organizations.
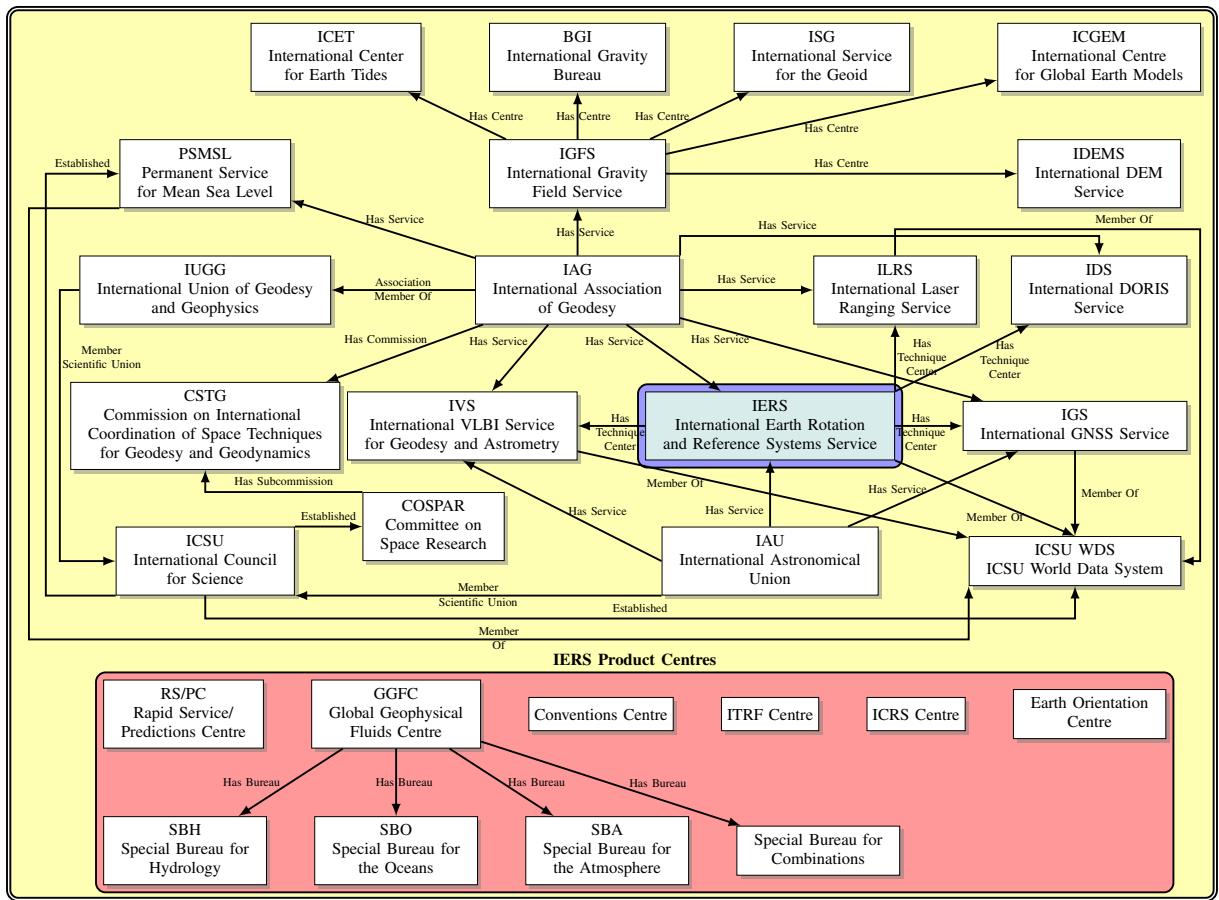
Fig. 2: A subset of the tangled web of international organizations behind many of the standards that form the basis of terrestrial and celestial coordinate systems. The IERS is the primary organization in internationally standardizing celestial and terrestrial coordinate systems, which are described in its conventions [257]. The ICSU WDS is a multidisciplinary organization that supplanted the Federation of Astronomical and Geophysical Data Analysis Services (FAGS). The ISG used to be known as the International Geoid Service (IGeS). A number of professional organizations, such as the Institute of Navigation (ION), as well as many governmental organizations, including the NGA and the Naval Observatory in the United States, also play a role in establishing standard coordinate systems.

A number of coordinate systems defined in the IERS conventions [257] are related to each other in Fig. 3. Though other celestial and terrestrial coordinate systems exist, such as the International Astronomical Union's (IAU's) galactic coordinate system [31], most such systems are not as useful to engineers designing tracking algorithms. The primary coordinate system for tracking distant objects in space, such as planets, meteors, or stars, is the BCRS. It is the ICRS with barycentric coordinate time (TCB) defined as the timescale. Whereas in relativity theory there is no "absolute rest" so all motion must be defined in a relative manner, there does exist an absolute state of non-rotation as exemplified by Mach's paradox [187, Ch. 3.1.5]. The ICRS defines a non-rotating, approximately inertial coordinate system whose origin is at the center of mass of the solar system, but does not explicitly define a timescale. Inertial or pseudo-inertial coordinate systems are useful for expressing orbital or ballistic dynamics as they avoid the need for "phantom" acceleration, such as the Coriolis effect, as explained in Appendix A.
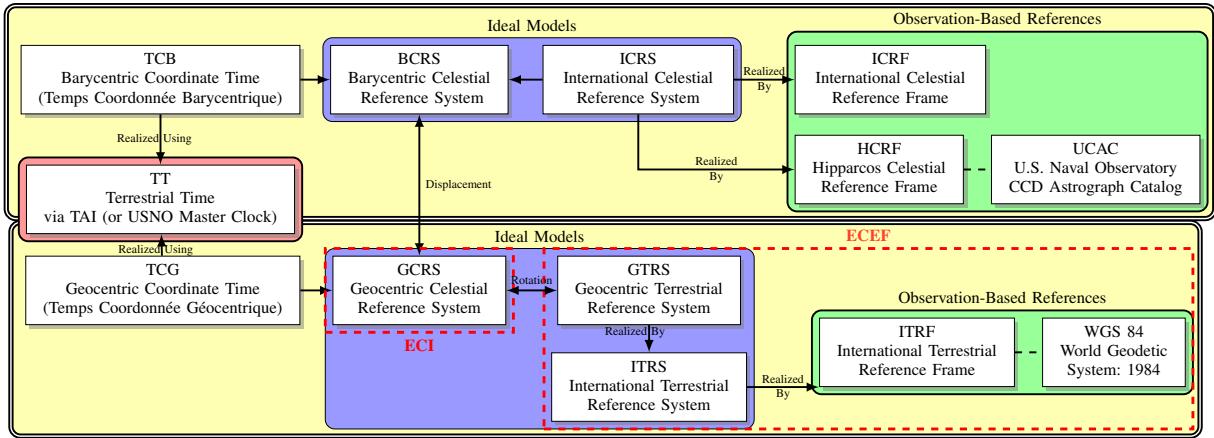
Fig. 3: The base coordinate system for tracking in the solar system is the BCRS, which is the ICRS, which has no explicit time component, with TCB added as time. The ICRS is realized using star catalogs as the ICRF in radio wavelengths and the HCRF in optical wavelengths. Alternatively, the UCAC can be used in place of the HCRF for more precise results. The pseudo-inertial reference frame for tracking near-Earth objects is the GCRS, which is a type of ECI coordinate system. The GCRS is related to the BCRS by an affine transform, placing its origin at the center of the Earth and using an appropriately relativistically scaled timescale, the TGB. The GTRS is a fixed-Earth model of which the common realization is the ITRS, whose definition is consistent with many models of the past. The ITRS is realized through the ITRF, which is essentially the same as the current version of the WGS 84 standard, except for the definition of the reference ellipsoid. Conversions between frames can be complicated and are generally performed with the aid of two intermediate reference frames, nam[...]the Terrestrial Intermediate Reference System (TIRS) [187, Ch. 9] [...]a timescale other than TCG.

On the other hand, the GCRS has its origin loca[...]geocentric coordinate time (TCG) scale but the orienta[...]axes. In much of the target tracking literature, whe[...]ballistic missiles, a nebulously defined Earth-centered[...]as realized using observation-based references can be a[...]for tracking.

The timescales associated with each of the coordinate systems are inherently linked to the *location* of the reference clock when determining the simultaneity of events to an extremely high precision. This is because, as discussed in [145], special relativity theory tells us that events that appear simultaneous to one observer might appear non-simultaneous to another moving observer, even after accounting for the propagation time of light. The offset between the clocks of the observers depends on their relative velocities. Thus, by defining the reference "clock" for TCB to be at the center of mass (or inertia) of the solar system and the reference clock for TCG to be located at the center of mass of the Earth, one defines time scales that are linked to spatial coordinate systems in which events can be deemed simultaneous or not. The relativity of simultaneity is usually ignored, but can be significant depending on the application. For example, as described in [4], one must account for the relativity of simultaneity to get GPS localization accuracy down to below one meter. The necessity of defining high-precision coordinate systems simultaneous with timescales arises from the link between space and time in relativity and theory and is discussed in more detail in Section 3.

Figure 4 shows the alignment of the axes in the BCRS and GCRS coordinate systems, which is that of the ICRS. The "celestial sphere" just represents sets of directions in space. The idea comes from the fact that the stars in the sky somewhat look as if they are placed on a faraway sphere (they are all around). The alignment of the axes is defined with respect to a specific date (called an epoch). The reference epoch for the ICRS is called J2000.0, which refers to noon (1200 hours) in terrestrial time (TT) on 1 January 2000 in the Gregorian calendar (the standard calendar used throughout most of the world today). Terrestrial time is shortly before noon time coordinated universal time (UTC) on that same date.
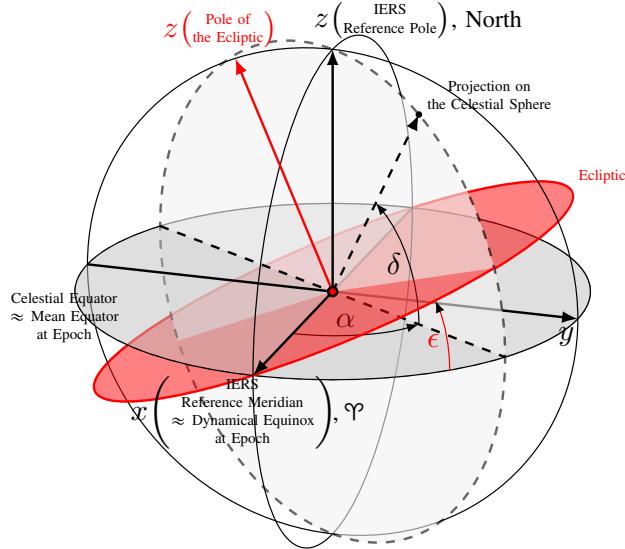
Fig. 4: The BCRS and GCRS coordinate systems have the same alignment of axes, that of the ICRS. In the BCRS, the origin is at the barycenter of the solar system. In the GCRS, it follows the center of mass of the Earth. The x-axis (sometimes labeled ♈) points approximately in the direction of the mean vernal equinox at epoch, and the celestial equator is approximately the mean equator at epoch. The mean ecliptic at epoch intersects the celestial equator along the x-axis. Over time, the ecliptic can shift. The z-axis is chosen to be in the direction of the northern hemisphere, perpendicular to the celestial equator. The y-axis completes a right-handed coordinate system. Right ascension α (celestial longitude) and declination δ (celestial latitude) form a spherical coordinate system. The angle of the ecliptic to the celestial plane ε is known as the obliquity of the ecliptic.

The orientation of the axes in the ICRS is nominally based on the orientation of the mean equator and dynamical equinox at the reference epoch. The *x*- and *y*-axes are in the plane of the celestial equator with the *x*-axis (also known as the origin of right ascension) pointing toward the dynamical vernal equinox at epoch.[17] The *z*-axis is orthogonal to the plane of the celestial equator and points in a general northerly direction. The celestial equator is the projection of the Earth's equator onto the celestial sphere. The ecliptic is a circle projected on the celestial sphere that coincides with the orbit of the Earth around the Sun and is tilted roughly 23.4° from the celestial equator along the *x*-axis [285, Ch. 3.53]. The ecliptic is the same as the apparent direction of the Sun in the sky as the Earth orbits the Sun. An equinox is when the ecliptic intersects the celestial equator. That is, the equinox occurs when the Sun appears to pass through these points in the sky. There are two equinoxes each year. The vernal equinox occurs when the Sun appears to be going from South to North in the sky. In reality, the ecliptic is not a perfect circle and the equator of the Earth wobbles with respect to the celestial sphere. Thus, the ICRS is nominally defined in terms of mean values of these quantities.

As noted in [354], practical systems align their axes based on the locations of stars, so the precise definitions of the mean equator and dynamical equinox at epoch (which are complicated) do not matter in practice. The International Celestial Reference Frame (ICRF) is a realization of the ICRS based on observations of the radio-emitting stars [257, Ch. 2.2], with the current version being the ICRF2, which is documented in [147] and can be downloaded from `http://hpiers.obspm.fr/icrs-pc/` . When using visible-light stars, the Hipparcos Celestial Reference Frame (HCRF) is a realization of the ICRF [257, Ch. 2.2], documentation and data for which can be found at the links in Table 2. However, only the most distant stars make good points of reference, as their angular displacements in the sky are minimal over time. For example, Fig. 5 illustrates the predicted motion of the stars near Barnard's star over a period of 80 years. Barnard's star has the highest proper motion in the ICRS, though it is not the angularly closest star next to the Sun.[18]

Since the Hipparcos catalog does not have a sufficiently high density of stars for very precise alignment in a small region, the U.S. Naval Observatory Charge-Coupled Device (CCD) Astrograph Catalog (UCAC) might often be preferred for high-precision applications [370]. The UCAC (the current version is UCAC4) is very large and cannot be downloaded, but can be obtained for free on digital versatile disc (DVD) as described in `http://www.usno.navy.mil/USNO/astrometry/optical-IR-prod/ucac` . If one simply wishes to look up the identity of a single star in the sky, the Set of Identifications, Measurements and Bibliography for Astronomical Data (SIMBAD) database can be used online, accessible through the Strasbourg Astronomical Data Center (CDS) at `http://cdsweb.u-strasbg.fr` , and also described in [358].

Whereas the axes of the BCRS and GCRS can, in practice, be determined from distant stars, the origins of the respective coordinate systems are more difficult to find. The origin of the BCRS is the barycenter of the solar system. However, the center of mass of the solar system is not something that can be directly measured from Earth, rather it must be inferred based on observations of planetary motion. The mathematics behind such determinations are very complicated due to the necessary inclusion of relativity theory [187, Ch. 4, 5,

---

[17]The symbol ♈, which also marks the *x*-axis in Fig. 4, represents the zodiacal constellation Aries. In ancient Greek times, the vernal equinox pointed in the direction of Aries. Nowadays, it points toward the constellation Aquarius due to precession (precession is discussed in detail in Appendix E). A brief discussion on the history of the constellations and the zodiacal precession is given in [280].

[18]Barnard's star is too dim to see with the naked eye.
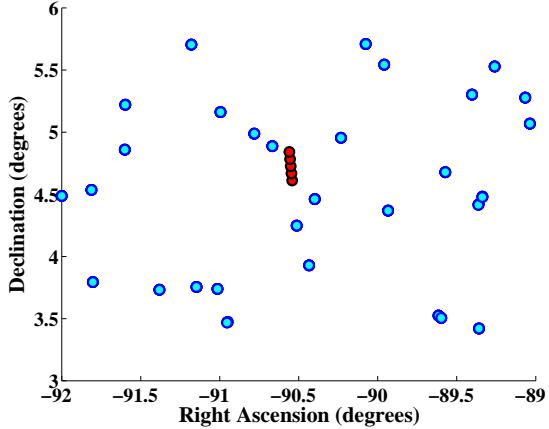
Fig. 5: The right ascension and declination in the ICRS of the stars near Barnard's star (in red) over a period of 80 years based on data in the Hipparcos catalog (Barnard's star is catalog entry 87937). One can see that Barnard's star has a large proper motion (the overlapping red circles), whereas the other stars barely move. The declination of the star is increasing as time progresses. The plot demonstrates how not all stars are poor for use as reference points in defining a non-rotating celestial coordinate system due to their large motion over the years. The function `iauPmsafe` in the IAU's Standards of Fundamental Astronomy (SOFA) library was used to change the epoch of the data. The points in red are at the epoch of the Hipparcos catalog (1994.25 TT), and 20 Julian years prior and 20, 40, and 60 Julian years posterior to the epoch of the catalog (a Julian year being precisely 365.25 days).

6]. In practice, precomputed planetary ephemeris tables,[19] or programs for efficient ephemeris calculation based on such tables, are generally used. Given a set of ephemerides and a time, one can relate the position of the Earth (and a terrestrial observer) to the barycenter.[20] The IERS conventions use the development ephemerides 421 (DE421) of the National Aeronautics and Space Administration (NASA) Jet Propulsion Laboratory (JPL) as the ephemerides for the ICRS standard [257, Ch. 3]. However, the DE421 ephemerides have been supplanted by the newer DE430 ephemerides, which can be obtained along with the code to use them through the site for the Spacecraft Planet Instrument C-matrix Events (SPICE) toolkit listed in Table 2. Note that the BCRS coordinate system uses TCB as its time parameter, whereas the DE421/ DE430 ephemerides use barycentric dynamical time (TDB) as described in [187, Ch. 9.5].

As most individuals designing target-tracking algorithms are concerned with near-Earth objects, the GCRS and Geocentric Terrestrial Reference System (GTRS)[21] are the most relevant coordinate systems. Both coordinate systems have their origin located at the center of the Earth and use TCG as their timescale, the rate that a theoretical clock located at the center of the Earth would tick if the mass of the Earth were not present.

---

[19]Ephemerides are tables of the position of celestial bodies as a function of time.

[20]Rather than relying on Earth-based detections, in the future, spacecraft might make use of pulsars for navigation. In [24], it was theoretically shown that mean position errors as low as 5 km might be possible when using three X-ray pulsars for navigation in space.

[21]The GTRS used to be known as the Conventional Terrestrial Reference System (CTRS) [257, Ch. 4.1.4].

The GCRS is the ECI coordinate system most relevant for target tracking. The GCRS is not a truly inertial frame of reference, because the origin of the system is in constant acceleration about the Sun. However, the equivalence principle of general relativity theory [187, Ch. 3.1.3, 3.1.4] states that locally,[22] the effects of gravity are indistinguishable from the effects of an accelerated coordinate system. Consequently, an observer in free fall would be unable to perform local experiments to tell that he is not in a co-moving inertial coordinate system. Consequently, the GCRS is often used as an approximately inertial frame for satellite tracking or for describing the motion of ballistic objects near the Earth. Since the axes of the GCRS are oriented in the same manner as the ICRS, stars in the form of the ICRF2 or other star catalog can be used to determine the alignment of the axes.

The GTRS is essentially the same as the GCRS, except it rotates with the Earth. The GTRS is an ECEF coordinate system for tracking. The orientation of the axes of the GTRS are determined by the ITRS, which is the GTRS without the time component. The ITRS is realized through the ITRF [257, Ch. 4], whereby the center of mass and the rotational angle of the Earth are determined using relativistic modeling and measurements from a network of observation stations through the technique centers of the IERS: the International Doppler Orbitography and Radiopositioning Integrated by Satellite (DORIS) Service (IDS), which uses Doppler techniques for celestial and terrestrial positioning; the International Laser Ranging Service (ILRS), which analyzes the orbits of the Laser Geodynamics Satellites (LAGEOS); the International GNSS Service (IGS), which provides a number of services based on global navigation satellites; and the International Very Long Baseline Interferometry (VLBI) Service for Geodesy and Astrometry (IVS), which precisely measures the rotation angle of the Earth based on distant quasars. When high-precision conversions between celestial and terrestrial coordinate systems are necessary, external Earth-orientation parameters as described in Table 3 are needed. Though research such as reported in [45,229] has provided insight into how changes in the Earth's rotation axis are correlated with other observable effects, Earth-orientation parameters cannot be predicted over long periods of time and must be obtained through observation.

Table 3: Earth-Orientation Parameters Necessary to Precisely Link ECEF and ECI Coordinate Systems

Orientation Parameter	Description
ΔT	$\Delta T \triangleq t_{\text{TT}} - t_{\text{UT1}}$. This quantity varies with changes to the Earth's rotation rate.
LOD	Length of day. The derivative of the ΔT with respect to TAI; proportional to the Earth's angular velocity.
dX,dY	Celestial pole offsets. Offsets of the modeled rotation axis to the true rotation axis in the GCRS.
dx,dy	Coordinates of the pole. Offsets of the modeled rotation axis of the Earth to the true rotation axis in the ITRS (i.e., with respect to the Earth's crust).

Celestial pole offsets are usually less than 1 mas in each coordinate and the coordinates of the pole are normally less than 600 mas in each coordinate as can be ascertained by plotting historical data from the sources in Table 2. On the other hand, ΔT is steadily increasing and as of 1 April 2014 was approximately 67.4 s according to the U.S. Naval Observatory's long-term parameters at the source in Table 2. ΔT is sometimes defined as a difference with respect to TAI or UTC and/or with a flipped sign. NOTE: As per the IERS conventions, tide and libration effects should be added to the celestial pole offsets via the function referenced in Table 2 before use.

---

[22]That is, in a sufficiently small region such that gravity appears to be uniform.

Table 2 lists the sources of Earth-orientation parameters used in this report. If one does not need better than arcsecond precision, then the celestial pole offsets, the coordinates of the pole, and the length of day (LOD) can be assumed to be zero. On the other hand, a rough estimate of the ΔT parameter is generally necessary. A low-precision estimate is to just use the cumulative number of leapseconds added to UTC. Section 3.2 describes LOD and ΔT in more detail as the parameters relate to various timescales. Note that some of the Earth-orientation parameters from the sources in Table 2 have been modified to have short-term tides removed so as to simplify interpolation. Such tidal effects must be added back using the software listed in the table.

Figure 6 shows how to convert between celestial and terrestrial coordinate systems using functions from the International Astronomical Union's (IAU's) standards of fundamental astronomy (SOFA) library. The equinox-based transformations, namely, the J2000.0 dynamical reference system as well as the mean-of-date (MOD) and true-of-date (TOD) reference systems, are older celestial coordinate systems that must be taken into consideration when using older celestial data. For example, the U.S. Navy's astronomical almanac [70] lists approximations for the locations of the Sun and the Moon in "apparent" coordinates, which are synonymous with the "true-of-date" reference system. When converting velocity and acceleration measurements between the ITRS and GCRS coordinate systems, one must account for the rotation rate of the Earth, which offsets the velocity and introduces additional accelerations due to the Coriolis effect, as discussed in Appendix A.

Figure 7 shows how to convert from a number of outdated coordinate systems to the ITRS. The True Equator Mean Equinox (TEME) system is used in the Simplified General Perturbations 4 (SGP4) orbital propagation algorithm, which is presented with code in [142, 339]. The TEME system is only of modern interest because the U.S. Strategic Command (USSTRATCOM)/the North American Aerospace Defense Command (NORAD) publishes/has published[23] satellite ephemerides in the form of "two-line element" (TLE) sets[24] that are given in the TEME coordinate system. Figure 7 also shows an older TOD coordinate system of which one should be aware to avoid confusion with the modern TOD reference system when reading older literature. One should avoid using the coordinate systems in Figure 7 in new tracking algorithms as they are based on outdated theories.

If one wishes to simply convert between GCRS and ITRS coordinates, then one might also want to consider the free[25] Naval Observatory Vector Astrometry Software (NOVAS) [337], which has the functions `ter2cel` and `cel2ter` to perform the conversions in one step. The NOVAS and SOFA routines for ECEF/ECI conversion are compared in [233] and are shown to convert directions between the coordinate systems to within microarcsecond precision of each other. The microarcsecond difference is because the SOFA code includes some minor corrections to nutation that are absent from the NOVAS code.

The origin of the ITRF2008, which is the latest realization of the ITRS, is not defined as the true center of gravity of the Earth. Rather, it uses a position averaged over time [257, Ch. 4]. Consequently, deformations of the Earth due to tides and other effects can shift the true center of gravity with respect to the reference frame, an effect termed "geocenter motion." Ground-based stations that form points of reference for satellite navigation systems to establish their coordinate systems with respect to the ground move relative to the true

---

[23]The TLEs are available from USSTRATCOM at `http://www.space-track.org` (registration required) and for certain satellites from `http://www.celestrak.com/NORAD/elements/`.

[24]The format of a TLE is described in [71].

[25]The NOVAS and SOFA libraries are free and, though one should check with a lawyer, it appears that the code can be incorporated into commercial products with just an acknowledgement to the source.

center of mass of the Earth due to the motion of the atmosphere, tides, and tectonic motion [363]. Models for such motion are given in [257, Ch. 7], [364, Ch. 5.4], and [28, Ch. 2.3].

If all receivers have the same Cartesian bias in their locations with respect to the average center of mass of the Earth, then one can still track orbital debris to a high precision relative to the stations. Consequently, it makes sense to track satellites not directly in the ITRF coordinate system but in a system defined by satellites, which orbit the center of mass of the Earth, which, as noted in [363], only varies a few millimeters from its mean value. As noted in [364, Ch. 5.4], if one localizes a station using GPS satellites, then the coordinates are consistent with the changing center of mass of the Earth. The use of a dynamic center-of-mass coordinate system is discussed in [363].

Finally, it should be noted that a number of physical effects must be taken into account when computing the observed location of an object in the sky. These include delays due to the finite speed of light and parallax when changing coordinate systems, atmospheric and general relativistic refraction, and special relativistic aberration. The effects are described in somewhat more detail in Appendix I, where it is detailed how one can transform planet locations from the coordinate system in which they come (the ICRS of the J2000.0 coordinate system) into observations for an observer near the Earth. Additionally, Appendix J quantifies the magnitude of the errors introduced by special relativistic aberration when a satellite observes other satellites, as the effect is often overlooked and can produce significant time-varying measurement biases.
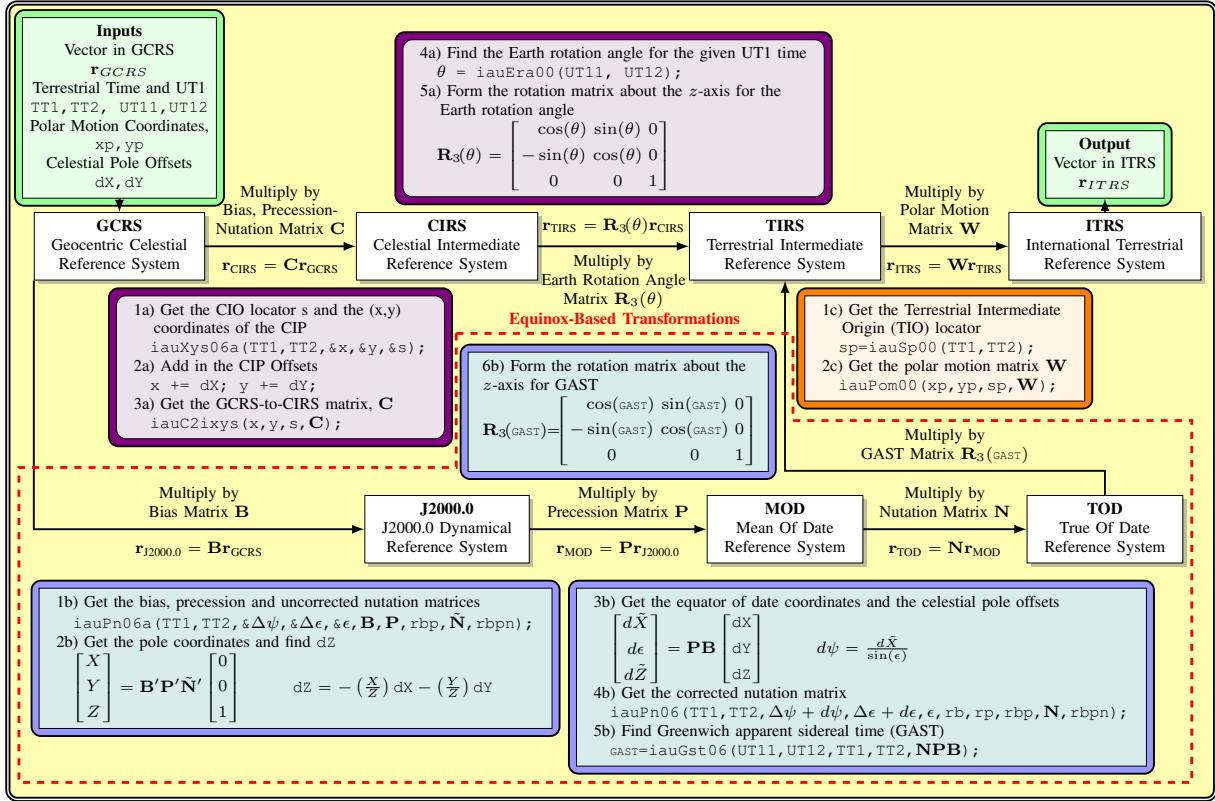
Fig. 6: Transformations between the GCRS, which is an ECI coordinate system, and the ITRS, which is an ECEF coordinate system. The modern transformation uses steps 1a–5a to get to the TIRS through the CIRS. An older, equinox-based method goes through three intermediate coordinate systems to get to the TIRS, using steps 1b through 6b. Steps 1c and 2c are used to compute the matrix to go from the TIRS to the ITRS. The functions referenced for some of the transformations refer to C-function calls in the IAU's SOFA library when using the IAU 2006/2000A precession-nutation model. Appendix E describes the origin and difference between precession and nutation. The full transformation using the modern celestial intermediate origin (CIO)-based model is $\mathbf{r}_{\text{ITRS}} = \mathbf{W}\mathbf{R}_3(\theta)\mathbf{C}\mathbf{r}_{\text{GCRS}}$. When using the equinox-based method, the transformation is $\mathbf{r}_{\text{ITRS}} = \mathbf{W}\mathbf{R}_3(\text{GAST})\mathbf{N}\mathbf{P}\mathbf{B}\mathbf{r}_{\text{GCRS}}$. Terrestrial time and universal time 1 (UT1), which is a measure of the Earth's rotation angle, are assumed to be given as two-part Julian dates. To convert terrestrial time to universal time, the function `iauTtut1(TT1,TT2,deltaT,&UT11,&UT12);` from the IAU's SOFA library can be used with the Earth-orientation parameter `deltaT`, which is the difference between TT and UT1. The polar motion coordinates and the celestial pole offsets are assumed to be given in radians. The inclusion of the celestial pole offsets in the equinox-based transformation is based on the technique of [175]. Inverse transformations are straightforward as all matrices are rotation matrices and the transpose of a rotation matrix is its inverse. Combinations of functions for more direct transformations between coordinate systems are tabulated in [137]. Note: the conversions for UT1 above are IERS-compliant. However, the WGS 84 coordinate system omits certain terms when computing UT1 for GPS satellite ephemerides [69, Ch. 2.1].
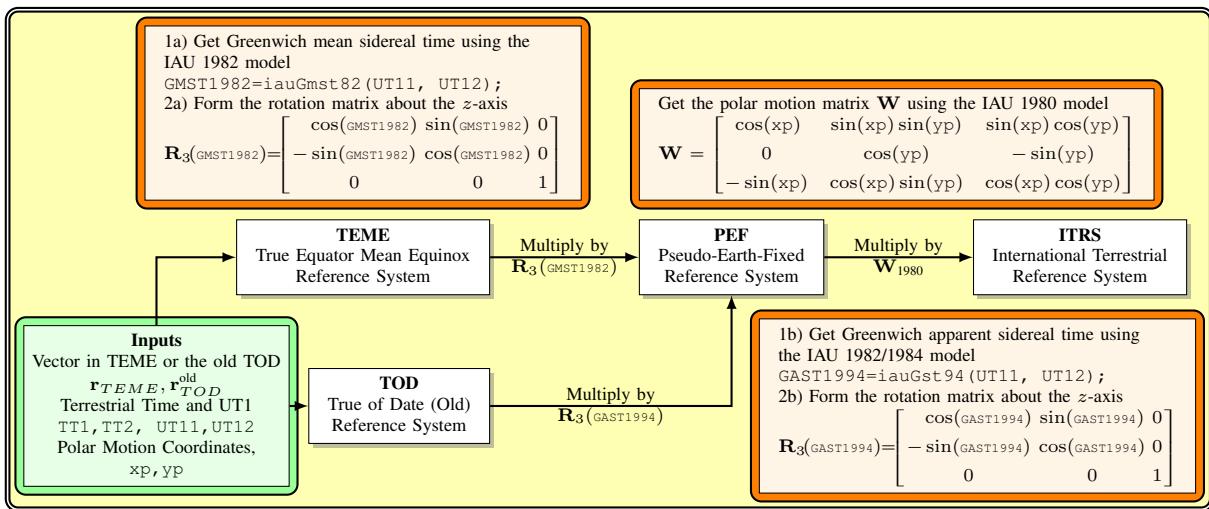
Fig. 7: The transformation between the TEME, which is a non-standard coordinate system used with the two-line element sets published by NORAD for the old SGP4 orbital propagator, and the ITRS, as ascertained from [340]. Also shown is the transformation between an outdated TOD system, which one should be aware of to avoid confusion with the more modern TOD in Fig. 6. Note that an outdated MOD system (related to the TOD system by a nutation correction) also exists. Relationships between older and modern coordinate systems are mapped out in [341]. The function references refer to C-function calls in the IAU's SOFA library. The polar motion coordinates are two of the Earth-orientation parameters. Terrestrial time and UT1, assumed given as two-part Julian dates, are related as described in the caption to Fig. 6. The TEME coordinate system shown is an "of date" system. A "mean" TEME coordinate system is also mentioned in the literature, but appears to not be in use.

3. TEMPORAL COORDINATE SYSTEMS

3.1 Defining Basic Temporal Coordinate Systems

The precise timing reference mandated for use by the United States (U.S.) Department of Defense (DoD) is the U.S. Naval Observatory's (USNO's) master clock [338]. However, the U.S. Navy does not single-handedly determine the time in the United States, but rather works in collaboration with a number of international organizations to determine standard timescales. Figure 8 maps out part of the complicated web of international organizations and national laboratories that determine the time around the world. Two good monographs for understanding the evolution and construction of the standard timescales maintained by these organizations are [226] and [16].
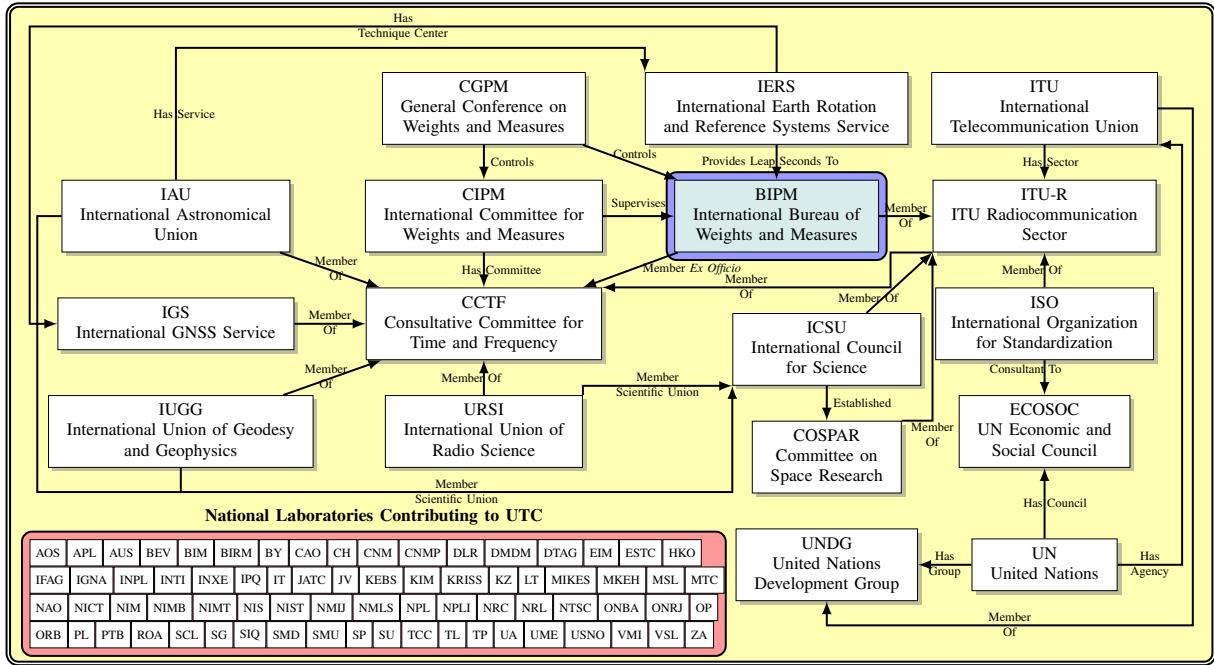
Fig. 8: A subset of the web of international organizations and national laboratories that contribute to the definition of international time standards. The BIPM is the primary organization responsible for determining UTC, though the ITU-R is the primary international legal authority for changes in the standards. The abbreviations for the labs correspond to those associated with the published deviations of national timescales from UTC and TAI given in `ftp://ftp2.bipm.org/pub/tai/publication/cirt/cirt.309` as of 9 October 2013. For example, NRL and USNO refer to the Naval Research Laboratory and the U.S. Naval Observatory in Washington, DC; DLR refers to the Deutsche Zentrum für Luft- und Raumfahrt in Oberpfaffenhofen, Germany, and OP stands for the Observatoire de Paris in Paris, France. A list of the acronym definitions is given in Appendix M.

The International Telecommunication Union (ITU) is an international agency created by the United Nations (UN) that, among other things, coordinates the shared global use of the radio spectrum, manages geostationary satellite orbital positions, and plays a significant role in defining legally binding international time

standards [23, 154].[26] Specifically, Working Party 7A (Time Signals and Frequency Standard Emissions) of Study Group 7 (Science Services) of the Radiocommunication Sector (ITU-R)[27] of the ITU is responsible for work related to time standards. However, the ITU does not solely determine the time internationally. The Convention of the Metre, an international treaty signed in 1875 and amended in 1921,[28] established the International Bureau of Weights and Measures (BIPM),[29] which is currently located in Sèvres, France, under the authority of the International Committee for Weights and Measures (CIPM), which itself is under the authority of the General Conference on Weights and Measures (CGPM), which is formed of delegates of all of the signing countries.[30] The CGPM is presided by the president of the French Academy of Sciences.

The BIPM manages a number of international timescales, the most notable being international atomic time (TAI), terrestrial time, and UTC [10].[31] UTC is TAI offset by leap seconds; terrestrial time is something of a frequency-stabilized version of TAI, but is offset from TAI by a constant number of seconds that has no relation to leap seconds and does not change. Some disagreement on the legal authority of BIPM over UTC, compared to the ITU, exists [265]. The U.S. Naval Observatory's clock maintains a representation of UTC, which is fed into the BIPM. BIPM combines the results with clocks from many different laboratories around the world [338]. Abbreviations for participating laboratories are shown in Fig. 8. BIPM then combines the time measures and feeds the results back to the national laboratories. The representation of UTC kept at a particular laboratory is given by UTC(k) where k is the abbreviation of a laboratory name [226, Ch. 13.4]. For example, UTC(MIKES) refers to the time maintained by the Center for Metrology and Accreditation[32] in Finland and UTC(USNO) refers to the time maintained by the U.S. Naval Observatory in Washington, DC.

The time feedback process between national laboratories and the BIPM is outlined in [16, Ch. 7.2], [226, Ch. 13.5], [10]. The details of the methods for transferring time between stations can vary, but generally involves the use of satellites to compare times between different laboratories. The realizations of TAI from different laboratories are combined at the BIMP to get the échelle atomique libre (EAL).[33] The EAL does not form the official realization of TAI at the BIPM because it can jump discontinuously as new time differences from the national laboratories comes in. Thus, a steering algorithm is used with various frequency standards at the BIPM to obtain a realization of TAI with no jumps. TT is a smoothed form of TAI plus a constant offset of 32.184 s [256].

While not directly involved in timekeeping, the International Organization for Standardization (ISO) plays a role in defining a number of aspects of how times and dates are formatted. For example, the ISO 8601:2004 standard[34] specifies how dates, times, and time intervals should be specified.

---

[26]Many of the ITU's time and frequency standards can be downloaded free at `http://www.itu.int/rec/R-REC-TF/`.

[27]The ITU-R was formerly known as the International Radio Consultative Committee (CCIR).

[28]The text of the amended Convention of the Metre is available (in French) at `http://www.bipm.org/utils/en/pdf/metre_convention.pdf`.

[29]Many of the acronyms do not correspond to the words that they are abbreviating, because the acronyms come from French. Such acronyms are tabulated in Appendix M.

[30]As listed at `http://www.bipm.org/en/convention/member_states/`, the United States is a member state, having signed in 1878.

[31]Greenwich mean time (GMT) is an obsolete time standard that came before UTC and that no longer exists. Presently, the term GMT is generally used to mean UTC, especially in the United Kingdom.

[32]The acronym MIKES comes from Mittatekniikan keskus in Finnish.

[33]No English translation of the scale's name is in wide use. The term "échelle atomique libre" means "free atomic scale."

[34]The ISO 8601:2004 standard can be purchased for 134 Swiss francs (about 147 U.S. dollars) at `http://www.iso.org/iso/catalogue_detail?csnumber=40874`. It is the opinion of the author that charging such high prices for fairly basic standards impedes their widespread adoption, thus hindering the mission of the ISO.

Figure 9 outlines the relationship between timescales that tend to be the most relevant for target-tracking algorithms. The timescales used internally in existing and developing GNSS, GPS (United States), Galileo (European Union), GLONASS (Russia), and BeiDou (China) are particularly relevant since such satellites are often used to synchronize clocks. BeiDou time (BDT), GPS time (GPST), and Galileo system time (GST) are all offset from TAI; the number of leap seconds needed to obtain UTC is also broadcast by the satellites. The times of the satellite systems are only notionally related to TAI by the given offsets as shown; the real times in the satellites can vary but are kept within certain error tolerances. For example, the BeiDou interface control document [48] states that BDT will remain within 100 ns of UTC as given by the National Time Service Center of the Chinese Academy of Sciences (NTSC), written as UTC(NTSC). Similarly, GPS timescale is held within 90 ns of UTC(USNO) [11] though offset by an integer number of seconds.
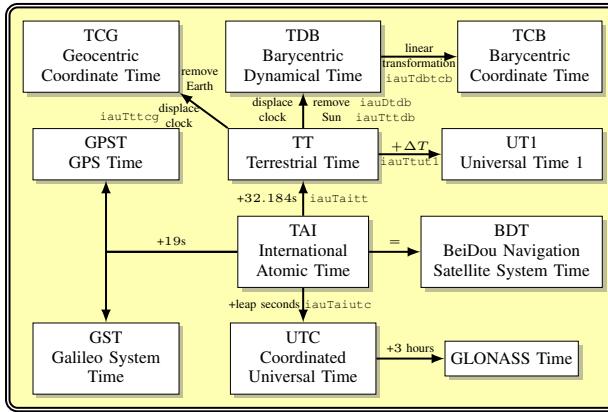
Fig. 9: The relationship between major modern timescales. Functions in the IAU's SOFA library to perform the transformations are indicated, when available. The Earth-orientation parameter ΔT must be obtained from an outside source to compute UT1 (see Table 2). The conversion from TT to TDB requires UT1 as an additional input to `iauDtdb`. TDB is a timescale used by NASA JPL that does not use the SI second as its base unit, though its relativistic correctness is the same as TCB [313]. TDB is also sometimes referred to as ephemeris time (ET). TT is not precisely an offset form of TAI; it is computed by smoothing TAI over a period of time. The U.S. Navy's astronomical almanac uses TT for expressing ephemerides [70, Ch. B]. GPST, GST, and BDT are broadcast with leap seconds information and can thus be easily transformed into UTC. GLONASS time matches the UTC offset for the time zone in which Moscow, Russia is located.

TT, TCG, and TCB have very specific definitions in terms of relativity theory. All are "coordinate" times, which has a certain meaning in terms of correctness to relativity theory and that should not be confused with a "coordinated" time, which is a standard time formed from multiple clocks. Special relativity theory plays a role in establishing a temporal coordinate system because moving clocks tick more slowly. General relativity theory also plays a role in standardizing timescales because clocks can tick at different rates depending upon the distribution of massive objects around them. Near the Earth, clocks tick faster at higher altitudes. Figure 10 illustrates how a clock on a satellite at varying altitudes is biased compared to TCG. The relativistic bias causes a frequency bias, when viewed by a TCG observer, that translates into a range-rate bias when performing detection. Overviews of the role of relativity theory in time synchronization are given in [16, Ch. 3] [226, Ch. 7,8] and a good overview of basic relativistic physics and its relation to standard coordinate systems and dynamic models is given in [187].

(a) Bias After One TCG Day   (b) Bias of a 2 GHz Clock
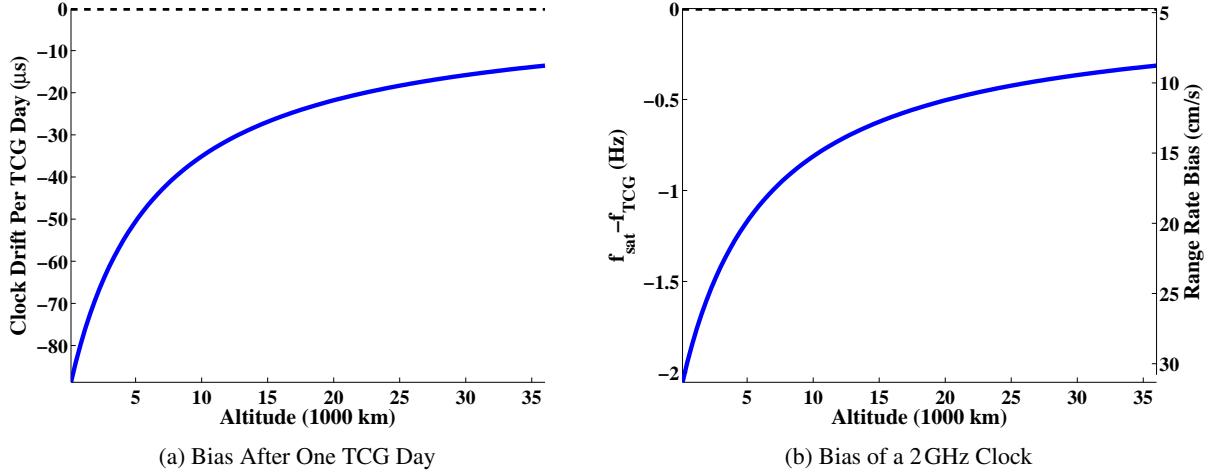
Fig. 10: Time dilation resulting from general and special relativity cause clocks on satellites to become biased compared to TCG, as plotted. The plots are relative to a TCG observer because the rate difference of a clock on a satellite and an (inertial) geocentric observer is time-invariant. With respect to an observer on the ground or another satellite, however, special relativity dictates that the bias varies with time since the relative velocities of the objects vary with time. Figure (a) is the time on a satellite clock minus the TCG time after one TCG day. A clock offset causes an offset in frequency. Figure (b) assumes that the satellite broadcasts a 2 GHz signal. The figures show the clock bias and the bias in the range-rate measurement due to ignoring relativity. The altitudes range from 100 km to 36,000 km, which is just above the altitude of a geosynchronous equatorial orbit. Appendix C provides more details in how the plots were computed.

TT is based on the rate that a clock located on the geoid, a hypothetical surface of equal gravitational potential of the rotating Earth defining mean sea level (MSL),[35] would tick (Section 4 discusses the geoid in more detail). Precise clocks at different altitudes on the Earth must correct for altitude to remain synchronized to TT (or TAI/UTC) when reporting to the BIPM. Measurement models including the effects of relativity on radar and optical measurements have been previously studied [158, 184, 323] [187, Ch. 7][36] and must often be considered when designing high-precision tracking algorithms for objects in space. Relativity theory affects more than just the rate at which different clocks in a detection system tick. Indeed, as explained in [145], special relativity can paradoxically cause non-collocated events that are simultaneous in one frame of reference to not be simultaneous in another frame of reference. Relativist corrections are essential for the accurate operation of GPS receivers [13] [364, Ch. 5.3]. For example, GPS signals are broadcast on 20.46 MHz wide bands at 1575.42 MHz and 1227.6 MHz carrier frequencies, which are derived from a common 10.46 MHz source [11, Sec. 3.3.1.1]. The source and carrier frequencies are only nominally defined for an observer on the ground. The true rate of the driving clock inside the satellite is 10.22999999543 MHz, whereby the 10.46 MHz comes from using special relativity to deal with relativistic

---

[35]Note that the both the gravitational potential of the geoid *as well as the handling of the permanent tide* must be provided to have a unique definition of MSL. The necessity of specifying the permanent tide model is often overlooked and is discussed in more detail in Section 6.

[36]Those interested in visualizing the effects of special relativity alone to gain a more intuitive understanding might have fun playing with some of the games created as part of the Massachusetts Institute of Technology's Open Relativity project [230].

time dilation relative to an average ground-based observer. Thus, satellite-based observers trying to use GPS need to make different adjustments.

TCG is a timescale defined as the rate a clock at the center of mass of the Earth would tick if the Earth were not present (and there were no Earth-rotation effects). Similarly TCB is a timescale defined as the rate a clock at the center of mass of the solar system would tick if all of the massive objects in the solar system were removed. TDB is a timescale similar to TCB that has been linearly transformed to remain closer, on average, to TT than TCB does. No clock directly measures TCG or TCB. Such coordinate timescales must be computed rather than measured.[37] When tracking targets in orbit around the Earth, TCG is a good approximation to a fully relativistically correct timescale to use in the tracker, whereas when tracking objects far in the solar system (or for very high-precision tracking of targets near the Earth), TCB is often more precise.

Coordinate timescales stand in contrast to proper timescales in relativity theory. Proper time is the time that would be read by a clock that is collocated with an observer [187, Ch. 2.2.4.6] [226, Ch. 7.4]. Observers moving at different relative velocities will not agree on the simultaneity of events. This comes up when using high-precision ephemerides. For example, the NASA SPICE toolkit, which can be downloaded from the link in Table 2, can be used with various sets of ephemerides to determine the location of the planets at a particular time. The time unit used for the ephemerides is TDB, which is a barycentric coordinate time linearly related to TCB. One could use the function `iauDtdb` in the IAU's SOFA library to convert from TT at the location of an Earthbound observer to TDB. The function `iauDtdb` uses the algorithm of [84] and requires the geocentric location of the observer because the Earth rotates and observers at different locations experience different proper times, meaning that the relative offsets between their clocks and TCB or TDB differ. Coordinate time is any unambiguous reference frame with respect to which various proper timescales can be compared. The fact that rotation is included in the definition of TT means that the definition of the relevant geoid includes the effects of general relativity (from gravity) and special relativity (due to the motion). Such a definition of the geoid including the rotation of the Earth is present in the WGS 84 standard [69], which is the coordinate system underlying GPS.

The link between time, motion, and position means that in high-precision applications, temporal and positional coordinate systems cannot be treated separately. This connection between time and space is one of the many reasons why Fig. 8 includes the IERS as well as the IAU, the IGS, and the International Union of Geodesy and Geophysics (IUGG), who all play important roles in the development of international positional coordinate systems, which are discussed in Section 2. Many such organizations are united through the ICSU. Despite its widespread standardization, UTC itself is not directly appropriate for use in target-tracking algorithms because it is a discontinuous timescale. UTC is occasionally adjusted with "leap seconds" to keep it relatively in synch with a timescale called Universal Time 1 (UT1), which is a timescale based on the rotation angle of the Earth with respect to distant quasars in space [226, Ch. 2.7, 14, 17] and to the location of a theoretical mean Sun. The distant quasars define the ICRF set by the IERS [257, Ch. 2.2], which is discussed in more detail in Section 2. Note that the current version (G1762) of the WGS 84 standard [69, Ch. 2.1] is not fully consistent with the IERS conventions, because it omits librations and polar motion when computing UT1. This matters when using government-provided precise ephemeris data

---

[37]It would be nice to have a universal timescale that can be directly measured anywhere in the universe regardless of the observer's motion and position in gravitational fields. However, there do not appear to be any physical processes that can be used to define such a scale. In other words "stardates," as used in the Star Trek television series, are going to have to remain fictional for the time being.

for GPS satellites. All simulations in this present report were done using an IERS-compliant routine for computing UT1.

Figure 11 illustrates the relationship between common physical, solar, and sidereal timescales. The sidereal timescales are defined only in terms of the rotational position of the Earth with respect to the vernal equinox and thus are not directly coupled to the position of the Sun on a daily basis. Note that the position of the vernal equinox with respect to distant stars slowly moves, so a sidereal day does not put an observer back in the same position with respect to the ICRS.[38] Figure 6 in Section 2 makes use of the sidereal timescales when considering equinox-based transformations, which, in light of the modern IERS conventions, are largely obsolete. Local apparent solar time (LAT) can be viewed as the time that one would measure based solely on the location of the Sun in the sky at a particular longitude. Note that as documented in [176], the East longitudes used for obtaining local mean sidereal time and local apparent sidereal time must be in the TIRS. In [224, Sec. 4.2-4.5], UT1 is presented as a definition of "Greenwich mean solar time" and is local mean solar time at $0°$ longitude.[39] As UT1 is defined in terms of a rotation in the TIRS, one can assume that the observer's East longitude for obtaining local mean solar time (LMT) must also be in the TIRS.
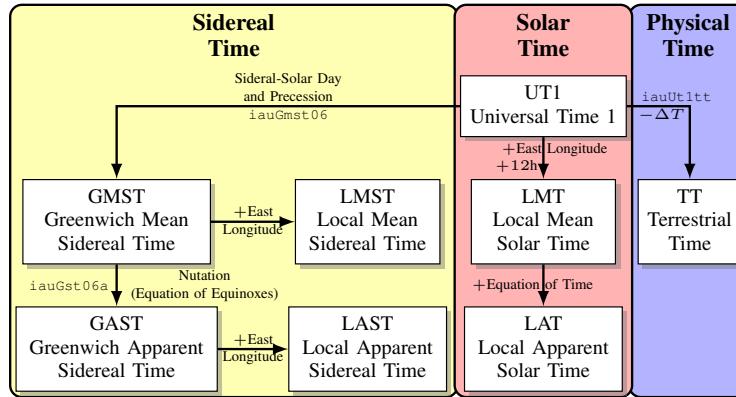

Fig. 11: The relationship between the modern physical time, TT, the modern solar time, UT1, and older solar and sidereal timescales. Functions in the IAU's SOFA library to perform the transformations are indicated, when available, though the inputs do not necessarily match the flow chart. For actual times, the East longitude of the observer is added under the convention that 2π radians ($360°$) is equivalent to 24 hours ($86,400$ seconds). Note that the East longitude is given in *TIRS coordinates*, not in ITRS coordinates, sidereal times are often given in radians, and LMT and LAT are often given in hours ($0-24$) and are thus periodic. The Earth-orientation parameter ΔT must be obtained from an outside source to compute UT1 (see Table 2). The 12 hour offset for LMT is because LMT and LAT days, when expressed as angles/hours start at midnight, not noon as in UT1. The equation of time must be obtained from ephemerides. It is tabulated in the Navy's astronomical almanac [70, Ch. C].

---

[38]The term for one rotation with respect to the ICRS is a "stellar day." The IERS lists a stellar day as $86164.098903691\,\mathrm{s}$, in comparison to sidereal day duration of $86164.09053083288\,\mathrm{s}$ and a conventional solar day (without leap seconds) of precisely $86,400\,\mathrm{s}$. A list of such constants is available from the IERS at http://hpiers.obspm.fr/eop-pc/models/constants.html.

[39]Days in UT1 begin at noon, not at midnight. Figure 11 has LAT and LMT offset from UT1 by 12 hours so that a zero hour of the day corresponds to midnight, not noon. This is the standard convention. However, if LAT and LMT are represented as a full Julian date, it makes more sense to not add the 12 hours, as the other common date formats (UTC, UT1, TAI, and TT) all reference Julian dates from noon, keeping with older conventions.

The definition of LAT is based on the "apparent" location of the Sun. However, as defined in [332, Appen. C], apparent places in astronomy take into account light-time and stellar aberration, but do not consider atmospheric refraction. LAT is not exactly the time one would read from a sundial, but it is close. One can find LAT (as an angle) by finding the local hour angle of the Sun in the TIRS and adding π radians. The local hour angle of the Sun is found by converting the direction of the Sun in the TIRS, accounting for aberration and light-time but not for atmospheric refraction, into spherical coordinates. The negative azimuth angle in spherical coordinates is the hour angle. The local hour angle is the hour angle of the Sun plus the East longitude of the receiver in the TIRS (not the ITRS). Conversion to a time of day occurs with the rule that 24 hours is 2π radians.

When a leap second is added, it occurs in all time zones around the world simultaneously (time zones are just offset from UTC by various increments). Leap seconds are added in the final minute of a particular day. That is, a minute might have 59 s or 61 s rather than 60 s. UTC cannot be set to always coincide with UT1 because UTC is meant to tick at a constant rate (minus intercalary [leap] seconds added to keep it in synch with UT1), whereas the duration of a day in UT1 varies because the instantaneous angular velocity of the Earth itself varies as a function of the positions of the Moon and other bodies in the solar system, as well as due to processes internal to the Earth. For example, the length of the day is estimated to have increased between $2.7 \, \mu$s and $6.8 \, \mu$s as a result of the 2004 Sumatra earthquake [114].

The accuracy and stability of the timescale needed in different parts of a multistatic tracking system vary. For updating target tracks, a relatively high degree of synchrony between sensors is required. In most cases, synchronizing the system to the clocks on the United States' GPS satellites will provide sufficient accuracy for tracker updates. For example, consider the case of accurately tracking a meteor. In [218], it was noted that very small meteors (with masses on the order of micrograms) detected by the Arecibo radar were observed traveling at speeds up to 63 km/s ($\approx$Mach 185), which is an order of magnitude faster than any aircraft or manmade satellite. In [226, Ch. 16.3], it is noted that timing accuracies as low as 20 ns can be obtained using GPS satellites and timing accuracies accuracies below 1 ns can be achieved using two-way satellite time and frequency transfer techniques. For an object traveling 63 km/s, a synchronization error of 20 ns corresponds to an offset of 1.3 mm in the position of the object (the amount the object moves over 20 ns); a timing error of 1 ns is a position offset of just $63 \, \mu$m. In both instances the bias is probably significantly smaller than the precision of the detecting radar.

When performing detection, the clock in the receiver needs to be very stable to measure Doppler during the measurement period. Frequency stability during such a short interval stands in contrast to the long-term time accuracy that was just discussed. In a bistatic system, frequency stability means that the clocks across sensors should be highly syntonous (have high short-term stability). For example, when transmitting a signal at a 2 GHz carrier, an offset in the frequency of the transmitting and receiving clocks of just 1.05 Hz is the same frequency offset due to the Doppler shift of a target moving 16 cm/s. Small Doppler biases also become important in Doppler-only localization applications such as in the IDS, which is a network of ground-based transmitters used by satellites for orbit determination.

When a time-synchronization accuracy only on the order of a few milliseconds is needed, as might be the case in an aviation radar network, then network time protocol (NTP) servers can be used for clock synchronization. Modern operating systems typically come with the software necessary to synchronize the clocks in computers to NTP servers over the internet. Many open-access servers, such as time-b.timefreq.bldrdoc.gov at the National Institute of Standards and Technology (NIST) in Boulder, Colorado, USA or ntp.neu.edu.cn at Northeastern University, Shenyang, Liaoning, China are available. Modern operating systems including

Mac OS X, Windows, and many versions of Unix and Linux come with software for querying network time servers.

In many applications the relative offset between two highly precise clocks is more important than the synchronization of either clock to an external timescale. For example, utilizing general relativity theory, a pair of modern atomic clocks have achieved sufficient accuracy that local variations in the geoid height can be measured to an accuracy of 1 cm (using general relativity theory) by comparing the rates of clocks in two different locations using a fiber-optic cable connection [32].

Table 4 lists a number of resources related to time transfer. Precise synchronization of a network of clocks over a wide area using global satellite systems is a complicated process. Basic training materials on the problem can be downloaded from the BIPM at the web site listed in Table 4. In practice, times and positioning obtained using GPS satellites can be improved with an augmented system. The ephemeris data (information on the orbital trajectories of the satellites) and clock corrections broadcast by each satellite are limited in precision. Users with internet connections can obtain more accurate data using the services of the IGS or the Global Differential GPS (GDGPS) System of the NASA JPL, where sub-nanosecond timing accuracies are possible. However, the GDGPS service is not guaranteed to be free. The standard for NTP communications is specified by the Internet Engineering Task Force through a number of standards listed in Table 4.

Table 4: Time Transfer Resources

Description	Internet Address
BIPM training materials for time standards and time transfer	http://www.bipm.org/ws/AllowedDocuments.jsp?ws=TAI_TRAINING
BIPM publications, including current biases of national laboratories' clocks from TAI and UTC	http://www.bipm.org/en/publications/scientif/tfg.html
ITU standards related to time transfer	http://www.itu.int/rec/R-REC-TF
GPSTk, Code for GPS localization and synchronization	http://www.gpstk.org/
Source code for GPS algorithms published in GPS Solutions Quarterly	http://www.ngs.noaa.gov/gps-toolbox/
Public network time protocol server lists	http://support.ntp.org/bin/view/Servers/
Internet Engineering Task Force standards related to the network time protocol	https://tools.ietf.org/html/rfc5905 http://tools.ietf.org/html/rfc5906 http://tools.ietf.org/html/rfc5907 http://tools.ietf.org/html/rfc5908
Real-Time Products of the IGS	http://rts.igs.org/access/
Information on the GDGPS System	http://www.gdgps.net/
Free online service for refining estimates from raw GPS data in Canada	http://www.nrcan.gc.ca/earth-sciences/products-services/land-geodetic-survey/gps-processing/online-global-gps-processing/5415

Parts of the GDGPS service are considered the intellectual property of institutions such as the California Institute of Technology and are not guaranteed to be free. However, everything else listed is free and the real-time products of the IGS are a free alternative to the GDGPS service. Current versions of Mac OS X, Windows, and many versions of Linux come with software for synchronization to an NTP server.

time to UT1 is very important for localizing oneself using the stars and for converting measurements from Earthbound observers into the GCRS or ICRS, the coordinate systems in which one is most likely to track satellites and celestial objects. For example, the maximum allowable offset between UTC and UT1 is 0.9 s [23]. Using the rotational velocity of the Earth of the WGS 84 coordinate system (given in Table 5 in Section 4.2), the maximum allowable time offset corresponds to an angular bias of 13.527 arcseconds. Considering an equatorial observer, using the WGS 84 Earth radius from the same table, the same angular bias when localizing oneself using stars corresponds to an offset on the surface of the Earth of 418.591 m.[40]

Figure 12 shows a plot of ΔT over time and a plot showing how UTC has been updated to keep in synch with UT1. In [208], a description of how ΔT is estimated based on observational data is provided. Though a number of papers try to fit curves to historical ΔT observations for purposes of interpolation and prediction [118, 156, 157, 238], the models are not accurate for long-term predictions and observational data must be used. Based upon past prediction methods, the authors of [208] concluded that predictions over a four-year interval have a root mean squared (RMS) accuracy of 0.4 s, with a peak of 0.8 s. However, in addition to determining ΔT by observing distant stars, ΔT can be approximated based on observations of the motion of GNSS satellites [169].

(a) The $\Delta T = \text{TT} - \text{UT1}$ Term

(b) UTC − UT1 with Leapsecond Jumps
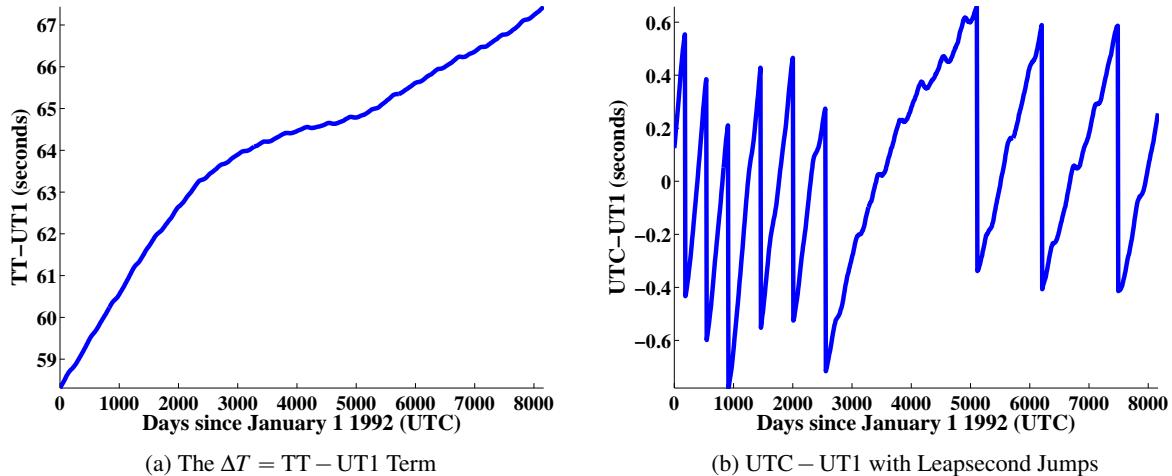
Fig. 12: Plots of (a) the ΔT Earth-orientation parameter and (b) the difference between UTC and UT1, which is discontinuous due to the inclusion of leapseconds in UTC. The data was taken from the U.S. Naval Observatory's `finals2000A.data` file available at the link in Table 2. Interpolation between points, including the addition of tidal terms, was performed using Matlab code based off of `interp.f` that the IERS provides at the link in Table 2. Though the UTC day duration is not quite uniform due to the presence of leapseconds, the scale of the chart is such that it is not noticeable.

---

[40]Longitudinal differences can be approximated by setting a clock for noon when the Sun is highest in the sky at a reference location and then observing when noon occurs after one has moved to a different location. This requires precise timekeeping, which was only possible after John Harrison invented the marine chronometer −a major improvement over some of the bizarre superstitious methods that some sailors tried (unsuccessfully) to use to keep time over distances. A monograph on the topic including discussions on why sailors thought they could tell time using injured dogs is [303].

The ΔT Earth-orientation parameter is directly linked to the LOD parameter. The LOD parameter is defined to be

$$\text{LOD} \triangleq -\frac{d(t_{\text{UT1}} - t_{\text{TAI}})}{dt_{\text{TAI}}}. \tag{1}$$

Consequently, by integrating over the LOD parameter in TAI, one obtains a version of ΔT in TAI time. Since a clock in TAI tics at the same rate as one in TT, one can replace TAI with TT in Eq. (1) without changing the value of LOD for an equivalent time in TT. The LOD parameter is related to the rotation rate of the Earth as

$$\omega = \omega^N \left(1 - \frac{\text{LOD}}{T_{\text{day, TAI}}} \right) \tag{2}$$

where ω is the instantaneous angular velocity of the Earth's rotation in radians per second, $T_{\text{day, TAI}} = 86400\,\text{s}$ is the nominal length of one day in TAI, and $\omega^N = 72921151.467064 \times 10^{-12}\frac{\text{rad}}{\text{s}}$ is the nominal angular velocity of the Earth at epoch 1820 based on the duration of the mean solar day being $T_{\text{day, TAI}}$. Note that $\omega^N T_{\text{day, TAI}} \neq 2\pi$, because the Earth's rotation around the Sun means that the Earth must rotate more than 2π radians between noon on one day and noon (as defined by the peak height of the Sun in the sky) the next day. The specific numerical value used is from `http://hpiers.obspm.fr/eop-pc/earthor/ ut1lod/UT1.html` . Though a very complicated explicit formula for LOD as a function of various celestial parameters has been derived [352], no accurate long-term predictions exist.

3.3 Units of Time

In general, to maximize the portability of data across sensor networks, it is good practice to always use SI units, which are defined in [39], because all countries except for the United States, Burma (Myanmar), and Liberia have legally adopted the SI standard [43]. The SI unit of time is the second and NASA SPICE software defines ET as seconds in TDB past the J2000.0 epoch.

However, ephemerides are often listed in terms of Julian dates, which are specified as a count of days, where a Julian day contains precisely 86400 s and a Julian year is precisely 365.25 Julian days. For example, noon in TT on the first of January in the year 2000 according to the Gregorian calendar (the calendar used by most countries) is JD 2451545.0 TT, where JD indicates Julian date and TT notes that the timescale is terrestrial time. An explanation of Julian dates and the related Julian calendar is given in [285, Ch. 1.25,12.7, 12.8]. Julian days begin at noon rather than midnight. A modified Julian date (MJD) is a Julian date minus 2400000.5. By subtracting off such a large constant term, Julian dates can be represented to a slightly higher degree of precision using the same number of bits. For example, a single-precision floating-point number has 6 digits of precision [149], meaning that the time resolution of a normal Julian date is worse than one day and that of a modified Julian date is $1/10$ of a day. On the other hand, a double-precision floating-point number has 15 digits of precision [149], allowing for $864\,\mu\text{s}$ precision for a regular Julian date and $8.64\,\mu\text{s}$ precision with a modified Julian date. Julian dates are used in the Navy's astronomical almanac [70, Ch. B, L]. Gregorian calendar years coupled with offsets in terms of Julian days are used in the TLE set data format used by NORAD for specifying orbital parameters [339]. The IAU SOFA software as well as the U.S. Navy's NOVAS software both use two-part Julian dates. The date is split into two double-precision floating-point numbers. The date can be split in any manner. However, it is common for the first number to be an integer number of days and the second number to be the fraction of the day. This means that 24 hours can be expressed with approximately 15 digits of precision (better than nanosecond precision).

It is recommended that, when possible, data in a target-tracking system be recorded with a full date, preferably a Julian date, since it is standard, rather than providing the time of the data as a simple offset from when the system was turned on. The use of true dates allows users to later associate the measurements with other relevant information collected at the same time. For example, radar measurements with appropriate global timestamps can be associated with ADS-B data that can serve as "truth" for assessing performance.

3.4 Time for Celestial Observations

When determining the location of a celestial object in the sky at a particular time, the finite speed of light must be taken into account. One does not see the current location of the object. Rather, one sees where the object was when the light being observed left the object. Appendix I describes how the light-time correction is performed (with an approximate general relativistic correction) for an observer on the Earth using NASA's SPICE toolkit, as the toolkit only provides estimates with respect to the center of the Earth. Uncertainty in the time light hits the target leads to uncertainty in the time to which a tracking algorithm should be predicted for a measurement update. Only a very small number of recursive tracking algorithms have been published that account for the light-time delay [97, 231]. When given full (bistatic range and angle) measurements, one can use the apparent time the light hit the target. However, certain high bistatic angle arrangements between the transmitter and the receiver can be particularly sensitive to error when using the apparent time [52].

Note, however, that analogous speed of light delays for the effects of gravitational forces should not be used when integrating using common Newtonian or post-Newtonian dynamic models to determine the orbits of objects. The IERS conventions suggest a parameterized post-Newtonian model for orbital dynamics [257, Ch. 10]. The papers [216, 344, 345] debate whether the "speed of gravity" is infinite. When using Newton's law of universal gravitation to compute the orbits of the planets, very large errors are introduced if one tries to limit the speed of gravity to the speed of light. However, the controversy is resolved in [40] where the general relativistic aberration of gravity explains the phenomenon: Orbits based on Newton's law of universal gravitation assuming an infinite speed of gravity are a good approximation to orbital dynamics using general relativity under which theory the speed of gravity is equal to the speed of light. More recent evidence considering the Shapiro time delay based on the bending of light from quasars around Jupiter confirms that under general relativity, the speed of gravity is finite [188]. Thus, when using a Newtonian or post-Newtonian gravitational model, gravitational forces should be taken as instantaneous. However, when using a full general relativistic model, gravitational effects travel at the speed of light.

4. COORDINATE SYSTEMS FOR DESCRIBING LOCATIONS ON AND NEAR THE EARTH

This section describes coordinate systems that are commonly used for describing points on or near the Earth. However, the results can be applied to other solar system bodies when given the appropriate data for the body. For example, whereas Earth gravitational models are discussed in this section regarding orthometric heights, similar models are available for the Moon and other planets. For example, a recent spherical-harmonic gravitational model for the Moon called GL0660B is described in [186] and the associated coefficients can be downloaded from the International Centre for Global Earth Models (ICGEM).

4.1 A Number of Common Spherical and Direction-Cosine Systems

A variety of non-Cartesian coordinate systems are used to describe the location of points with respect to near-Earth observers. Unfortunately, there is often little consensus on how many such coordinate systems are implemented. For example, Fig. 13 illustrates the various ways that a set of Cartesian axes is mapped to various coordinate systems for applications that might arise when performing tracking and navigation. When considering points on the Earth using spherical coordinates, one often uses longitude and geocentric latitude, as illustrated in Fig. 13. Note, however, that except when synthesizing magnetic and gravitational potential models, as discussed in Appendix F, points near the Earth are generally given in longitude and geodetic latitude, which is an ellipsoidal coordinate system, discussed in Section 4.2.
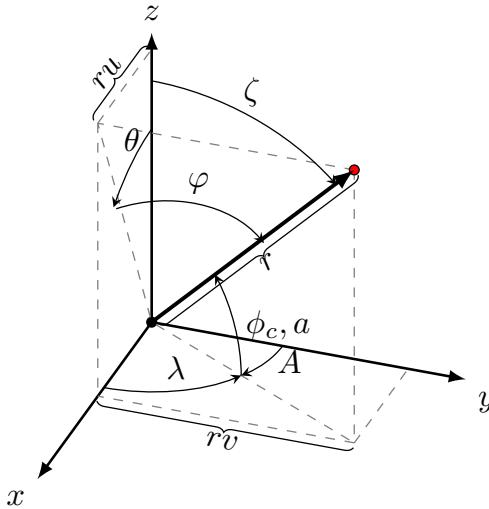
Fig. 13: Various quantities related to spherical coordinate systems commonly used for target tracking and lo[...] instances, r is one-way range. When discussing points on the Earth, one often uses longitude λ and geocentric [...] the z-axis is the axis of rotation of the Earth. When discussing the local horizon coordinate system, one o[...] uses azimuth A measured clockwise from the y-axis (East) and an angle called the zenith distance ζ measured from the z-axis, which is the gravitational vertical. Alternatively, instead of the zenith angle, one sometimes uses the altitude a (which is another name for ϕ_c in this system). When discussing measurements by a radar, one might use the $r - u - v$ coordinate system, where the z-axis is the pointing direction of the radar (boresight) and it is assumed that the z component is positive (in front of the radar). Alternatively, spherical coordinates for a radar often use azimuth θ and elevation φ, where the $(x - z)$-plane is level with the radar face. In some instances, θ is measured clockwise as opposed to counterclockwise as shown, or a different axis is chosen to be the boresight.

The horizon coordinate system, which is mentioned in [332, Ch. 5.2.5.1], is often used as a local coordinate system for astronomical observation. The z-axis is the gravitational vertical (the zenith), which points in the opposite direction of acceleration due to gravity. Such a system often specifies points using an azimuth angle A, which can be viewed similarly to a co-longitude, as it is measured from the y-axis clockwise in the $(x-y)$-plane, and an angle called a zenith distance ζ measured from the gravitational vertical, or an angle called an altitude a (an elevation angle), measured from the $(x-y)$-plane.

In general, however, it is better to express directions using the zenith distance instead of the altitude angle as it eliminates possible confusion regarding the definition of the "horizon." In the horizon coordinate system, the x and y axes are nominally located in the plane of the horizon. One understands the horizon to be the boundary between land and sky. However, refractive effects cause the apparent horizon to dip below the local tangent plane. Approximations to determine the dip angle as a function of the height of the observer are given in [332, Ch. 12.3.3.1]. However, atmospheric turbulence can make observations near the horizon (or observations of the horizon itself) unreliable. For example, in [367], it is concluded that refraction within approximately $5°$ of the horizon is so variable that angular measurements of astronomical objects are limited to approximately one arcminute when considering visible light. Confusion when using altitude measurements can arise depending upon whether they are with respect to the apparent, refraction-corrupted horizon or with respect to the true geometric horizon. Though tracking and navigation algorithms such as those in [266] have made use of measurements of the horizon for the purposes of navigation and orientation estimation, horizon measurements are unreliable due to atmospheric turbulence. Moreover, the apparent location of the horizon that a sensor might detect can vary due to the presence of mountains versus ocean. Note that it is usually possible to see objects over the geometric horizon. Figure 14 illustrates this fact when considering a sunrise viewed from Hilo, Hawaii.

In addition to illustrating angular relations when discussing a spherical coordinate system for points on the Earth or astronomical observations, Fig. 13 also shows the angular relationship often used when discussing measurements by a radar. In the context of radar signal processing, the z-axis is often the pointing direction of the radar, and azimuth θ and elevation φ are defined in completely different planes than are used when discussing longitude and geocentric latitude. Such a spherical coordinate system provides the basis of the $r-u-v$ direction cosine system, which is described in the first tutorial [55] in the series [54, 55, 57].

For the purposes of this report, the spherical coordinate systems most relevant to target tracking are the longitude, geocentric latitude system, where a point consists of (r, λ, ϕ_c), and the range-azimuth-elevation system (r, θ, φ). The former is necessary for using gravitational- and magnetic-field models and the latter is commonly used to describe measurements by a radar.

Given a point (r, λ, ϕ_c) in the longitude, geocentric latitude system at range r, longitude λ, and geocentric latitude ϕ_c, the location in Cartesian coordinates is given by

$$x = r\cos(\lambda)\cos(\phi_c) \tag{3}$$
$$y = r\sin(\lambda)\cos(\phi_c) \tag{4}$$
$$z = r\sin(\phi_c). \tag{5}$$
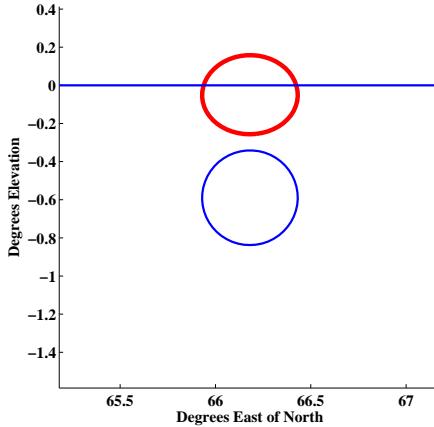
Fig. 14: A view of the rising Sun from Hilo, Hawaii (19.7056° geodetic latitude, −155.0858° longitude) at sea level (assumed to be the location of the ground, which is assumed to have zero WGS 84 ellipsoidal height), facing Northeast on 1 June 2013, at 15:42 UTC assuming an ambient temperature of 20°C, 70% humidity, and standard pressure (101,325 Pa). The horizontal line is the horizon. The lower, blue circle is the outline of the Sun, ignoring atmospheric refraction, based on the DE430 ephemerides accessed using the SPICE toolkit available at the links in Table 2. The method of Appendix I for loading the Sun's ephemerides was used along with the method of Appendix L for determining the outlining points of the Sun. The upper red circle is the apparent location of the Sun when using the numerical integration ray-tracing method of [138] and [332, Ch. 7.2] with the Sinclair atmospheric model of [295]. An observer at sea level can see the Sun over the horizon. The look direction in degrees East of North and the vertical for determining the horizon are based on the ellipsoidal East-North-Up model described in Section 4.2 and not on a true horizon coordinate system.

Similarly, the conversion from Cartesian coordinates to spherical geodetic coordinates is

$$r = \sqrt{x^2 + y^2 + z^2} \tag{6}$$

$$\lambda = \arctan2(y, x) \tag{7}$$

$$\phi_c = \arcsin\left(\frac{z}{r}\right), \tag{8}$$

where the function arctan2 represents a four-quadrant inverse tangent of y/x. In such a system, a local Cartesian set of orthogonal basis vectors can be defined at each point by differentiation of Eqs. (3), (4), and

(5) by r, λ, and ϕ_c to get

$$\frac{d\mathbf{r}}{d\lambda} = c_1\mathbf{u}_1 = \begin{bmatrix} -r\sin(\lambda)\cos(\theta_c) \\ r\cos(\lambda)\cos(\theta_c) \\ 0 \end{bmatrix} \tag{9}$$

$$\frac{d\mathbf{r}}{d\phi_c} = c_1\mathbf{u}_2 = \begin{bmatrix} -r\cos(\lambda)\sin(\theta_c) \\ -r\sin(\lambda)\sin(\theta_c) \\ r\cos(\theta_c) \end{bmatrix} \tag{10}$$

$$\frac{d\mathbf{r}}{dr} = \mathbf{u}_3 \begin{bmatrix} \cos(\lambda)\cos(\theta_c) \\ \sin(\lambda)\sin(\theta_c) \\ \sin(\theta_c) \end{bmatrix} \tag{11}$$

where $\mathbf{u}_1$, $\mathbf{u}_2$, and $\mathbf{u}_3$ form an orthonormal basis and the constants c_1 and c_2 in Eqs. (9), (10), and (11) represent the fact that the vectors do not have unit magnitudes. This local coordinate system is the spherical equivalent to the local East-North-Up (ENU) coordinate system discussed in Section 4.2 when using ellipsoidal coordinates.

On the other hand, if a point is given in the range-azimuth-elevation system (r, θ, φ) at range r, azimuth θ and elevation φ, then the location in Cartesian coordinates is given by

$$x = r\sin(\theta)\cos(\varphi) \tag{12}$$
$$y = r\sin(\varphi) \tag{13}$$
$$z = r\cos(\theta)\cos(\varphi) \tag{14}$$

so the inverse transformations are

$$r = \sqrt{x^2 + y^2 + z^2} \tag{15}$$
$$\theta = \arctan2(x, z) \tag{16}$$
$$\varphi = \arcsin\left(\frac{y}{r}\right). \tag{17}$$

Though geocentric spherical coordinates are often used for physical Earth models, ellipsoidal coordinates, which use geodetic latitude, are more commonly used for discussing the location of objects near the Earth. Section 4.2 discusses ellipsoidal coordinates and the reference ellipsoid, which is a good approximation to the shape of the Earth.

4.2 Coordinates on the Reference Ellipsoid

The Earth is approximately oblate spheroidal in shape[41] (an ellipsoidal shape), as illustrated in Fig. 15, which shows an ellipsoid with a graticule (lines of geodetic latitude [horizontal] and longitude [vertical] drawn). The true shape of the Earth can be defined either in terms of the terrain or gravitationally, in terms of

---

[41] The study of the shape of the Earth is termed geodesy; the use of computers to aid in geography is geomatics.

a hypothetical surface of equal gravitational potential called the geoid, which defines MSL. Understanding the geoid and geoidal heights is important for using terrain data and various physical models. Sections 5 and 6 discuss the gravitational shape of the Earth and the effects of the geoid and tides on coordinate-system determination.
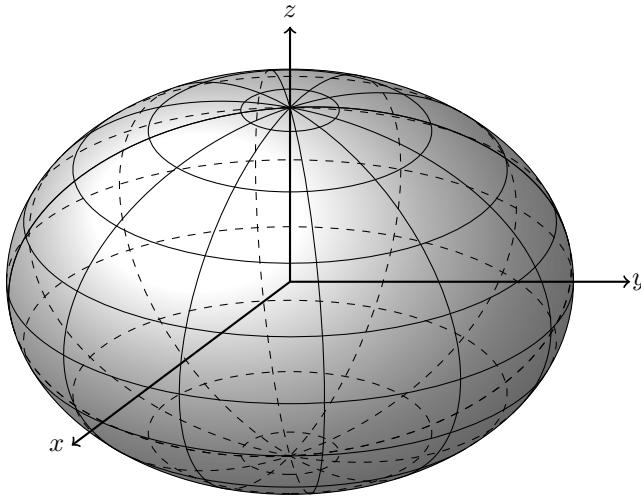
Fig. 15: The Earth is approximately shaped like an oblate spheroid; that is, an ellipse rotated about the *z*-axis (a type of ellipsoid). The non-spheroidal nature of the Earth's shape has been exaggerated in the diagram. The horizontal lines represent lines of latitude; vertical lines represent lines of longitude. Longitude is an angle measured with respect to the *x*-axis in the $(x - y)$-plane. It is analogous to right ascension in Fig. 4. This figure was also used in [58].

Geodetic latitude and longitude form the most common coordinate system used on maps and require the definition of a reference ellipsoid. A history of the development of the reference ellipsoid is given in [136, Ch. 2.11]. The WGS 84 standard [69, Ch. 3] and the IERS conventions [257, Ch. 4.2.6] define reference ellipsoids for the Earth to serve as horizontal datums. Datums serve as reference systems for positioning. The reference ellipsoid suggested in the IERS conventions is the Geodetic Reference System 1980 (GRS 80), which is a standard set by the IUGG [236]. Table 5 lists the defining parameters of the two aforementioned reference ellipsoids, as well as the parameters used specifically in ephemerides broadcast to GPS receivers and the parameters of two reference ellipsoids associated with the Earth Gravitation Model 2008 (EGM2008), which is used in gravitational models in this report.[42] The non-geometric parameters $GM_⊕$ and $\omega_⊕$ are explained below. The subscript ⊕ on the parameters in the table is a symbol representing the Earth.[43] Such subscripts are omitted when discussing reference ellipsoids in general.

---

[42]Though the EIGEN-6C4 model described in [102], which is available from the ICGEM's web site at `http://icgem.gfz-potsdam.de/ICGEM/`, is potentially more accurate than the EGM2008 model, the EGM2008 model is used in this report due to its widespread use and the availability of geoid models based on it.

[43]An alternative symbol for the Earth is ⊕. A number of astronomical symbols exist, such as ☉ for the Sun, ☾ for the Moon, ♂ for Mars, and ♀ for Venus. The IAU's style manual [361] discourages the use of such symbols and recommends that they be defined if they are used. However, such symbols are commonly used as subscripts in mathematical expressions in technical articles.

Table 5: Parameters for Various Ellipsoidal Models

Quantity	WGS 84 GPS Navigation	WGS 84	GRS-80 (IERS Suggested)	EGM2008 Mean-Earth Ellipsoid	EGM2008 for Geopotential Coefficients
$GM_\oplus$	$3.9860050 \times 10^{14} \frac{\text{m}^3}{\text{s}^2}$	$3.986004418 \times 10^{14} \frac{\text{m}^3}{\text{s}^2}$	$3.986005 \times 10^{14} \frac{\text{m}^3}{\text{s}^2}$		$3.986004415 \times 10^{14} \frac{\text{m}^3}{\text{s}^2}$
$a_\oplus$		$6378137.0\,\text{m}$	$6378137.0\,\text{m}$	$6378136.58\,\text{m}$	$6378136.3\,\text{m}$
$1/f_\oplus$		298.257223563	298.257222101	298.257686	
$\omega_\oplus$	$7.2921158553 \times 10^{-5} \frac{\text{rad}}{\text{s}} +$ $4.3 \times 10^{-15} \frac{UT1-2451545}{36525} \frac{\text{rad}}{\text{s}}$	$7292115 \times 10^{-11} \frac{\text{rad}}{\text{s}}$	$7292115 \times 10^{-11} \frac{\text{rad}}{\text{s}}$		

$GM_\oplus$ is the universal gravitational constant times the mass of the Earth; $a_\oplus$ is the semi-major axis of the Earth; $f_\oplus$ is the flattening factor of the ellipsoidal Earth; and $\omega_\oplus$ is the mean rotational velocity of the Earth. The WGS 84 reference is [69, Ch. 3]. The GPS version of it is used only when dealing with ephemerides broadcast by GPS satellites. The Geodetic Reference System 1980 is recommended by the IERS in [257, Sec. 4.2.6]. The parameters for the EGM2008 mean-Earth ellipsoid and the ellipsoid parameters for the EGM2008 geopotential coefficients are taken from the links for the EGM2008 model in Table 2. The values for the EGM2008 geopotential coefficients do not fully define an ellipsoid.

The reference ellipsoids are obtained by rotating a two-dimensional ellipse defined in the $(x-y)$-plane about the z-axis to make it three dimensional. Latitude and longitude define locations on the surface of a reference ellipsoid. Altitude (the height; not the angle), on the other hand, can be expressed in terms of a height above the ellipsoid, or in terms of another vertical datum, as discussed in Section 5. The WGS 84 standard [69, Ch. 3] defines the standard ellipse approximating the Earth shape (sometimes referred to as the "figure of the Earth") to be centered at the center of mass of the Earth with the radius being the equatorial radius of the Earth $a_\oplus$ and the inverse of the flattening factor being $1/f_\oplus$ as given in Table 5. For a generic ellipse or ellipsoid, the flattening factor is related to the equatorial radius a (distance from the center to a point on the equator), which is the same as the semi-major axis, and the polar radius b (distance from the center to the North or South pole), which is the same as the semi-minor axis, of the ellipse/ellipsoid by

$$f = \frac{a-b}{a}. \tag{18}$$

The difference between the equatorial radius and the polar radius of the reference ellipsoid is approximately $a_\oplus - b_\oplus \approx 21.4\,\text{km}$, meaning that the Earth is nearly spherical. Points on a reference ellipsoid in three dimensions satisfy the equation

$$\frac{x^2 + y^2}{a^2} + \frac{z^2}{a^2(1-f)^2} = 1. \tag{19}$$

Longitude is an angle measured counterclockwise (when looking down from the North pole) from the x-axis in the $(x-y)$-plane, analogous to right ascension in Fig. 4.[44] However, latitude is more complicated. To be able to properly locate points on a map and to use common gravitational models in tracking algorithms, one must differentiate between geocentric latitude (spherical coordinates) and geodetic latitude (ellipsoidal

---

[44]On other planets, planetocentric and planetographic longitudes can differ in direction. Planetocentric longitudes are measured counterclockwise from the x-axis when looking down from the North pole. On the other hand, planetographic longitudes are measured positively in the direction opposite the rotation direction of the planet [285, Ch. 4.22]. The two coincide for the Earth.

coordinates), because both are needed. Figure 16 shows the difference between geocentric latitude ϕ_c and geodetic latitude ϕ. Geocentric latitude is essentially the "elevation" in a spherical coordinate system. It is an angle measured up from the $(x-y)$-plane (the equatorial plane). Geodetic latitude, on the other hand, for a particular point is obtained by drawing a line from the point perpendicularly intersecting the reference ellipse. The angle obtained due to the intersection of that line and the equatorial plane is the geodetic latitude.
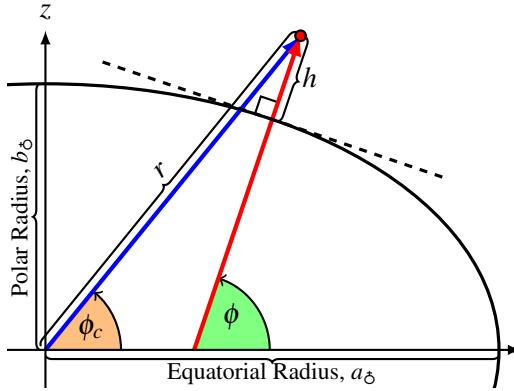
Fig. 16: An illustration of how latitude is measured. When discussing the latitude of a point (the red circle), unless specified otherwise, one generally means the geodetic latitude ϕ, which is taken with respect to a normal to the reference ellipsoid and generally does not intersect the origin. On the other hand, the geocentric latitude ϕ_c, which is seldom used, is the angle measured with respect to the origin. h is the ellipsoidal height of the point. The horizontal axis is anywhere in the $(x-y)$-plane. This diagram is also used in [58].

Unless otherwise specified, the latitude shown on maps is almost always geodetic latitude. While the definition of geodetic latitude is more complicated than that of geocentric latitude, before the advent of satellite geodesy using GPS and other means, geodetic latitude was significantly easier to measure than geocentric. A normal vector to a point on the ellipsoid of the Earth is *approximately* the gravitational vertical, which is what one perceives as "up," so geodetic latitude can be approximately ascertained by measuring the positions of stars relative to the local vertical. However, high precision determination of the local "up" vector in a global coordinate system cannot rely on an ellipsoidal approximation. As mentioned in [87], gravitational deflections of the vertical from the ideal ellipsoidal model can be as high as 70 arcseconds (about 1.94×10^{-3} degrees) and are quantified in more detail in Section 5.4.

Figure 16 shows a point above the reference ellipsoid with its height h (the ellipsoidal height) measured with respect to the normal to the reference ellipsoid. The conversion of a point given in geodetic latitude,

longitude, and height (ϕ, λ, h) coordinates to global Cartesian coordinates can be done as

$$x = (N_e + h)\cos(\phi)\cos(\lambda) \tag{20}$$

$$y = (N_e + h)\cos(\phi)\sin(\lambda) \tag{21}$$

$$z = \left(N_e(1 - e^2) + h\right)\sin(\phi) \tag{22}$$

$$N_e = \frac{a}{\sqrt{1 - e^2\left(\sin(\phi)\right)^2}} \tag{23}$$

$$e \triangleq \sqrt{2f - f^2}, \tag{24}$$

where ϕ and λ are the latitude and longitude, respectively, e is the first numerical eccentricity of the ellipsoid, and N_e is the radius of curvature in the meridian [285, Ch. 4.22]. On the other hand, the conversion from Cartesian coordinates is significantly more complicated and is given in Appendix B.

As described in [58], a set of local orthogonal basis vectors for defining a local ENU coordinate system can be obtained by differentiating Eqs. (20), (21), and (22) with respect to ϕ, λ, and h to get

$$\frac{d\mathbf{r}}{d\lambda} = c_1\mathbf{u}_1 = \begin{bmatrix} -(N_e + h)\cos(\phi)\sin(\lambda) \\ (N_e + h)\cos(\phi)\cos(\lambda) \\ 0 \end{bmatrix} \tag{25}$$

$$\frac{d\mathbf{r}}{d\phi} = c_2\mathbf{u}_2 = \begin{bmatrix} \left(\cos(\phi)\dfrac{dN_e}{d\phi} - (N_e + h)\sin(\phi)\right)\cos(\lambda) \\ \left(\cos(\phi)\dfrac{dN_e}{d\phi} - (N_e + h)\sin(\phi)\right)\sin(\lambda) \\ \left(N_e(1 - e^2) + h\right)\cos(\phi) + (1 - e^2)\dfrac{dN_e}{d\phi}\sin(\phi) \end{bmatrix} \tag{26}$$

$$\frac{d\mathbf{r}}{dh} = \mathbf{u}_3 = \begin{bmatrix} \cos(\phi)\cos(\lambda) \\ \cos(\phi)\sin(\lambda) \\ \sin(\phi) \end{bmatrix}, \tag{27}$$

where

$$\frac{dN_e}{d\phi} = \frac{ae^2\cos(\phi)\sin(\phi)}{\left(1 - e^2\left(\sin(\phi)\right)^2\right)^{\frac{3}{2}}}. \tag{28}$$

The constants c_1 and c_2 in Eqs. (26) and (25) represent the fact that the vectors do not have unit magnitudes. To form basis vectors for the ENU coordinate system, note that $\frac{d\mathbf{r}}{dh}$ points up, $\frac{d\mathbf{r}}{d\phi}$ points in the direction of geographic North along the surface of the ellipse, and $\frac{d\mathbf{r}}{d\lambda}$ points East along the surface of the ellipse. The ENU coordinate system refers to the normalized forms of the bases in Eqs. (25) through (27).

The East vector $\mathbf{u}_1$ cannot be uniquely determined at the poles because $\frac{d\mathbf{r}}{d\lambda}$ has zero magnitude. To guarantee the existence of a local ENU coordinate system at all locations in ellipsoidal coordinates (ϕ, λ, h), it is better to define $\mathbf{u}_1$ by the cross product

$$\mathbf{u}_1 = \mathbf{u}_2 \times \mathbf{u}_3 \tag{29}$$

to guarantee that it always exists. The longitude λ determines the orientation of the North and East axes at the poles.

Table 5 provides more parameters than are necessary to define the reference ellipsoid of the Earth. Specifically, some models define the universal gravitational constant times the mass of the Earth, $GM_\oplus$, and the angular velocity of the Earth's rotation, $\omega_\oplus$, in addition to the necessary semi-major axis $a_\oplus$ and inverse flattening factors $1/f_\oplus$. Those two additional parameters suffice to define a full ellipsoidal gravitational approximation for the Earth. Taken together, the full set of parameters defining the WGS 84 and similar ellipsoids imply a surface of constant gravity potential (a geoid), where the potential is [136, Ch. 2.7]

$$U_0 = \frac{GM}{E}\arctan(\varepsilon) + \frac{1}{3}\omega^2 a^2, \tag{30}$$

where GM is the universal gravitational constant times the mass of the body in question and

$$\varepsilon \triangleq \frac{e}{1-f} \tag{31}$$

$$E \triangleq ae \tag{32}$$

are the second ε numerical eccentricity and the linear eccentricity E of the reference ellipsoid, respectively. The first numerical eccentricity e is given by Eq. (24). The gravity potential has units of watts per meter. As noted in [136, Ch. 2.7], when discussing gravity potentials other than those due to ellipsoidal approximations, the symbol W is generally used instead of U. A subscript of 0 on U in Eq. (30) indicates that the value is taken on the surface of the ellipsoid.

Knowledge of the relationship between an ellipsoidal gravitational model of the Earth and the reference ellipsoid is important, as some sources do not explicitly provide the flattening factor of the reference ellipsoid. Rather, they provide a single spherical-harmonic gravitational coefficient from which the flattening factor must be deduced. This is the case in the appendix of [252], where instead of a flattening factor, the second-degree, fully normalized second zonal coefficient for a spherical-harmonic model of the Earth's gravitational potential $\bar{C}_{2,0}$ is given. Such models are discussed in more detail in Appendix F. Here, the transformation of such a coefficient into the flattening factor for the reference ellipsoid is of interest.

The fully normalized second zonal coefficient for a spherical-harmonic model of the Earth's gravitational potential $\bar{C}_{2,0}$ is related to the unnormalized second zonal coefficient $C_{2,0}$, which is sometimes just called C_2, as

$$C_2 = \bar{C}_{2,0}\sqrt{5}. \tag{33}$$

Similarly, C_2 is related to the coefficient J_2, which as in [202] is often referred to as a Jeffery constant, by

$$J_2 = -C_2. \tag{34}$$

Given J_2, ω, and GM for a particular ellipsoidal-Earth model, the corresponding flattening factor of the Earth can be found through estimation of the first numerical eccentricity e of the reference ellipsoid using

the iterative relations from [236], which are

$$\tilde{e}_n = \frac{e_n}{\sqrt{1 - e_n^2}} \tag{35}$$

$$q_n = \frac{1}{2}\left(\left(1 + \frac{3}{\tilde{e}_n^2}\right)\arctan(\tilde{e}_n) - \frac{3}{\tilde{e}_n}\right) \tag{36}$$

$$e_{n+1} = \sqrt{3J_2 + \left(\frac{4}{15}\right)\left(\frac{\omega^2 a^3 e_n^3}{2GMq_n}\right)} \tag{37}$$

where e_n is the first numerical eccentricity at iteration n. A reasonable starting value is $e_0 = 0.8$. One iterates Eqs. (35) through (37) until e_n no longer changes significantly. The first numerical eccentricity can be converted into the flattening factor for the ellipsoid using

$$f = 1 - \sqrt{1 - e^2}. \tag{38}$$

When given with ω and GM, reference ellipsoids directly define the gravitational potential and acceleration due to gravity anywhere on Earth. The direction of acceleration due to gravity under an ellipsoidal-Earth model is simply given by normalizing (27) to get $\mathbf{u}_3$. However, the magnitude of the gravitational acceleration under the ellipsoidal-Earth model can be useful for estimating the reading of a linear accelerometer that is on the ground, not accelerating, relative to the surface of the Earth. As derived in [136, Ch. 2–8], acceleration due to gravity under an ellipsoidal model can be explicitly written in terms of ellipsoidal harmonic coordinates (β, λ, u), where β is the reduced latitude, λ is the longitude, and u is the ellipsoidal harmonic semi-major axis. Appendix D provides the equations for converting to and from ellipsoidal harmonic coordinates. Given a point (β, λ, u), in ellipsoidal harmonic coordinates, and the linear eccentricity E of the reference ellipsoid, as well as associated values of GM and ω, the acceleration vector $\mathbf{g}$ due to gravity seen by a stationary observer in an Earth-centered Earth-fixed frame of reference is

$$\mathbf{g} = \gamma_\beta \mathbf{u}_\beta + \gamma_\lambda \mathbf{u}_\lambda + \gamma_u \mathbf{u}_u \tag{39}$$

where $\mathbf{u}_\beta$, $\mathbf{u}_\lambda$, and $\mathbf{u}_u$ are unit vectors in the directions of β, λ, and u as given in Appendix D and

$$\gamma_\beta = \frac{1}{w} \left(\frac{\omega^2 a^2 q}{q_0 \sqrt{u^2 + E^2}} - \omega^2 \sqrt{u^2 + E^2} \right) \sin(\beta) \cos(\beta) \tag{40}$$

$$\gamma_\lambda = 0 \tag{41}$$

$$\gamma_u = -\frac{1}{w} \left(\frac{GM}{u^2 + E^2} + \left(\frac{\omega^2 a^2 E q_p}{q_0 (u^2 + E^2)} \right) \left(\frac{1}{2} \sin^2(\beta) - \frac{1}{6} \right) \right) + \frac{1}{w} \omega^2 u \cos^2(\beta) \tag{42}$$

$$w = \sqrt{\frac{u^2 + (E \sin(\beta))^2}{u^2 + E^2}} \tag{43}$$

$$q_p = 3 \left(1 + \frac{u^2}{E^3} \right) \left(1 - \left(\frac{u}{E} \right) \arctan \left(\frac{E}{u} \right) \right) - 1 \tag{44}$$

$$q_0 = \frac{1}{2} \left(\left(1 + 3 \frac{b^2}{E^2} \right) \arctan \left(\frac{E}{b} \right) - 3 \frac{b}{E} \right) \tag{45}$$

$$q = \frac{1}{2} \left(\left(1 + 3 \frac{u^2}{E^2} \right) \arctan \left(\frac{E}{u} \right) - 3 \frac{u}{E} \right). \tag{46}$$

Note that if the flattening factor is zero (the ellipsoid is actually a sphere) then E is zero and one will have $0/0$ errors in the computation of various terms. In such an instance, one can use the asymptotic values. That is, in (40), substitute the value

$$\lim_{E \to 0} \frac{q}{q_0} = \frac{b^3}{u^3} \tag{47}$$

and in (42) substitute

$$\lim_{E \to 0} \frac{E q_p}{q_0} = 3 \frac{b^3}{u^2}. \tag{48}$$

While the issue of a zero flattening factor would not arise when dealing with coordinate systems on the Earth, it can arise when dealing with coordinates on other celestial bodies. For example, in [274], a zero flattening factor is suggested for an ellipsoidal model of the Moon.

On the other hand, if the gravity acceleration is only needed on the surface of the reference ellipsoid $\mathbf{g}_0$, then Somigliana's formula can be used to easily find the magnitude of the gravitational acceleration vector. The direction of the acceleration vector is then the normalized version of the "up" vector in (27). Somigliana's formula is [237, Ch. 2]

$$\|\mathbf{g}_0\| = \frac{a g_e \cos^2(\phi) + b g_p \sin^2(\phi)}{\sqrt{a^2 \cos^2(\phi) + b^2 \sin^2(\phi)}} \tag{49}$$

where g_e is the magnitude of acceleration due to gravity at the equator, g_p is the magnitude of acceleration due to gravity at the poles, ϕ is geodetic latitude (the formula does not depend on longitude), a is the semi-major axis of the reference ellipsoid, and b is the semi-minor axis of the reference ellipsoid, which can be found by inverting (18) to get

$$b = a(1 - f). \tag{50}$$

If the gravitational potential due to the ellipsoidal-Earth model is needed everywhere in space, not just on the surface of the reference ellipsoid, one can use the formula from [136, Ch. 2–7] in terms of ellipsoidal harmonic coordinates

$$U = \frac{GM}{E} \arctan\left(\frac{E}{u}\right) + \frac{\omega^2 a^2 q}{2q_0}\left(\sin^2(\beta) - \frac{1}{3}\right) + \frac{\omega^2}{2}(u^2 + E^2)\cos^2(\beta). \tag{51}$$

Section 5 demonstrates the importance of gravitational potential and acceleration due to gravity in using data in different coordinate systems.

When considering the use of ellipsoidal latitude and longitude coordinates with common commercial products, one must be aware that a number of companies base their coordinates on a warped, incorrect map projection. The Mercator projection is one of the most commonly used map projections because it is conformal, meaning that angles are locally preserved, though distances are warped. However, many common online and mobile map applications use a warped Mercator projection called the "web Mercator projection" that was invented by Google, does not preserve angles, and on which latitude and longitude coordinates usually do not correctly correspond to the WGS 84 ellipsoidal coordinate system. The NGA has a presentation detailing why the web Mercator projection produces maps that are incompatible with the WGS 84 coordinate system, causing positional biases to be as high as 40 km in some areas [243].

Additional details and derivations related to the geometry of ellipsoidal-Earth models are given in [270, 271], including how parameters for the reference ellipsoid are empirically found from measurements.

5.   VERTICAL HEIGHT AND GRAVITY

5.1   Definitions of Height

Whereas altitudes (heights) in the IERS conventions (when not using a Cartesian coordinate system) are defined as h with respect to the reference ellipsoid [257, Ch. 4.2.6], the WGS 84 standard defines vertical datums with respect to the geoid. The geoid is a surface of constant gravitational potential defining MSL, or a local measure of MSL. An older version of the WGS 84 standard used to make an exception when describing the depth of the ocean [67, Pgs. xii–xiv], where local sounding datums were suggested, but the current version suggests that all heights be reported at ellipsoidal heights [69, Ch. 10.6].

Figure 17 illustrates the differences between ellipsoidal and MSL (orthometric) elevations for a point on the surface of the Earth. The geoid is a hypothetical surface of constant gravitational potential[45] chosen to approximately coincide with the height of the sea surface in the absence of tides. (This is one possible definition of MSL. Multiple definitions of MSL exist [75].) The distance between the geoid and the reference ellipsoid measured on a vertical from the reference ellipsoid is the geoid undulation N. The orthometric height H of a point is the distance measured from that point to the geoid by following the direction of gravity downward. This is the usual definition of "height" when one describes the height of a mountain, for example. The variable direction of gravity is referred to as the "curvature of the plumb line." Though orthometric heights are defined in a manner related to how acceleration due to gravity changes as one moves, surfaces of constant orthometric height are *not* surfaces of constant gravity or gravitational potential. The ellipsoidal height h is *approximately* the sum of the orthometric and geoidal heights.

Figure 18 plots (a) the EGM2008 geoid with magnified undulations and (b) the actual terrain according to the Earth2012 model with altitudes magnified with respect to MSL. Based solely upon the distance from the center of the Earth, one might expect there to be no ocean near Europe based on the elevation in (b). However, since the geoid is high (red) near Europe, the level of the ocean by Europe is more distant from the center of the Earth than the level of the ocean in the Caribbean. Orthometric height determines how high something seems in terms of properties such as the thinness of the air. The air on the top of Mount Everest (the highest mountain in the world in terms of MSL) is thin because the top of Mount Everest is far above MSL. On the other hand, using the Earth2012 terrain data, one finds that the most distant point from the center of the Earth is not Mount Everest, but rather is located in the northern Andes mountain range in South America.[46] This is because the Earth is roughly ellipsoidal in shape, so points near the equator tend to be farther from the center of the Earth.

Table 6 lists a number of different definitions of height/altitude that one might have to deal with when designing a target-tracking system. Absolute altitude is often the simplest height measure to use when tracking satellites and ballistic objects. Orthometric heights (MSL heights) are seldom used as components of a target state in a tracking algorithm. However, they are often used in atmospheric models and terrain height models. For example, the Naval Research Laboratory Mass Spectrometer and Incoherent Scatter Radar Extended Model 2000 (NRLMSISE-00) empirical atmospheric model[47] described in [74, 261] is parameterized in terms of orthometric heights. Similarly, the Global Multi-Resolution Terrain Elevation Data

---

[45]Contrary to what one might expect, the magnitude of acceleration due to gravity is generally not constant on a surface of constant gravitational potential.

[46]The farthest point from the Earth's center was the topic of the final question in the 2013 National Geographic Bee, with Chimborazo in Ecuador being the most distant peak from the Earth's center [14].

[47]The official Fortran release can be obtained from `http://ccmc.gsfc.nasa.gov/modelweb/atmos/nrlmsise00.html` and an unofficial C-code release is at `http://www.brodo.de/space/nrlmsise/`.
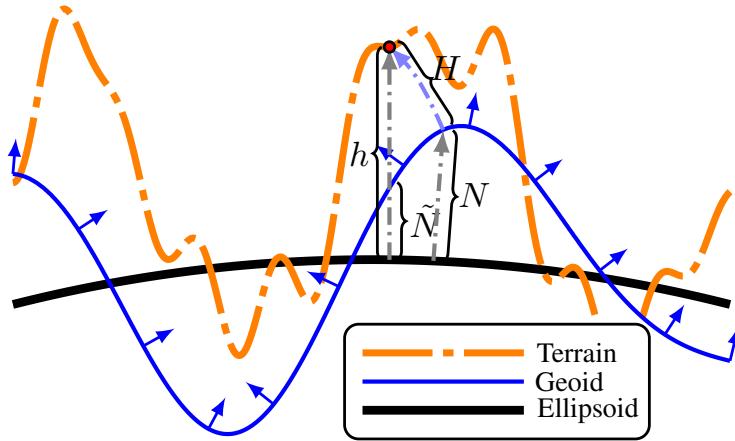
Fig. 17: A grossly exaggerated representation of the deviations between the reference ellipsoid, the geoid, and the terrain. The solid blue arrows represent the local gravitational vertical on the reference geoid (MSL) as determined by gravity. The elevation of a marked point on the terrain above the reference ellipsoid is h (ellipsoidal height), which is calculated from a normal to the ellipsoid. Similarly, the geoid undulation N is the height of a point on the geoid above the reference ellipsoid traced out by a normal vector. On the other hand, the orthometric height H is the height that would be measured from the point to the geoid by following the (curved) direction gradient from the point up or down until it intersected the geoid (dashed blue arrow). If the land were not there, it is the path that an ideal plumb line would follow. The distance $\tilde{N}$ is often very close to N (both defined along line normal to the surface of the reference ellipsoid), so sometimes one approximates $H \approx h - \tilde{N}$.

2010 (GMTED2010) model provided free online[48] by the U.S. Geological Survey (USGS) and the NGA provides terrain heights in terms of orthometric heights based on a geoid defined by the EGM96 gravitational model [61]. Terrain heights are important in target-tracking algorithms for predicting where ballistic objects will land (Will it go over the mountain or run into the side of the mountain?), and for determining whether terrain is obstructing the view of a target in a multistatic network. MSL heights are also used in the code released with the Enhanced Magnetic Model 2010 (EMM2010) (see Table 2 for documentation and a link to the code). The EMM2010 model is used in Sections 7 and 8.2, though implemented in a manner not using MSL heights. Pressure altitudes are commonly reported by transponders on civilian aircraft, including the common mode S transponder [150]. Geopotential heights are often used in atmospheric models. For example, the U.S. Standard Atmosphere 1976 [241] uses an approximate geopotential height.

Today, it would be significantly more convenient for terrain elevation data to be given in ellipsoidal heights when tracking in GTRS coordinates. However, prior to the use of satellites for measuring the terrain, the elevation of the terrain was determined through the direct or indirect measurement of changes in the gravitational potential on the ground [136, Ch. 4] [160], making elevations with respect to the geoid the ones directly measured. Researchers still make use of traditional leveling techniques for height determination to validate and augment newer GPS-aided techniques, such as when Chinese researchers sought to more accurately determine the height of Mount Everest [44]. The use of gravitational potentials for altitude measurements is unlikely to change for high-precision measurements, as modern atomic clocks have achieved sufficient accuracy that local variations in the geoid height can be measured to an accuracy of 1 cm by comparing the rates of clocks in two different locations [32].

---

[48]One can download the terrain elevation data from `https://lta.cr.usgs.gov/earth_explorer`.

(a) The Geoid, with Magnified Undulations   (b) The Terrain, with Magnified Features
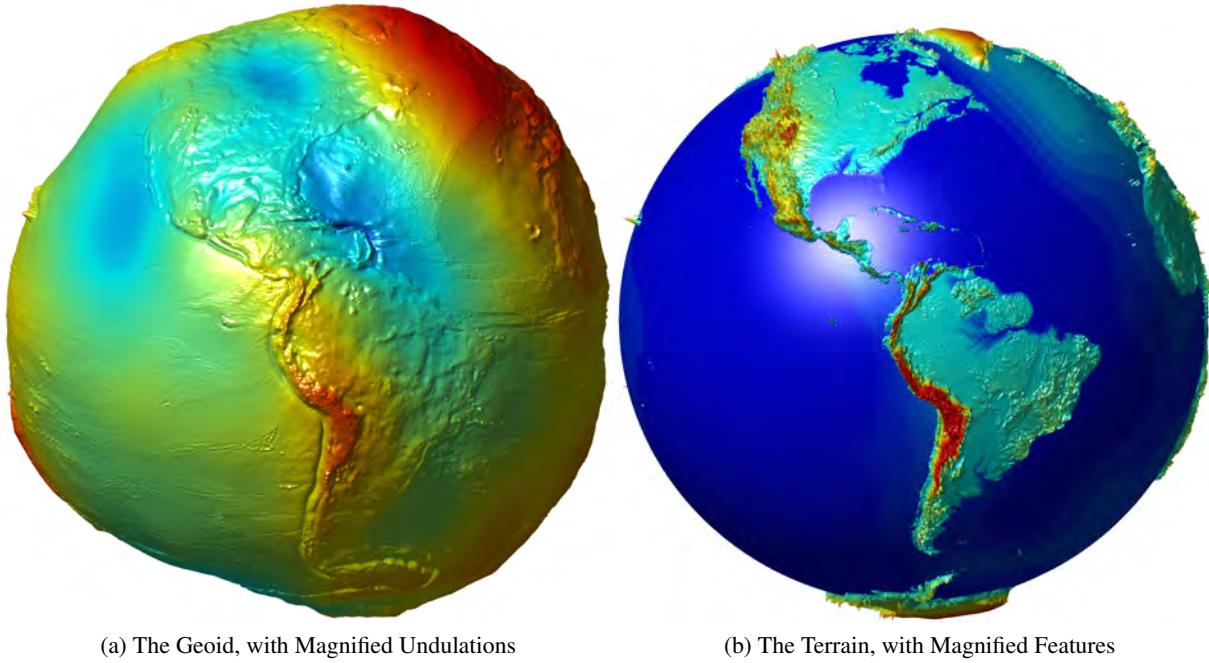
Fig. 18: In (a), the tide-free EGM2008 geoid with undulations magnified by a factor of 10^4 is displayed viewing North and South America. One can make out the Andes mountain range in South America. In (b), the Earth2012 terrain model with mean ocean, which is the distance of the terrain from the center of the Earth, is shown with the height above MSL (as given by the WGS 84 reference ellipsoid) exaggerated by a factor of 100. The spherical-harmonic coefficients used to make each plot were obtained from the sources in Table 2. The undulations and terrain heights were evaluated on a 2500×2500 grid in ellipsoidal latitude and longitude for the geoid and in spherical coordinates for the terrain.

5.2   Computing Orthometric Heights

A number of steps are necessary to convert between the different definitions of height in Table 6 and to utilize publicly available data models to reproduce the geoid and terrain plots in Fig. 18. A large amount of terrain data is only easily obtainable in terms of orthometric heights. For example, Fig. 19 plots the Digital Terrain Model 2006.0 (DTM2006.0), which is provided in terms of spherical-harmonic coefficients for orthometric heights with respect to the EGM2008 model. The coefficients can be downloaded from the link in Table 2. This section discusses the definition of the geoid and how geoid and orthometric heights are related.

A number of methods of estimating the geopotential at MSL are presented in [297]. Some utilize satellite altimetry along with terrain density models and Earth geopotential models, and others simply try to average measures of the geopotential over the oceans. The definition of "mean seal level" that is suggested for use with the EGM2008 geopotential model is based on the geopotential implied by the EGM2008 mean-Earth ellipsoid, whose parameters are given in Table 5 and which is defined with the height-anomaly-to-geoid undulation coefficients at the link in Table 2. The documentation for the EGM2008 mean-Earth ellipsoid does not define the necessary $GM_{\oplus}$ term or the rotation rate of the Earth $\omega_{\oplus}$ that are needed to use (30) to define the potential of the geoid. Thus, it is assumed that the values for the WGS 84 model from Table 5 are

Table 6: Common Height Measures Arising in Target Tracking Problems

Height Type	Description
Absolute Altitude	Distance from the center of the Earth
Orthometric Height	Height measured along the curved plumb line with respect to MSL
Pressure Altitude	Altitude based on a local pressure reading and a standard atmospheric model
Geoid Height Geoid Undulation	The distance between the reference ellipsoid and MSL (the geoid)
Geodetic Height Ellipsoidal Height	Height above the reference ellipsoid
Geopotential Height	Geopotential difference from surface, divided by a standard acceleration magnitude g_0

In many applications, only approximate values of orthometric height and geopotential height are used.

used. Using the EGM2008 mean-Earth ellipsoid with the additional parameters for the WGS 84 ellipsoid, (30) produces a gravity potential on the geoid of

$$W_0^{\text{EGM2008}} = 6.263685171456948 \times 10^7 \frac{\text{m}^2}{\text{s}^2}. \tag{52}$$

Note that the symbol W_0 is used rather than U_0. The difference in notation shall be explained shortly. The gravity potential of the EGM2008 model is used to define the geoid in this report. However, different applications use different definitions. For example, the U.S. Department of Transportation's Standard for Aeronautical Surveys and Related Products in the United States stipulates that orthometric heights shall be referenced to the North American Vertical Datum of 1988 (NAVD 88) [333].

Given a definition of the gravity potential of the geoid, to determine the height of the geoid above the reference ellipsoid using terrain and geopotential models, which is a necessary step in computing orthometric heights, one must first differentiate between the different potentials that are listed in Table 7. The gravity potential W of the Earth at a particular point $\mathbf{r} = [r_x, r_y, r_z]'$ in space under Newtonian mechanics is defined to be

$$W \triangleq \overbrace{V(\mathbf{r})}^{\substack{\text{Gravitational} \\ \text{Potential}}} + \overbrace{\Omega(\mathbf{r})}^{\substack{\text{Centrifugal} \\ \text{Potential}}} \tag{53}$$

where $V(\mathbf{r})$ is the gravitational potential at $\mathbf{r}$, which is given by the mass distribution of the Earth, and $\Omega(\mathbf{r})$ is the potential due to the rotation of the Earth. All of the potentials have units of m^2/s^2, which is the same as joules (energy) per unit mass in kilograms. Since the WGS 84 and ITRF standards set the z-axis of their ECEF reference frames to be the axis of rotation of the Earth, the centrifugal potential is

$$\Omega(\mathbf{r}) = \frac{1}{2}\omega_\ominus^2(r_x^2 + r_y^2). \tag{54}$$

The discussion in this section focuses on the potential of the Earth as expressed in Newtonian mechanics. Though more theoretically sound relativistic geodesy techniques exist as discussed in [187, Ch. 8],

Fig. 19: The DTM2006.0 terrain/bathymetric model plotted on a 2500×2500 uniform grid in latitude and longitude. The model provides terrain heights and bathymetric depths as orthometric heights. The tide-free EGM2008 geoid height was added to the orthometric heights (Helmert's projection) to obtain ellipsoidal heights with respect to the WGS 84 reference ellipsoid to plot. The heights above the reference ellipsoid were exaggerated by a factor of 100 when plotted. At the current scale, an omission of the geoid height correction would not have noticeably changed the plot. However, to use the data to a high precision, one must consider the geoid height.

for example, they are complicated and Newtonian models appear to be the primary ones in use. The gravity potential W is the *negative* of the potential energy per unit mass of an object rotating with the Earth. Consequently, the gradient of the gravity potential is the gravity acceleration

$$\mathbf{g} = \nabla W(\mathbf{r}) \tag{55a}$$

$$= \nabla V(\mathbf{r}) + \omega_\oplus^2 \begin{bmatrix} r_x \\ r_y \\ 0 \end{bmatrix} \tag{55b}$$

where the gradient operator is defined in Cartesian coordinates as

$$\nabla \triangleq \left[\frac{\partial}{\partial r_x}, \frac{\partial}{\partial r_y}, \frac{\partial}{\partial r_z} \right]'. \tag{56}$$

The ellipsoidal potentials U and U_0 play an important role when one wishes to express geoid heights in WGS 84 coordinates even though the reference ellipsoid defining MSL for the EGM2008 model uses different values of the semi-major axis and flattening factors of the Earth. The ellipsoidal potential $U(\mathbf{r})$

Table 7: Commonly Used Symbols for the Different Earth Gravitational Potentials

Symbol	Name	Description
W	Gravity Potential	Potential of an observer rotating with the Earth
V	Gravitational Potential	Potential of an observer not rotating with the Earth
Ω	Centrifugal Potential	Potential due to the Earth's rotation
U	Ellipsoid Potential	Potential under an ellipsoidal-gravity model
W_0	Geoid Potential	Potential defining MSL
U_0	Ellipsoid Surface Potential	Potential on the surface of a reference ellipsoid
∇V	Gravitational Acceleration	Acceleration due to gravity, not counting the Earth's rotation.
g	Gravity Acceleration	Acceleration due to gravity, including the Earth's rotation

Many papers do not differentiate between the gravity acceleration and the gravitational acceleration and use **g** for both. To avoid confusion, this report uses different symbols for each.

is the gravity potential at a point **r** under a particular ellipsoidal-Earth model, as given by (51), and U_0 is the gravity potential on the surface of a specific ellipsoid as per (30). Usually, depending on the reference ellipsoid chosen, $U_0 \neq W_0$.

At a point **r** chosen to be *outside* of all of the mass of the Earth, the gravitational potential V due to the Earth can be expressed in terms of spherical-harmonic coefficients [136, Ch. 1, 2] [29, Ch. 3.4].[49] Though the spherical-harmonic representation is not technically valid at points within the mass of the Earth, it is usually assumed valid within the atmosphere. The gravitational potential of the Earth as represented by the NGA's EGM2008 standard is given as a set of normalized spherical-harmonic coefficients. The same is true of the many other models listed by the ICGEM. The EGM2008 model is the recommended geopotential model in the IERS conventions [257, Ch. 6] and in the current version of the WGS 84 standard [69, Ch. 5] and it was shown to be the best available model based on laser satellite-tracking observations [307], though a newer model might be more accurate [102]. The mathematics of using spherical-harmonic coefficients can be difficult and are reviewed in Appendix F. It is worth noting that naïve implementations of the harmonic equations can lead to a loss of precision [140] or can result in numerical overflow or underflow problems.

The geoid is always within the mass of the Earth as it is always within the atmosphere, and is often underground. In practice, the effects of the atmosphere are often neglected but the effects of terrain must be taken into account, necessitating information on both the height and density of the terrain. A commonly used technique for using gravitation and terrain models for determining the height of the geoid above a reference ellipsoid is that of Rapp [269]. Rapp's method assumes that the gravitational potential implied by the reference ellipsoid by (30) is the same as the geoid potential W_0. However, when using the geoid potential given by (52) for the EGM2008 model with the WGS 84 ellipsoid, Rapp's assumption is false. Thus, a modified expression of Rapp's method as given by Eq. 2-347 in [136, Ch. 2.17], as well as in [300], corrects for using a reference ellipsoid with an implied surface potential different from that of the geoid. The key equations for geoid height at point p, which might be expressed as (λ, ϕ_c) in spherical coordinates

---

[49]Note that even if the gravitational potential everywhere outside of a massive body is known, one can not directly infer the mass distribution within the body. Additional information, such as seismic data, is necessary [136, Ch. 1.13].

or as (ϕ, λ) in ellipsoidal coordinates,[50] when using the data provided with the EGM2008 model, are[51]

$$N_p = \zeta_p + K_p \tag{57}$$

$$\zeta_p = \frac{T_p}{\gamma_p} - \frac{W_0 - U_p}{\gamma_p} \tag{58}$$

where ζ_p is the height anomaly on the surface of the reference ellipsoid, W_0 is the defining gravity potential of the geoid (for example, (52)), U_p is the gravity potential on the surface of the reference ellipsoid at point p as computed using (30), γ_p is the magnitude of the acceleration due to gravity at point p on the surface of the reference ellipsoid using an ellipsoidal gravitational model via (39) or (49); that is,

$$\gamma_p \triangleq \|\mathbf{g}_0\|. \tag{59}$$

The computation of $\mathbf{g}_0$ and U_0 uses the value of GM_δ that is associated with the reference ellipsoid, not the value of GM that is used in the geopotential model, which might be different. The disturbing potential for a point on the surface of the reference ellipsoid is given by T_p, which is defined as

$$T_p = W_p - U_p \tag{60}$$

where W_p is the gravity potential at point p as defined in (53). The disturbing potential T_p is often evaluated by modifying the fully normalized even spherical-harmonic coefficients $\bar{C}_{n,m}$ that are used to evaluate the gravitational potential V. Such coefficients are described in Appendix F. As described in [300], the modified spherical-harmonic coefficients to directly compute T_p are the same odd coefficients $\bar{S}_{n,m}$ as are used to compute V along with

$$\bar{C}_{n,m}^{T_p} = \bar{C}_{n,m} - \frac{GM_{\text{ellipsoid}}}{GM_\delta} \left(\frac{a_{\text{ellipsoid}}}{a_\delta} \right)^n \bar{C}_{n,m}^{\text{ellipsoid}} \tag{61}$$

where GM_δ and a_δ are the the values of GM and the semi-major axis of the Earth as used by the gravitational potential model (e.g., the values for the EGM2008 model) and $GM_{\text{ellipsoid}}$ and $a_{\text{ellipsoid}}$ are the same as those used by the reference ellipsoid with which one wants the geoid undulation values (e.g., the values for the WGS 84 model).[52] The value $\bar{C}_{n,m}^{\text{ellipsoid}}$ is a fully normalized spherical-harmonic coefficient for an ellipsoidal gravitational model, which, as can be ascertained from [136, Ch. 2.5, 2.7–2.9], is given by multiplying $C_{2k,0}$ in Eq. (F85) of Appendix F.4 by $1/\sqrt{4k+1}$ for $k \geqslant 0$. Note that the values of C given in Appendix F.4 are only for even values of $C_{n,m}$, hence the $C_{2k,0}$ notation. Value of C for other subscripts can be assumed to be zero.

Unlike as described in [300], the geoid height in (57) is not iteratively computed since the NGA has provided a set of spherical-harmonic coefficients to convert from height anomalies on the reference ellipsoid to geoid undulations. K_p is the $\zeta-$to$-N$ coefficient that the NGA provides at a site listed in Table

---

[50] The lack of a radius or ellipsoidal height is because the geoid height does not depend on elevation. For all evaluations, the height is taken as 0, the surface of the reference ellipsoid.

[51] When using the older EGM96 gravitational model, the value of K_p obtained using the coefficients provided by the NGA is scaled too large by a factor of 100. Thus, Eq. (57) would have K_p divided by 100 when using the older EGM96 model.

[52] In the NGA's algorithm for evaluating geoid heights with the older EGM96 model, the F477 function at http://earth-info.nga.mil/GandG/wgs84/gravitymod/egm96/egm96.html , it is approximated that the coefficients of $\bar{C}_{n,m}$ are all 1. This approximation is dropped in the reference implementation of the EGM2008 geoid.

2.[53] The computation of W_p and K_p requires the evaluation of spherical-harmonic coefficients as described in Appendix F. To understand the origin of the model and the assumptions that must have gone into the K_p term, one is encouraged to consult [269] and [136, Ch. 2.17]. A large number of undocumented assumptions regarding the height and density of the land must have been used to obtain the spherical-harmonic coefficients for K_p.

Based on the code and documentation on the NGA's web site, it appears that the NGA uses the approximation that

$$\zeta_p \approx \frac{T_p}{\gamma} - \bar{C}_{0,0} \frac{GM_\eth}{\gamma r_E} - 0.41 \tag{62}$$

where $GM_\eth$ is the value of *GM* as used by the gravitational potential model, $\bar{C}_{0,0}$ is a fully normalized spherical-harmonic coefficient as discussed in Appendix F, and r_E is the distance from the center of the Earth to point p on the surface of the reference ellipsoid, which can be found by taking the magnitude of the Cartesian point obtained by using (20), (21), and (22) to convert the ellipsoidal point $(\phi, \lambda, 0)$ (zero ellipsoidal height) from ellipsoidal to Cartesian coordinates. The 0.41 constant assumes that everything is expressed in SI units and represents an approximation to the second term in (58) plus the second term in (62).[54] The NGA approximation was used when plotting Fig. 19. The difference between the NGA approximation and (58) when using the EGM2008 model is on the order of a few tenths of a centimeter, but is larger when using the older EGM96 gravitational model.

Geoid heights above the reference ellipsoid vary from from a high of approximately $+84$ m to a low of -107 m. The values can be determined either by evaluating N_p directly as described or by using the precomputed geoid height values available from the NGA [240]. Consequently, the magnitudes of treating orthometric heights as ellipsoidal heights, such as when using terrain elevation data, is close to the same range.

The rigorous determination of orthometric heights is complicated by the presence of terrain and is described in [327]. When orthometric height H in Fig. 17 of a point is found by correctly following the curved plumb line from the geoid through any terrain up to the point, then one is discussing Pizzetti's orthometric height. On the other hand, when one simply uses the approximation that

$$H = h - \tilde{N} \tag{63}$$

one is said to use Helmert's orthometric height. The value $\tilde{N}$ is the geoid undulation at the latitude and longitude of the point, whereas N is the geoid undulation at wherever following the curved plumb line down from the point intersects the geoid. As discussed in [136, Ch. 5-2], the difference between Helmert's and Pizzetti's orthometric heights is often negligibly small. As most applications using orthometric heights do not require high precision, and rigorously determining orthometric heights can be difficult, techniques for determining Pizzetti's orthometric heights are not given in this report. In general, it is most convenient if those designing target-tracking algorithms entirely avoid the use of orthometric heights and simply express everything in terms of WGS 84 ellipsoidal or Cartesian coordinates.

---

[53]The NGA also provides precomputed tables of geoid undulations with interpolation software in Fortran.

[54]Under the older EGM96 model, the NGA used -0.53 instead of -0.41. As documented in the latest WGS 84 standard [69, Sec. 6.2], the discrepancy is due to an error in an oscillator drift correction in satellite-measured altimeter data underlying the EGM96 model.

The discussion of orthometric heights thus far has assumed that "the" EGM2008 geopotential model is used for geoid determination. However, the unique definition of the geoid requires both a defining potential W_0, as in (53), and a specification of the tide model. As noted in [77], different countries use different tide models when defining orthometric heights. Orthometric heights are always defined without consideration to the time-variant part of a tidal model. However, time-invariant effects of the Sun and the Moon, permanent tides, also work to deform the Earth and change the gravity potential. The three permanent tide systems are tide-free, zero-tide, and mean-tide. The various permanent tide systems are defined in Section 6 where the effects of time-variant as well as time-invariant tides are analyzed.

The basic spherical-harmonic coefficients for the EGM2008 geopotential model (which lets one compute V in (53)) and for the K_p terms to go from height anomaly to geoid undulations are given in a tide-free geoidal model. The conversion of a geoid from a tide-free system to other tide systems requires the addition of extra terms as discussed in Section 6.

5.3   Considering Pressure Altitudes

A pressure altitude is an altitude that is computed based on an air-pressure measurement and an atmospheric model. In the U.S., aircraft above $18,000$ ft (5484.6 m) generally navigate based on pressure altitudes that have been calibrated to a standard setting for air pressure and temperature at MSL. No air-pressure model can perfectly match reality. However, when used in aviation, if all aircraft are using the same incorrect model, they will experience the same model-based biases in altitude measurements and can thus maintain a safe vertical separation. The use of air-pressure measurements as reported by Mode C transponders in aircraft in the context of target tracking and sensor registration has been considered in [235]. In the U.S., the Federal Aviation Administration (FAA) stipulates [334] that altimeters in aircraft should be tested using the 1976 U.S. Standard Atmosphere of [241]. The U.S. Standard Atmosphere is also valid for civilian aviation outside of the U.S., because up to an altitude of 32 km (which is above the ceiling of current commercial jets), the U.S. Standard Atmosphere is identical to the standard atmosphere of the International Civil Aviation Organization (ICAO), as noted in [8], where a number of atmospheric models are contrasted. Many commercial atmospheric pressure sensors, such as that described in [8], use the U.S. Standard Atmosphere to provide the user with an orthometric altitude reading.

For the purposes of target tracking using transponders, if one wants to use the altitude readings, one must convert the standard pressure altitude used by the aircraft into an altitude that the tracker can use. This generally means finding the actual air pressure measured by the aircraft from the reported altitude and then putting the air-pressure measurement into a more accurate model. This section reviews the pressure model of the U.S. Standard Atmosphere, so that one can extract air-pressure readings from transponder data. Due to the preponderance of high-fidelity atmospheric models,[55] no specific model is considered for converting the aircraft's air-pressure reading into an accurate height usable for tracking (such as an ellipsoidal height). However, using the U.S. Standard Atmosphere with an accurate local altimeter setting (rather than the standard one used above $18,000$ ft) can provide less-biased orthometric heights that can be converted into a format usable in a tracking algorithm.

To use the U.S. Standard Atmosphere 1976 to compute an orthometric height from a pressure altitude or vice versa, an intermediate conversion to a geopotential height is necessary, as the model below 86 km altitude is parameterized on geopotential heights. A geopotential height is essentially a gravitational potential

---

[55]Consider, for example, some of the models listed on NASA's model web site at `http://ccmc.gsfc.nasa.gov/modelweb/`.

difference divided by a standard acceleration due to gravity. It can be defined as

$$H_{\mathrm{gp}} \triangleq \frac{W_p - W_0}{g_0} \tag{64a}$$

$$= \frac{1}{g_0} \int_0^{z_p} g \, dZ \tag{64b}$$

where W_p is the gravity potential of (53) at the target and W_0 is the gravity potential on the reference surface, typically on a specific definition of the geoid. The integral form of the geopotential height integrates from an orthometric height of 0 (on the geoid) to the points, which is at an orthometric height z_p. The magnitude of acceleration due to gravity g depends on position. The integral is a path integral (there are multiple ways to get from an orthometric height of 0 to z_p), but the actual path taken does not matter, only the endpoints. The dZ is a differential orthometric height. The U.S. Standard Atmosphere takes $g_0 = 9.80665\,\mathrm{m/s^2}$ as the reference acceleration due to gravity.

The standard atmosphere uses a low-precision approximation of the conversion from orthometric heights to geopotential heights. Using Newton's law of universal gravitation, which one can find in most introductory physics textbooks, one can express the magnitude of acceleration due to gravity g at a height of h above a spherical Earth with radius $r_⊕$ as

$$g = \frac{GM_⊕}{(r_⊕ + h)^2}. \tag{65}$$

Assuming that g_0 is the acceleration due to gravity when $h = 0$, multiplying both sides of (65) by the inverse of the right side of Eq. (65), one obtains

$$g\left(\frac{h^2 + 2hr_⊕ + r_⊕^2}{GM_⊕}\right) = 1 \tag{66a}$$

$$g\left(\frac{h^2}{r_⊕^2 g_0} + 2h\left(\frac{1}{r_⊕ g_0}\right) + \frac{1}{g_0}\right) = 1 \tag{66b}$$

which can be solved to get

$$g = \frac{g_0 r_⊕^2}{(h + r_⊕)^2}, \tag{67}$$

which no longer requires one to know $GM_⊕$. The standard atmosphere takes the radius of the spherical Earth to be $r_⊕ = 6{,}356{,}766\,\mathrm{m}$. Substituting the approximation of acceleration due to gravity of (67), into the integral definition of geopotential height of (64b), one obtains the approximation

$$H \approx \frac{r_⊕ z_p}{r_⊕ + z_p} \tag{68}$$

The standard atmosphere uses (68) to convert between orthometric height z_p of a point and geopotential height H. However, some air-pressure sensors that provide height readings do not perform the conversion. Since $86{,}000\,\mathrm{m}$ orthometric height corresponds to $84{,}852\,\mathrm{m}$ geopotential height, this can introduce a notable bias at higher altitudes.

Given the geopotential height H of a point, the standard air pressure for altitudes $86\,\text{km}$ and below, which are relevant for general aviation, in units of pascals (N/m^2) is

$$P = P_b \begin{cases} \left(\dfrac{T_{M,b}}{T_{M,b} + L_{M,b}(H - H_b)} \right)^{\frac{g_0 M_0}{R^* L_{M,b}}} & \text{If } L_{M,b} \neq 0 \\[2ex] \exp\left(-g_0 M_0 \dfrac{H - H_b}{R^* T_{M,b}} \right) & \text{If } L_{M,b} = 0 \end{cases} \tag{69}$$

where $R^* = 8.31432\,\text{Nm}/(\text{mol\,K})$ is a 1962 standard value for the universal gas constant and $M_0 = 28.9644 \times 10^{-3}\,\text{kg/mol}$ is the mean molecular weight of the atmosphere at sea level. The values $L_{M,b}$ and $T_{M,b}$ are constants that depend on the geopotential altitude H whose values are listed in Table 8 for different values of b. The value of b is chosen such that $H_b \leqslant H$. In some areas, the land may lie a significant distance below MSL. For example, the land around the Dead Sea between Israel and Jordan is between $700\,\text{m}$ and $730\,\text{m}$ below MSL, though it is rising by approximately $4\,\text{mm}$ per year due to the crust rebounding after water loss [244]. The standard says that the atmospheric pressure model is valid down to $5\,\text{km}$ below MSL. The pressure P_b is the air pressure at geopotential height H_b. Given P_b, one can find P_{b+1} by using (69) at b with $H = H_{b+1}$. The model is parameterized on P_0 and T_0, the air pressure and temperature at MSL. Local pressure and temperature settings that are above sea level can be extrapolated back down to sea level using the model and knowing the orthometric height of the observer.

Table 8: Constants for Air Pressure and Orthometric Altitude Conversion

b	$H_b(\text{m})$	$L_{M,b}(\text{K/m})$	$T_{M,b}(\text{K})$
0	0	-6.5×10^{-3}	288.150
1	11000	0	$T_{M,0} + L_{M,0}(H_1 - H_0) = 216.650$
2	20000	1×10^{-3}	$T_{M,1} = 216.650$
3	32000	2.8×10^{-3}	$T_{M,2} + L_{M,2}(H_3 - H_2) = 228.650$
4	47000	0	$T_{M,3} + L_{M,3}(H_4 - H_3) = 270.650$
5	51000	-2.8×10^{-3}	$T_{M,4} = 270.650$
6	71000	-2.0×10^{-3}	$T_{M,5} + L_{M,5}(H_6 - H_5) = 214.650$
7	84852	0	$T_{M,6} + L_{M,6}(H_7 - H_6) = 186.946$

The constants are for the U.S. Standard Atmosphere 1976 model up to $86\,\text{km}$ altitude. The numerical values for $T_{M,b}$ have not been rounded nor truncated.

Figure 20 plots altitude as a function of air pressure in the U.S. Standard Atmosphere 1976. The pressure P_0 and temperature T_0 at MSL, which define the model, were taken to be the standard pressure and temperature used by aircraft over $18,000\,\text{ft}$ altitude in the United States, a pressure of $101,325\,\text{Pa}$ and a temperature of $288.15\,\text{K}$ ($15°\text{C}$) [335].[56]

---

[56] The FAA's aeronautical information manual lists the standard air pressure as 29.92 inches of mercury, which depending on the chosen temperature and altitude of the sensor, is not precisely $101,325\,\text{Pa}$. However, $101,325\,\text{Pa}$ is the generally used conversion. The National Institute of Standards and Technology (NIST) lists multiple standard conversions from inches of mercury to pascals on their site at `http://physics.nist.gov/Pubs/SP811/appenB9.html`. Inches of mercury should generally not be used to specify pressures as it is ambiguous and archaic.
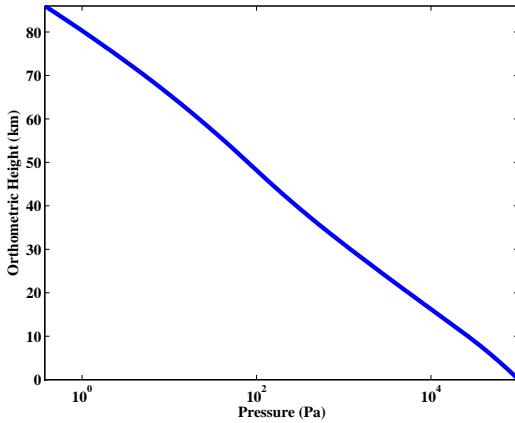
Fig. 20: The orthometric height as a function of air pressure in the U.S. Standard Atmosphere 1976 using standard temperature and pressure at MSL. The pressure scale is logarithmic.

5.4 Gravitational Models and the Local Vertical

A frequently used local coordinate system in target-tracking systems is the ENU system. The coordinate system can be useful as one can approximate ellipsoidal "up" by the gravitational vertical and North using a gyrocompass, though more accurate results are theoretically possible using stars. As mentioned in Section 8.1.1, given at least two vectors in multiple coordinate systems, one can easily find the rotation matrix between the systems. Section 4.2 discusses the ENU coordinate system in terms of coordinates on the reference ellipsoid. However, if one assumes that the local ellipsoidal vertical coincides with the vertical implied by the reference ellipsoid, one loses precision. This section quantifies how much the non-ellipsoidal nature of the Earth can matter. The ability to relate the gravitational vertical direction to a global coordinate system can play an important role in the design of inertial-navigation devices. For example, in [193], the navigation error of an inertial measurement unit (IMU) operating using various gravitational models is investigated. It is shown that the best models offer horizontal-position accuracies better than 5 m after a period of 53 minutes. A similar analysis performed with respect to moving vehicles on land is in [191], where it is noted that the navigation errors can be reduced if the vehicle periodically stops and recalibrates its "motion-free" gravitational acceleration.

Using the EGM2008 zero-tide spherical-harmonic gravitational model and the method of Appendix F for utilizing such models, Fig. 21 plots the bias in the magnitude and direction of the gravity-acceleration vector as obtained using the WGS 84 reference ellipsoid versus using the zero-tide EGM2008 model. An altitude of 9 km is used as it is above all terrain albeit still in the atmosphere. The angular distance between two vectors $\mathbf{v}_1$ and $\mathbf{v}_2$, determining the direction of the vertical in both models, was determined using the cross-product relation

$$\theta = \arctan\left(\|\mathbf{v}_1 \times \mathbf{v}_2\|, \mathbf{v}_1 \cdot \mathbf{v}_2\right) \tag{70}$$

rather than the simpler dot product relation

$$\theta = \arccos\left(\frac{\mathbf{v}_1 \cdot \mathbf{v}_2}{\|\mathbf{v}_1\|\|\mathbf{v}_1\|}\right) \tag{71}$$

as it was observed (most notably in Section 6 when considering the effects of tides) that the cross-product formulation is more robust to numerical precision limitations.


(a) Magnitude Bias   (b) Direction Bias
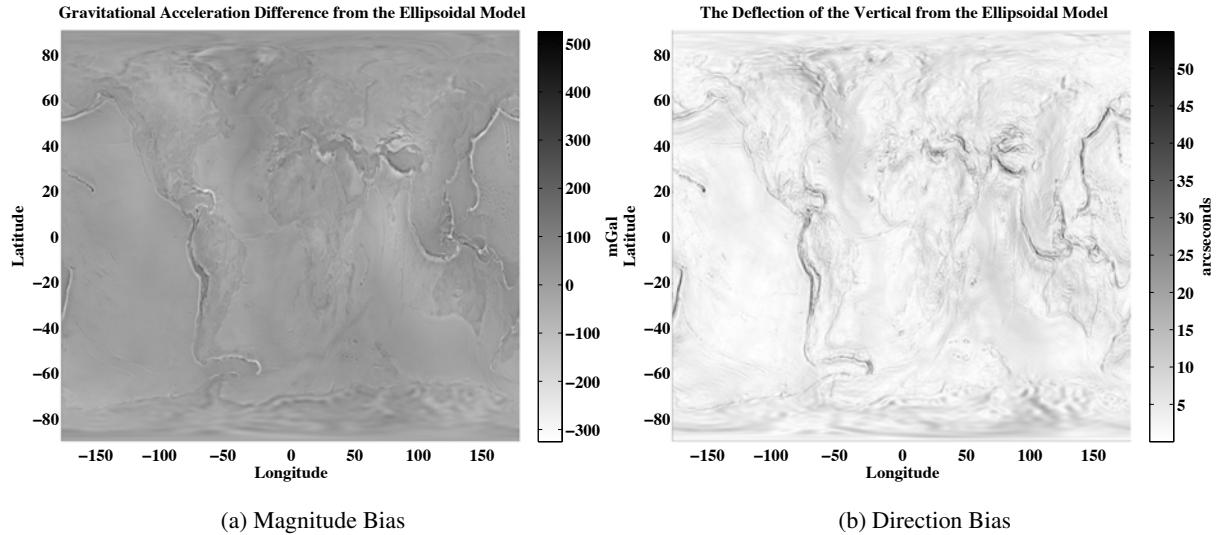
Fig. 21: The difference in the magnitude (a) and the angle (b) between the gravity-acceleration vector **g** under the EGM2008 zero-tide model and the WGS 84 ellipsoidal model using the parameters of Table 5 and Eq. (39) for the acceleration vector under an ellipsoidal gravitational model for points 9 km above the reference ellipsoid. One milliGal (mGal) is equal to $1 \times 10^{-5}\,\mathrm{m/s^2}$. The points were evaluated on a 2500×2500 grid of points in latitude and longitude. As noted in [28, Ch. 3.8], the gravitational-acceleration differences of (a) will tend to bias the prediction of a low-Earth orbiting satellite by approximately 3.5 km after one day.

The directional bias of the vertical direction according to the EGM2008 model in Fig. 21 is observed to exceed 50 arcseconds. This is line with with [87], which notes that the deflection of the vertical can be as high as 70 arcseconds. While probably insignificant when performing radar tracking of aircraft, such an angular bias can be significant when trying to perform high-precision optical tracking of space debris. The acceleration biases compared to using the ellipsoidal model in Fig. 21 appear to be quite small. However, they are many orders of magnitude larger than the highest reported 3D accelerometer accuracy, which is on the order of $9.8 \times 10^{-13}\,\mathrm{m/s^2}$ [279].[57] Also, as quantified in [28, Ch. 3.8], ignoring higher order terms of the gravitation model can lead to errors in the direction of motion of a low-Earth orbital object on the order of 3.5 km after one day, which is likely to be significant when tracking orbital debris. Both [28, Ch.

---

[57]The citation [279] refers only to the numbers reported in a very long abstract. The actual paper as well as the complete conference proceedings appear to be unobtainable.

3.8] and [234, Ch. 3.1] quantify the magnitudes of the effects of various forces on satellites. In [234, Ch. 3.1], it is noted that a constant radial gravitational-acceleration bias of 10^{-8} m/s^2 changes the semi-major axis of the orbital ellipse of a geostationary satellite by approximately 1 m. Note, however, that acceleration contribution due to the Sun and Moon are on the order of 10^{-8} m/s^2 to 10^{-9} m/s^2, as noted in [234, Ch. 3.1] and verified for the Moon in Section 6.3.

If one wishes to use measurements of the gravitational vertical for orientation estimation, as an input in a dynamic model in a target-tracking algorithm, or in an inertial-navigation unit, it is generally desirable to have covariance matrices expressing the accuracy of the model. The EGM2008 model comes with standard-deviation terms for all of the coefficients in the model. Using the method of Appendix F.3, one can find a covariance matrix for the gravitational-acceleration vector implied by the EGM2008 model at any point. Figure 22 plots the average bias in the magnitude of acceleration due to gravity and the bias in the direction of the vertical implied by the standard deviations of the spherical-harmonic coefficients in the EGM2008 model. In [134], the vertical deflection error of the EGM2008 model is analyzed in the mountains of Bavaria and Switzerland. The RMS empirical accuracy of the model is observed to be as high as 4.19 arcseconds, which is larger than the magnitude of the error predicted in Fig. 22, though one would expect errors in the mountains to be higher than elsewhere. In [159], the magnitudes of various approximations used in the deflection of the vertical calculations, such as truncating the spherical-harmonic series or using different permanent tide system, are quantified.



(a) Acceleration Bias   (b) Direction Bias
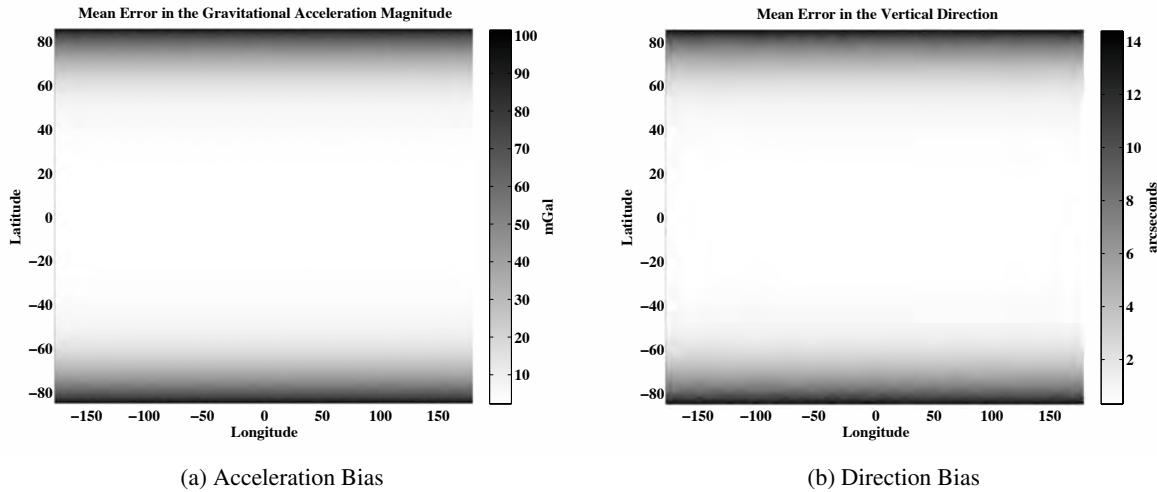
Fig. 22: The average bias of the gravity-acceleration vector (a) and the direction of the vertical (b) as implied by the standard-deviation terms that come with the zero-tide EGM2008 gravitational model evaluated on a 256×256 grid in latitude and longitude at 9 km altitude. The method of Appendix F.3 was used to obtain covariance matrices for the acceleration vector due to gravity at each point. Then, Monte Carlo simulation of the errors assuming additive Gaussian noise was performed to determine the expected vertical bias. At $60°$ latitude (the latitude of southern Greenland), the acceleration bias is on the order of 17 mGal and the vertical orientation bias is on the order of 2 arcseconds. The errors are larger than the commission errors plotted in [252]. The results become worse near the poles. The plots only go up to $\pm 85°$ latitude, due to numerical issues discussed in Appendix F.3. The issues can be avoided by using quadruple precision instead of double-precision floating-point numbers.

The average biases in Fig. 22 were determined through Monte Carlo simulation. Given the covariance matrix of gravitational acceleration $\Sigma_{\nabla V}$, as well as the nominal gravity-acceleration vector based on the EGM2008 model $\mathbf{g}$ at a particular point, noisy samples of the gravity-acceleration vector were drawn assuming that they were normally distributed. That is,

$$\mathbf{g}_{\text{samp}} = \mathbf{g} + \Sigma_{\nabla V}^{\frac{1}{2}} \mathbf{w} \tag{72}$$

where $\mathbf{w}$ is a 3×1 standard $\mathcal{N}\{\mathbf{0}, \mathbf{I}\}$ random vector and the matrix square root is meant to be a lower-triangular Cholesky decomposition, which is `chol(Sigma,'lower')` in Matlab and which can be implemented using the algorithm of [111, Ch. 4.2].[58] The noise could be added directly to the gravity-acceleration $\mathbf{g}$ rather than the gravitational acceleration, since they differ by only an additive constant. The deflection of the vertical was computed using (71) with $\mathbf{g}_{\text{samp}}$ and $\mathbf{g}$ as $\mathbf{v}_1$ and $\mathbf{v}_2$ for each random sample and the results were then averaged. The bias in gravity-acceleration was computed by averaging the magnitude of $\|\mathbf{g} - \mathbf{g}_{\text{samp}}\|$.

The gravitational model considered in this section is time-invariant. Section 6 discusses time-invariant and time-variant tide models and quantifies the magnitude of the error in the vertical direction estimate due to time-varying tides. It is demonstrated that the vertical direction error due to time-variant tides is far less than the precision of the vertical in the EGM2008 model, as plotted in Fig. 22.

---

[58]Strictly speaking, as noted in [111, Ch. 4.2.4], the Cholesky decomposition is not a matrix square root, though it is often called one. Note that if $\Sigma_{\nabla V}^{\frac{1}{2}}$ is the Cholesky decomposition of $\Sigma_{\nabla V}$, then $\Sigma_{\nabla V} = \Sigma_{\nabla V}^{\frac{1}{2}} \left(\Sigma_{\nabla V}^{\frac{1}{2}} \right)'$ and usually $\Sigma_{\nabla V} \neq \Sigma_{\nabla V}^{\frac{1}{2}} \Sigma_{\nabla V}^{\frac{1}{2}}$.

6. THE EFFECTS OF TIDES ON COORDINATE SYSTEMS

6.1 Why Tides Can Matter

The oceans and crust of the Earth are constantly in motion. Many are familiar with the diurnal to semidiurnal ebb and flow of ocean tides, which can be quite large. For example, the largest observed mean range of tides is at Burntcoat Head, Minas Basin, Bay of Fundy, Nova Scotia, where the difference between mean high-tide and mean low-tide water levels is 38.4 ft (≈ 11.7 m) [42]. However, the crust of the Earth moves due to the effects of tides as well. While tides might initially appear to be rather irrelevant to those designing target-tracking algorithms, the motion of the ground due to tides can be larger than the precision of sensors for laser tracking of satellites. For example, laser detection and tracking of orbital debris has been demonstrated [3, 182], producing monostatic range detections of 0.7 m RMS accuracies for targets less than $0.3 \, \text{m}^2$ [183]. The IERS conventions have set an accuracy goal for satellite laser ranging to a millimeter-level accuracy [257, Ch. 9.1.3]. In contrast, the total variation in the position of the ground over time due to solid-Earth tides can be on the order of 30 cm. This is shown in Fig. 23, where the offset of the ground due to solid-Earth tides using the models described in the caption is plotted. Consequently, one cannot simply localize a receiver in an ECEF coordinate system, such as the ITRF, once and never update the position. Rather, the location of the receiver must be updated constantly during the day.
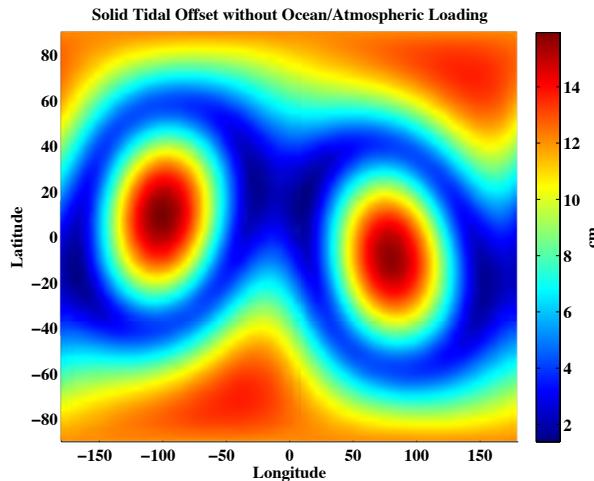

Fig. 23: The magnitude of the Cartesian offset of the ground due to solid-Earth tides on 12 June 2012 at 14:00 UTC without the permanent tide, plotted on a 1000×1000 grid in latitude and longitude, using the model described in the IERS conventions [257], not including ocean and atmospheric loading effects. The IERS provides a reference implementation in Fortran called `dehanttideinel`, which can be obtained from a link in Table 2. As the direction changes over time, the total displacement over time is actually on the order of 30 cm. The algorithms in the included subroutines `step2diu` and `step2lon`, which provide tidal corrections due to mantle anelasticity in the diurnal and long-period bands respectively, are not completely documented in the IERS conventions. The necessary Moon and Sun direction vectors were obtained using the DE430 ephemerides, which were read using the `cspice_spkezr` function in NASA's SPICE toolkit for Matlab (see Appendix I). Time-conversion routines from the IAU's SOFA library were also used.

Due to the periodic tidal motion of the ground, when using a GNSS receiver to localize a sensor for tracking, one must know the specific algorithms for tidal compensation, if any. For example, the data processing routines in the European Space Agency's book on GNSS data processing contain models for the motion of ground due to tides [320, Ch. 5.7]. Solid-Earth tide estimation routines are included in the software accompanying the book,[59] allowing one to provide a user their location on the Earth in coordinates that (ideally) do not drift over time due to tidal effects. Similarly, when one examines the source code of the open-source GPS Toolkit, which is described in [120],[60] one sees that code for solid-Earth tide corrections is also present. However, when performing high-precision tracking of orbital objects, the actual time-varying ECEF location of the receiver is generally desired, in which case, one will not want to use a GPS receiver that provides coordinates that do not change over time due to tides. Minute variations in the displacement of the ground over moderate distances have proven significant in numerous other high-precision applications. For example, the motion of the ground due to tides matters when considering the calibration of large particle accelerators. In such an application, relative displacements less than the size of a human hair can be significant [287].

When considering target tracking, tides affect more than just the location of a sensor in a global coordinate system. One must understand the basics of tidal models to properly use high-precision gravitational models, which are provided in terms of varying permanent tide systems. Knowledge-based target identification can utilize a wide variety of parameters about the environment in which a target is being detected [109, Ch. 9]. For example, a ship detected in a region where the current water level is low must have a shallow draft or have run aground. If the ship is moving in the shallow region, it cannot be any type of ship with a deep draft.

The development of numerical tide models, as described in [171], is extremely complicated. Figure 24 provides an overview of many of the international organizations that play various roles in the development of tidal models. One designing target-tracking algorithms does not necessarily need to know how such models are developed, but must understand the terminology surrounding tide models and should know how significant tidal effects are. The following sections provide an overview of the terminology and models surrounding the effects of tides when considering the motion of the ground and sea as well as when using gravitational models.

6.2   Tides in Terms of Ground and Ocean Motion

Table 9 lists a number of terms that arise when discussing the motion of the ground, sea, and atmosphere due to tidal forces. The periodic motion of the ground due to tides is not the same thing as an earthquake. Whereas the magnitude 9.0 earthquake off the Pacific coast of Tohoku, Japan in 2011, which lasted approximately 180 s, had peak ground acceleration up to 3 times acceleration due to gravity [101, Fig. 3], solid-Earth tides are the slow daily motions of the ground due to external tidal forces. The total motion of the sea surface and/or ground due to time-variant tides is often decomposed into many parts. Whereas Fig. 23 in the previous section showed the motion of the ground due to solid-Earth tides, the total motion of the ground due to tides involves a number of other tidal components. Table 0.1 in the IERS conventions quantifies the magnitudes of the effects of many tidal components beyond solid-Earth tides, with ocean loading being on the order of centimeters, atmospheric loading millimeters, the ocean pole tide on the order of 2 cm

---

[59]The book as well as the accompanying software CD can be downloaded from the European Space Agency's Navipedia web site at `http://www.navipedia.net/index.php/GNSS:Tools`.

[60]The source code for the GPS Toolkit can be obtained on the web site `http://www.gpstk.org/`.
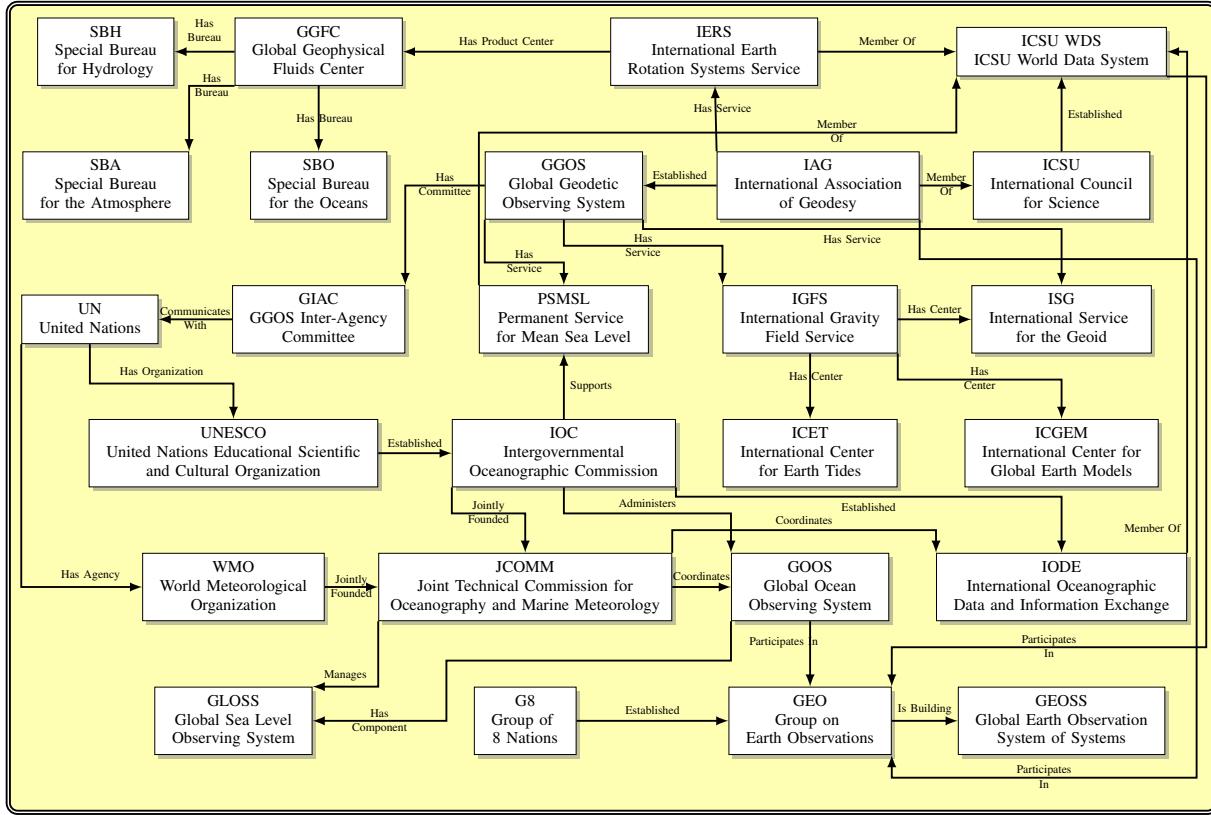
Fig. 24: A subset of the tangled web of international organizations that play a role in monitoring and modeling tides. This includes both gravitational models and models for the physical motion of the Earth. No one organization can be viewed as a definitive source of tidal information. Rather one must often draw data and models from multiple sources. Numerous other organizations, such as the International Hydrographic Organization (IHO), play various additional roles in mapping the sea surface and floor and in monitoring tides.

radially and in millimeters tangentially, and the ocean-pole-tide loading on the order of $2\,\mathrm{mm}$ radially and less than $1\,\mathrm{mm}$ tangentially [257, Ch. 0.2]. Additionally, sea levels can be affected by wind as well as the inverse barometric effect, which as discussed in [116, 217]. The inverse barometric effect explains the difficult-to-model phenomenon that local sea levels rise when the local barometric pressure drops.

Global models for the displacement of points for ocean loading are very complex and include Some Programs for Ocean-Tide Loading (SPOTL) available at `http://igppweb.ucsd.edu/~agnew/Spotl/spotlmain.html` and the programs `olfg` and `olgg` available at the links on the web site `http://holt.oso.chalmers.se/loading/faq.html`. Various tidal-loading models are compared in [254]. The IERS conventions describe models for pole tides and atmospheric loading [257, Ch. 7]. Many tidal models, both for the motion of the ground as well as for changes in Earth geopotential models, decompose tidal components into sets of periodic values with periods that are proportional to the duration of lunar and solar effects [281]. The coefficients for the periodic terms are generally called Doodson parameters, which stem from Doodson's harmonic development of the tidal generating potential [72].

Table 9: Commonly Used Terminology Relating to Time-Variant Tides that Move the Sea Surface and Ground

Term	Definition
Elastic Ocean Tide/ Geocentric Ocean Tide	The sum of the ocean tide and the radial load tides.
Ocean Tide	The vertical displacement of the ocean above the sea floor (which moves) due to time-variant tides.
Ocean Loading	The vertical displacement of the ground due to the weight of the ocean moving due to time-variant tides.
Atmospheric Loading	The vertical displacement of the ground due to the weight of the atmosphere moving due to time-variant tides.
Solid-Earth Tide	The motion of the ground due to tidal forces, not including the effects of ocean and atmospheric loading.
Radial-Load Tides	The combined effect of ocean and atmospheric loading as well as the solid-Earth tides.
Radiational Tide	The motion of the crust, oceans, and atmosphere due to heating from the Sun.
Pole Tide/ Polar Motion	A change in the direction of the Earth's figure axis (the figure axis is defined in Appendix E).
Solid Earth Pole Tide	Motion of the ground due to the centrifugal effects of changes in the Earth's figure axis.
Ocean-Pole-Tide Loading	An offset in the location of points due to the motion of the oceans resulting from the pole tide.
Dynamic Topography/ Dynamic Sea-Surface Topography/ Absolute Dynamic Topography/ Sea-Surface Topography/ Ocean-Surface Topography/	The true height of the sea surface with respect to the geoid; that is, the orthometric sea-surface height. It is the sum of the elastic ocean tide and the mean dynamic topography (and possibly the radiational tide). Sometimes, the terms are used to (ambiguously) mean the mean dynamic topography.
Mean Dynamic Topography/ Quasi-Stationary Sea Surface Topography (QSST)	The (nearly) time-invariant part of the dynamic topography. Does not include seasonal variations, non-permanent winds, eddies. Does include permanent currents, circulation linked to the Earth's rotation, permanent winds.
Sea-Surface Height (SSH)	The height of the sea surface with respect to the reference ellipsoid. SSH = MSS + SLA
Mean Sea Surface (MSS)	The ellipsoidal height of the mean dynamic topography. Approximately, the geoid height plus the mean dynamic topography
Sea-Level Anomaly (SLA)/ Sea-Surface Height Anomaly (SSHA)	The height of the sea surface above the MSS.
Mean Sea-Level Anomaly	A mean sea level anomaly (sometimes just referred to as an SLA, lending confusion to the previous definition of the SLA), as defined by the NOAA [44], occurs when the 5-month running average of the interannual variation is at least 0.1 m greater than or less than the long-term trend.
Interannual Variation	The monthly MSL after the trend (increasing/decreasing over time) and the average seasonal cycle are removed.
Sea-State Bias/ Electromagnetic Bias	A bias in altimeter ranging to the sea surface due to wave troughs reflecting more energy than wave crests.
Tidal Aliasing	An aliasing problem in tidal estimation when the revisit period of an altimeter satellite is too low to observe high-frequency periodic tidal components.
Inverse Barometric Effect	The observation that tides are higher on the order of 1 cm when atmospheric pressure goes down 1 mbar.

The definitions have been inferred from common usage in many papers.

The tidal models discussed in the IERS conventions are specified in terms of a tide-free permanent tide model. Permanent tides are time-invariant theoretical tidal deformities of the Earth that arise due to theoretical modeling of how the Earth deforms in the presence of other bodies in the solar system (permanent tides are discussed in the following section). As noted in [320, Ch. 5.7.1], the tide model under which the ground displacements are taken can be changed by adding constant latitude-dependent offsets to the time-variant tidal offsets. Such offsets change the locations of points on the Earth if one attempts to take raw GNSS positions and reduce them to time-invariant locations, which is desirable when making or using maps, but which is not desirable when localizing a sensor for high-precision tracking. As sensors can often use filtered real-time GNSS signals to monitor their positions in a global ECEF coordinate system without directly using tidal models, the modeling of the motion of the solid ground due to tidal effects is not further considered in this report.

The geoid is often synonymous with the concept of MSL: a surface of equal gravitational potential to which the Earth's oceans would rest in the absence of time-variant tides, under a certain permanent tide definition. However, the true definition of MSL and the ocean sea surface is somewhat more complicated

due to semi-permanent currents in the oceans. Just as swirling water around in a cup makes the water at the sides of the cup higher than the water in the center of the cup, the motion of water in the oceans causes some parts of the ocean to be constantly higher than others after compensating for tidal effects. The quasi-stationary sea-surface topography (QSST) is the mean distance between the actual surface of the sea and the geoid after time-variant tides have been removed. As plotted in [196], the maximum difference between the high and low values of the QSST worldwide is approximately 2 m. In [252], it is plotted as approximately 3 m. To put this in context, the World Meteorological Organization defines sea-state codes on a scale from 1 to 9, where waves having a height of 2 m fall into sea states 4 and 5, which is moderate to rough seas [362, Pg. 326]. On the Beaufort scale of wind, such waves are typical when the wind 10 m above the ground is about 8 m/s to 10.7 m/s. Consequently, without detailed, high-resolution, real-time oceanic wave measurements, it is unlikely that QSST will matter when predicting ahead trajectories of ships at sea. Indeed, in extreme conditions, the difference between the geoid and the mean sea surface can be very large. For example, the highest reported wave height appears to be 112 ft ($\approx$ 34.14 m) reported by the USS *Rampao* on 7 February 1933 during winds of 60 kt ($\approx$ 31 m/s) [360].[61]

6.3 Tides in Terms of the Gravitational Field

Table 10 defines a number of terms that are important for describing the effects of tides when discussing the effects of tides with respect to gravitational models. The gravitational potential models discussed in Sections 5 and 5.4 are defined in terms of various permanent tide systems. Permanent tides are time-invariant distortions of the Earth's shape and gravitational potential resulting from the presence of other bodies in the solar system. Gravitational potential models, and thus geoids, are generally defined in terms of one of three permanent tide models, tide-free, zero-tide, and mean-tide systems, onto which time-variant components can be added. This section explains the difference between the tidal models, and demonstrates that the direct tidal contribution as well as all time-variant tidal contributions can usually be ignored in algorithms for determining the vertical direction of an observer on the ground, as the effects are an order of magnitude smaller than the precision of the zero-tide EGM2008 model.

In a tide-free system, the gravitational potential V of a point in an ECI coordinate system is computed based on the shape that the Earth would be if the Earth were the only object in space (the external potential [direct tidal potential] has been removed) and all time-variant and time-invariant tidal effects were removed. The tide-free model can only be computed based upon models of the elasticity of the Earth; it cannot be directly observed. The zero-tide system computes the gravitational potential of an observer in an ECI coordinate system based on the mass distribution of the true shape of the Earth after time-variant components and the external potential have been removed. Consequently, the zero-tide model is the best choice to use when one wishes to consider the gravitational effects of the Earth independent of other bodies in the solar system without regard to time-variant tides.

The mean tidal model is the zero-tide model with the direct tidal potential added. The direct tidal potential is the apparent change in potential experienced by an observer in an ECI or ECEF coordinate system due to the physical presence of bodies other than the Earth. To understand this, consider a coordinate system whose origin is at the Newtonian center of mass of a system containing N bodies. In an arbitrary

---

[61]That is the highest reported wave not caused by a seismic disturbance. The highest tsunami wave appears to have been a 1720 ft ($\approx$ 524 m) wave in Lituya Bay on the northeast shore of the Gulf on Alaska on 9 July 1958 caused by a rockslide into the bay resulting from an earthquake [228].

Table 10: Definitions of the Different Tidal Potentials, Tide Systems, and Tides

Term	Definition
Non-Tidal Potential	The potential of the Earth if no other bodies existed in space. Changes over time are due to Earth mechanics, such as volcanism.
Indirect Tidal Potential	The potential due to the deformation of the Earth's crust by other celestial bodies (Sun, Moon, etc). There are time-invariant as well as time-variant parts.
Direct/External Tidal Potential	The time-variant and invariant gravitational potential due entirely to other celestial bodies, almost always computed with respect to an observer *accelerating with the Earth* through space.
Centrifugal Potential	The apparent change in gravitational potential experienced by a stationary observer on a rotating Earth compared to an observer on a theoretical non-rotating Earth.
Tide-Free/Non-Tidal System	A system influenced only by the non-tidal potential.
Zero-Tide System	A system influenced only by the non-tidal potential and the permanent indirect-tidal potential.
Mean-Tide System	A system influenced only by the non-tidal potential and the permanent direct-and-indirect-tidal potentials.
Permanent Tide	Contributions to the tidal potential (or the shape of the Earth) that are time-invariant.
Solid-Earth Tide	Indirect tidal-potential contributions due to the deformation of the non-oceanic (or any water) and atmospheric parts of the Earth. Sometimes, direct tidal potentials are included.
Ocean Tide	The indirect tidal-potential contribution due to the movement of water in the oceans.
Pole Tide/ Polar Motion	Changes in the orientation of mass within the Earth leading to a change in the Earth's figure axis, which changes acceleration due to gravity with respect to fixed points on the crust.
Solid Earth Pole Tide	A time-variant solid-Earth tidal potential arising from the motion of the Earth's figure axis with respect to the ITRS (polar motion), presumably due to motions in the Earth's core and mantle with respect to the crust.
Ocean Pole Tide	A time-variant tidal potential due to the motion of the ocean as a result of the centrifugal effect of polar motion.

The definitions are based on information in [257, 298, 299].

coordinate system, the location of the center of mass $\mathbf{r}_{\text{center}}$ is

$$\mathbf{r}_{\text{center}} = \frac{1}{\sum_{i=1}^{N} M_i} \left(\sum_{j=1}^{N} M_j \mathbf{r}_j \right) \tag{73}$$

where M_i is the mass of the ith body whose center of mass is located at $\mathbf{r}_j$. A coordinate system defined such that the center of mass is the origin has $\mathbf{r}_{\text{center}} = \mathbf{0}$ over all time. Consequently, the location of the first object in the center-of-mass coordinate system can be expressed as

$$\mathbf{r}_1 = -\frac{1}{M_1} \left(\sum_{j=2}^{N} M_j \mathbf{r}_j \right). \tag{74}$$

Now, consider moving the origin of the coordinate system to the center of mass of the first object. A point in the center-of mass coordinate system $\mathbf{p}$ can be expressed in the coordinate system at the center of mass of the first object $\tilde{\mathbf{p}}$ by the affine transformation

$$\mathbf{p} = \mathbf{r}_1 + \tilde{\mathbf{p}}. \tag{75}$$

Using (74), taking the second derivative of (75) with respect to time, and solving for $\tilde{\mathbf{p}}$, one finds that an acceleration can be transformed from the center-of-mass system to the center of mass of Object 1's system using

$$\ddot{\tilde{\mathbf{p}}} = \ddot{\mathbf{p}} + \frac{1}{M_1} \left(\sum_{j=2}^{N} M_j \ddot{\mathbf{r}}_j \right). \tag{76}$$

The acceleration due to the direct tidal potential (both permanent and time-variant) on Object 1 is $\ddot{\tilde{\mathbf{p}}}$ minus the contribution to gravitational acceleration due to Object 1 itself. The direct tidal potential is thus the potential whose gradient (or negative gradient, depending on the definition) gives the acceleration due to the direct tidal potential.

The significance of the transformation from an inertial center-of-mass coordinate system and its relation to tidal potentials can be easily understood when considering the ideal Earth-Moon system on its own, as illustrated in Fig. 25, where the Earth is approximated as a sphere having radius $r_{\oplus}$ and the center of mass of the Moon is a distance of $R_{\mathbb{C}}$ from the center of mass of the Earth. The example here is inspired by a similar example in [171, Ch. 6.1]. Points A, B, and C are all on the surface of the spherical Earth. Using the law of cosines and the law of sines, one can find that

$$R_{BM}^2 = R_{\mathbb{C}}^2 + r_{\oplus}^2 - R_{\mathbb{C}} r_{\oplus} \cos(\theta) \tag{77}$$

$$\alpha = \arcsin\left(\frac{r_{\oplus}}{R_{BM}} \sin(\theta)\right). \tag{78}$$

The force per unit mass (acceleration) experienced by a small object at point p on the surface of the spherical
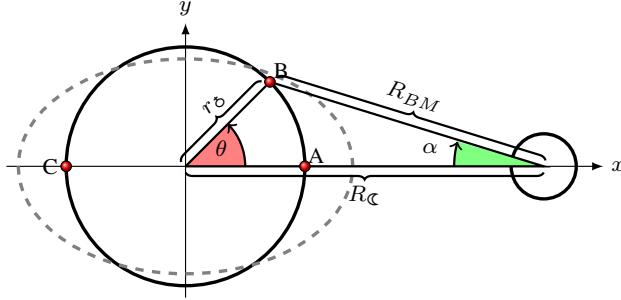
Fig. 25: The geometry of the Earth and the Moon used in the discussion on the direct tidal potential. When the gravitational force of the Moon on the Earth is transformed into an ECI coordinate system, the transformed forces point roughly towards the center of the Earth at the poles (along the *y*-axis) and away from the center of the Earth at the equator (along the *x*-axis) resulting in an equatorial bulge and explaining why there are two high tides per day on most of the Earth. The gravitational potential associated with the force of the Moon and all other solar system bodies in ECI coordinates is the direct potential. The time-invariant part is the permanent direct potential. The relative radii of the Earth and Moon are to scale, but the Earth-Moon distance is not to scale.

Earth, but not rotating with the Earth, is

$$\mathbf{a}_p = \nabla V_{\oplus} + \nabla V_{\mathbb{C}} \tag{79a}$$

$$\approx \frac{GM_{\oplus}}{r_{\oplus}^2} (-\mathbf{u}_x \cos(\theta) - \mathbf{u}_y \sin(\theta)) + \frac{GM_{\mathbb{C}}}{R_{BM}^2} (\mathbf{u}_x \cos(\alpha) - \mathbf{u}_y \sin(\alpha)) \tag{79b}$$

where simple uniform-mass-distribution approximations were used to model the gravitational effects of the Earth and Moon. $GM_{\oplus}$ and $GM_{\mathbb{C}}$ are the universal gravitational constant times the mass of the Earth and the

mass of the Moon, respectively. $r_\oplus$ is the radius of the Earth, and $\mathbf{u}_x$ and $\mathbf{u}_y$ are unit vectors in the directions of the x and y axes, respectively. Noting that the acceleration of the Moon due to the Earth is

$$\mathbf{a}_{\mathbb{C}} = -\frac{GM_\oplus}{R_{\mathbb{C}}^2}\mathbf{u}_x \tag{80}$$

where $R_{\mathbb{C}}$ is the distance between the centers of mass of the Earth and Moon, the acceleration of the point transformed into a coordinate system centered at the center of mass of the Earth using (76) is

$$\tilde{\mathbf{a}}_p = \mathbf{a}_p - \frac{GM_{\mathbb{C}}}{R_{\mathbb{C}}^2}\mathbf{u}_x. \tag{81}$$

The direct tidal contribution to the acceleration in (81) is all accelerations resulting from forces that are not due directly to the physical mass of the Earth. That means that one must subtract off $\nabla V_\oplus$ to get the direct tidal acceleration contribution

$$\tilde{\mathbf{a}}_p^{\text{direct}} = \frac{GM_{\mathbb{C}}}{R_{BM}^2}\left(\mathbf{u}_x\cos(\alpha) - \mathbf{u}_y\sin(\alpha)\right) - \frac{GM_{\mathbb{C}}}{R_{\mathbb{C}}^2}\mathbf{u}_x. \tag{82}$$

In the examples below, the following values are used:

$$GM_\oplus = 3.986004418 \times 10^{14}\,\frac{\text{m}^3}{\text{s}^2} \tag{83}$$

$$\mu = 0.0123000371 \tag{84}$$

$$GM_{\mathbb{C}} = \mu GM_\oplus \tag{85}$$

$$r_\oplus = 6378136.6\,\text{m} \tag{86}$$

$$R_{\mathbb{C}} = 3.994833385218484 \times 10^8\,\text{m}. \tag{87}$$

All of the values except for that of $R_{\mathbb{C}}$ are taken from the IERS conventions [257, Ch. 1]. The value of $R_{\mathbb{C}}$ was determined using the DE430 ephemerides read using the `cspice_spkezr` function in NASA's SPICE toolkit for Matlab for the date of 12 June 2012 at 14:00 UTC (see Appendix I). At point A in Fig. 25, when $\theta = 0$, Eq. (82) simplifies to

$$\tilde{\mathbf{a}}_p^{\text{direct}}\Big|_{\theta=0} = GM_{\mathbb{C}}\left(\frac{1}{(R_{\mathbb{C}} - r_\oplus)^2} - \frac{1}{R_{\mathbb{C}}^2}\right)\mathbf{u}_x \tag{88a}$$

$$\approx 1.005 \times 10^{-6}\,\frac{\text{m}}{\text{s}^2}\mathbf{u}_x. \tag{88b}$$

Similarly, at point C in Fig. 25, when $\theta = \pi$, (82) simplifies to

$$\tilde{\mathbf{a}}_p^{\text{direct}}\Big|_{\theta=\pi} = GM_{\mathbb{C}}\left(\frac{1}{(R_{\mathbb{C}} + r_\oplus)^2} - \frac{1}{R_{\mathbb{C}}^2}\right)\mathbf{u}_x \tag{89a}$$

$$\approx -9.580 \times 10^{-7}\,\frac{\text{m}}{\text{s}^2}\mathbf{u}_x. \tag{89b}$$

On the other hand, when $\theta = \frac{\pi}{2}$, then

$$\tilde{\mathbf{a}}_p^{\text{direct}}\Big|_{\theta=\frac{\pi}{2}} = \frac{GM_{\mathbb{C}}}{R_{\mathbb{C}}^2 + r_{\bar{o}}^2}\left(\mathbf{u}_x\sqrt{1 - \frac{r_{\bar{o}}^2}{R_{\mathbb{C}}^2 + r_{\bar{o}}^2}} - \mathbf{u}_y\frac{r_{\bar{o}}}{\sqrt{R_{\mathbb{C}}^2 + r_{\bar{o}}^2}}\right) - \frac{GM_{\mathbb{C}}}{R_{\mathbb{C}}^2}\mathbf{u}_x \tag{90a}$$

$$\approx -1.174 \times 10^{-8}\mathbf{u}_x - 4.903 \times 10^{-7}\mathbf{u}_y. \tag{90b}$$

From (88b), (89b), and (90b), it can be seen that the total direct tidal potential of the Moon produces a force per unit mass on the order of $10^{-6}\,\text{m/s}^2$ around the globe. As the Moon orbits the Earth, the directions of the accelerations will change. However, since the Moon stays in roughly the same plane, the acceleration of a particle near the poles contains a time-invariant portion in the y direction, thus compressing the Earth. This time-invariant contribution is the direct permanent tidal potential.

The direct permanent tidal potential due to the Moon is on the order of $10^{-6}\,\text{m/s}^2$. In comparison, the bias of acceleration due to gravity in the tide-free EGM2008 model in Fig. 22 is on the order of 10^{-5}m/s^2. As shown in a plot in [234, Ch. 3.1], the acceleration experienced in an ECI coordinate system due to the Sun is less than that due to the Moon. Consequently, when using a gravitational-acceleration measurement to determine the orientation of an observer on or near the surface of the Earth, one can probably ignore the direct tidal potential. Consequently, the zero-tide permanent-tide model is often sufficient.

In [77], theoretical inconsistencies that arise with the use of a mean-tide model are highlighted. In [264], it is noted that the determination of GPS locations on the surface of the Earth in terms of a tide-free coordinate system is physically meaningless, and it is suggested that a zero-tide model be used. However, the WGS 84 standard uses a tide-free model for defining the geoid and reference ellipsoid [69, Ch. 6]. The tide systems used by other countries vary, as noted in [77], where conversions between tide systems are provided.[62] When considering the physical location of points on the Earth, the difference between a mean-tide and a tide-free model is approximately $-12\,\text{cm}$ at the poles and $+6\,\text{cm}$ at the equator [257, Ch. 7.1.1].

The pole tide also affects the Earth's gravitational field. The pole tide arises from a redistribution of mass within the Earth with regard to the crust, which changes the figure axis of the Earth. A definition of the figure axis and more details on the nature of the pole tide are given in Appendix E. The IERS 2010 conventions [257, Ch. 6.1, Eq. 6.5] says that two of the lower-order terms in the EGM2008 model must be modified to be consistent with the wobbling rotation axis of the Earth in the ITRS. The modified parameters depend on the values of other spherical harmonic gravitational parameters, and the pole tide modifications should be made *after* accounting for the drift of the model's coefficients over time. The drift of the coefficients was noticed in [366] and is documented for the EGM2008 model in [257, Ch. 6.1].[63]

Figure 26 quantifies the difference in acceleration due to gravity and the direction of the vertical vector under a complete-tide model based on the descriptions in [332, Ch. 5] and [257, Ch. 6] compared to a zero-tide model. Eq.(70) was used to determine the angular difference between the gravitational-acceleration

---

[62]Chapter 6.2.2 of the WGS 84 standard [69] provides the same formula as in [77] for converting from a tide-free to a zero-tide geoid model.

[63]The pole tide correction listed in [332, Ch. 6.9.2.1] is not the same as that in [257, Ch. 6.1]. It is not clear which one is better. The one from [257, Ch. 6.1] is used in this report as it is a standard.

vectors in each instance. Again, it can be seen that the effects of time-variant tides are less than the accuracy of the EGM2008 gravitational model, so those designing tracking and navigation algorithms can often ignore the effects of time-variant tides on the Earth's gravitational potential.


(a) Magnitude Bias   (b) Direction Bias
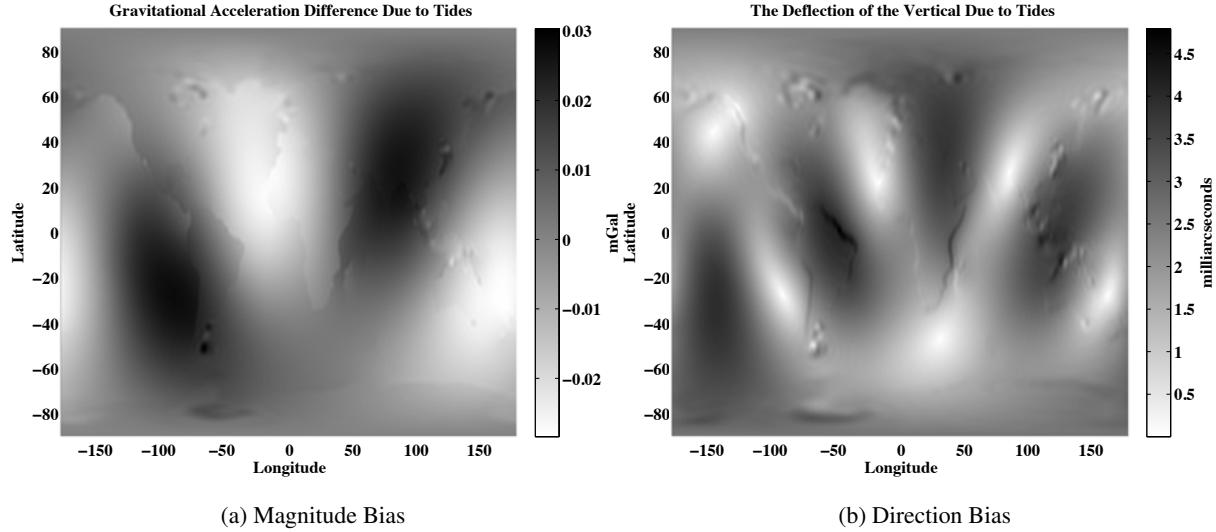
Fig. 26: Plots of the difference between the EGM2008 zero-tide model and the EGM2008 tide-free model with added tides for 12 June 2012 at 14:00 UTC. The quantities were computed without the contribution of the centrifugal potential of the rotating Earth. The solid-Earth tidal effects on the geopotential were added using the model in [332, Ch. 5], where values for $k_{2m}^{(+)}$ were taken from [257, Ch. 6] (as they are missing from [332, Ch. 5]). The pole tidal effects and the ocean tidal effects were added using the models of [257, Ch. 6], where coefficients for the FES2004 tidal model were downloaded from the link in Table 2. The necessary Moon and Sun direction vectors were obtained using the DE430 ephemerides, which were read using the `cspice_spkezr` function in NASA's SPICE toolkit for Matlab (see Appendix I). Time-conversion routines from the IAU's SOFA library were also used.

Additionally, due to inconsistent documentation, the accuracy of the gravitational tidal models is limited for anyone trying to reproduce the results, meaning that one cannot truly recreate the models without access to the original code of the developers, which has not been made public online. For example, in the IERS conventions [257, Ch. 6], it is unclear whether an elastic or an anelastic Earth model is recommended, or whether some combination of the two is preferred. In particular, the second step in the solid tide offset for the IERS conventions is unclear and the algorithm provided in [332, Ch. 5] omits a number of coefficients that are provided in the IERS conventions.

Furthermore, inconsistencies exist between the tide model assumed in the IERS conventions and that implied by the coefficients given for the EGM2008 gravitational model. If one uses the formula of Section 6.2.2 of the IERS conventions to convert the zero-tide EGM2008 spherical harmonic gravitational coefficient into the tide-free system using the value of the Love number $k_{2,0}$ given in Table 6.3 in the conventions, one obtains a different result than the tide-free value given in the EGM2008 itself. Whereas the Love

number in the IERS conventions is $k_{2,0} = 0.29525$, using the value $k_{2,0} = 0.3$ in the conversion of the zero-tide spherical harmonic coefficient into a tide-free value is consistent with the tide-free value given in the EGM2008. This is in line with the documented conversion between zero-tide and tide-free models in the EGM96 model [198, Sec. 3.3.1] and the WGS 84 standard's ideal Love number [69, Ch. 6.2]. Since the EGM2008 model derived its tide-free coefficients using a different $k_{2,0}$ Love number than the tide model suggested by the IERS conventions, one would expect a loss of accuracy when using the gravitational tide model of the IERS conventions with the EGM2008 gravitational model.

7. THE EARTH'S MAGNETIC FIELD

Though coordinate systems based on the Earth's magnetic field exist [115, 131], such systems are typically best suited for modeling the trajectories of charged particles in the solar wind approaching the Earth. For target tracking applications, magnetic-field-based coordinate systems are generally of little interest insofar as they are not required for modeling of various physical effects. However, accurate models of the Earth's magnetic field can play an important role in target tracking. For example, the Lorentz force experienced by charged satellites traveling through the Earth's magnetic field can be harnessed to perform limited maneuvers without using thrusters [15, 105, 106, 318, 330]. Similarly, the magnetic-field measurements can be used to help determine the orientation of a sensor to a moderate precision. This section looks at basic spherical-harmonic magnetic-field models that are used in Section 8.2 for sensor orientation estimation.

Models of the Earth's magnetic field are typically decomposed into the four parts shown in Table 11. Ideally, one would use a model that includes the combined effects of all the fields in real time. In practice, however, simpler models are used. The most prevalent Earth magnetic-field models only model the main field. The World Magnetic Model (WMM) and the International Geomagnetic Reference Field (IGRF) are the two most prominent main field models. The IGRF is meant to represent the Earth magnetic field at times in the past, whereas the WMM is a predictive model for times in the future. Table 2 lists sources and documentation for the WMM. As described in [223], the WMM is used by the U.S. Department of Defense, the U.K. Ministry of Defense, the North Atlantic Treaty Organization (NATO), and the International Hydrographic Organization. On the other hand, the IGRF, which is described in [91], is created by a task force of the International Association of Geomagnetism and Aeronomy (IAGA) and can be obtained from `http://www.ngdc.noaa.gov/IAGA/vmod/igrf.html` . The magnetic field for the IGRF as well as for the WMM is defined in terms of spherical-harmonic coefficients, which can be used as described in Appendix F. Neither the IGRF nor the WMM is a static model. Rather, the values of the spherical-harmonic coefficients drift over time. The models come with drift-rate coefficients that are used to tailor the models to a specific date. New versions of the models are released every five years.

Table 11: Components of the Earth's Magnetic Field

Field Type	Description
Core Field Main Field	The part of the Earth's magnetic field generated by the dynamo process in the fluid outer core of the Earth.
Anomaly Field Crustal Field	The part of the Earth's magnetic field arising from magnetic materials in the Earth's crust.
External Field	The part of the Earth's magnetic field due to electrical currents in the ionosphere.
Induced Field	The part of the Earth's magnetic field from currents induced in the crust due to electrical currents in the ionosphere.

Models of the Earth's magnetic field are typically decomposed into the parts described above.

The WMM and IGRF are commonly used on navigation charts. Figure 27 is an example of a subset of an FAA map for pilots flying under visual flight rules (VFR). Such maps can be obtained for free from [336]. FAA VFR flight maps list the offset in the direction of the Earth's magnetic field from true North to help

pilots navigate. The numbers at the ends of runways are the first two digits of the three-digit magnetic heading that a pilot must fly to land the plane on the runway. For example, a pilot approaching a runway labeled 09 will be heading East (90° clockwise from magnetic North) and the other side of the runway would be numbered 27 corresponding to 270°. However, due to field effects not modeled in the WMM, FAA flight maps are labeled when there exists a large deviation in magnetic north from the WMM model. As can be seen in Fig. 27, an 8° deviation exists near Aberdeen Proving Ground in Aberdeen, Maryland.

Fig. 27: An excerpt of the FAA's sectional aeronautical raster chart dated 25 July 2013 for Washington, DC illustrating the local magnetic disturbance near the Aberdeen Proving Ground in Aberdeen, Maryland. FAA aeronautical charts are available online for free at [336].

For the purposes of determining the orientation of a sensor near the ground, better models to use are the high-definition geomagnetic model (HDGM) and the enhanced magnetic model (EMM). The HDGM includes the effects of the main field as well as the crustal field and part of the external field, as described in [222]. The HDGM is put out by the National Oceanic and Atmospheric Administration (NOAA) every year and, as of 24 July 2014, costs $20,060$ U.S. as given on `http://www.ngdc.noaa.gov/geomag/hdgm.shtml` though U.S. government agencies can generally obtain it free of cost. The primary market for the HDGM is oil-well drillers. As described in [38], it is common for well drillers to drill multiple wells horizontally underground from a single hole in the ground. Well drillers use gravitational- and magnetic-field measurements to determine the location of the bit underground to try to avoid colliding with neighboring wells and to reach desired geological features.

The EMM is similar to the HDGM, but is published only every five years. The EMM with documentation can be obtained from the sources given in Table 2. Though the spherical-harmonic model of the EMM is the

same degree and order as the HDGM, it is not published as often, making the EMM less suitable for real-time high-precision drilling than the HDGM. For the purposes of this report, however, the 2010 release of the EMM is used. Figure 28 shows the difference between the EMM and the WMM near the Aberdeen Proving Ground. Though the map in Fig. 27 notes a deviation of $8°$, the maximum deviation in Fig. 28 is only on the order of $1°$, indicating that the EMM is not capable of modeling small-scale magnetic disturbances. However, higher-fidelity models are possible using data from aeromagnetic surveys taken by aircraft to map local magnetic variations. As noted in [38, 222], it is possible for the spherical-harmonic models such as the HDGM to be combined with aeromagnetic survey data to produce better overall results. However, there does not appear to be a simple, published algorithm for accurately combining such models, even though a number of small companies exist that provide such services.
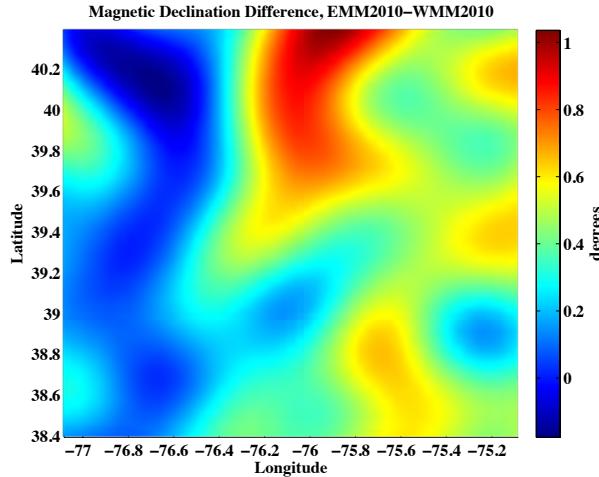
Fig. 28: The difference in the magnetic declination from the WMM2010 and the EMM2010 magnetic models near the Aberdeen Proving Ground in Aberdeen, Maryland for points on the WGS 84 reference ellipsoid. The time for the models was set to 25 July 2013, the same as the date of the FAA's chart excerpt in Fig. 27. Since the largest difference is only on the order of $1°$, one can conclude that the resolution of the EMM2010 is not sufficiently high to model the $8°$ deviations that are marked on the FAA chart in Fig. 27.

Figure 29 plots the deviation between magnetic North and true North as well as the magnetic inclination for the 2010 version of the EMM at its epoch year. It can be seen that over significant portions of the Earth, large deviations between the direction of the geographic pole and the magnetic pole are present. Despite the shortcomings of the EMM, the error of the model is significantly less than $8°$ over most of the globe. Indeed, as noted in [223], the error requirement for the direction of magnetic North (declination) in the WMM, which is less precise than the EMM, is a RMS error of $1°$ during its period of validity. In [222], the declination uncertainty of the HDGM (presumably RMS error) was given to be $0.3°$, which one might assume is on the order of the accuracy of the EMM. Interestingly, the RMS precision of the WMM listed in [223] is actually better than the precision listed for the HDGM. However, one might expect that the precision is only with reference to the "main field" and not with respect to crustal variations.
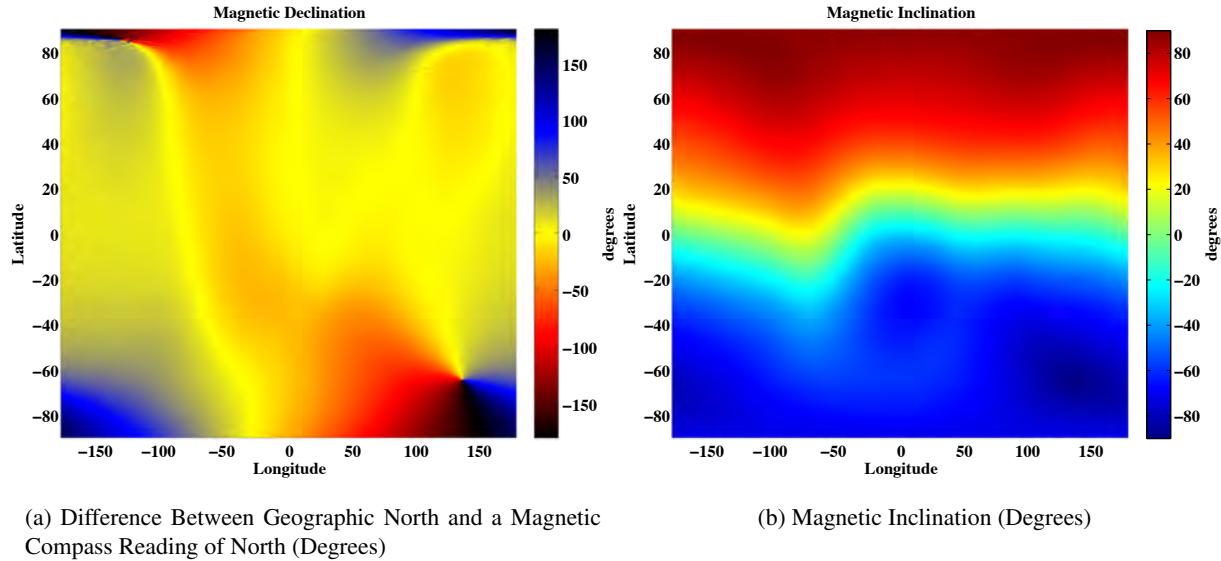
(a) Difference Between Geographic North and a Magnetic Compass Reading of North (Degrees)

(b) Magnetic Inclination (Degrees)

Fig. 29: Plots of (a) the difference in direction of geographic North and a local compass reading of North (magnetic declination), and (b) magnetic inclination, with points evaluated on a grid of 2500×2500 points in latitude and longitude. For both plots, magnetic-field values using the EMM2010 model at the epoch year (2010) were used for points on the surface of the WGS 84 reference ellipsoid. In (a), the magnetic poles (which do not coincide with the geographic poles) can be identified as points in the upper left and lower right about which the bias in the compass reading completes a $180°$ cycle. Note that the magnetic pole in the geographic northern hemisphere is *magnetic* South. Magnetic inclination is the angle between the local tangent plane (in this case, on the WGS 84 ellipsoid) and the direction of the magnetic-field vector **B** with "down" being the positive direction.

Unlike spherical-harmonic gravitational models, such as the EGM2008, neither the EMM nor the HDGM come with coefficients for computing a covariance matrix for the vector magnetic-field measurement at a given point. On the other hand, the British Geological Survey Global Geomagnetic Model (BGGM) has associated tabular accuracy data, which can be downloaded from `http://www.geomag.bgs.ac.uk/data_service/directionaldrilling/bggm.html` and is described in [210]. However, the BGGM is less accurate than the HDGM [222] and is also not a free model. Free geomagnetic models of an accuracy higher than the HDGM exist, such as the EMAG2 model described in [220]. However, the EMAG2 model only tabulates the magnitude of the Earth's magnetic field on a grid of points. It does not provide three-dimensional magnetic-field vectors and thus it is not particularly useful for direction estimation. A precursor to EMAG2 forms the basis of the World Digital Magnetic Anomaly Map, which is described in [221] and can be downloaded from `http://geomag.org/models/wdmam.html` .

Initially, it may seem like magnetic-field measurements are completely unsuited for direction determination for target tracking. With a model accuracy probably not better than $0.3°$ on average and possible outlier model errors on the order of $7°$ to $8°$, the precision of the direction estimation is unsuitable for any long-range sensing applications. However, joint-vector magnetic and gravitational sensors are very inexpensive and thus can be very useful for determining the orientation of a short-range sensor to a reasonable accuracy. For example, the STMicroelectronics LSM303D is listed at less than $2.13 U.S. on `www.digikey.com` as of 24 July 2014. The least significant bit (LSB) in the documentation [315] for the accelerometer component

is 0.061mg, where 1g is assumed to be the standard value of acceleration due to gravity, which in the SI standard [39] is $9.80665\,\text{m/s}^2$. For the magnetic field sensor component, the LSB is $0.008\,\mu\text{T}$. To transform the LSB precisions into angular accuracies that have more meaning for directional estimation, consider the case where the true acceleration due to gravity is aligned with the *z*-axis, meaning that

$$\mathbf{g} = \begin{bmatrix} 0 \\ 0 \\ 9.80665\,\dfrac{\text{m}}{\text{s}^2} \end{bmatrix}. \tag{91}$$

The maximum 1-bit perturbation in each component means offsetting the *x* and *y* components by 0.061×10^{-3} times $9.80665\,\frac{\text{m}}{\text{s}^2}$ and reducing the *z* component by the same amount, so as to maximize the angular offset. This offset vector is thus

$$\mathbf{g}_{\text{perturb}} = \begin{bmatrix} 5.9820565 \times 10^{-4}\,\dfrac{\text{m}}{\text{s}^2} \\ 5.9820565 \times 10^{-4}\,\dfrac{\text{m}}{\text{s}^2} \\ 9.80665 - 5.9820565 \times 10^{-4}\,\dfrac{\text{m}}{\text{s}^2} \end{bmatrix} \tag{92}$$

an offset of approximately 17.79 arcseconds ($\approx 0.00494°$). A typical low value of the Earth's magnetic-field strength is on the order of $31\,\mu\text{T}$. Thus, using a similar logic as determining the 1-bit error offset of the direction estimation, the offset of the direction of the magnetic-field measurement is on the order of 1.25 arcminutes ($\approx 0.02°$). Though the inherent bias and noise in the sensor is much larger than the LSB, with proper calibration, after averaging a number of measurements, one might be able to achieve directional measurements that are on the order of the accuracy of the EMM model, which should be sufficient for a number of short-range sensing applications.

Magnetic-field models also arise when tracking objects in space for purposes of ionospheric modeling, for example. Real-time external field information can be obtained from `http://www.geomag.us/models/RTDFC.html` and the data-source links provided therein. Additionally the International Real-time Magnetic Observatory Network (INTERMAGNET), which was formed by the USGS and the British Geological Survey (BGS) through the IAGA/IUGG [312], provides real-time Earth magnetic-field measurements from around the world. However, it is up to users of the data to create their own real-time magnetic-field models from the data.

Finally, it should be noted that the presence of power lines and numerous other things on land can bias magnetic-field measurements. At sea, ocean waves can also bias magnetic-field measurements. However, it has been demonstrated that the bias is on the order of 0.2 nT [356], which is insignificant considering the limited precision of the Earth magnetic-field models.

8. DETERMINING THE ORIENTATION OF A SENSOR

Though a large number of techniques for residual sensor bias estimation exist within the context of the target-tracking literature, as discussed in Section 1, less focus is placed on determining the location and/or pointing direction of a sensor in the first place. For the purposes of this report, the problem of sensor localization is omitted, as global navigation satellite systems, such as GPS, can easily be used for high-precision sensor localization. Although such systems have failed for short times, for example, on 6 December 2006, when a solar flare rendered GPS inoperable for approximately 15 minutes on the sunlit side of the Earth [2], and are vulnerable to other failures and to low-powered jammers [194], satellite navigation systems are reliable in most conditions. When satellite navigation is not possible, localization using stars can be considered [172, 173, 177, 276].[64] The Defense Advanced Research Projects Agency (DARPA) has started a number of projects to improve GPS-free localization and navigation [63].

This section discusses how one can determine the orientation of a sensor. Orientation estimation can be done using GPS signals. However, as described in [96], it necessitates the use of a two-antenna GPS receiver, is limited to an accuracy of $0.4°$, and aspects of the technique are patented.[65] On the other hand, on a ship one might consider using the direction of "North" provided by the ship's gyrocompass. However, such direction information is complicated by the fact that large ships bend. For example, when transferring alignment information between IMUs on large ships (or spaceships), the flexure (bending) of the material making up the ship must be taken into account [33, 163, 178]. Additionally, the best gyrocompasses advertised appear to have an accuracy no better than $0.1°$ secLat [272, 326]. The term "secLat" refers to the secant of the latitude, meaning that the direction estimates become increasingly bad near the geographic poles. Thus, at $60°$ latitude, which is near southern Greenland, the best gyrocompass accuracy should be on the order of $0.2°$.

Stars or satellites with known ephemerides can be used as points of reference for determining one's orientation. For example, in [174], it is noted that strategic missile systems have used star-tracking algorithms to determine their orientation to sub-arcsecond accuracy. However, commercial-off-the-shelf (COTS) navigation systems are not nearly as accurate as missile systems in terms of orientation-estimation accuracy, as it is not as critical for their use in most systems. Additionally, COTS solutions must deal with atmospheric refraction, whereas long-range missiles will presumably spend a portion of their trajectory outside of most of the atmosphere. For example, Northrop Grumman's commercially available stellar-inertial-GPS navigation system estimates the heading of an aircraft to an accuracy of approximately 20 arcseconds and roll and pitch to an accuracy of approximately 72 arcseconds [245].

While stars are always visible to satellites (that are pointed in the correct direction) and are visible to the naked eye at night when it is not cloudy, stars (other than the Sun) can be seen during the day in the infrared region. Infrared star spectroscopy is possible during daytime, and stars are better seen through dust in the infrared region than in the visible region [227]. Indeed, daytime star tracking has been studied since at least the 1960s as a tactical inertial-navigation system alignment reference [141]. However, stars often cannot be seen well when it is cloudy. In such instances, one can consider using satellites. For example, as

---

[64]Interestingly, some GPS-free localization techniques rely on how the atmosphere warps the apparent location of stars at different elevation angles [112, 275].

[65]In [181], it is claimed that multi-antenna GPS systems provide attitude accuracy on the order of 1 mrad, which is approximately $0.05°$.

of 26 November 2012, the ITU listed 466 non-planned[66] geostationary satellites and 584 non-planned non-geostationary satellites between $-10°$ and $10°$ longitude that broadcast within the *S*-band region $(2-4\,\text{GHz})$ [153] that is also used by radars. However, simply because a satellite has been allocated a specific band of frequencies does not mean that it will be broadcasting all the time. Thus, the passive use of satellites for orientation estimation can be problematic. However, there do exist satellites specifically designed for radar calibration [162], which might be particularly suitable for determining the orientation of a radar.

This section demonstrates how most of the coordinate systems and physical effects discussed in the previous sections of this report must be considered jointly when determining the orientation of a sensor. Section 8.1 reviews a generic algorithm for estimating a rotation matrix given common observations in two coordinate systems, demonstrating how it is equivalent to a maximum-likelihood algorithm under certain conditions. Section 8.2 pulls together the results from previous discussions on models of the Earth's gravitational and geomagnetic field to demonstrate how one can determine orientation using magnetic and gravitational (accelerometer) measurements by means of the algorithm of Section 8.1, which is shown to produce identical results to a globally optimal solution. Section 8.3 pulls together previous discussions on celestial and terrestrial coordinate systems to discuss how one's orientation can be determined using observations of stars, without knowing *a priori* the association of observed stars to catalogued stars.

8.1 Orientation Estimation Using Sets of Common Observations

8.1.1 An Explicit Estimation Algorithm

A large number of algorithms for determining the orientation (also known as attitude) of a sensor, missile, or spacecraft exist, in part, due to the fact that a large number of mathematical representations of 3D orientation exist. Whereas it is possible to represent the 3D orientation of an object using three parameters, such as Euler angles, it has been proven that no singularity-free three-parameter representation of an orientation is possible [319]. Consequently, orientation-estimation algorithms often parameterize the rotation space with more than three parameters, adding constraints to account for redundancy. In [290] as well as in [259, 260, 342, 369], a number of attitude representations are surveyed along with dynamic equations for how the attitude of a sensor might change over time. Some representations are better suited for modeling rotations than others.

The ability to filter measurements to estimate the changing orientation of a rotating sensor is important in navigation systems. In [51, 197], a number of recursive algorithms for dynamic rotation estimation are surveyed. However, all of the surveyed algorithms require initial estimates for orientation that are then updated over time. This section focuses on the task of obtaining such initial estimates from measurements at a single time. The dynamic estimation problem is not addressed.

The problem of designing an algorithm to determine the orientation of a sensor is related to the problem of designing a cost function over which optimization can be performed. Depending on the formulation of the problem, maximum-likelihood estimation techniques must be designed so as to take the spherical statistics of 3D directional measurements into account, though the maximum-likelihood cost function considered in Section 8.2 for estimating using magnetic and gravitational measurements does not depend on such statistics. A strict mathematical treatment of orientation/directional estimation generally involves circular and spherical statistics. Monographs on circular and spherical statistics are [92, 93, 211]. To understand the necessity

---

[66]Non-planned satellites use non-planned frequency bands. These are regions of the spectrum that are taken on a first-come, first-served basis. Planned frequency allotments are managed by the ITU.

for circular and spherical statistics when making directional measurements, consider the measurement of wind directions. If one were given two measurements of wind directions, one being ε radians, where ε is a small number, and the other being $2\pi - \varepsilon$ radians, then for a very small ε, it can be seen that the best way to average the measurements will result in a direction estimate of 0 radians. However, the numerical mean of the directions results in an estimate of π radians, which is clearly very bad. Thus, directional measurements often need to be handled in a different manner than other types of measurements. Similarly, orientation data adds an additional degree of freedom to pure directional measurements, requiring its own unique methods of averaging estimates [46, 121, 161, 215], and its own probability distributions, such as the uninformative (uniform) distributions presented in [291].

In [314], a variety of cost functions for orientation estimation are presented along with a number of orientation-estimation techniques. One particularly simple cost function for directional estimation was suggested by Wahba [353] and an initial solution for a rotation matrix minimizing the cost was given in [86]. The cost function is

$$C_W \triangleq \sum_{i=1}^{N} \|\mathbf{u}_i - \mathbf{R}\tilde{\mathbf{u}}_i\|^2 \tag{93}$$

where $\mathbf{R}$ is a rotation matrix, $\mathbf{u}_i$ is one of N unit-direction vectors in Coordinate System 1 and $\tilde{\mathbf{u}}_i$ is a unit-direction vector in Coordinate System 2. The choice of whether $\mathbf{u}_i$ consists of measured directions and $\tilde{\mathbf{u}}_i$ reference values or vice versa is arbitrary. The rotation matrix for the inverse transformation is just the matrix transpose: $\mathbf{R}^{-1} = \mathbf{R}'$. As shown in [12], the minimization of Wahba's cost function over the rotation matrix $\mathbf{R}$ can be rewritten as the maximization problem

$$\arg\min_{\mathbf{R}} C_W = \arg\max \mathrm{Tr}\left(\mathbf{R}\mathbf{H}\right) \tag{94}$$

$$\mathbf{H} = \sum_{i=1}^{N} \tilde{\mathbf{u}}_i \mathbf{u}_i'. \tag{95}$$

In comparison, in the area of directional statistics, the matrix von Mises-Fisher probability-density function (PDF), initially defined in [73], is

$$p(\mathbf{R}) = a(\mathbf{H}) \exp\left(\mathrm{Tr}\left(\mathbf{R}\mathbf{H}\right)\right) \tag{96}$$

where $\mathbf{R}$ is constrained to the set of rotation matrices and $a(\mathbf{H})$ is a scalar normalization constant. Thus, optimization over Wahba's cost function is equivalent to performing likelihood maximization of the matrix von Mises-Fisher PDF. The maximization of the matrix von Mises-Fisher distribution is considered in [165] and such optimization shall form the basis of the orientation-estimation algorithm presented in this section.

Many of the earliest algorithms for orientation estimation appear to be within mathematics and the space sciences. Wahba's problem was initially presented in the context of satellite attitude estimation [86, 353] and a number of algorithms such as the DOAOP algorithm [50, 62], the TRIAD algorithm, and the quaternion estimator (QUEST), which are compared in [293], among others as discussed in [213, 214, 288, 293], have been developed within the context of outer space applications or by those in the space field. Of note, however, is that a number of solutions to orientation estimation outside of space applications have been developed and authors in the separate fields seldom cite the work of each other. Indeed, Wahba's problem

is just a variant of the orthogonal Procrustes problem of mathematics [283], though the two problems are seldom mentioned together.

In [76], a number of orientation-estimation algorithms developed outside of the context of space applications are compared. Many of the solutions to the problem utilize singular value decomposition (SVD). The solution given in the mathematics literature [165] appears to be the first to use SVD for rotation-matrix estimation. However, authors in the space literature [212, 213] as well as authors outside of the space literature [12, 170, 331] have developed similar algorithms based on SVD, generally without regard to work done outside of their respective fields. In this report, the SVD algorithm of [331] is used, because it optimally solves the orientation-estimation problem using Wahba's cost function, and can be used to solve more general sensor registration problems as well.

The SVD algorithm of [331] can be used to solve for the least-squares rotation, translation, and/or scaling between two sets of corresponding vectors, and the rotations do not have to be limited to three dimensions.[67] The general form of the algorithm finds the rotation matrix $\mathbf{R}$, the translation vector $\mathbf{t}$, and the scale factor c that minimizes the cost function

$$C_U = \sum_{i=1}^{N} \|\mathbf{z}_i - (c\mathbf{R}\tilde{\mathbf{z}}_i + \mathbf{t})\|^2 \tag{97}$$

where $\tilde{\mathbf{z}}_i$ can be viewed as the ith vector (not necessarily a unit vector) in one coordinate system that is scaled by c, rotated using rotation matrix $\mathbf{R}$ and translated by $\mathbf{t}$ to arrive in the second coordinate system, where $\mathbf{z}_i$ is a corresponding vector in that system.

By omitting certain steps, Umeyama's algorithm for orientation estimation [331] can be used to just estimate $\mathbf{R}$, to estimate $\mathbf{R}$ and $\mathbf{t}$, or to estimate $\mathbf{R}$, $\mathbf{t}$, and c. When just the rotation matrix $\mathbf{R}$ is desired, the algorithm is as follows:

1. Given $\mathbf{Z}$, and $\tilde{\mathbf{Z}}$, which are $m \times N$ matrices of the N m-dimensional column-vectors $\mathbf{z}_i$ and $\tilde{\mathbf{z}}_i$, respectively, in the two coordinate systems, stacked next to each other.

2. Perform a singular value decomposition on the matrix product $\mathbf{A} = \mathbf{Z}\tilde{\mathbf{Z}}'$ to obtain unitary matrices $\mathbf{U}$ and $\mathbf{V}$ such that $\mathbf{A} = \mathbf{U}\mathbf{D}\mathbf{V}'$ where $\mathbf{D}$ is a diagonal matrix. In Matlab, this can be done using the command `[U,D,V]=svd(A);` .

3. Create the matrix $\mathbf{S} = \mathbf{I}_{m,m}$, where $\mathbf{I}_{m,m}$ is an $m \times m$ identity matrix.

4. Set r equal to the rank of $\mathbf{A}$. This can be done in Matlab using `r=rank(A);` . Note that if $r < m-1$, then no unique solution for the rotation matrix exists.

5. If $r = m-1$ and the product of the determinants of $\mathbf{U}$ and $\mathbf{V}$ is less than zero (use the comparison `det(U)*det(V)<0` in Matlab), of if $r > m-1$ and the determinant of $\mathbf{A}$ is less than zero (`det(A)<0` in Matlab), then set $\mathbf{S}_{m,m} = -1$ (the element in the last row and column of $\mathbf{S}$ should be set to -1). This implements equations (3) and (5) in [331].

---

[67]The algorithm works well with 2D rotations. Though the Lorentz transformation of special relativity theory can be expressed as a four-dimensional (4D) rotation [290], the rotation expression uses complex numbers (the time-component is made imaginary). The all-real formulation of the Lorentz transformation, derived in [206, Ch. 1.2.2], is not, however, a rotation. Thus, the algorithm of [331] cannot be used to estimate the Lorentz transformation between special relativistic inertial frames.

6. The rotation matrix is given by

$$\mathbf{R} = \mathbf{USV}';\qquad(98)$$

This implements Eq. 4 in [331].

In comparison, the complete algorithm for estimating $\mathbf{R}$, $\mathbf{t}$, and optionally c is slightly different and is given in Appendix G.

8.1.2 Accounting for Measurements of Varying Accuracy

With the proper weighting, it is shown in [289] that Umeyama's algorithm can be viewed as maximizing a clipped likelihood function when given measurements of varying accuracy. This subsection considers how the cost function can be modified to account for varying measurement accuracy.

When one has direction estimates in the form of unit vectors and one wishes to estimate the rotation matrix $\mathbf{R}$ in $\mathbf{u} = \mathbf{Ru}$, Umeyama's algorithm is good, because one can use a modified version of Wahba's cost function to take into account the varying accuracy of the direction estimates. For example, the Mahalanobis distance–like cost function

$$C_M = \sum_{i=1}^{N} \frac{1}{\sigma_i^2} (\mathbf{u}_i - \mathbf{R\tilde{u}}_i)' (\mathbf{u}_i - \mathbf{R\tilde{u}}_i)\qquad(99)$$

is equivalent to the cost function C_U in Umeyama's problem (97) where

$$\mathbf{z}_i = \frac{1}{\sigma_i}\mathbf{u}_i\qquad(100)$$

$$\tilde{\mathbf{z}}_i = \frac{1}{\sigma_i}\tilde{\mathbf{u}}_i\qquad(101)$$

and σ_i is a scaling matrix that is related to the accuracy of the measurements. However, the choice of a good scalar σ_i for weighting each of the measurements is not straightforward and it is not immediately clear whether changing σ_i will change the results.

In [289], the problem of maximum-likelihood orientation estimation is addressed. Under the assumption that the $\mathbf{u}$ terms are the measurements and the $\tilde{\mathbf{u}}_i$ terms are ideal reference values (thus $\mathbf{R}$ converts from global to local coordinates), it is assumed that the measurements are given as unit vectors having a distribution of the form

$$p(\mathbf{u}_i) = \frac{1}{k}e^{-\frac{1}{2\sigma_i^2}\|\mathbf{u}_i - \mathbf{R\tilde{u}}_i\|^2}\qquad(102)$$

where k is a normalization constant, $\mathbf{u}_i$ is defined over the unit sphere, and σ_i is a known standard-deviation quantity. It is then shown that to a high numerical precision for measured pointing accuracies better than $1°$, the optimal value of $\mathbf{M}_i$ is actually the scalar value $1/\sigma_i^2$.

Though in [289], it is implied that σ_i should have units of angle, that is incorrect. Expanding the squared difference of two unit vectors $\mathbf{u}_1$ and $\mathbf{u}_1$, one gets

$$\|\mathbf{u}_1 - \mathbf{u}_2\|^2 = 2 - 2\cos(\theta) \tag{103}$$

where the relation in (71) was used and θ is the angle between the unit vectors. Thus, for the exponent in (102) to be dimensionless, σ_i^2 must have units of the cosine of an angle, not of the angle itself. Thus, an *ad hoc* choice of σ_i^2 is

$$\sigma_i^2 \approx 2 - 2\cos(\sigma_\theta) \tag{104}$$

where σ_θ is the (presumably simple to measure) RMS directional error of the measurement. It can be shown that for small values of σ_θ, such as $1°$ or less, one finds that the numerical value of $\sigma_i \approx \sigma_\theta$ (in radians), validating the use of σ_θ in place of σ_i in [289]. The problem of the optimal choice of weights is also discussed in [292].

Whereas in the example in Section 8.3 it is reasonable to assume that the measurement accuracy can be expressed in terms of a simple standard deviation proportional to an angular sensor accuracy, in the discussion in Section 8.1.3, this is an unrealistic model, because the covariance matrices for the gravitational- and magnetic-field measurements have cross terms and the diagonal elements are not all the same magnitude. Moreover, in Section 8.1.3, the measurements are not unit-direction vectors and there is no reason to assume that improved estimation results will be obtained by normalizing them. Umeyama's algorithm can be used with vectors of any magnitude.

An *ad hoc* adaptation of the cost function in (99) to the case in Section 8.1.3 is to set the set σ_i to the square root of the largest diagonal element in the covariance matrix associated with the ith measurement. In the case of Section 8.1.3, the covariance matrix is for the model ("truth" is uncertain) rather than for the measurement. The estimation technique is not necessarily globally optimal, but it is simple and requires no iterations.

8.1.3 Estimation Accuracy

If orientation estimates obtained using Umeyama's algorithm are going to be used in a recursive orientation estimation, such as those based on variants of the Kalman filter considered in [51, 197], then a covariance matrix or similar second-order information for the directional estimates is needed. The covariance matrix will have to be tailored to the rotation representation chosen. (Rotation representations are surveyed in [290].) Similarly, when fusing multiple orientation estimates, information on the accuracy of the estimates is also desirable for optimal fusion. The fusion of orientation estimates is deemed the "generalized Wahba problem" in [292]. The problem of optimally representing the uncertainty in an orientation estimate is inherently linked to the coordinate system used to represent the estimate uncertainty. In [161], the pros and cons of various attitude representations with regard to data fusion are considered.

In [212, 289, 292, 293], various simple methods of estimating the covariance matrix associated with orientation estimates are provided along with various orientation-estimation techniques. The covariance matrix is the Fisher information matrix for the terms of an angular error vector of minute rotations about the body x, y, and z axes. The vector is termed the "attitude-error vector" ε and is explained in [290]. The Fisher

information matrix is essentially a covariance matrix associated with the (assumed zero-mean) attitude-error vector. The matrix is $E\{\varepsilon\varepsilon'\}$, where $E\{\}$ is the expected value operator.

For the purposes of assessing the utility of a particular attitude-estimation algorithm in this report, it is assumed that one wishes to determine how accurately one can orient themselves in the WGS 84 coordinate system. Consequently, expressing the uncertainty in determining the location of the local ellipsoidal North and up vectors is probably of more utility to a system designer than the expected value of the square of the attitude-error vector. Thus, the orientation accuracy statistics used in Sections 8.2 and 8.3 are the mean angular error of the ellipsoidal North and Up vectors determined using the estimated local-to-global rotation matrix.

Let $\hat{\mathbf{R}}$ be the estimated rotation matrix from global coordinates into an observer's local coordinates at the point (ϕ,λ,h) in geodetic latitude, longitude, and height, and $\mathbf{R}$ is the true rotation matrix. In global coordinates, the ellipsoidal North vector can be obtained using (26) to get $\mathbf{u}_2$, and the ellipsoidal up vector can be obtained using (27) to get $\mathbf{u}_3$. Using (70), one can compute the magnitude of the angular distance between the vectors $\mathbf{Ru}_i$ and $\hat{\mathbf{R}}\mathbf{u}_i$, where i is 2 or 3 to represent the error in the estimates of ellipsoidal North and Up. Sections 8.2 and 8.3 average the angular errors in the North and Up directions over multiple Monte Carlo runs to determine the average pointing accuracy in those directions.

8.2   Orientation Estimation from Magnetic and Gravitational Measurements

Whereas many view GPS as the *non plus ultra* of navigation technology, a GPS receiver with a single antenna cannot provide estimates of the orientation of the platform on which it is located, though one can estimate the heading of a moving vehicle over time. Though it is possible to estimate the orientation of an object using a GPS receiver with multiple antennas, the technique has been patented [96, 355].

Joint magnetometer-accelerometers on a single chip have become increasingly inexpensive. Many cell phones include such chips and consequently physicists have been increasingly using cell phones as sensors in physics demonstrations/experiments. A bibliography of a number of such experiments is given in [192]. Inexpensive magnetometers, such as those in cell phones, can even be used, after appropriate magnetic mapping, to perform indoor localization [125, 127, 317].[68] Orientation estimation using gravitational and/or magnetic-field measurements has been considered for use in applications including satellite-orientation estimation [369] and short-range projectile navigation [277]. Using the EMM2010 magnetic-field model, mentioned in Section 7, and the EGM2008 gravitational model, mentioned in Section 5.4, along with reasonably accurate, calibrated accelerometer and magnetometer measurements, one can easily determine the orientation of a sensor in a global coordinate system without an initial estimate using Umeyama's algorithm, described in Section 8.1.1.

This subsection discusses how joint gravitational/magnetic-orientation estimation can be performed for a sensor at a known location, and estimates the accuracy of the orientation estimates based on model limitations. Model limitations rather than sensor-accuracy limitations are used, because, when cost and time are no concern, the errors in the magnetic- and gravitational-field models are multiple powers of ten greater than the most precise reported sensors.[69] For example, in [268], it is mentioned that the magnetometer (a

---

[68]Though the concept of indoor magnetic sensor-based localization is appealing, the most logical methods for such localization are covered by numerous patents including [122–124, 126].

[69]Even the fundamental physics on which gravitational models are based is often, at high precisions, inconsistent with observations. For example, measurements of the universal gravitational constant G using different techniques disagree with each other outside of the measurement confidence intervals [232] and it is not known whether or not G slowly varies with time [47, 107, 343].

superconducting quantum interference device [SQUID]) in the satellite named Gravity Probe B can measure magnetic fields down to 5×10^{-18} T when given enough time.[70] Similarly, accelerometer precision as low as 9.8×10^{-13} m/s^2 has been claimed [279].

Using the EGM2008 gravitational model and the EMM2010 magnetic-field model with the spherical-harmonic synthesis routines discussed in Appendix F, one can obtain the theoretical magnetic-field vector Φ_B and the gravity-acceleration vector $\mathbf{g}$ of (55b), which is the theoretical acceleration felt by a stationary observer on the surface of the Earth.[71] From the EGM2008 model, one can obtain a covariance matrix $\Sigma_{\nabla V}$ for $\mathbf{g}$. Unfortunately, no covariance matrix is available for the EMM2010 model. However, one can create an *ad hoc* covariance matrix based upon the reported precision of the model.

The precision of the HDGM model, which one might expect to be comparable to the EMM2010 model, is listed in [222]. However, for the purposes of this analysis, the precision estimates of the WMM in [223] will be used instead. The reasons for using the "incorrect" WMM error model to analyze the EMM2010 are that except for localized disturbances, a large part of the errors are probably from the main field, and the error model in [223] provides explicit standard deviations in local WGS 84 ENU Cartesian coordinates for the WMM2005 model at the end of its valid period (in 2010). This can be the assumed accuracy of the WMM2010 (or EMM2010 in this case), allowing one to easily construct a diagonal covariance matrix for the estimate. The covariance matrix is

$$\mathbf{P}_{\Phi_B}^{\text{ENU}} = \begin{bmatrix} (61 \times 10^{-9})^2 & 0 & 0 \\ 0 & (58 \times 10^{-9})^2 & 0 \\ 0 & 0 & (101 \times 10^{-9})^2 \end{bmatrix}. \tag{105}$$

The units of the entries of $\mathbf{P}_{\Phi_B}$ are squared tesla and the covariance matrix is given in local ellipsoidal ENU coordinates. For the purposes of the simulation in this section, the covariance matrix was represented in global WGS 84 coordinates. The converted covariance matrix is given by

$$\mathbf{P}_{\Phi_B}^{\text{global}} = \mathbf{R}_{\text{ENU2Glob}} \mathbf{P}_{\Phi_B}^{\text{ENU}} \mathbf{R}_{\text{ENU2Glob}}'. \tag{106}$$

The rotation matrix from ENU to global coordinates was found by finding the vectors of the local ENU coordinate axes using the formulae in Section 4.2, and noting that in local coordinates, East corresponds to $[1,0,0]'$, North to $[0,1,0]'$, and Up to $[0,0,1]'$. Thus Umeyama's algorithm can be used to get the transformation matrix. Note that the solution using Umeyama's method in this instance is *not* an approximation.

To perform least-squares orientation estimation using a magnetic- and a gravitational-field measurement (assuming that the precision of the sensor is significantly higher than the precision of the magnetic- and gravitational-field models), if $\hat{\mathbf{g}}$ and $\hat{\Phi}_B$ are the *measured, local* gravity acceleration and magnetic field, then, based on the discussion in Section 8.1.2, the inputs to Umeyama's orientation-estimation algorithm of

---

[70]Cheaper and more practical than a SQUID is a chip-scale magnetometer. In [282], one is described as achieving a sensitivity of $50 \times 10^{-9} T/Hz$ (for time-varying magnetic signals).

[71] If the observer were accelerating with respect to the rotating surface of the Earth, then $\mathbf{g}$ would have to be modified accordingly.

Section 8.1.1 are the vectors $\tilde{\mathbf{Z}}$ and $\mathbf{Z}$,

$$\tilde{\mathbf{Z}} = \left[\frac{1}{\sigma_B} \Phi_B^{\text{global}} \quad \frac{1}{\sigma_{\nabla V}} \mathbf{g}^{\text{global}} \right] \tag{107}$$

$$\mathbf{Z} = \left[\frac{1}{\sigma_B} \hat{\Phi}_B \quad \frac{1}{\sigma_{\nabla V}} \hat{\mathbf{g}} \right] \tag{108}$$

$$\sigma_B = \max\left(\text{diag}\left(\mathbf{P}_{\Phi_B}^{\text{global}} \right) \right) \tag{109}$$

$$\sigma_{\nabla V} = \max\left(\text{diag}\left(\Sigma_{\nabla V} \right) \right) \tag{110}$$

where the final estimate $\mathbf{R}$ rotates a vector from the global coordinate system into the observer's local coordinate system, and the diag operator extracts the diagonal elements of the matrices. Note that while scaling by σ_B and $\sigma_{\nabla V}$ has a minimal effect on the results, it can avoid numerical problems in implementations of Umeyama's algorithm near the magnetic poles where the magnetic field and gravitational field are nearly aligned and the observability of the rotation matrix is poor.

Figure 30 plots the theoretical average angular error in a local observer's estimates of ellipsoidal North and Up based on gravity- and magnetic-field measurements. Gravity- and magnetic-field measurements were corrupted by multivariate Gaussian noise whose accuracy was given by the aforementioned covariance matrices. Using the EMM2010 and EGM2008 to get reference values, the observer could thus obtain a transformation matrix from his local coordinate system to the global coordinate system and vice versa. Using the formulae of Section 4.2, the direction of the local East-North-Up coordinates at the observer could be determined. The plots are of the angular difference between the true directions of ellipsoidal "North" and "Up" in the observer's local coordinate system and the directions implied by the observer's rotation matrix.

The observer's "true" local coordinate system (the orientation of which had to be estimated) is defined rotated from the local ENU system. The coordinate system is built by rotating $15°$ counterclockwise (right-handed) about the local ENU x-axis and then rotating $15°$ counterclockwise about the rotated z-axis. In [55], it is described how a rotation matrix can be constructed to perform a rotation about an arbitrary axis and how multiple rotations can be concatenated.

As was the case in Section 5.4 for assessing the accuracy of the gravitational-field model, independent realizations of the gravitational and magnetic fields were drawn based on the reported accuracies of the models to create the plots in Fig. 30. Umeyama's model was run and (71) was used to average the magnitudes of the deflections of an estimate of the direction of ellipsoidal North and an estimate of ellipsoidal Up as a function of the observer's location on the Earth.

From Fig. 30, it can be seen that the accuracies of the orientation estimates implied by the model covariance matrices are sufficient for short-range estimation, but leave much to be desired for highly accurate long-range sensing, where pointing errors on the order of $0.1°$ would be considered unacceptable. Note that the scaling of the vectors is necessary to avoid finite precision limitations due to the difference in magnitude between $\hat{\mathbf{g}}$ and $\hat{\Phi}_B$ and not just due to the varying accuracies of the measurements. The algorithm was also run without adding noise, in which finite precision limitations produced errors less than 10^{-6} degrees (0.0036 arcseconds) everywhere except in the vicinity of a magnetic pole, when the same scaling based on covariance values was used. However, when the error-free values were used without scaling, the algorithm sometimes failed as the matrix $\mathbf{A}$ in Umeyama's algorithm did not have sufficient rank. Additionally, when run without scaling, the errors were multiple powers of ten larger when the algorithm did not fail.
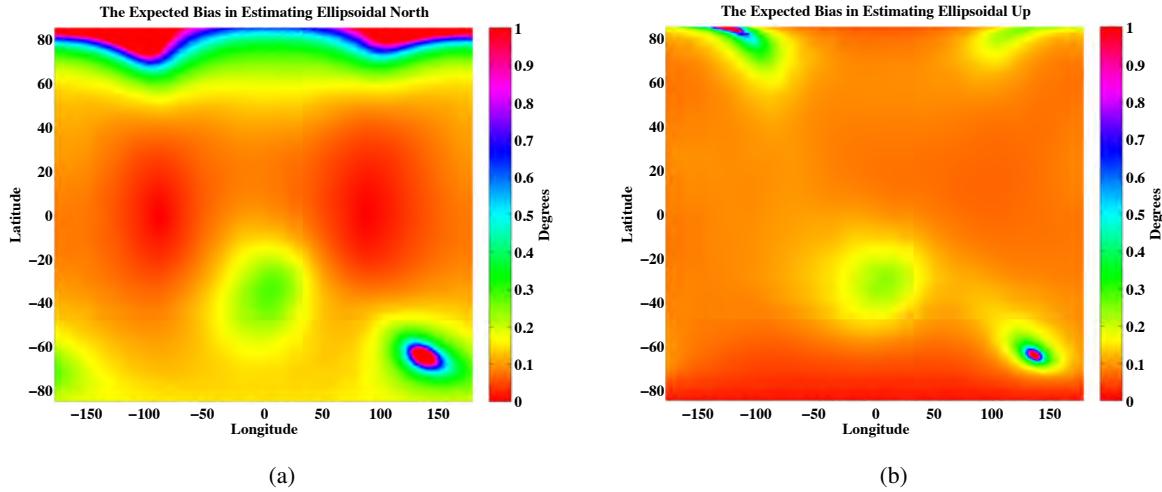
Fig. 30: The angular offsets between the true ellipsoidal North (a) and Up (b) vectors and a local observer's estimates of them based on a gravity measurement and a magnetic-field measurement on a 256×256 grid in latitude and longitude at an altitude of 9 km, assuming the observer stationary with respect to the surface of the rotating Earth. Latitude values only up to $\pm 85°$ were used. The "true" gravity and magnetic-field measurement values were those given by the EGM2008 model used in Eq. (55b) and the "true" magnetic-field model was given by the EMM2010 coefficients (at the 2010.0 epoch). The "noisy" values were those offset by Gaussian noise whose covariance matrix was that inherent in the models. Thus, the plots represent the expected accuracy of the models worldwide. One thousand Monte Carlo runs were performed. The true observer's orientation at each place on the globe is described in the text. The colors are clipped to $1°$ to accentuate errors far from the poles, where the errors can well exceed $1°$. Note that the errors in the estimate of ellipsoidal North are not independent of those of ellipsoidal Up.

Because Umeyama's algorithm is not actually optimizing over the true likelihood function of the data, one might wonder whether the performance could be improved by performing likelihood maximization. The likelihood function of the problem at hand is

$$p(\hat{\mathbf{g}}, \hat{\Phi}_B | \mathbf{R}) = \mathcal{N}\left\{ \mathbf{R}\hat{\mathbf{g}}; \mathbf{g}^{\text{global}}, \Sigma_{\nabla V} \right\} \mathcal{N}\left\{ \mathbf{R}\hat{\Phi}_B; \Phi_B^{\text{global}}, \mathbf{P}_{\Phi_B}^{\text{global}} \right\} \tag{111}$$

where the notation $\mathcal{N}\{a; b, c\}$ refers to the Gaussian PDF evaluated at point a with mean b and variance (or covariance matrix) c. The simplest method of maximizing the likelihood function (111) is to try different rotation matrices $\mathbf{R}$ and to choose the one with the highest likelihood.

To determine whether likelihood maximization offered any benefits, points at 9 km ellipsoidal height and ellipsoidal latitude, longitude locations of $(85°, 180°)$ and $(0.33°, 103.76°)$ were considered. The first is a point of high mean-error, as seen in Fig. 30, where the average error in North using Umeyama's method is $2.58°$ and the average error in Up is $0.23°$. The second point has low error, where the average error in North using Umeyama's method is $0.02°$ and the average error in Up is $0.07°$. The likelihood function of (111) was maximized at those two points using a brute-force computation of $1,030,301$ different variations of $\mathbf{R}$, the rotation matrix from local to global coordinates. The searched values of $\mathbf{R}$ were built by taking Umeyama's solution and perturbing it using a grid of Euler angles, with the values of each angle broken into 101 distinct points. For the high mean-error point, the grid of rotation angles went from $-3°$ to $3°$, leaving

a fineness of $0.06°$. For the low mean-error point, the grid of rotation angles went from $-0.08°$ to $0.08°$, leaving a fineness of $0.0016°$.

The three Euler angles define subsequent rotations about the x, y, and z axes. The rotations about the y and z axes are about the respective axes after the previous rotations. The rotation matrix given by left-handed Euler angles in x, y, and z of (ϕ, θ, ψ) are [290]

$$\mathbf{R}^{\text{Euler}} = \mathbf{R}^Z \mathbf{R}^Y \mathbf{R}^X \tag{112}$$

$$\mathbf{R}^Z = \begin{bmatrix} \cos(\psi) & \sin(\psi) & 0 \\ -\sin(\psi) & \cos(\psi) & 0 \\ 0 & 0 & 1 \end{bmatrix} \tag{113}$$

$$\mathbf{R}^Y = \begin{bmatrix} \cos(\theta) & 0 & -\sin(\theta) \\ 0 & 1 & 0 \\ \sin(\theta) & 0 & \cos(\theta) \end{bmatrix} \tag{114}$$

$$\mathbf{R}^X = \begin{bmatrix} 1 & 0 & 0 \\ 0 & \cos(\phi) & \sin(\phi) \\ 0 & -\sin(\phi) & \cos(\phi) \end{bmatrix}. \tag{115}$$

The rotation hypotheses were obtained by left-multiplying the rotation matrix obtained using Umeyama's algorithm with the Euler-angle-based perturbation matrix.

Averaged over 100 Monte Carlo runs performing the grid-search likelihood maximization,[72] the results were no different from Umeyama's algorithm, indicating that there is no benefit to performing additional likelihood maximization and that the limitations in the accuracies of the gravitational- and magnetic-field models are limiting factors. Umeyama's algorithm is considerably simpler than nonlinear maximum-likelihood orientation-estimation techniques that are better known to the tracking community, such as [132].

From Fig. 30, one can see that orientation estimation using gravitational- and magnetic-field models is very unreliable near the geomagnetic poles, where the gravitational vector and the magnetic-field vector are nearly aligned. For that reason, Section 8.3 looks at high-precision orientation estimation using stars.

Note that if Umeyama's algorithm were used with a real magnetometer and accelerometer, the sensor would have to be calibrated with respect to the platform on which it is mounted. Part of this includes estimating the magnetic bias of the platform itself, which is discussed in [5].

8.3 Orientation Estimation Using Stars

8.3.1 *Describing the Algorithm*

When high-precision pointing accuracy is required, then then one might wish to consider using stars or reference satellites. As of 1985, optical star sensors with an accuracy of $10\,\mu$rad to $20\,\mu$rad (2 to 4 arc-seconds) for satellite attitude determination were available [103], and typical sensor accuracies on satellites

---

[72]The algorithm was actually implemented to minimize the negative logarithm of the likelihood, discarding constant terms. In other words, minimization of the Mahalanobis distances was performed.

were still on the order of an arcsecond in 2001 [203]. The limitations to orientation estimation accuracy using stars is explained in [36, Ch. 2.3.4], where it is noted that atmospheric turbulence limits optical measurement accuracy to approximately 1 arcsecond for long exposures of ground-based sensors, though the use of adaptive optics using laser guide stars can reduce the limiting resolution to the diffraction limit of the telescope. Optical imaging compensating for atmospheric turbulence can be done using arrays of orthogonal transfer charge-coupled devices (OTCCDs) with multiple telescopes pointed at guide stars [166]. If the association of observed stars to stars in a star catalog is known, then the problem of direction estimation is fairly simple as one can just apply Umeyama's algorithm in the same manner as in Section 8.2 when using gravitational- and magnetic-field measurements. However, the correct assignment of observations to catalogued stars will generally not be known *a priori*.

In [248, 309], a number of algorithms for identifying stars are surveyed. The techniques generally try to match geometric patterns among stars to a reference star catalog. Various data structures specialized for searching the star catalog are utilized to speed up the algorithm. In [203], an overview of the hardware and signal processing in a star tracker is presented. Of note is also the large number of patents that surround techniques for orientation estimation using stars.[73] For example, methods of determining the attitude and/or location of a spacecraft or high-altitude aircraft using a star sensor are given in [26, 167, 168, 181]. Similarly, star-sensor-based attitude-estimation techniques for non-space-based observers are patented in [25, 34]. People have even patented a method of optically observing the (known) locations of GPS satellites instead of stars to determine the orientation of a satellite [181].

The problem of orientation estimation using catalogued stars overlaps with the problem of track-to-track association that arises when fusing track estimates from multiple networked sensors. Interestingly it appears that the communities interested in star identification for attitude estimation and the communities interested in track-to-track association for data fusion do not share algorithms across fields. This section presents a generic algorithm for star-based attitude estimation to demonstrate the role of coordinate systems and similarities to aspects of common target-tracking algorithms. Thus, rather than designing an algorithm that can efficiently provide an attitude estimate with no prior information at all, such as the "lost in space" algorithms of [248, 309], this section discusses how a very coarse attitude estimate can be refined and how one can (inefficiently) determine orientation without prior information based on a logic similar to that used in track-to-track association algorithms and not beholden to a particular piece of hardware.

Two of the algorithms in the literature for track-to-track association that are most similar to popular techniques in the space literature for associating observations to catalogued stars are [328, 374], as the algorithms utilize the relative geometry of neighboring targets. However, these two algorithms are limited by assumptions such as that one is working in a 2D Cartesian space and that any biases are purely additive. In the star-to-catalog association problem, the number of entries in the catalog can be many orders of magnitude larger than the number of tracks one would expect in a track-to-track association problem among multiple radars. For example, as mentioned in [286], the Naval Observatory Merged Astrometric Dataset (NOMAD) is over 100 gigabytes in size.[74] Thus, track-to-track association algorithms have often focused on optimality rather than speed. The majority of algorithms start from a Bayesian model of some sort. For example, a large

---

[73]Many patents cover star-based orientation-estimation devices, which can make it difficult for an engineer to design such systems without paying royalties. However, the patent coverage in this area is much less of a burden than, for example, in the cell phone industry. In [239], it is estimated that the typical $400 smartphone is subject to potential patent royalties averaging $120 and almost equal to the cost of the components.

[74]NOMAD is a compilation of multiple star datasets. Instructions on how to access NOMAD are at `http://www.nofs.navy.mil/nomad/`.

number of cost functions are derived in [316], where a fast-Fourier-transform (FFT) method is suggested to remove 2D biases prior to association. In [190], maximum *a posteriori* cost functions are derived assuming a zero-mean Gaussian prior distribution on additive biases. A Bayesian method involving a large number of integrals is derived in [90], and in [249] a cost function expressed by taking the expected value over the bias is given where the bias is modeled as additive having a zero-mean Gaussian prior distribution.

The technique chosen in this report for determining orientation using observations of stars is conceptually similar to the methods of [119, 199, 200], which condition a likelihood function on a bias estimate, perform maximum-likelihood data association (in those instances track-to-track association, here associating observations to catalogued stars), and then estimate the "bias" given the associations, which in the context of this report is the unknown sensor orientation.

The first step to determining one's orientation using catalogued stars is to determine where the stars should appear to be, given the time and one's location. For the purpose of this discussion, the Hipparcos star catalog, which can be obtained from the link in Table 2, is used. The determination of the predicted locations where the stars should appear to an observer requires more than just the transformation of Fig. 6, because the stars are catalogued in BCRS coordinates and one must account for parallax (transformation to GCRS requires a shift of the origin), aberration (special relativity warps one's perception of the star's locations), general relativistic bending of light, most notably due to the mass of the Sun, and atmospheric refraction. All these effects are too complicated to review in this report. The reader is referred to the resources in Table 1. For the purposes of simulation in this section, the `iauAtco13` function from the IAU's SOFA library was used to account for all of those effects and is documented to produce results with an accuracy of 0.05 arcseconds for optical observations, and 1 arcsecond for radio observations for zenith distances $\zeta < 70°$, where the limiting factor is the low-fidelity atmospheric refraction model used.

Figure 31 shows how the predicted apparent locations of the stars in the sky move over time at two locations on Earth. It is important that a precise time be used when making stellar observations for orientation estimation. To put things into perspective, as mentioned in Section 3.1, a stellar day, which is one rotation of the Earth with respect to the fixed stars, is 86164.098903691 s. That means the Earth is rotating 15.04 arcseconds per second.[75] Consequently, if times are taken manually, rather than electronically with the image, then the orientation-estimation bias can be expected to exceed the inaccuracy in the `iauAtco13` function by a factor of approximately 15.

Planets, the Moon, and the Sun can also be present in addition to stars. The Sun, Moon, and planet locations can be obtained using the DE430 ephemerides and NASA's SPICE toolkit, both available at the links in Table 2. Note, however, that the `cspice_spkezr` function in the current version (version N0064) of the toolkit does not provide the directions of the celestial objects with respect to an observer on the Earth. Rather, it provides them with respect to an observer at the center of the Earth. Thus, it is necessary to iteratively perform parallax, aberration, and atmospheric refraction corrections, as described in Appendix I. Aberration and the magnitude of the errors introduced by ignoring aberration are quantified in Appendix J, since aberration due to special relativity is an often-overlooked cause of apparent measurement biases.

Having converted a catalog of star directions into the predicted observed directions given the observer's known location on the Earth and the time, then if observed stars can be associated with the predicted directions of the catalogued stars, Umeyama's algorithm of Section 8.1.1 can be used to determine the observer's

---

[75]In comparison, for an observer on the equator of the WGS 84 reference ellipsoid, assuming the rotation axis is perfectly aligned with the z-axis, a 1 s time bias adds the same orientation bias to stellar observations as moving 465 m along the equator.

(a) $90°$ latitude, $0°$ longitude

(b) $45°$ latitude, $0°$ longitude
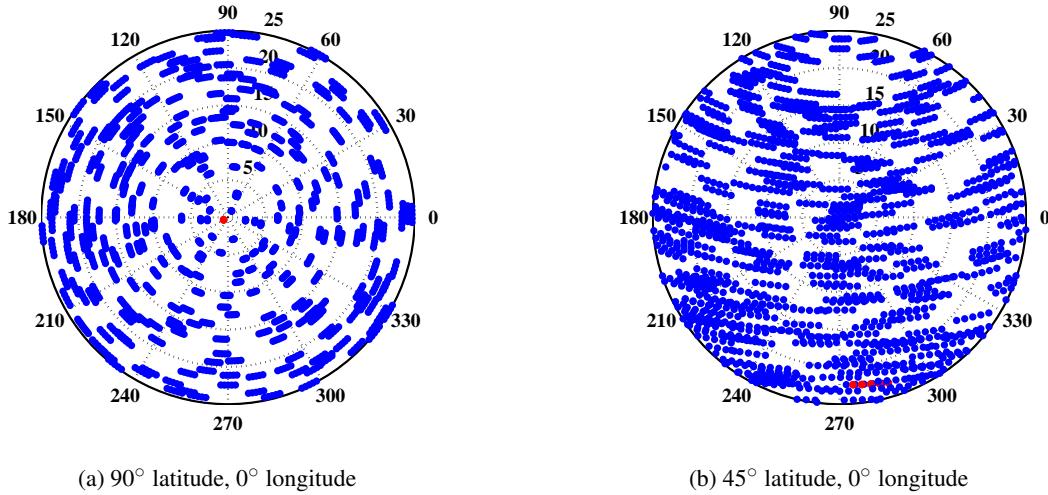
Fig. 31: North pole azimuthal projections of stars on 1 January 2014 are plotted at 0:00, 0:05, 0:10, 0:15, and 0:20 UTC from two different points on the Earth. The zenith distance ζ (see Fig. 13) plotted with respect to the WGS 84 vertical is the distance from the center of the plot and goes from $0°$ to $25°$. The angle around the plot is degrees North of East in the local ENU coordinate system. In (a), the observer is at the North pole. In (b), the observer is at $45°$ latitude (using the WGS 84 reference ellipsoid). In both instances, the observer is at $0°$ longitude. The stars are those in the Hipparcos catalog. In (a), the North star is marked in red. In (b), Jupiter is marked in red. In (a), the stars are moving clockwise with time, in (b), they are moving mostly right-to-left. The functions `iauPmsafe` and `iauAtco13` from the IAU SOFA library, among others, were used to perform the conversion of the stars including parallax, proper motion, and a very simple refraction model for which an observation wavelength of $0.574\,\mu\text{m}$ (yellow light), zero humidity, standard atmospheric pressure of $101,325\,\text{Pa}$, and a temperature of $15°\text{C}$ were used. NASA's SPICE toolkit was used, as described in Appendix I, to find planet locations (only Jupiter is visible) and the refraction code from the IAU's SOFA library was used to add refraction to Jupiter.

orientation. The problem of associating observed stars to catalogued stars is where work from track-to-track association algorithms can be used. To begin, the problem of associating stars to observations given a known observer orientation is discussed.

Suppose that the orientation of the observer is known. One wishes to determine the most probable association of observed stars to catalogued stars. Appendix H derives a general score function for that purpose. For the example in this section, a few additional assumptions are added for the simulation. Specifically, the probability of detecting the tth star in the star catalog is assumed to be known to be P_D^t and detections are taken in terms of spherical azimuth λ and elevation θ_c in the local coordinate system, where detection is performed on a grid of points in azimuth and elevation. No additional feature measurements, such as star intensity or wavelength, are used. The false-alarm density per squared radian in azimuth-elevation is assumed to be known and is given by λ_c, which should not be confused with azimuth. Based on the derivation in Appendix H, the marginal additive cost of assigning catalogued star t to observation i is

$$\Delta\Lambda_{t,i} = \begin{cases} \ln\left(P_D^t \dfrac{p_t\left(\mathbf{z}_i | I_p\right)}{\lambda_c} \right) & \text{if } i \neq 0 \\ \ln(1 - P_D^t) & \text{if } i = 0 \end{cases} \tag{116}$$

where I_p is prior hypothesized information (irrelevant in this problem), and $\mathbf{z}_i$ is the ith observation. If one were to follow the method of [119, 199, 200], then p_t would be some type of a Gaussian PDF. However, due to the spherical nature of the measurements, a Gaussian PDF is not appropriate for this problem. For example, the distance between an angular measurements of $-\pi - \varepsilon$ and $\pi + \varepsilon$, for some small offset ε, would be $2\pi - 2\varepsilon$ rather than a more logical 2ε.

A number of PDFs for the directional measurements in three dimensions are presented in [211]. However, due to the often high precision of star measurements (better than $20\,\mu$rad [103]), many common PDFs for directional measurements are not suitable for use. For example, consider the Fisher distribution, also known as the von Mises-Fisher distribution, which is unimodal on the unit sphere, and which can be written

$$p_t\left(\mathbf{z}_i | I_p\right) = \frac{\kappa}{2\pi\left(e^\kappa - e^{-\kappa}\right)} e^{\kappa \mathbf{u}(\mu_t)'\mathbf{u}(\mathbf{z}_i)} \tag{117}$$

where the normalization constant is taken from the formula in [311], the unit vector $\mathbf{u}(\mu_t)$ is the mean apparent direction of the tth element in the star catalog, and $\mathbf{u}(\mathbf{z}_i)$ is the unit-direction vector associated with the ith observation, which itself might be given in terms of azimuth and elevation. The value κ is a concentration parameter. The uncertainty is symmetrically distributed around the mean with the distribution increasing as κ increases. The problem with many common distributions on the unit sphere is that parameters such as κ must be extremely large for measurement errors to be on the order of $20\,\mu$rad, which leads to numerical precision problems. This is demonstrated in Appendix K.

Thus, as opposed to using a circular distribution, a spherical generalization to the clipped mod normal distribution introduced in [60] is chosen. Such a distribution clips the tails of the normal distribution (rather than wrapping them back around) and uses something akin to a modulo function to avoid problems near the $\pm\pi$ boundary in azimuth. The 2D clipped mod normal distribution for this problem is

$$p_t\left(\mathbf{z}_i | I_p\right) = \frac{1}{c_1} e^{-\frac{1}{2} w(\mathbf{z}_i - \mu_t)' \mathbf{P}^{-1} w(\mathbf{z}_i - \mu_t)} \tag{118}$$

where c_1 is a normalization constant and the function w is defined

$$w(\mathbf{z}_i - \mu_t) \triangleq \begin{bmatrix} w_{\text{wrap}}(\lambda_i - \lambda_t, x_{\min}, x_{\max}) \\ \phi_i - \phi_t \end{bmatrix} \tag{119}$$

$$w_{\text{wrap}}(x, x_{\min}, x_{\max}) \triangleq \text{mod}\{x - x_{\min}, x_{\max} - x_{\min}\} + x_{\min} \tag{120}$$

where $x_{\min} = -\pi$, $x_{\max} = \pi$. The function w_{wrap} wraps the difference in azimuth values to the given range. The function $\text{mod}(a, b)$ is the modulo operation (the remainder after division). For example, $\text{mod}(17, 4) = 1$ and $\text{mod}(-5, 4) = 3$.[76] The elevation values do not need to be wrapped, as there is no discontinuity in their scale. The matrix $\mathbf{P}$ is a covariance matrix and μ_t is the azimuth-elevation vector of the tth entry in the star catalog. If the measurements are very accurate (very little from the tails of the normal distribution is cut off), the normalization constant can be approximated using the normalization constant of the equivalent normally distributed random variable

$$c_1 \approx \|2\pi\mathbf{P}\|^{\frac{1}{2}} \tag{121}$$

---

[76]The `mod` command in Matlab performs the modulo operation.

where the vertical bars indicate the matrix determinant operation. One would expect that in instances where the approximation in (121) fails, the measurement would be sufficiently noisy that the von Mises-Fisher distribution of (117) could be used without many numerical precision problems.

During simulation, it is convenient to simply generate the noise values as in (72); that is,

$$\mathbf{z}_{\mathrm{samp}} = \mu + \mathbf{P}^{\frac{1}{2}} \mathbf{w} \tag{122}$$

where $\mathbf{w}$ is a 2×1 random vector distributed $\mathcal{N}\{\mathbf{0}, \mathbf{I}\}$ and $\mathbf{P}^{\frac{1}{2}}$ is a lower-triangular Cholesky decomposition of $\mathbf{P}$. However, for observations near the poles, such noisy values will push the elevation measurement over the pole. If that occurs, the elevation measurement should be brought back below the pole, and the latitude measurement shifted by $180°$. Similarly, the latitude measurement can be pushed outside of the valid range, which shall be assumed to be $\pm\pi$. Thus, if $\mathbf{z}_{\mathrm{samp}} = [\lambda, \phi]'$, then it should be transformed as

$$\mathbf{z}_{\mathrm{samp}}^{\mathrm{wrap}} = \begin{cases} \begin{bmatrix} w_{\mathrm{wrap}}(\lambda, -\pi, \pi) \\ \arcsin(\sin(\phi)) \end{bmatrix} & \text{if} \operatorname{mod}\left\{ \frac{|\theta| - \frac{\pi}{2}}{\pi}, 2 \right\} > 1 \\ \begin{bmatrix} w_{\mathrm{wrap}}(\lambda + \pi, -\pi, \pi) \\ \arcsin(\sin(\phi)) \end{bmatrix} & \text{otherwise} \end{cases} \tag{123}$$

before use. In practice, however, the field of view should be sufficiently small and the measurements sufficiently accurate that (123) is not necessary.

Using (118) as the measurement PDF and discarding the constant term, the assignment cost function of (116) becomes

$$\Delta\Lambda_{t,i} = \begin{cases} \ln\left(\frac{P_D^t}{\lambda_c c_1} \right) - \frac{1}{2} w \left(\mathbf{z}_i - \mu_t \right)' \mathbf{P}^{-1} w \left(\mathbf{z}_i - \mu_t \right) & \text{if } i \neq 0 \\ \ln(1 - P_D^t) & \text{if } i = 0 \end{cases} \tag{124}$$

where one can use the approximation of (121) for the normalization constant c_1. The problem of assigning observed stars to catalogued stars thus becomes the familiar 2D assignment problem from tracking: Each catalogued star must either be assigned to a measurement or declared unobserved. Measurements that do not associate with catalogued stars are assumed to be false detections or simply detections from things that are not in the catalog. Given N_T catalogued stars and N_M measured stars, the 2D-assignment problem is formulated as

$$\mathbf{X}^* = \arg\max_{\mathbf{X}} \sum_{t=1}^{N_T} \sum_{i=1}^{N_M} c_{i,j} x_{t,i} \tag{125}$$

$$\text{subject to} \sum_{i=1}^{N_M} x_{i,j} = 1 \quad \forall i \qquad \begin{array}{c} \text{Every catalogued star} \\ \text{is assigned.} \end{array} \tag{126}$$

$$\sum_{t=1}^{N_T} x_{t,i} \leqslant 1 \quad \forall j \qquad \begin{array}{c} \text{Not every measurement is} \\ \text{assigned to a star.} \end{array} \tag{127}$$

$$x_{t,i} \in \{0, 1\} \quad \forall x_{i,j} \tag{128}$$

where if $x_{t,i} = 1$, then catalogued star t is assigned to measurement i, and the cost matrix $\mathbf{C}$, having elements in row t and column i $c_{t,i}$ is

$$
\tilde{\mathbf{C}} \triangleq \begin{bmatrix} \overbrace{\Delta\Lambda_{1,1} \quad \ldots \quad \Delta\Lambda_{1,N_M}}^{\substack{\text{Assignment} \\ \text{Costs}}} & \overbrace{\Delta\Lambda_{1,0} \quad -\infty \quad \ldots \quad -\infty}^{\substack{\text{Missed Detection} \\ \text{Costs}}} \\ \Delta\Lambda_{2,1} \quad \ldots \quad \Delta\Lambda_{2,N_M} & -\infty \quad \Delta\Lambda_{2,0} \ldots \quad -\infty \\ \vdots \quad \ddots \quad \vdots & \vdots \quad \vdots \quad \ddots \quad \vdots \\ \Delta\Lambda_{N_T,1} \ldots \Delta\Lambda_{N_T,N_M} & -\infty \quad -\infty \quad \ldots \Delta\Lambda_{N_T,0} \end{bmatrix}.
$$

(129)

The cost function arises from building the hypothesis cost of Appendix H using the marginal costs of adding new measurements. The 2D-assignment problem can be optimally solved in polynomial time using the shortest augmenting path algorithm of [53, 56], where the source code is also provided. For that reason the solution of the problem is not explicitly described in this report.

Up until now, the problem of assigning measurements to stars assuming that the observer's orientation is perfectly known has been presented. If a reasonably accurate initial estimate of the orientation is known, one could perform the above 2D assignment to determine which observations correspond to catalogued stars, and then use Umeyama's algorithm of Section 8.1.1 to estimate the orientation given the assignments. If the measurement noise is distributed the same for all measurements and in all directions ($\mathbf{P}$ is diagonal), then the σ terms mentioned in Section 8.1.2 should be unnecessary and Umeyama's algorithm should produce the globally optimal orientation estimate given the assignment of stars to catalogued entries.

In general, however, the initial estimate of the orientation is likely to be fairly poor, such as when using magnetic- and gravitational-field measurements as in Section 8.2. In such an instance, small biases can be compensated by inflating $\mathbf{P}$, as was done for Mahalanobis distances without circular statistics in [164]. In [164], it is shown that if the "bias" can be characterized as additive to the measurement and Gaussian with zero mean, then one can just add the covariance matrix of the bias to the measurement covariance matrix. Here, the bias is not additive, but one can inflate $\mathbf{P}$ in a similar *ad hoc* manner. On the other hand, if the initial estimate is too bad, one might have to try multiple orientation hypotheses in a brute-force manner using an inflated $\mathbf{P}$. All together, an outline for an algorithm is the following:

1. Using the time, the observer's location, and any available atmospheric data, convert the positions of the catalogued stars into apparent star directions for an observer at the given location (for example use the `iauAtco13` function in the IAU's SOFA library). The rotation between the apparent directions of the stars, given, for example, in WGS 84 ellipsoidal ENU coordinates, and the local coordinate system of the observer is to be found.

2. Inflate the measurement covariance matrix $\mathbf{P}$ an *ad hoc* amount, and perform 2D assignment of observations to stars using the cost matrix in (129) and the globally optimal assignment algorithm of [53,56], where the rotation matrix from global to local coordinates is either given by a single initial estimate, or is done on a grid of initial estimates. The goal is to maximize the cost. The covariance inflation is performed so that the initial estimate grid does not have to be too fine.

3. If a grid of initial orientation estimates was used in step 1, then choose the solution with the highest cost to use in the next step.

4. Given a solution to the 2D-assignment problem, compute the orientation estimate from Umeyama's algorithm of Section 8.1.1.

5. Redo the 2D-assignment problem using the new orientation estimate and the correct measurement covariance matrix **P**.

6. Re-run Umeyama's algorithm using the new assignment of measurements to catalogued stars.

The algorithm is re-run a second time, under the assumption that the orientation estimate from the first 2D assignment set is sufficiently accurate that the optimal measurement-to-star assignment will be achieved.

The above method is conceptually similar to those of [119, 199, 200] in that it can be viewed as a joint likelihood maximization algorithm over the orientation and the assignments. In [119, 199, 200], the track-to-track assignment problem across sensors is considered. An unknown "bias" is added to the likelihood function and maximization is performed over the bias and the assignments of tracks between sensors. In the problem at hand, the unknown orientation is implicitly added to the likelihood function in (118). That is, the values of the catalogued stars can be written as

$$\mu_t = \mathbf{u}^{-1}\left(\mathbf{R}\mathbf{u}\left(\mu_t^{\text{ENU}}\right)\right). \tag{130}$$

That is, if the data in the catalog is given in local ENU coordinates, after adjusting for the receiver's location, time, and propagation effects, convert the orientation data into a unit vector. Then, rotate the unit vector using the rotation matrix **R**. Subsequently, convert the rotated unit vector back into the coordinate system of the orientation measurement in the receiver's coordinate system. Thus, the μ_t in (124) implicitly includes the unknown rotation matrix **R**.

In [199, 200], the unknown "bias" is solved using a greedy pattern-based assignment algorithm, whereby multiple assignment hypotheses are formed and pruned.[77] The approach described in this report is more similar to the track-to-track association method of [119]. Note, however, that [119, 199, 200] probably will not work well given no prior information on the observer's orientation. Indeed, the algorithm described here will be very slow if no prior information is provided as the programmer must design the algorithm to do a grid search over a very large number of orientation hypotheses. In such an instance, one of the "lost in space" algorithms described in [248, 309] is best used to obtain an initial estimate, though the necessary data structures for such an algorithm to operate efficiently can be tedious to program.

8.3.2 *Demonstrating the Algorithm*

To demonstrate the algorithm for determining one's orientation using a star catalog, an example of orientation determination using parameters that are realistic for a smartphone is presented. Programs such as SkyView [205] and Star Chart [80] for the iPhone use GPS data, the phone's camera, and compass and accelerometer information to help tell the user which stars they might be looking at. Such programs

---

[77]In [199, 200], a pattern-based assignment algorithm is compared to a 2D assignment-based method, whereby the pattern-based method is shown to be better. The algorithm described in this report is not the same as the 2D-assignment method used for comparison in [199, 200], because the authors did not perform a search over the bias (unknown orientation), thus leading to poor results. The concept of pattern matching for sensor registration as in [199, 200] is similar to the "lost in space" algorithms used for orientation estimation in space literature [248, 309], which are not presented in this report.

generally overlay a map of stars onto stars shown through the phone's camera or show their own map aligned with stars that one could see looking past the phone. However, the fact that such programs actually work well enough for a user to easily identify which catalogued stars correspond to stars in the sky demonstrates that initial orientation estimates derived from magnetic and gravitational readings should provide a sufficiently accurate initial orientation estimate such that one can achieve good automatic star-to-catalog assignments without doing a very extensive grid search of possible orientation hypotheses and without using a "lost-in-space" algorithm to determine one's orientation with no prior information whatsoever.

For the purpose of the simulation here, the parameters for an inexpensive cell phone camera are used. As an example, certain parameters from the iPhone 5S camera are used. Its parameters are not all explicitly in Apple's developer documentation, but application programming interfaces (APIs) are available to query the values of the various parameters and one can use exchangeable image file format (EXIF) data from photographs taken by the camera to find parameters such as the focal length of the lens. The relevant parameters are pixels $1.5\,\mu$m wide, a resolution of 3264×2448 pixels, and a focal length of 4.12 mm. This means that the sensor is 4.895 mm $\times 3.672$ mm in size. Using the equation from [179, Ch. 2.2] for the angular width of the field of view of a camera when focused on something at an infinite distance,

$$\alpha = 2\arctan\left(\frac{d}{2f}\right) \tag{131}$$

where f is the focal length of a lens and d is the height of the sensor behind the lens. This says that the angular field of view of the iPhone camera is 0.7543 rad $\times 0.5776$ rad (or $43.2187 \times 33.0920°$). Dividing the angular field of view by the number of pixels, one finds a pixel size of $(0.23$ mrad $\times 0.24$ mrad$)$ $(47.7 \times 48.7$ arcseconds). In an ideal imaging system without lens defects and free of optical aberration, the mapping of pixels to degrees in spherical coordinates is not perfectly uniform across a flat sensor due to Petzval curvature [179, Ch. 3.1.4]. One solution to the problem is to use a curved sensor. Another is to use a field flattening lens [179, Ch. 3.1.5]. While there is no evidence that cell phone cameras use a curved sensor or field flattening lenses, for the purposes of this simulation, it is assumed that there is no Petzval curvature and the pixels linearly map to locations in the field of view in spherical coordinates.

Consider observers at two locations on the Earth. The first is located on the surface of the WGS 84 reference ellipsoid at an ellipsoidal latitude and longitude of $(-22.5°, 180°)$ (in the Pacific Ocean in the general vicinity of Tonga and Fiji). The second is located at $(45°, 180°)$ (South of the Aleutian Islands between Alaska and Russia). The "true" orientation of the observer in both locations is defined with respect to the local ellipsoidal ENU coordinate system. The observer's orientation is obtained by rotating $60°$ counterclockwise (a right-handed rotation) about the x-axis followed by a counterclockwise rotation of $15°$ about the rotated z-axis. The orientation is of a high enough elevation that the ground should not be within the field of view of the observer. The field of view of the observer is that associated with an iPhone camera, to use typical parameters. The time of the observation is taken to be 1 June 2014 at 0:00 UTC. Under those parameters, the Hipparcos catalog lists 8027 stars that would be in the field of view of the first observer (after accounting for refraction using the function `iauAtco13` in the IAU's SOFA library) and using NASA's SPICE toolkit with the DE 430 ephemerides, there would be two planets in the field of view (asteroids and non-Earth moons were not considered).

However, a camera is not infinitely sensitive and can not necessarily detect very dim stars, especially when there is a lot of light pollution from a nearby city. The Hipparcos catalog (version 311) provides

star magnitude information along with star locations. The catalog provides the "Hipparcos magnitude," which is a weighted measure of the brightness of a star in wavelengths from 340 nm to 850 nm outside of the atmosphere and is documented to be similar to standard visual "V" scale magnitudes. The Hipparcos magnitude along with its relation to other visual magnitude systems is described in the survey paper [27]. However, the survey does not relate the magnitudes to what one can be expected to see with the naked eye. In [133], it is mentioned that the dimmest star one can see in the visual scale is approximately magnitude 6. Smaller magnitudes correspond to brighter stars. For the purpose of the simulation, celestial bodies above magnitude 6 are discarded, leaving 343 stars and one planet (Uranus) in the first observer's field of view. The visual magnitudes of the planets were taken from [70, Ch. E].[78]

Figure 32 displays the stars in the simulated first observer's field of view without missed detections and false alarms. To test the orientation-estimation algorithm described in Section 8.3.1, it is assumed that one has determined the detection probability of the sensor to be approximately $P_D = 0.8$ for all of the stars. In reality, one would expect the detection probability to be lower for stars with higher magnitudes (dimmer stars). It is also assumed that the average number of false detections in the scene is 25. This implies that $\lambda V = 25$, so $\lambda = 25/(0.7543 \, \text{rad} \cdot 0.5776 \, \text{rad}) = 57.38 \, \text{rad}^{-2}$, where the terms in radians are the extent of the viewing region in radians in azimuth and elevation. A rough approximation of the measurement accuracy is to assume that regardless of whatever centroiding[79] might be done to turn adjacent pixels into a single star measurement, the measurement components in azimuth and elevation are independent and the standard deviations of the components are the same as the uniform distribution over a pixel. This results in a measurement covariance matrix of

$$\mathbf{P} = \text{diag}\left(\frac{1}{12}(0.23 \times 10^{-3})^2, \frac{1}{12}(0.24 \times 10^{-3})^2\right). \tag{132}$$

For the simulation, it is assumed that the stars are all well resolved and that the best available gravitational- and magnetic-field measurements are available. The parameters of Section 8.2 are used. From the biases in estimating ENU Up and North illustrated in Fig. 30, which are based on the model inaccuracies, it is reasonable to assume that one can obtain an inexpensive magnetometer/accelerometer chip where direction estimation is primarily limited by the quality of the Earth's magnetic and gravitational models and not by the precision of the chip itself.

Using the aforementioned parameter for the true observer's orientation and the field of view, if one were to run a simulation of the star-based orientation algorithm using a magnetic and gravitational measurement as an initial estimate in the algorithm of Section 8.3.1 without inflating $\mathbf{P}$ in the estimation routine, it is quite likely that the star-to-catalog assignment algorithm would produce no assignments at all and one could not estimate the orientation using the stars.[80] However, for the purposes of the first iteration of the simulation, the inflated value of

$$\mathbf{P}_{\text{inflated}} = \text{diag}\left(\left(0.2 \times \frac{\pi}{180}\right)^2, \left(0.2 \times \frac{\pi}{180}\right)^2\right) \tag{133}$$

---

[78]Note that the "apparent magnitude" of a star includes the effects of the atmosphere. For the purpose of this simple example, no atmospheric losses were taken into account.

[79]Centroiding is a weighted average of neighboring pixels that exceed a detection threshold. A centroiding technique is given in [20].

[80]Note that the field of view used for the estimation algorithm, given a low-precision initial orientation estimate, will not match the true field of view because the estimated field of view depends on the estimated orientation. Thus, stars at the edges of the true viewing area can be cut off and non-visible stars might be present in the estimated viewing area.
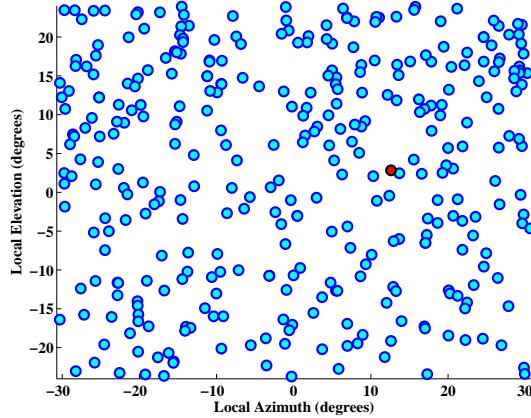
Fig. 32: The field of view of the first observer (in the South Pacific) for the example star-based orientation-estimation problem described in the text without false detections and missed detections. The coordinates are spherical coordinates from the center of the observer's field of view. Only stars and planets with a magnitude $\leqslant 6.0$ are displayed. Only one planet, Uranus, is visible and is marked in red.

is used for the first observer; that is, a standard deviation of $0.2°$ is used in azimuth and elevation. For the second observer, the inflation is $0.5°$. Using an inflated covariance like (133) for the first observer in the first iteration, the algorithm never failed in any Monte Carlo runs.

Table 12 summarizes the results of the algorithm run over 1000 Monte Carlo runs on the example described in this section. The accuracy in estimating the WGS 84 ellipsoidal North and Up vectors is shown. The use of moderate-precision star measurements greatly improved estimates of North in a WGS 84 ellipsoidal context, though not necessarily the estimates of the Up direction. The close agreement of ellipsoidal up with gravitational up in Fig. 21 at moderate latitudes and the relatively high accuracy of the measurements as shown in Fig. 22 explain why star-based orientation estimation with a low-fidelity camera might provide a worse estimate of the vertical direction than that obtained from a high-precision accelerometer measurement. Thus, when using moderate fidelity optical measurements of the stars, one might wish to use an orientation-estimation algorithm that fuses gravitational data with celestial measurements.

The second observer (near the Aleutian Islands) had a slightly worse initial estimate than the first observer, because as illustrated in Fig. 30, the models are less accurate near the poles. Had the observer been pushed up to $60°$ latitude, the simulation would likely have not been able to complete a full 1000 Monte Carlo runs, because in at least one run, the 2D-assignment algorithm would have been unable to assign enough stars to catalogued stars to obtain an initial estimate. In such an instance, one would have to perform a brute-force search over initial estimates. Thus, close to the magnetic poles, as well as in a region of the South Atlantic where the magnetic field is weaker, initial orientation estimates using magnetic and gravitational measurements will generally not provide usable initial estimates for the algorithm demonstrated in this subsection.

In the example provided, the Sun and Moon happened to not be in the viewing region. When the Sun and Moon are visible, one might worry that they might block a significant number of stars. However, the Sun

Table 12: Orientation Estimation Errors

	Observer 1		Observer 2	
	North Error	Up Error	North Error	Up Error
No Stars	472.84	1.8969	550.91	9.6405
Single Iteration	15.357	12.986	71.720	67.505
Two Iterations	2.8997	2.8173	6.0104	5.6760

The average angular error (in arcseconds) in estimating the directions of WGS 84 ellipsoidal North and Up using the star-based orientation-estimation algorithm with magnetic and gravitational-sensor readings as the initial estimate. Observer 1 is at $-22.5°$ latitude, observer 2 at $50°$. The estimates are made using only magnetic and gravitational measurements (no stars), using one iteration of the algorithm of Section 8.3.1 (skipping steps 5 and 6) and using two iterations (running the full algorithm). The measurement accuracy is on the order of that of a cell phone camera, though the detection sensitivity might be higher than one would expect with a cell phone camera. The other parameters are given in the text.

and Moon are both on the order of 30 arcminutes in diameter. Thus, unless using a sensor with a very narrow viewing angle, or a sensor that is blinded by having the Sun in the viewing region, neither celestial body would be expected to interfere significantly with the detection method (not counting atmospheric scattering during the day preventing one from seeing the stars in the visible spectrum).

When performing particularly high-fidelity direction estimation, a number of additional physical effects need to be taken into account. In [184], it is shown that numerous corrections for the effects of relativity need to be taken into account to achieve microarcsecond precision.

9. CONCLUSION

This report reviews common celestial and terrestrial coordinate systems and the international organizations that define them. Sources of data and code for concrete realizations of major celestial and terrestrial coordinate systems are provided. Contrary to what is often implied in the tracking literature, the conversion from an ECEF to an ECI coordinate system is not a fixed transformation. Rather, a high-precision conversion requires Earth-orientation parameters that must be monitored in real time.

When considering measuring heights near the surface of the Earth, gravity plays a major role in the definition of orthonormal heights, which are commonly used on maps, and for specifying terrain heights. Gravity also plays a role in models for air-pressure altitudes. Often, a nominal ellipsoidal approximation to the Earth is used to define a local ENU coordinate system. The magnitude of the deflection of the vertical from gravitational up compared to ellipsoidal up was quantified here along with the accuracy of the estimates. The degree to which tides move the surface of the Earth and change the gravitational potential of the Earth was quantified. Inconsistencies in published descriptions of tide models were also highlighted, as was the fact that one cannot recreate a full, high-precision gravitational tide model from published results alone.

Due to the prevalence of inexpensive magnetic sensors (compasses), the accuracy of the best freely available Earth magnetic-field model was considered. It was shown that large small-scale deviations that are significant enough to be charted on an FAA map are not adequately modeled. However, the model is sufficiently accurate away from land to be of use for oil companies to steer their drills from offshore oil rigs.

The concepts discussed were then brought together to tackle the orientation-estimation problem. That is, how can an observer determine in which direction he is looking? The algorithm of Umeyama is a simple, computationally efficient manner for determining the affine transformation between two coordinate systems given vectors in both systems. When the vectors are error free, the algorithm is exact, allowing one to avoid often tedious computations of rotations between systems. When the vectors are corrupted by noise, the algorithm is approximate. The algorithm was applied to the problem of estimating one's orientation using magnetic and gravitational sensors, where it was shown that the inaccuracies in existing magnetic-field and gravitational models are multiple orders of magnitude larger than the accuracy of the best sensors.

The problem of determining one's orientation using stars brings together celestial and terrestrial coordinate systems. When gravitational and magnetic estimates are used to obtain an initial orientation estimate, then almost all of the concepts of the report come into play. The star-based orientation-estimation problem can be viewed as another form of the general track-to-track association problem that is familiar to those designing target-tracking algorithms. The problem was solved in the report in a manner very similar to existing track-to-track association methods. However, those performing target tracking should consider the extensive literature on star-to-catalog association routines, which generally take a very different approach to the association problem than is traditionally used by the tracking community. It was shown that when using a moderate-fidelity optical sensor, the estimate of the local vertical might be worse than simply using a gravitational measurement. On the other hand, due to the poor quality of magnetic field sensors, it is generally much better to use star measurements.

The astronomical community has very detailed definitions of celestial and terrestrial coordinate systems that are often overlooked by those designing target-tracking algorithms. When the highest track precisions

are required, especially for tracking high-speed orbital objects, coordinate-system definitions with strict definitions consistent with relativistic physics are necessary. The tracking community has generally neglected such strict definitions in the literature.

   This report brings together many existing concepts found in the literature, that are needed to define and determine the accuracy of a radar system. It also highlights a number of details that are not present in the literature:

1. It is shown that techniques for sensor registration in the target tracking literature and for sensor orientation estimation in the space literature solve the same problems and can be shared between disciplines.

2. The accuracy of pointing estimation from gravitational and magnetic field models is quantified. The accuracy is limited due to the due to limitations in the accuracy of the models themselves.

3. The changes in gravitational acceleration and the deflection of the vertical due to time-variant tidal components is quantified.

4. Expressions for the gravitational-acceleration covariance matrix associated with spherical-harmonic coefficient standard deviations are derived in Appendix F.3.

5. The significant deviation between the EMM2010 and the direction of magnetic North near Aberdeen Proving Ground according to the FAA's charts is noted, indicating a high unreliability in the EMM2010 in certain localized areas.

6. The score function is modified to allow the detection domain to be different than the measurement domain in Appendix H.

7. Maps of organizational relationships are given in Figures 2, 8, and 24.

ACKNOWLEDGMENTS

Appendix A

ACCELERATING REFERENCE FRAMES AND THE CORIOLIS EFFECT

To better demonstrate why tracking in an inertial coordinate system is often desirable, this appendix derives the "phantom" forces that arise when a non-inertial coordinate system is used. Dynamic models under Newtonian mechanics are used. The problem becomes significantly more complicated when considering the use of non-inertial coordinates in relativity theory. A solution under special relativity theory (using the clock hypothesis) for an accelerated, rotating frame of reference is given in [242].

As illustrated in Fig. A1, a non-inertial coordinate system is defined at a particular time by an offset $\mathbf{l}$ and the positions of three unit vectors that define its three coordinate axes $\tilde{\mathbf{u}}_x$, $\tilde{\mathbf{u}}_y$, and $\tilde{\mathbf{u}}_z$. Under Newtonian mechanics, following the development in [322, Ch. 7], the relationship between a target in the inertial system specified $\mathbf{r}$ and that in the non-inertial system $\tilde{\mathbf{r}} = [\tilde{r}_x, \tilde{r}_y, \tilde{r}_z]'$ is

$$\mathbf{r} = \mathbf{l} + \sum_{i \in \{x,y,z\}} \tilde{r}_i \tilde{\mathbf{u}}_i. \tag{A1}$$

The first and second derivatives of this with respect to time are thus

$$\dot{\mathbf{r}} = \dot{\mathbf{l}} + \sum_{i \in \{x,y,z\}} \dot{\tilde{r}}_i \tilde{\mathbf{u}}_i + \sum_{i \in \{x,y,z\}} \tilde{r}_i \dot{\tilde{\mathbf{u}}}_i \tag{A2}$$

$$\ddot{\mathbf{r}} = \ddot{\mathbf{l}} + \sum_{i \in \{x,y,z\}} \ddot{\tilde{r}}_i \tilde{\mathbf{u}}_i + 2 \sum_{i \in \{x,y,z\}} \dot{\tilde{r}}_i \dot{\tilde{\mathbf{u}}}_i + \sum_{i \in \{x,y,z\}} \tilde{r}_i \ddot{\tilde{\mathbf{u}}}_i. \tag{A3}$$

Since $\dot{\tilde{\mathbf{u}}}_i$ represents a rotation, and the same rotation must be applied to all axes to keep them orthogonal, one can write

$$\dot{\tilde{\mathbf{u}}}_i = \Omega \times \mathbf{u}_i, \tag{A4}$$

where the direction of Ω is the axis of rotation and the magnitude of Ω is the rotation rate ω in radians per second, which can be determined to a high precision using the length-of-day (LOD) Earth orientation parameter (EOP) as in Eq. (2). When converting velocities between coordinates in the International Terrestrial Reference System (ITRS) and the Geocentric Celestial Reference System (GCRS), the direction of Ω is the z-axis in the Terrestrial Intermediate Reference System (TIRS), a system between the ITRS and GCRS.

The TIRS is the ITRS perturbed by a polar motion rotation matrix, which is determined using the polar motion coordinates, which are two additional EOPs. Using the International Astronomical Union's (IAU's) Standards of Fundamental Astronomy (SOFA) library, the polar motion matrix to go from the ITRS to the TIRS can be found using `iauPom00`, which requires the Terrestrial Intermediate Origin (TIO) locator, which one can get using the `iauSp00` function. From Figure 6, it can be seen that one can obtain a unit vector along the axis of rotation in the ITRS by multiplying the vector $[0,0,1]'$ by the polar motion matrix $\mathbf{W}$.
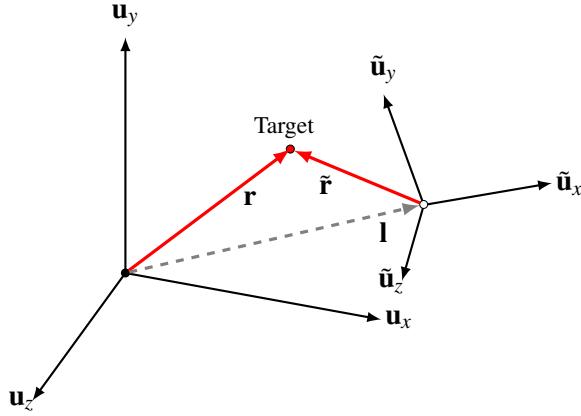
Fig. A1: The inertial coordinate system is defined by the standard orthogonal *x*-, *y*-, and *z*-axes, which can be defined by three unit vectors $\mathbf{u}_x$, $\mathbf{u}_y$, $\mathbf{u}_z$. This non-inertial, possibly rotating coordinate system is offset by the vector $\mathbf{l}$ and is defined by three other orthogonal unit vectors $\tilde{\mathbf{u}}_x$, $\tilde{\mathbf{u}}_y$, $\tilde{\mathbf{u}}_z$ (expressed in the inertial coordinate system).

Using (A4),

$$\ddot{\mathbf{r}} = \ddot{\mathbf{l}} + \sum_{i\in\{x,y,z\}} \ddot{\tilde{r}}_i \tilde{\mathbf{u}}_i + 2 \sum_{i\in\{x,y,z\}} \dot{\tilde{r}}_i \Omega \times \mathbf{u}_i + \sum_{i\in\{x,y,z\}} \tilde{r}_i \frac{d}{dt}\{\Omega \times \mathbf{u}_i\}. \tag{A5}$$

Note that

$$\sum_{i\in\{x,y,z\}} \tilde{r}_i \frac{d}{dt}\{\Omega \times \mathbf{u}_i\} = \sum_{i\in\{x,y,z\}} \tilde{r}_i \left(\dot{\Omega} \times \mathbf{u}_i + \Omega \times (\Omega \times \mathbf{u}_i) \right). \tag{A6}$$

Using (A6) and the definitions of the position, velocity, and acceleration of the target *as seen by an observer in the non-inertial coordinate system*,

$$\tilde{\mathbf{r}} \triangleq \sum_{i\in\{x,y,z\}} \tilde{r}_i \tilde{\mathbf{u}}_i \tag{A7}$$

$$\dot{\tilde{\mathbf{r}}} \triangleq \sum_{i\in\{x,y,z\}} \dot{\tilde{r}}_i \tilde{\mathbf{u}}_i \tag{A8}$$

$$\ddot{\tilde{\mathbf{r}}} \triangleq \sum_{i\in\{x,y,z\}} \ddot{\tilde{r}}_i \tilde{\mathbf{u}}_i. \tag{A9}$$

Eq. (A5) can be rewritten as[A.1]

$$\ddot{\tilde{\mathbf{r}}} = \ddot{\mathbf{r}} - \ddot{\mathbf{l}} - 2 \overbrace{\Omega \times \dot{\tilde{\mathbf{r}}}}^{\substack{\text{Coriolis}\\\text{Acceleration}}} - \overbrace{\Omega \times (\Omega \times \tilde{\mathbf{r}})}^{\substack{\text{Centrifugal}\\\text{Acceleration}}} - \dot{\Omega} \times \tilde{\mathbf{r}}. \tag{A10}$$

[A.1] Note that $\ddot{\mathbf{l}}$ remains in the original inertial coordinate system.

Thus, if an observer is thought to be in an inertial coordinate system and uses only the inertial accelera-tion term, $\ddot{\mathbf{r}}$ in the dynamic equations, a dynamic mismatch equivalent to all of the other terms shown will be observed. This mismatch is the cause of the Coriolis effect [294]. The Coriolis effect is the velocity-dependent phantom acceleration that an observer at a fixed location on the Earth ($\ddot{\mathbf{l}} = 0$) observes acting on a ballistic target assuming that the axis of rotation of the Earth is constant during the period of observation ($\dot{\Omega} = 0$).

This page
intentionally
left blank

Appendix B

CONVERTING FROM CARTESIAN TO GEODETIC ELLIPSOIDAL COORDINATES

This appendix is taken in part from an appendix of an article discussing the use of flat-Earth dynamic models on a curved Earth [58, Appen. B]. The conversion from Cartesian (x_0, y_0, z_0) to ellipsoidal (ϕ, λ, h) coordinates is a difficult problem. A table of 80 references addressing the topic is given in [88]. Generally, an explicit, numerically stable solution is the most desirable. In this appendix, the solution of [305], which is a stabler form of [304], is reviewed. Note that [305] is similar to [351], which is a stabler form of [350].

When using typical parameters for the Earth's ellipse, it is noted in [304, 305] that this conversion is valid for all points outside of a small ellipsoid around the center of the Earth, whose radius is about 43 km. (The same restriction applies to [350, 351].) Considering that no one has ever managed to drill through the 6 km of crust of the Earth to reach the mantle, though it might be technically feasible [325], this restriction is in practice meaningless for all applications of this coordinate conversion outside of, perhaps, seismic research.

It is assumed that the semi-major axis a and semi-minor axis b of the reference ellipsoid are known and that the reference ellipsoid is centered on the Cartesian origin. The latitude, longitude, and ellipsoidal height are given by

$$\phi = \arcsin\left(\frac{z\left(\varepsilon^2 + 1\right)}{N_e}\right) \tag{B1}$$

$$\lambda = \arctan2\left(y_0, x_0\right) \tag{B2}$$

$$h = r_0 \cos(\phi) + z_0 \sin(\phi) - \frac{a^2}{N_e}, \tag{B3}$$

where the terms in Eqs. (B1) and (B3) are given by computing

$$e^2 = 1 - \frac{b^2}{a^2} \qquad\qquad \varepsilon^2 = \frac{a^2}{b^2} - 1 \tag{B4}$$

$$r_0 = \sqrt{x_0^2 + y_0^2} \qquad\qquad p = \frac{|z_0|}{\varepsilon^2} \tag{B5}$$

$$s = \frac{r_0^2}{e^2 \varepsilon^2} \qquad\qquad q = p^2 - b^2 + s \tag{B6}$$

$$u = \frac{p}{\sqrt{q}} \qquad\qquad v = \frac{b^2 u^2}{q} \tag{B7}$$

$$P = 27 \frac{vs}{q} \qquad\qquad Q = \left(\sqrt{P+1} + \sqrt{P}\right)^{\frac{2}{3}} \tag{B8}$$

$$t = \frac{1}{6}\left(1 + Q + Q^{-1}\right) \qquad\qquad c = \sqrt{\max(0, u^2 - 1 + 2t)} \tag{B9}$$

$$w = \frac{c - u}{2} \tag{B10}$$

101

$$z = \text{sign}(z_0)\sqrt{q}\left(w + \sqrt{\max\left(0, \sqrt{t^2 + v} - uw - \frac{t}{2} - \frac{1}{4}\right)}\right) \tag{B11}$$

$$N_e = a\sqrt{1 + \frac{\varepsilon^2 z^2}{b^2}}. \tag{B12}$$

The term e is known as the first numerical eccentricity; ε is the second numerical eccentricity. The sign function returns 1 for a positive argument, -1 for a negative argument, and 0 for a zero argument. The max operators in (B11) and (B9) are to safeguard against taking the square root of a negative value in the face of finite precision limitations.

The four-quadrant inverse tangent in (B2) is not uniquely defined at the poles (when $x = 0$ and $y = 0$). However, many implementations of the four-quadrant inverse tangent, such as the `atan2` function in Matlab, will return zero in that instance. On the other hand, the `ArcTan` function in Mathematica correctly returns an indeterminate quantity. In a practical system, it is often preferable for a zero longitude to be returned at the poles rather than an indeterminate value.

Appendix C

EXPLAINING THE RELATIVISTIC TIME DILATION PLOT

A number of simple approximations were made to create Fig. 10, plots of the bias of a satellite-borne clock compared to a clock at geocentric coordinate time (TCG) due to relativistic time dilation. First, a spherical-Earth approximation is used and the effects of other celestial bodies are ignored. Second, the Newtonian approximation to the gravitational potential U at point $\mathbf{r}$ outside the Earth,

$$U(\mathbf{r}) = \frac{GM_\oplus}{\|\mathbf{r}\|} \tag{C1}$$

is used where $\|\mathbf{r}\|$ is the magnitude of the position vector $\mathbf{r}$ and the origin of the coordinate system is assumed to coincide with the center of the Earth. The values $GM_\oplus$ are the universal gravitation constant times the mass of the Earth. The value for $GM_\oplus$ from Table 5 is used. Note that the gradient of (C1) provides Newton's law of universal gravitation.

Basic (non-perturbed) orbital parameters describe the orbit of an object if the Earth were a perfect airless sphere and no other massive objects were present. They are described in detail in [29, Ch. 4] and [19, Ch. 1, 4]. The speed of a satellite in a circular orbit at a particular altitude can be easily derived from Keplerian orbital parameters to obtain

$$v_{sat} \triangleq \|\dot{\mathbf{r}}_{sat}\| = \sqrt{\frac{GM_\oplus}{\|\mathbf{r}_{sat}\|}}, \tag{C2}$$

where $\dot{\mathbf{r}}_{sat}$ is the velocity of the satellite. On the other hand, an observer at the equator would be traveling at a speed of $v_\oplus = r_\oplus \omega_\oplus$, where $r_\oplus$ and $\omega_\oplus$ are, respectively, the radius of the Earth and the rotational velocity of the Earth in the World Geodetic System 1984 (WGS 84) coordinate system as given in Table 5.

In [184, 258], among many other sources, an approximation for the rate of time of a clock at position $\mathbf{r}$ moving with velocity $\mathbf{v}$ compared to the rate of time of a clock at the coordinate-system origin in the absence of gravity (in this case, the time is TCG) is

$$\frac{dt}{dt_{TCG}} \approx 1 - \frac{1}{c^2}\left(\frac{\|\dot{\mathbf{r}}\|^2}{2} + U(\mathbf{r})\right), \tag{C3}$$

where c is the speed of light. The bias of the moving clock in seconds compared to TCG after one TCG day is

$$1 \text{ TCG Day Bias} = \left(\frac{dt}{dt_{TCG}} - 1\right)86400 \tag{C4}$$

as there are $86,400$ seconds in a Julian day.

Since frequency is the inverse of a time interval, one can relate the frequency of a clock on a satellite, f, to the frequency that a TCG observer would see, f_{TCG}, as

$$f_{\text{TCG}} = \frac{dt}{dt_{\text{TCG}}} f. \tag{C5}$$

The bias of the frequency of a clock in a satellite to a TCG clock is thus

$$\Delta_f = f - f_{TCG}. \tag{C6}$$

Given a frequency bias, a corresponding range-rate measurement bias can be obtained using a simple approximation. First, it is assumed that the geometry is such that the true range rate of the target is zero as the bias can depend on the true range rate of the target. A satellite in a circular orbit relative to TCG (which is defined at the center of mass of the Earth) has a zero range-rate. Next, since the range-rate bias is expected to be small, it is assumed that a slow-target approximation for the Doppler shift of the moving target would suffice in the receiver. That is,

$$-\Delta_f \approx \frac{v_{rr}}{c} f_{\text{trans}}, \tag{C7}$$

where f_{trans} is the frequency of the transmitter, Δ_f is the Doppler shift, and v_{rr} is the range rate, which is positive for a target moving away from the receiver. (This can be derived by multiplying the non-relativistic range-rate shift equations derived in [55] by $1/c$ and simplifying.) Thus, solving for v_{rr}, one obtains the simple expression for the range rate in terms of the Doppler shift,

$$v_{rr} = -\frac{\Delta_f c}{f}, \tag{C8}$$

where the TCG observer erroneously expects to see a frequency of f if the satellite is not moving. By inserting (C6) and (C5), one obtains the range-rate bias due to ignoring the effects of relativity on the clock in the transmitter and receiver.

Appendix D

CONVERTING TO AND FROM ELLIPSOIDAL HARMONIC COORDINATES

Ellipsoidal harmonic coordinates play a role in Section 4.2 in providing explicit expressions for the gravitational potential and the acceleration due to gravity at any point given an ellipsoidal gravitational approximation. This appendix summarizes the conversions between Cartesian and ellipsoidal harmonic coordinates.

Ellipsoidal harmonic coordinates are defined with respect to an ellipsoid having a given linear eccentricity E. Using (32) and (24), the linear eccentricity can be expressed in terms of the semi-major axis a and flattening factor of the reference ellipsoid as

$$E = a\sqrt{2f - f^2}. \tag{D1}$$

Given a point (β, λ, u) in ellipsoidal harmonic coordinates, where β is the reduced latitude, λ is the longitude, and u is the ellipsoidal harmonic semi-major axis, the corresponding point in Cartesian coordinates is [136, Ch. 1.15]

$$x = \sqrt{u^2 + E^2}\cos(\beta)\cos(\lambda) \tag{D2}$$

$$y = \sqrt{u^2 + E^2}\cos(\beta)\sin(\lambda) \tag{D3}$$

$$z = u\sin(\beta). \tag{D4}$$

The inverse transformation is more difficult and comes from inverting (D2) through (D4). Given a point (x, y, z) in Cartesian space, one can invert the equations to get

$$\beta = \frac{\pi}{2} - \phi \tag{D5}$$

$$\lambda = \arctan 2\,(y, x) \tag{D6}$$

$$\begin{bmatrix} u \\ \phi \end{bmatrix} = \begin{cases} \begin{bmatrix} u_p \\ \arccos\left(\max\left(\min\left(\dfrac{z}{u_p}, 1\right), -1\right)\right) \end{bmatrix} & \text{If } t > 0 \\[2em] \begin{bmatrix} \dfrac{z}{\cos(\phi)} \\ \arccos(\operatorname{sign}(z))\dfrac{u_p}{E} \end{bmatrix} & \text{Otherwise} \end{cases} \tag{D7}$$

where

$$t = x^2 + y^2 + z^2 - E^2 \tag{D8}$$

$$q_p = 1 + \sqrt{1 + 4\left(\frac{Ez}{t}\right)^2} \tag{D9}$$

$$u_p = \begin{cases} \sqrt{\left(\frac{|t|}{2}\right) q_p} & \text{If } q_p \text{ is finite.} \\ 0 & \text{Otherwise.} \end{cases} \tag{D10}$$

Note that if $t > 0$, one must first solve for ϕ before finding u in (D7). The max and min commands in (D7) help to deal with numerical precision limitations. The test in (D10) is also meant to deal with numerical precision problems when t is very small. The sign function returns 1 if the argument is positive, and -1 if the argument is positive, -1 if the argument is negative, and 0 if the argument is zero. The angle ϕ is the complement of the reduced latitude.

Cartesian unit vectors $\mathbf{u}_\beta$, $\mathbf{u}_\lambda$, and $\mathbf{u}_u$ in the directions of the β, λ, and u coordinates, respectively, at a particular point are given by differentiating (D2) through (D4) by β, λ, and u to get

$$c_1\mathbf{u}_\beta = \begin{bmatrix} -\sqrt{E^2 + u^2}\sin(\beta)\cos(\lambda) \\ -\sqrt{E^2 + u^2}\sin(\beta)\sin(\lambda) \\ u\cos(\beta) \end{bmatrix} \tag{D11}$$

$$c_2\mathbf{u}_\lambda = \begin{bmatrix} -\sqrt{E^2 + u^2}\cos(\beta)\sin(\lambda) \\ \sqrt{E^2 + u^2}\cos(\beta)\cos(\lambda) \\ 0 \end{bmatrix} \tag{D12}$$

$$c_3\mathbf{u}_u = \begin{bmatrix} \left(\dfrac{u}{\sqrt{E^2 + u^2}}\right)\cos(\beta)\cos(\lambda) \\ \left(\dfrac{u}{\sqrt{E^2 + u^2}}\right)\cos(\beta)\sin(\lambda) \\ \sin(\beta) \end{bmatrix} \tag{D13}$$

where c_1, c_2, and c_3 are scalar multipliers indicating that the arguments on the right-hand side do not necessarily have unit magnitude. Thus, one must divide the vectors by their magnitudes to get the desired unit vectors.

Note that if a point is too close to the poles, then it is possible that c_2 is nearly zero. However, since $\mathbf{u}_\lambda$ is orthogonal to $\mathbf{u}_\beta$ and $\mathbf{u}_u$, it is best to define $\mathbf{u}_\lambda$ in terms of the cross product

$$\mathbf{u}_\lambda = \mathbf{u}_\beta \times \mathbf{u}_u. \tag{D14}$$

Appendix E

PRINCIPAL AXES, PRECESSION, NUTATION, AND THE POLE TIDE

The principal axis coordinate system plays a role in understanding the coordinate system usually used for gravitational models as well as what the pole tide is. The inertia matrix and angular momentum vector in the definition of the principal axis coordinate system also play roles in understanding what precession and nutation with regard to the Earth's orientation are, and how the two terms differ.

The angular momentum vector $\mathbf{h}$ of a rotating body at a particular instant is defined to be the volume integral

$$\mathbf{h} = \int_{\mathbf{r} \in \mathbf{V}_{obj}} \rho(\mathbf{r}) \mathbf{r} \times \mathbf{v} \, dx \, dy \, dz \tag{E1}$$

where $\rho(\mathbf{r})$ is the density of the object at point $\mathbf{r}$, and $\mathbf{v}$ is the direction of motion of point $\mathbf{r}$. The integral is over the volume of the object; however, it could be extended to be over all of three-dimensional space, $\mathbb{R}^3$, by letting $\rho(\mathbf{r})$ be zero outside of the object.

The angular momentum vector can be rewritten in terms of an inertia matrix (generally referred to as an inertia *temsor*, even though it is only a 3×3 matrix). This is simplest to do if the origin is chosen to be the center of mass of the object. In such an instance, one can replace the velocity term with a cross product as

$$\mathbf{h}_G = \int_{\mathbf{r} \in \mathbf{V}_{obj}} \rho(\mathbf{r}) \mathbf{r} \times (\omega \times \mathbf{r}) \, dx \, dy \, dz \tag{E2}$$

where the subscript of G on $\mathbf{h}$ indicates that it is taken with respect to the center of mass of the object, and ω is an angular velocity vector (the axis of rotation, the magnitude of which is the rotation rate, usually in radians per second) such that $\mathbf{v} = \omega \times \mathbf{r}$ at the point $\mathbf{r}$. If the body that is rotating is *rigid*, then ω will be the same for all points[E.1] and (E2) can be rewritten as

$$\mathbf{h}_G = \left(\overbrace{\int_{\mathbf{r} \in \mathbf{V}_{obj}} \rho(\mathbf{r}) \left(\|\mathbf{r}\|^2 \mathbf{1}_{3,1} - \mathbf{r}\mathbf{r}' \right) dx \, dy \, dz}^{\mathbf{I}_G} \right) \omega \tag{E3}$$

where $\mathbf{I}_G$ is the inertia matrix when the origin is chosen to be at the center of mass of the object and $\mathbf{1}_{3,1}$ is a 3×1 vector of ones.

In (E1), it can be seen that the value of the angular momentum vector $\mathbf{h}$ depends on the choice of the origin and on the alignment of the axes. When the origin is chosen to not be the center of mass of the object, $\mathbf{h}$ can still be written in terms of a general inertia matrix $\mathbf{I}$ as discussed in [322, Ch. 10.5] and [49, Ch.12.5.3].

[E.1]Note that the axis of rotation of a rigid body passes through the center of mass of the body.

In such an instance, if $\mathbf{r}_G$ is the location of the center of mass of the object with respect to the desired origin of the object, the inertia matrix transforms to become

$$\mathbf{I} = \mathbf{I}_G + M\left(\|\mathbf{r}_G\|^2 \mathbf{1}_{3,1} - \mathbf{r}_G \mathbf{r}_G'\right) \tag{E4}$$

where M is the mass of the object. In such an instance, one can still write

$$\mathbf{h} = \mathbf{I}\omega \tag{E5}$$

where ω has not changed.

On the other hand, if the origin is kept at the center of mass of the object but the coordinate system is rotated by a rotation matrix $\mathbf{R}$, the angular momentum, the inertia matrix, and the axis of rotation all change as

$$\mathbf{h} = \mathbf{R}\mathbf{h}_G \tag{E6a}$$
$$\mathbf{I} = \mathbf{R}\mathbf{I}_G\mathbf{R}' \tag{E6b}$$
$$\omega_{\text{rotated}} = \mathbf{R}\omega \tag{E6c}$$

such that $\mathbf{h} = \mathbf{i}\omega_{\text{rotated}}$ instead of $\mathbf{h}_G = \mathbf{I}_G\omega$. Rotations do not change the magnitude of $\mathbf{h}$.

The principal axis coordinate system is one such that the origin is at the center of mass of the object and the orientation of the axes is chosen such that the inertia matrix $\mathbf{I}$ is diagonal. Given $\mathbf{I}_G$ and *omega* with the axes rotated in an arbitrary manner, the task of finding the principal axes is the same as performing an eigenvalue decomposition of $\mathbf{I}_G$. In Matlab, the rotation matrix and the inertia matrix in principal axis form can be found using the command `[R,I]=eig(IG)` where `IG` corresponds to $\mathbf{I}_G$. The eigenvalues of $\mathbf{I}_G$ are known as the principal moments of inertia. The axes associated with the eigenvalues are known as the principal axes. The axis corresponding to the largest eigenvalue is known as the figure axis. Gravitational models are often derived in terms of the principal axes.

The principal axis coordinate system is important for understanding the origin of precession and nutation of a planet. If the planet is assumed to be *rigid*, then the inertia matrix $\mathbf{I}$ in the principal axis coordinate system is constant and, as derived in [322, Ch. 11.2] and [49, Ch. 12.6], the rotation axis with respect to the principal axis coordinate system varies over time as per Euler's equations of motion of a rigid body

$$\dot{\omega} = \mathbf{I}^{-1}\left(\begin{bmatrix} \omega_2\omega_3(I_2 - I_3) \\ \omega_3\omega_1(I_3 - I_1) \\ \omega_1\omega_2(I_1 - I_2) \end{bmatrix} + \frac{d\mathbf{h}}{dt}\right) \tag{E7}$$

where I_j is the jth diagonal element of $\mathbf{I}$, $\omega = [\omega_1, \omega_2, \omega_3]'$, and $\frac{\partial \mathbf{h}}{\partial t}$ is any externally applied torque to the system. In the absence of externally applied forces, the angular momentum $\mathbf{h}$ remains constant.

If the massive body is symmetric about a particular axis and ω coincides with the axis of mass symmetry, then (E7) is trivial: $\dot{\omega} = 0_{3,1}$. Note that changing any of the principal moments of inertia (changing $\mathbf{I}$)

changes $\dot{\omega}$. While the Earth may be approximated as being rigid, it is not. The effects of pole tides arise when external forces move the crust of the Earth with respect to the inner mantle/core or deform the Earth, changing the direction of the figure axis. This means that **I** has changed, and thus the rotation axis of the Earth has changed.

In the absence of external forces, precession arises when the axis of rotation of the massive object is not aligned with the mass axis of symmetry. Consider, for example, the case where $I_1 = I_2 = I$ (the body is symmetric about the third axis). In such an instance, (E7) can be written

$$\dot{\omega} = \begin{bmatrix} -k\omega_2 \\ k\omega_1 \end{bmatrix} \tag{E8}$$

where $k = \frac{I_3 - I}{I}$. As discussed in [49, Ch. 12.6], the solution to this differential equation has the form of simple harmonic motion:

$$\omega_1 = A\cos(kt + \phi_0) \qquad\qquad \omega_2 = A\sin(kt + \phi_0) \tag{E9}$$

where A is the maximum amplitude of the offset and ϕ_0 is an initial phase. Thus, precession is a smooth, periodic rotation of $\dot{\omega}$.

As discussed in [49, Ch. 12.8] and [322, Ch. 11.5], if the torque $\frac{d\mathbf{h}}{dt}$ in (E7) is nonzero, high-frequency oscillations can be superimposed on the lower-frequency motion of $\dot{\omega}$ that would arise with torque-free precession. These high-frequency variations are known as nutation. Earth orientation models generally include precession and nutation (due to forces from other massive bodies in the solar system) together as a single model.

This page
intentionally
left blank

Appendix F

EVALUATING SPHERICAL-HARMONIC POTENTIALS AND THEIR GRADIENTS

Spherical harmonics can be used to describe both real and complex scalar and vector potential fields, as discussed for range-independent harmonics in [9, Ch. 12.6, 12.12] and in terms of gravitation in [187, Appen. A]. When considering gravitational and magnetic models, a commonly used formulation of the gravitational potential/scalar magnetic-field potential is

$$V(r, \phi_c, \lambda) = \frac{c}{r} \sum_{n=0}^{N} \left(\frac{a}{r} \right)^n \sum_{m=0}^{n} P_n^m(\sin(\phi_c))(C_{n,m}\cos(m\lambda) + S_{n,m}\sin(m\lambda)) \tag{F1}$$

where r, ϕ_c, and λ are respectively range, geocentric latitude, and longitude, $C_{n,m}$ and $S_{n,m}$ are real scalar coefficients, the function P_n^m is the associated Legendre function of degree n and order m, and c and a are constants, and N is the highest degree. In gravitational models, including the Earth Gravitation Model 2008 (EGM2008) from the National Geospatial Intelligence Agency (NGA), $c = GM_\oplus$ and $a = a_\oplus$, the semi-major axis of the Earth (see Table 5). In magnetic-field models, including the World Magnetic Model 2010 (WMM2010) and the Enhanced Magnetic Model 2010 (EMM2010), $c = a_\oplus^2$ and $a = a_\oplus$. On the other hand, when synthesizing coefficients for a model that depends only on the latitude and longitude, but not the distance from the center of the Earth, such as when using the coefficients for the Earth2012 terrain model, the NGA's Digital Terrain Model 2006.0 (DTM2006.0) orthometric height (and bathymetric depth) model, and when synthesizing the K_p term in (57) from the NGA's geoid model, one simply sets $a = c = r = 1$, because those terms are not needed in the spherical-harmonic sum. Note that when using the EGM2008 model, V is the gravitational potential and the gradient of V is acceleration due to gravity. However, when using the WMM2010 and EMM2010 models, V is a scalar magnetic-field potential and the *negative* of the gradient of V is the magnetic field.

Though (F1) is the generic form of a spherical-harmonic coefficient model, the vast majority of such models use different definitions of the associated Legendre functions. The function P_n^m is the non-normalized associated Legendre function of degree n and order m, defined in terms of derivatives of the Legendre polynomial P_n as

$$P_n^m(x) \triangleq (-1)^m (1 - x^2)^{\frac{m}{2}} \frac{d^m}{dx^m} P_n(x). \tag{F2}$$

The Legendre polynomial is itself defined in terms of derivatives as [357]

$$P_n(x) \triangleq \frac{1}{n! 2^n} \frac{d^n}{dx^n} (x^2 - 1)^n \tag{F3a}$$

$$= \frac{1}{2^n} \sum_{k=0}^{n} \binom{n}{k} (x - 1)^{n-k} (x + k)^k. \tag{F3b}$$

On the other hand, the EGM2008 model, the Earth2012 model, the DTM2006.0 model, and the model used for the K_p term in (57) from the NGA's geoid model do not directly use the coefficients and associated Legendre functions as expressed in (F1). Rather, they use fully normalized, unitless spherical-harmonic coefficients with fully normalized associated Legendre functions.[F.1] Additionally, the models use an alternate notation/definition for the associated Legendre functions, specifically

$$P_{n,m}(x) \triangleq (1-x^2)^{\frac{m}{2}} \frac{d^m}{dx^m} P_n(x) \tag{F4a}$$

$$= (1-x^2)^{\frac{m}{2}} \frac{1}{n!2^n} \frac{d^{m+n}}{dx^{m+n}} (x^2-1)^n \tag{F4b}$$

This differs from (F2) by the omission of the $(-1)^m$ term, which is simply absorbed into the coefficients, $C_{n,m}$ and $S_{n,m}$. The fully normalized associated Legendre functions and coefficients used in the EGM2008 model are given by

$$\bar{P}_{n,m} = N_{n,m} P_{n,m} \tag{F5}$$

$$\bar{C}_{n,m} = \frac{C_{n,m}}{N_{n,m}} \tag{F6}$$

$$\bar{S}_{n,m} = \frac{S_{n,m}}{N_{n,m}} \tag{F7}$$

where the normalization factor is

$$N_{n,m} = \sqrt{\frac{(n-m)!(2n+1)(2-\delta(m))}{(n+m)!}} \tag{F8}$$

and is chosen such that the harmonics have a mean-squared value of one on the unit sphere. The normalized coefficients $\bar{C}_{n,m}$ and $\bar{S}_{n,m}$ are called Stokes coefficients. Thus, the basic form of the EGM2008 model is

$$V(r, \phi_c, \lambda) = \frac{c}{r} \sum_{n=0}^{N} \left(\frac{a}{r}\right)^n \sum_{m=0}^{n} \bar{P}_n^m(\sin(\phi_c)) \left(\bar{C}_{n,m}\cos(m\lambda) + \bar{S}_{n,m}\sin(m\lambda)\right). \tag{F9}$$

Note, however, that documentation for the EGM2008 model often uses geocentric colatitude (90° minus the latitude) instead of latitude, which turns the argument of $\bar{P}_{n,m}$ into a cosine. Also, the normalization used here differs from the normalization that Matlab's built-in `legendre` function uses. The following subsections discuss how to evaluate (F9) and its gradient in Cartesian coordinates.

On the other hand, the EMM2010 and the WMM2010 magnetic-field models do not express the magnetic potential in terms of fully normalized associated Legendre functions. Rather, the models use coefficients for Schmidt-normalized Legendre functions. This appendix only considers the synthesis of fully normalized

---

[F.1]Documentation is available at `http://earth-info.nga.mil/GandG/wgs84/gravitymod/egm2008/README_FIRST.pdf`.

spherical-harmonic coefficients as used in the EGM2008 model. The conversion from Schmidt-normalized $\tilde{C}_{n,m}$ and $\tilde{S}_{n,m}$ spherical-harmonic coefficients to fully normalized coefficients is performed as

$$\bar{C}_{n,m} = \frac{1}{\sqrt{1+2n}}\tilde{C}_{n,m} \qquad\qquad \bar{S}_{n,m} = \frac{1}{\sqrt{1+2n}}\tilde{S}_{n,m}. \tag{F10}$$

Data files for many gravitational models including the EGM2008 often omit the first few Stokes coefficients. This is because, as mentioned in [29, Ch. 3.4], by keeping the $c = GM_\oplus$ term in (F9) out front (rather than absorbing it in the coefficients) and including the equatorial radius in the expression, the coefficients are kept unitless and $C_{0,0}$ is always one. If the center of mass of the Earth is the origin, then $C_{1,0}$, $C_{1,1}$, and $S_{1,1}$ are all zero. The EGM2008 model takes advantage of these simplifications to rewrite (F9) as

$$V(r,\phi_c,\lambda) = \frac{GM_\oplus}{r}\left(1 + \sum_{n=2}^{N}\left(\frac{a_\oplus}{r}\right)^n \sum_{m=0}^{n}\bar{P}_{n,m}(\sin(\phi_c))\left(\bar{C}_{n,m}\cos(m\lambda)+\bar{S}_{n,m}\sin(m\lambda)\right)\right) \tag{F11}$$

where, in practice, the outer sum is truncated to a finite number of terms. The method described in the following subsections does not take advantage of the simplification used for the first few terms of the EGM2008 model and thus when using such coefficients zeros should be inserted as appropriate.

Note that the coefficients in many spherical-harmonic magnetic field and gravitational models slowly drift over time. The WMM and EMM2010 model coefficients come with additional terms to estimate the Earth's magnetic field within 5 years of the release of each model. The drift of the gravitational coefficients is noted in [366], among other sources. However, the modeling and documentation surrounding the use and incorporation of such terms is inconsistent.

The International Earth Rotation Systems Service (IERS) conventions lists expressions for the drift of low-degree coefficients in spherical-harmonic geopotential models [257, Ch. 6.1] for the EGM2008 model.[F.2] The value at the epoch year of J2000.0 (0:00 on 1 January 2000 UTC) for $\bar{C}_{3,0}$ and $\bar{C}_{4,0}$ matches that in the coefficients for the EGM2008 model, implying that the model has an epoch date of J2000.0. However, a different value of the *zero-tide* $\bar{C}_{2,0}$ coefficient is provided ($-0.4841694810 \times 10^{-3}$) citing a prepublication version of [45] as being more accurate than the value used in the EGM2008 model itself. Section 6.2 of the IERS conventions [257] lists the tide-free value as $-0.48416531 \times 10^{-3}$. Note, however, that the WGS 84 standard [69] does not use the IERS' more accurate value for $\bar{C}_{2,0}$.

Numerical-precision problems make the evaluation of (F9) and its gradient challenging. The EGM2008 model contains complete coefficients up to degree and order 2159 and from degree 2160 to 2190, the non-zero coefficients only go up to order 2159. In unnormalized form, the magnitude of $P_{n,m}(x)$ would greatly exceed the maximum floating-point value, which is slightly less than 2^{1024} [149]. In normalized form, the coefficients and associated Legendre polynomials can be computed avoiding overflow issues. However, it has been shown that underflow problems arise for orders $m > 1900$ [140], though algorithms have been developed to avoid such problems. The techniques presented in this appendix allow one to use the EGM2008

[F.2]The drift rates shown are $\dot{\bar{C}}_{2,0} = 11.6 \times 10^{-12}$, $\dot{\bar{C}}_{3,0} = 4.9 \times 10^{-12}$ and $\dot{\bar{C}}_{4,0} = 4.7 \times 10^{-12}$ per year, where the time system for "year" is not further defined, but one might assume a terrestrial time (TT) Julian year of exactly 365.25 days of exactly 86400 seconds.

model without resorting to using quadruple-precision arithmetic or techniques to extend the exponent of floating-point numbers, as mentioned in [100], except the formulae for computing second-order moments for estimates from the EGM2008 model, which run into overflow and underflow problems close to the geographic poles when using double-precision arithmetic.

In [41], and later improved and in more detail in [85], four techniques for derivatives of the gravitational potential are considered.[F.3] Two of the methods have singularities at the poles, and two have been designed to have no problem evaluating gravitational gradients at or near the poles. A mission-critical system should be numerically stable everywhere on Earth, so the possible failure of the algorithm near the poles is unacceptable. Unfortunately, both analyses demonstrated that the singularity-free algorithms suffer a minor loss of precision near the equator, suggesting that the best method for finding the acceleration due to the Earth's gravity would be a combination of singular and non-singular techniques.

Section F.1 describes an implementation of Pines' singularity-free algorithm from [85, 207, 262, 308], which can be used near the geographic poles (in the simulations in this report, it was used within $2°$ of the poles). For points that are not near the poles, the modified forward row (MFR) algorithm of [140] is chosen and is explained in Section F.2. The MFR algorithm was shown in [140] to outperform the types of algorithms described in [41, 85] for points far from the poles.

In additional to spherical-harmonic gravitational coefficients, the EGM2008 model comes with standard deviations for all of the coefficients. Assuming the errors corrupting the gravitational coefficients are independent, the standard deviations can be synthesized to obtain a variance for gravitational potential computations and to obtain a covariance matrix for gravitational-acceleration computations. Section F.3 explains how Pines' method can be modified to synthesize the standard deviations.

Finally, Section F.4 describes the relationship between the J_2 gravity model, which is a truncated spherical-harmonic model, which often appears in tracking literature, such as in [202], and the "exact" ellipsoidal-Earth model. It is demonstrated that the J_2 model is actually a truncated spherical-harmonic expansion of the ellipsoidal-gravity model. Thus, if the full EGM2008 model cannot be used, but the exact ellipsoidal model is not too computationally intensive to use, then there is no point in using the J_2 approximation.

F.1   Pines' Singularity-Free Method

In [85, 207, 262, 308], Pines' singularity-free method of spherical-harmonic synthesis is developed with a special consideration for gravitational models. The method of Pines expresses the gravitational potential at a Cartesian point (x, y, z) in terms of a range r and the direction cosines s, t, and u, which are defined in Eq. (42) in [85] as

$$s \triangleq x/r = \cos\phi_c \cos\lambda \tag{F12}$$

$$t \triangleq y/r = \cos\phi_c \sin\lambda \tag{F13}$$

$$u \triangleq z/r = \sin\phi_c, \tag{F14}$$

[F.3] A number of methods for computing higher order derivatives are also considered in [41, 85]. Higher order derivatives are necessary for computing the torque that a satellite experiences due to the gravitational gradient [110].

where r, ϕ_c, and λ are the spherical coordinates (range, elevation [spherical latitude], azimuth [longitude]) of the point (x, y, z). As in Eq. (44) of [85], the gravitational potential at (x, y, z) is

$$V = \frac{c}{r} \sum_{n=0}^{N} \rho_n \sum_{m=0}^{n} D_{nm}(s,t) \bar{H}_n^m(u), \tag{F15}$$

$$\rho_n \triangleq \left(\frac{a}{r}\right)^n \tag{F16}$$

$$D_{nm}(s,t) \triangleq \bar{C}_{nm} r_m(s,t) + \bar{S}_{nm} i_m(s,t), \tag{F17}$$

where $\bar{H}_n^m(u)$ is a fully normalized Helmholtz polynomial of degree n and order m (the evaluation of which is discussed below), $\bar{C}_{nm}$ and $\bar{S}_{nm}$ are fully normalized spherical-harmonic coefficients, GM is the universal gravitational constant times the mass of the Earth, and the terms $r_m(s,t)$ and $i_m(s,t)$ can be found recursively using

$$r_m = s r_{m-1} - t i_{m-1} \tag{F18}$$

$$i_m = s i_{m-1} + t r_{m-1} \tag{F19}$$

starting with $r_0 = 1$ and $i_0 = 0$, as in Eq. (49) of [85]. The parameterizations on s and t have been omitted for compactness of notation. Alternatively, the r_m and i_m terms can be written non-recursively as

$$r_m = \cos(m\lambda) \cos^m(\phi_c) \tag{F20}$$

$$i_m = \sin(m\lambda) \cos^m(\phi_c). \tag{F21}$$

The components of the gradient of the gravitational potential derived in [262] are

$$\nabla V = \begin{bmatrix} V_x \\ V_y \\ V_z \end{bmatrix} = \frac{c}{r^2} \begin{bmatrix} a_1 + s a_4, \\ a_2 + t a_4 \\ a_3 + u a_4 \end{bmatrix} \tag{F22}$$

where

$$a_1 = \sum_{n=0}^{N} \rho_n \sum_{m=1}^{n} m \left(\bar{C}_{nm} r_{m-1} + \bar{S}_{nm} i_{m-1} \right) \bar{H}_n^m(u) \tag{F23}$$

$$a_2 = \sum_{n=0}^{N} \rho_n \sum_{m=1}^{n} m \left(-\bar{C}_{nm} i_{m-1} + \bar{S}_{nm} r_{m-1} \right) \bar{H}_n^m(u) \tag{F24}$$

$$a_3 = \sum_{n=0}^{N} \rho_n \sum_{m=0}^{n} \left(\bar{C}_{nm} r_m + \bar{S}_{nm} i_m \right) \frac{d\bar{H}_n^m(u)}{du} \tag{F25}$$

$$a_4 = -\sum_{n=0}^{N} \rho_n \sum_{m=0}^{n} \left(\bar{C}_{nm} r_m + \bar{S}_{nm} i_m \right) \bar{L}_n^m \tag{F26}$$

where

$$\bar{L}_n^m \triangleq (n+1+m)\bar{H}_n^m(u) + u\frac{d\bar{H}_n^m(u)}{du}. \tag{F27}$$

The method of evaluating the Helmholtz polynomials needed to evaluate the potential in (F15) and the gradient of the potential in (F22) is taken from [85]. The Helmholtz polynomial of degree n and order m is defined to be

$$H_n^m(u) \triangleq \frac{1}{n!2^n}\frac{d^{n+m}}{du^{n+m}}\left(u^2-1\right)^n. \tag{F28}$$

Consequently,

$$H_n^m(u) = 0 \,\forall m > n. \tag{F29}$$

A fully normalized Helmholtz polynomial is defined to be

$$\bar{H}_n^m(u) \triangleq H_n^m(u) \begin{cases} \sqrt{\dfrac{(2n+1)(n-m)!}{(n+m)!}} & \text{if } m = 0 \\[4mm] \sqrt{\dfrac{2(2n+1)(n-m)!}{(n+m)!}} & \text{otherwise.} \end{cases} \tag{F30}$$

The fully normalized Helmholtz polynomials can be computed recursively starting with

$$\bar{H}_0^0(u) = 1 \tag{F31}$$

$$\bar{H}_1^1(u) = \sqrt{3} \tag{F32}$$

$$\bar{H}_0^1(u) = u\sqrt{3}. \tag{F33}$$

Then, all terms of the form $\bar{H}_n^n(u)$ and $\bar{H}_n^{n-1}(u)$ are computed recursively using

$$\bar{H}_n^n(u) = \sqrt{\frac{2n+1}{2n}}\bar{H}_{n-1}^{n-1}(u) \tag{F34}$$

$$\bar{H}_n^{n-1}(u) = u\sqrt{2n}\bar{H}_n^n(u). \tag{F35}$$

Then, all of the other fully normalized Helmholtz polynomials are computed using

$$g = \sqrt{\frac{(2n+1)(2n-1)}{(n+m)(n-m)}} \tag{F36}$$

$$h = \sqrt{\frac{(2n+1)(n-m-1)(n+m-1)}{(2n-3)(n+m)(n-m)}} \tag{F37}$$

$$\bar{H}_n^m(u) = ug\bar{H}_{n-1}^m(u) - h\bar{H}_{n-2}^m(u). \tag{F38}$$

First derivatives of fully normalized Helmholtz polynomials are computed from the Helmholtz polynomials as

$$\frac{d\bar{H}_n^m(u)}{du} = \begin{cases} 0 & \text{if } m=0, n=0 \\ \sqrt{\dfrac{n(n+1)}{2}}\bar{H}_n^1(u) & \text{if } m=0, n>0 \\ \sqrt{(n-m)(n+m+1)}\bar{H}_n^{m+1}(u) & \text{otherwise.} \end{cases} \tag{F39}$$

The aforementioned equations for computing a spherical-harmonic potential and its gradient will tend to suffer from overflow problems when used as written above with high degree and high order models, such as the Earth Gravitation Model 2008 (EGM2008) model. A workaround for the problem is to scale all of the fully normalized Helmholtz polynomials and their derivatives and then to unscale the result. This is analogous to the scaling that is suggested in Section F.2 when using the MFR algorithm.

Let c_S be the scale factor. In the simulations for this report, $c_S = 10^{-280}$ was used. All of the fully normalized Helmholtz polynomials' derivatives can be computed in a scaled manner by replacing the seed values in (F31), (F32), and (F33) with

$$\bar{H}_{0,\text{scaled}}^0(u) = c_S \tag{F40}$$
$$\bar{H}_{1,\text{scaled}}^1(u) = c_S\sqrt{3} \tag{F41}$$
$$\bar{H}_{0,\text{scaled}}^1(u) = c_S u\sqrt{3}. \tag{F42}$$

After computation of the scaled potential V_{scaled} and gradient ∇V_{scaled}, the unscaled values can be obtained as

$$V = \frac{V_{\text{scaled}}}{c_S} \qquad\qquad \nabla V = \frac{\nabla V_{\text{scaled}}}{c_S}. \tag{F43}$$

F.2 The Modified Forward Row Algorithm

When considering the use of spherical-harmonic synthesis models away from the geographic poles, the modified forward row algorithm of [140] seems to be one of the best methods to use. Defining

$$t \triangleq \cos(\theta_c) \qquad\qquad u \triangleq \sin(\theta_c) \tag{F44}$$

the algorithm does not directly compute the fully normalized Legendre functions in (F9), but rather it computes the ratio $\frac{\bar{P}_{n,m}(t)}{u^m}$ using the recursion

$$
\frac{\bar{P}_{n,m}(t)}{u^m} = \begin{cases}
0 & \text{for } n < m \\
1 & \text{for } n = m = 0 \\
\sqrt{3} & \text{for } n = m = 1 \\
\sqrt{\dfrac{2m+1}{2m}} \dfrac{\bar{P}_{m-1,m-1}(t)}{u^{m-1}} & \text{for } n = m \neq 1 \\
g_{n,m}t\left(\dfrac{\bar{P}_{n,m+1}(t)}{u^{m+1}}\right) - h_{n,m}u^2\left(\dfrac{\bar{P}_{n,m+2}(t)}{u^{m+2}}\right) & \text{for } n > m,\, m \neq 0 \\
\dfrac{1}{\sqrt{2}}\left(g_{n,m}t\left(\dfrac{\bar{P}_{n,m+1}(t)}{u^{m+1}}\right) - h_{n,m}u^2\left(\dfrac{\bar{P}_{n,m+2}(t)}{u^{m+2}}\right)\right) & \text{for } n > m,\, m = 0
\end{cases}
\tag{F45}
$$

where

$$
g_{n,m} = \frac{2(m+1)}{\sqrt{(n-m)(n+m+1)}}
\tag{F46}
$$

$$
h_{n,m} = \sqrt{\frac{(n+m+2)(n-m-1)}{(n-m)(n+m+1)}}.
\tag{F47}
$$

The potential V is then computed using Horner's method, as described in [140]. This involves computing the terms

$$
X_C(m) = \sum_{m=0}^{N} \sum_{n=m}^{N} \left(\frac{a}{r}\right)^n \bar{C}_{n,m} \frac{\bar{P}_{n,m}(t)}{u^m}
\tag{F48}
$$

$$
X_S(m) = \sum_{m=0}^{N} \sum_{n=m}^{N} \left(\frac{a}{r}\right)^n \bar{S}_{n,m} \frac{\bar{P}_{n,m}(t)}{u^m}
\tag{F49}
$$

$$
\Omega_m = X_C(m)\cos(m\lambda) + X_S(m)\sin(m\lambda)
\tag{F50}
$$

and then evaluating the nested expression

$$
V = \frac{c}{r}\left(\left(\left(\ldots\left(\left(\Omega_N u + \Omega_{N-1}\right)u + \Omega_{N-2}\right)u\ldots\right)u + \Omega_1\right)u + \Omega_0\right).
\tag{F51}
$$

The gradient of the potential can be computed by taking the partial derivatives of (F51) in spherical coordinates, and then transforming the derivatives to Cartesian coordinates. It is desirable to maintain a form similar to (F51) for the derivatives. However, when computing the derivatives with respect to r, the $\frac{c}{r}$

term must be taken into account. The derivative with respect to r can be computed using

$$X_C^{dr}(m) = \sum_{m=0}^{N} \sum_{n=m}^{N} (n+1) \left(\frac{a}{r}\right)^n \bar{C}_{n,m} \frac{\bar{P}_{n,m}(t)}{u^m} \tag{F52}$$

$$X_S^{dr}(m) = \sum_{m=0}^{N} \sum_{n=m}^{N} (n+1) \left(\frac{a}{r}\right)^n \bar{S}_{n,m} \frac{\bar{P}_{n,m}(t)}{u^m} \tag{F53}$$

$$\Omega_m^{dr} = X_C^{dr}(m) \cos(m\lambda) + X_S^{dr}(m) \sin(m\lambda) \tag{F54}$$

to get

$$\frac{dV}{dr} = -\frac{c}{r^2} \left(((\ldots((\Omega_N^{dr} u + \Omega_{N-1}^{dr})u + \Omega_{N-2}^{dr})u \ldots)u + \Omega_1^{dr})u + \Omega_0^{dr} \right). \tag{F55}$$

Eq.(31) of [140] demonstrates that the Horner form of (F51) can be retained when evaluating derivatives of the potential with respect to spherical latitude, θ_c. Specifically, the results are written in terms of the ratio of the derivative of $\bar{P}_{n,m}(t)$ with respect to u^m. The derivative ratio is computed using

$$e_{nm} = \begin{cases} \sqrt{\dfrac{(n+m+1)(n-m)}{2}} & \text{if } m = 0 \\ \sqrt{(n+m+1)(n-m)} & \text{otherwise} \end{cases} \tag{F56}$$

$$\frac{\frac{d}{d\theta}\bar{P}_{n,m}(t)}{u^m} = m \frac{t}{u} \frac{\bar{P}_{n,m}(t)}{u^m} - e_{nm} u \frac{\bar{P}_{n,m+1}(t)}{u^{m+1}}. \tag{F57}$$

The derivative of the potential with respect to θ_c then uses

$$X_C^{d\theta}(m) = \sum_{m=0}^{N} \sum_{n=m}^{N} \left(\frac{a}{r}\right)^n \bar{C}_{n,m} \frac{\frac{d}{d\theta_c}\bar{P}_{n,m}(t)}{u^m} \tag{F58}$$

$$X_S^{d\theta}(m) = \sum_{m=0}^{N} \sum_{n=m}^{N} \left(\frac{a}{r}\right)^n \bar{S}_{n,m} \frac{\frac{d}{d\theta_c}\bar{P}_{n,m}(t)}{u^m} \tag{F59}$$

$$\Omega_m^{d\theta} = X_C^{dr}(m) \cos(m\lambda) + X_S^{dr}(m) \sin(m\lambda) \tag{F60}$$

to get

$$\frac{dV}{d\theta} = -\frac{c}{r} \left(((\ldots((\Omega_N^{d\theta} u + \Omega_{N-1}^{d\theta})u + \Omega_{N-2}^{d\theta})u \ldots)u + \Omega_1^{d\theta})u + \Omega_0^{d\theta} \right). \tag{F61}$$

On the other hand, the partial derivative with respect to longitude uses the original values of X_C and X_S in (F48) and (F49), resulting in the following expression for the derivative of the potential

$$\Omega_m^{d\lambda} = m \left(-X_C^{dr}(m) \sin(m\lambda) + X_S^{dr}(m) \cos(m\lambda) \right) \tag{F62}$$

$$\frac{dV}{d\lambda} = \frac{c}{r}\left(((\ldots((\Omega_N^{d\lambda}u+\Omega_{N-1}^{d\lambda})u+\Omega_{N-2}^{d\lambda})u\ldots)u+\Omega_1^{d\lambda})u+\Omega_0^{d\lambda}\right). \tag{F63}$$

Given the partial derivatives of the potential in spherical coordinates, the gradient of the potential may be obtained by multiplying the stacked partial derivatives by the Jacobian of the spherical coordinate transformation (this just applies the chain rule). Given the Jacobian

$$\mathbf{J} = \begin{bmatrix} \dfrac{x}{r} & \dfrac{y}{r} & \dfrac{z}{r} \\[2ex] -\dfrac{y}{x^2+y^2} & \dfrac{x}{x^2+y^2} & 0 \\[2ex] -\dfrac{xz}{r^2\sqrt{x^2+y^2}} & -\dfrac{yz}{r^2\sqrt{x^2+y^2}} & \dfrac{\sqrt{x^2+y^2}}{r^2} \end{bmatrix} \tag{F64}$$

where the first column consists of derivatives of (r,λ,θ_c) with respect to x, the second column is derivatives with respect to y and the third with respect to z (the Cartesian coordinates x, y, and z can be obtained using (3), (4), and (5)), the gradient of the potential in Cartesian coordinates is

$$\nabla V = \mathbf{J}' \begin{bmatrix} \dfrac{dV}{dr} \\[2ex] \dfrac{dV}{d\lambda} \\[2ex] \dfrac{dV}{d\theta_c} \end{bmatrix}. \tag{F65}$$

The singularity at the poles is evident in the x^2+y^2 terms in denominators in (F64).

In [140], it is noted that to avoid overflow problems when using double-precision arithmetic, the normalized Legendre polynomial ratios should be scaled, and consequently, the final estimates must be unscaled accordingly. A scale factor of $c_S = 10^{-280}$ is suggested in [140] and is what was used in the simulations in this report. The scaling is introduced by altering (F45) such that

$$\frac{\bar{P}_{0,0}(t)}{u^0} = c_S \tag{F66}$$

$$\frac{\bar{P}_{1,1}(t)}{u^1} = c_S\sqrt{3}. \tag{F67}$$

The scaling is removed from the potential using

$$V = \frac{V_{\text{scaled}}}{c_S} \tag{F68}$$

and the scaling is removed from the gradient of the potential prior to the transformation using

$$
\begin{bmatrix} \dfrac{dV}{dr} \\[2mm] \dfrac{dV}{d\lambda} \\[2mm] \dfrac{dV}{d\theta_c} \end{bmatrix} = \frac{1}{c_S} \begin{bmatrix} \dfrac{dV_{\text{scaled}}}{dr} \\[2mm] \dfrac{dV_{\text{scaled}}}{d\lambda} \\[2mm] \dfrac{dV_{\text{scaled}}}{d\theta_c} \end{bmatrix} .
\tag{F69}
$$

F.3 Synthesizing the EGM2008 Error Terms

The EGM2008 model comes with a set of standard-deviation terms $\sigma_{\bar{C}_{n,m}}$ and $\sigma_{\bar{S}_{n,m}}$ for each of its fully normalized spherical-harmonic coefficients, $\bar{C}_{n,m}$ and $\bar{S}_{n,m}$, respectively. Under the assumption that the error terms are zero-mean and the errors between the terms are not correlated,[F.4] the standard deviations can be used to obtain the variance of a gravitational-potential estimate and a covariance matrix for the gravitational-acceleration vector. There does not appear to be any method documented in the literature for using $\sigma_{\bar{C}_{n,m}}$ and $\sigma_{\bar{S}_{n,m}}$ to compute the variance of the gravitational potential or a covariance matrix for the gravitational-acceleration vector. Thus, this appendix describes how that can be done based on Pines' method of Section F.1.

Consider a random vector $\mathbf{a}$ that is the weighted sum of N independent random variables $\mathbf{v}_i$ plus constant terms $\mathbf{c}_i$,

$$
\mathbf{a} = \sum_{i=1}^{N} \mathbf{B}_i \left(\mathbf{v}_i + \mathbf{c}_i \right)
\tag{F70}
$$

where the $\mathbf{B}_i$ terms are deterministic matrices. Let the covariance matrix of $\mathbf{v}_i$ be $\mathbf{R}_i^v$. It can be shown that the covariance matrix of $\mathbf{a}$ is

$$
\mathrm{E}\left\{ (\mathbf{a} - \mathrm{E}\{\mathbf{a}\}) (\mathbf{a} - \mathrm{E}\{\mathbf{a}\})' \right\} = \sum_{i=1}^{N} \mathbf{B}_i \mathbf{R}_i^v \mathbf{B}_i'.
\tag{F71}
$$

The principle behind (F71) shall be used to determine the variance and covariance matrix of the geoid potential and gravitational-acceleration vector. In this instance, the $\mathbf{R}_i^v$ are the squares of the scalar standard-deviation terms associated with the EGM2008 model, and the $\mathbf{B}_i$ matrices are the terms in the spherical-harmonic sums that multiply the $\bar{C}_{n,m}$ and $\bar{S}_{n,m}$ terms.

To apply (F71) to the gravitational potential V expressed in (F15), one just has to substitute $\sigma_{\bar{C}_{n,m}}^2$ and $\sigma_{\bar{S}_{n,m}}^2$ for $\bar{C}_{n,m}$ and $\bar{S}_{n,m}$ and square all of the terms that come out front. The result is

$$
\sigma_V^2 \triangleq \mathrm{E}\left\{ (V - \mathrm{E}\{V\})^2 \right\}
\tag{F72a}
$$

$$
= \left(\frac{c}{r}\right)^2 \sum_{n=0}^{N} \rho_n^2 \sum_{m=0}^{n} \sigma_{\bar{C}_{n,m}}^2 \left(r_m(s,t) \bar{H}_n^m(u) \right)^2 + \left(\frac{c}{r}\right)^2 \sum_{n=0}^{N} \rho_n^2 \sum_{m=0}^{n} \sigma_{\bar{S}_{n,m}}^2 \left(i_m(s,t) \bar{H}_n^m(u) \right)^2 .
\tag{F72b}
$$

[F.4]In reality, the errors corrupting the spherical-harmonic coefficients are correlated. However, in lieu of additional information, the non-correlation assumption is necessary.

The expression for the covariance matrix of the gravitational-acceleration estimate is found in the same manner from (F22) and is

$$\mathbf{R}^{\nabla V} \triangleq E\{(\nabla V - E\{\nabla V\})(\nabla V - E\{\nabla V\})'\} \tag{F73a}$$

$$= \frac{c^2}{r^4} \begin{bmatrix} a_{11} + 2sa_{14} + s^2 a_{44} & a_{12} + sa_{24} + ta_{14} + sta_{44} & a_{13} + sa_{34} + ua_{14} + sua_{44} \\ a_{12} + sa_{24} + ta_{14} + sta_{44} & a_{22} + 2ta_{24} + t^2 a_{44} & a_{23} + ta_{34} + ua_{24} + tua_{44} \\ a_{13} + sa_{34} + ua_{14} + sua_{44} & a_{23} + ta_{34} + ua_{24} + tua_{44} & a_{33} + 2ua_{34} + u^2 a_{44} \end{bmatrix} \tag{F73b}$$

The a terms in (F73b) originate from the expected values of the quadratic products of (F23), (F24), (F25), and (F26) and are

$$a_{11} = \sum_{n=0}^{N} \rho_n^2 \sum_{m=1}^{n} m^2 \left(\sigma_{\bar{C}_{n,m}}^2 r_{m-1}^2 + \sigma_{\bar{S}_{n,m}}^2 i_{m-1}^2 \right) (\bar{H}_n^m(u))^2 \tag{F74}$$

$$a_{22} = \sum_{n=0}^{N} \rho_n^2 \sum_{m=1}^{n} m^2 \left(\sigma_{\bar{C}_{n,m}}^2 i_{m-1}^2 + \sigma_{\bar{S}_{n,m}}^2 r_{m-1}^2 \right) (\bar{H}_n^m(u))^2 \tag{F75}$$

$$a_{33} = \sum_{n=0}^{N} \rho_n^2 \sum_{m=0}^{n} \left(\sigma_{\bar{C}_{n,m}}^2 r_m^2 + \sigma_{\bar{S}_{n,m}}^2 i_m^2 \right) \left(\frac{d\bar{H}_n^m(u)}{du} \right)^2 \tag{F76}$$

$$a_{44} = \sum_{n=0}^{N} \rho_n^2 \sum_{m=0}^{n} \left(\sigma_{\bar{C}_{n,m}}^2 r_m^2 + \sigma_{\bar{S}_{n,m}}^2 i_m^2 \right) (\bar{L}_n^m)^2 \tag{F77}$$

$$a_{12} = \sum_{n=0}^{N} \rho_n^2 \sum_{m=1}^{n} m^2 \left(-\sigma_{\bar{C}_{n,m}}^2 r_{m-1} i_{m-1} + \sigma_{\bar{S}_{n,m}}^2 i_{m-1} r_{m-1} \right) (\bar{H}_n^m(u))^2 \tag{F78}$$

$$a_{13} = \sum_{n=0}^{N} \rho_n^2 \sum_{m=1}^{n} m \left(\sigma_{\bar{C}_{n,m}}^2 r_{m-1} r_m + \sigma_{\bar{S}_{n,m}}^2 i_{m-1} i_m \right) \bar{H}_n^m(u) \frac{d\bar{H}_n^m(u)}{du} \tag{F79}$$

$$a_{14} = -\sum_{n=0}^{N} \rho_n^2 \sum_{m=1}^{n} m \left(\sigma_{\bar{C}_{n,m}}^2 r_{m-1} r_m + \sigma_{\bar{S}_{n,m}}^2 i_{m-1} i_m \right) \bar{H}_n^m(u) \bar{L}_n^m \tag{F80}$$

$$a_{23} = \sum_{n=0}^{N} \rho_n^2 \sum_{m=1}^{n} m \left(-\sigma_{\bar{C}_{n,m}}^2 i_{m-1} r_m + \sigma_{\bar{S}_{n,m}}^2 r_{m-1} i_m \right) \bar{H}_n^m(u) \frac{d\bar{H}_n^m(u)}{du} \tag{F81}$$

$$a_{24} = -\sum_{n=0}^{N} \rho_n^2 \sum_{m=1}^{n} m \left(-\sigma_{\bar{C}_{n,m}}^2 i_{m-1} r_m + \sigma_{\bar{S}_{n,m}}^2 r_{m-1} i_m \right) \bar{H}_n^m(u) \bar{L}_n^m \tag{F82}$$

$$a_{34} = -\sum_{n=0}^{N} \rho_n^2 \sum_{m=0}^{n} \left(\sigma_{\bar{C}_{n,m}}^2 r_m^2 + \sigma_{\bar{S}_{n,m}}^2 i_m^2 \right) \frac{d\bar{H}_n^m(u)}{du} \bar{L}_n^m. \tag{F83}$$

Due to the squares of the terms, overflow and underflow problems when computing the variance σ_V^2 of the gravitational potential and the covariance matrix $\mathbf{R}^{\nabla V}$ of the gravitational-acceleration are more serious than when computing the potential or the gravitational-acceleration using the method of Section F.1. To minimize overflow and underflow problems, the coefficients were scaled by $c_S = 2^{-500}$. Note that when

removing the scale factor, unlike in Section F.1, one must divide by c_S^2 rather than by c_S, because all of the terms involving c_S are squared. Despite the scaling, when using double precision, overflow and underflow errors occur near the poles. For that reason, the plots in Fig. 22 of Section 5.4 only go up to $85°$. Thus, when a variance or covariance term is needed for a mission-critical application that must be valid worldwide, one must either use quadruple-precision arithmetic or rewrite the sums in a manner that avoids overflows and underflows.

F.4 The Ellipsoidal Approximation and the J_2 Model

A large number of papers related to target tracking make use of the so-called J_2 gravity model, which is described in [144, 202]. This appendix demonstrates that although the J_2 model is often called an ellipsoidal gravitational model, it is actually a truncated spherical-harmonic approximation to an ellipsoidal-gravity model. Thus, for purposes of gravitationally establishing coordinate systems, unless it is mathematically expedient to use the J_2 model, one should just use the explicit solution given in Section 4.2 of this report instead.

Combining various equations in [136, Ch. 2.7, 2.8, 2.9], a spherical-harmonic expansion of the gravity potential under the ellipsoidal approximation using only the defining parameters of the World Geodetic System 1984 (WGS 84) reference ellipsoid can be assembled yielding

$$U(\mathbf{r}) = \frac{GM}{\|\mathbf{r}\|}\left(1 + \sum_{n=1}^{\infty} C_{2n,0}\left(\frac{a}{\|\mathbf{r}\|}\right)^{2n} P_{2n}^0(\sin(\phi_c))\right) \tag{F84}$$

where

$$C_{2n,0} = (-1)^n \frac{3e^{2n}}{(2n+1)(2n+3)}\left(1 - n + \frac{5}{3}n\left(1 - \frac{2}{15}\left(\frac{m\varepsilon}{q_0}\right)\right)\right) \tag{F85}$$

$$m \triangleq \frac{\omega^2 a^3 (1-f)}{GM} \tag{F86}$$

$$q_0 = \frac{1}{2}\left(\left(1 + \frac{3}{\varepsilon^2}\right)\arctan(\varepsilon) - \frac{3}{\varepsilon}\right). \tag{F87}$$

In (F85), e is the first numerical eccentricity as defined in (24). Since the associated Legendre polynomials P in (F84) rapidly decrease as n increases, the $C_{2n,0}$ terms actually matter less as n increases despite increasing in magnitude.

The so-called J_2 approximation of the Earth's potential is an approximation to the ellipsoidal approximation of the Earth. Since an associated Legendre function, as defined in (F2), is equivalent to just a Legendre polynomial, one can use (F3b) to evaluate P_{2n}^0. Using the fact that $\sin(\phi_c) = \frac{z}{\|\mathbf{r}\|}$ when using spherical coordinates, one obtains the expression for the potential

$$U(\mathbf{r}) \approx \frac{GM}{\|\mathbf{r}\|}\left(1 + C_{2,0}\left(\frac{a}{\|\mathbf{r}\|}\right)^2 \left(\frac{3}{2}\left(\frac{z}{\|\mathbf{r}\|}\right)^2 - \frac{1}{2}\right)\right). \tag{F88}$$

Taking the gradient of the truncated potential in (F88), one obtains a convenient expression for acceleration due to gravity as a function of position:

$$
-\nabla U(\mathbf{r}) \approx \overbrace{-\frac{GM}{\|\mathbf{r}\|^2}\left(\frac{\mathbf{r}}{\|\mathbf{r}\|}\right)}^{\substack{\text{Newton's Law for a}\\\text{Point or Sphere}}} + \frac{3GMa^2C_{20}}{2\|\mathbf{r}\|^5} \overbrace{\begin{bmatrix} r_x\left(1 - 5\dfrac{r_z^2}{\|\mathbf{r}\|^2}\right) \\[2mm] r_y\left(1 - 5\dfrac{r_z^2}{\|\mathbf{r}\|^2}\right) \\[2mm] r_z\left(3 - 5\dfrac{r_z^2}{\|\mathbf{r}\|^2}\right) \end{bmatrix}}^{\text{First-Order Oblateness Correction}}. \tag{F89}
$$

This is the J_2 approximation to the Earth's gravitational acceleration used for low-precision ballistic tracking.

Appendix G

UMEYAMA'S ALGORITHM FOR GENERAL TRANSFORMATION ESTIMATION

The following algorithm from [331] can be used to estimate the rotation matrix $\mathbf{R}$, the translation vector $\mathbf{t}$, and the scaling parameter c that minimize the cost function (97) for transformations of the form $\mathbf{z} = c\mathbf{R}\tilde{\mathbf{z}} + \mathbf{t}$ given noisy sets of $\mathbf{z}$ and $\tilde{\mathbf{z}}_i$ measurements. Such general transformations are known in the field of geodesy as "Helmert transformations" [296]. The steps of the algorithm are:

1. Given $\mathbf{Z}$, and $\tilde{\mathbf{Z}}$, which are $m \times N$ matrices of the N m-dimensional column-vectors $\mathbf{z}_i$ and $\tilde{\mathbf{z}}_i$, respectively, in the two coordinate systems, stacked next to each other.

2. Compute the following mean quantities from Eqs. (34) and (35) of [331]:

$$\mu^{\tilde{z}} = \frac{1}{N}\sum_{i=1}^{N}\tilde{\mathbf{z}}_i \qquad\qquad \mu^z = \frac{1}{N}\sum_{i=1}^{N}\mathbf{z}_i \qquad\qquad \text{(G1)}$$

3. Form the matrices $\Delta^{\tilde{z}}$ and Δ^z where the ith column of each is

$$\Delta^{\tilde{z}}_{:,i} = \tilde{\mathbf{z}}_i - \mu^{\tilde{z}} \qquad\qquad \Delta^z_{:,i} = \mathbf{z}_i - \mu^z \qquad\qquad \text{(G2)}$$

   which can be implemented using `diffTZ=bsxfun(@minus,ZT,muZT);` and `diffZ=bsxfun(@minus,Z,muZ);` in Matlab.

4. Compute the product matrix from Eq. (38) of [331]:

$$\Sigma^{z,\tilde{z}} = \frac{1}{N}\Delta^z\left(\Delta^{\tilde{z}}\right)' \qquad\qquad \text{(G3)}$$

   and set r to the rank of $\Sigma^{z,\tilde{z}}$ (`r=rank(Sigma);` in Matlab).

5. Perform a singular value decomposition on $\Sigma^{z,\tilde{z}}$ to obtain unitary matrices $\mathbf{U}$ and $\mathbf{V}$ and diagonal matrix $\mathbf{D}$ such that $\Sigma^{z,\tilde{z}} = \mathbf{U}\mathbf{D}\mathbf{V}'$ where $\mathbf{S}$ is a diagonal matrix. In Matlab, this can be done using the command `[U,D,V]=svd(Sigma);`.

6. Create the matrix $\mathbf{S} = \mathbf{I}_{m,m}$, where $\mathbf{I}_{m,m}$ is an $m \times m$ identity matrix.

7. If $r = m - 1$ and the product of the determinants of $\mathbf{U}$ and $\mathbf{V}$ is less than zero (use the comparison `det(U)*det(V)<0` in Matlab), or if $r > m - 1$ and the determinant of $\mathbf{A}$ is less than zero (`det(A)<0` in Matlab), then set $\mathbf{S}_{m,m} = -1$ (the element in the last row and column of $\mathbf{S}$ should be set to -1). This implements Eqs. (43) and (39) in [331].

8. The rotation matrix is given by

$$\mathbf{R} = \mathbf{USV}';\tag{G4}$$

This implements Eq. (40) in [331].

9. If a scaling parameter is desired as a return value, then set

$$c = \frac{1}{\sigma_{z,\tilde{z}}^2}\mathrm{Tr}(\mathbf{DS})\tag{G5}$$

which implements Eq. 42 of [331], and where Tr is the matrix-trace operation (sum of the diagonal elements) and $\sigma_{z,\tilde{z}}^2$ is given by

$$\sigma_{\tilde{z}}^2 = \frac{1}{N}\sum_{i=1}^{N}\|\tilde{\mathbf{z}}_i - \mu^{\tilde{z}}\|^2\tag{G6}$$

which implements Eq. (36) of [331] and which can be implemented using
`sigmaTZ2=(1/N)*sum(sum(diffTZ.*diffTZ));` in Matlab.

If a scaling parameter is not desired, then just set $c = 1$.

10. The translation vector is given by

$$\mathbf{t} = \mu^z - c\mathbf{R}\mu^{\tilde{z}}.\tag{G7}$$

This implements Eq. (41) of [331].

Appendix H

A DERIVATION OF THE SCORE FUNCTION FOR STAR-TO-CATALOG ASSIGNMENT

This appendix derives the marginal cost increment for assigning a celestial measurement to a star (or planetary body) in a catalog. The derivation is similar to those in [22, Ch. 6.3,7.5] and [21] for target tracking, except care is taken to allow the false alarms to have a nonuniform distribution.

Define θ as a particular hypothesis of celestial observations to catalogued stars at a particular time, $Z = \{\mathbf{z}_1, \mathbf{z}_2, \ldots, \mathbf{z}_M\}$ is the set of all observations at the given time, m is the cardinality of Z, and I_p is all prior hypotheses and information that might aid the association. One can write

$$\Pr\{\theta, I_p | Z\} = \Pr\{\theta, I_p | Z, m\} \tag{H1a}$$

$$= \frac{1}{c_1} p(Z|m, \theta, I_p) \Pr\{\theta, I_p | m\} \tag{H1b}$$

$$= \frac{1}{c_1} p(Z|m, \theta, I_p) \Pr\{\theta | m, I_p\} \Pr\{I_p | m\} \tag{H1c}$$

$$= \frac{1}{c_1} p(Z|m, \theta, I_p) \Pr\{\theta | m, I_p\} \Pr\{I_p\} \tag{H1d}$$

where in (H1a), the extra conditioning on m added no new information, since it is already in Z; the transition to (H1b) used Bayes' theorem, where c_1 is a normalization constant; the transition to (H1c) comes from the Kolmogorov definition of conditional probability; and the transition to (H1d) is from assuming that the prior information is independent of the number of observations in the current set. Such an assumption is reasonable if the prior information is, for example, the information in the star catalog.

Let the function $\phi(\theta)$ provide the number of false measurements in the catalog-to-star association hypothesis θ. The prior information in I_p is assumed to provide information on T stars. The function $\xi_t(\theta)$ returns the observation that is associated with the tth catalogued star in the catalog under the hypothesis θ; if the star is hypothesized as not being seen, then $\xi_t(\theta)$ returns the empty set $\oslash$. The function $\bar{\xi}(\theta)$ returns all observations that are from false alarms and $\bar{\bar{\xi}}_i(\theta)$ returns the ith false alarm in the assignment. The probability density function (PDF) that is the first term of (H1d) can thus be written

$$p(Z|m, \theta, I_p) = p_c\left(\bar{\xi}(\theta)|m, \theta, I_p\right) \prod_{i=1}^{T} p_t\left(\xi_t(\theta)|m, \theta, I_p\right) \tag{H2}$$

using the law of total probability, where it is assumed that all observations are conditionally independent. This means, for example, that there are no unresolved closely spaced stars, as might occur with double stars. The PDF p_c is the PDF of the clutter measurements and p_t the PDF of the tth target. p_t can be written as

$$p_t\left(\xi_t(\theta)|m, \theta, I_p\right) = \begin{cases} 1 & \text{if } \xi_t(\theta) = \oslash \\ \tilde{p}_t\left(\xi_t(\theta)|m, \theta, I_p\right) & \text{otherwise} \end{cases} \tag{H3}$$

where $\tilde{p}_t\left(\xi_t(\theta)|m,\theta,I_p\right)$ is the PDF of the assigned measurement given the catalog entry. Under the assumption that the false alarms are independent of each other, one can also write

$$p_c\left(\bar{\bar{\xi}}(\theta)|m,\theta,I_p\right) = \prod_{i=1}^{\phi(\theta)} p_c\left(\bar{\bar{\xi}}_i(\theta)|m,\theta,I_p\right). \tag{H4}$$

Define $\delta(\theta)$ as a set of Boolean detection indicators for the association hypothesis θ such that $\delta_t(\theta)=1$ if star t was observed, then the second term of (H1d) can be written

$$\Pr\{\theta|m,I_p\} = \Pr\{\theta|m,I_p,\delta(\theta),\phi(\theta)\}\Pr\{\delta(\theta),\phi(\theta)|m,I_p\} \tag{H5}$$

using the law of total probability. The first term of H5 is the probability of a particular association of measurements to targets given that one knows which stars have been observed and how many measurements are present. However, since the actual measurements are not available, one can only assume that all possible observation-to-star assignment hypotheses are equally likely (the prior information I_p should not be informative), and thus the first term can be found by counting

$$\Pr\{\theta|m,I_p,\delta(\theta),\phi(\theta)\} = \left(\overbrace{\binom{m}{m-\phi(\theta)}}^{\substack{\text{Choose measurements}\\\text{originating from targets}}}\overbrace{(m-\phi(\theta))!}^{\substack{\text{Assign chosen measurements}\\\text{to targets}}}\right)^{-1} \tag{H6a}$$

$$=\frac{\phi(\theta)!}{m!} \tag{H6b}$$

where it is assumed that $m-\phi(\theta)\geqslant 0$, i.e., that the hypothesis in question is valid.

Suppressing the argument (θ) in δ (Boolean indicators for star detection) and ϕ (number of non-star detections) for brevity, the second term of (H5) can be decomposed as

$$\Pr\{\delta,\phi|m,I_p\} = \Pr\{\delta|m,\phi,I_p\}\Pr\{\phi|m,I_p\} \tag{H7a}$$

$$=\left(\frac{\Pr\{\delta\bigcap(m-\phi)\text{ targets seen}|\phi,I_p\}}{\Pr\{(m(k)-\phi)\text{ targets seen}|\phi,I_p\}}\right)\left(\frac{\Pr\{m|\phi,I_p\}\Pr\{\phi\}}{\Pr\{m\}}\right) \tag{H7b}$$

$$=\left(\frac{\prod_{t=1}^{T}(P_D^t)^{\delta_t}(1-P_D^t)^{1-\delta_t}}{\Pr\{(m(k)-\phi)\text{ targets seen}|\phi,I_p\}}\right)\left(\frac{\Pr\{(m(k)-\phi)\text{ targets seen}|\phi,I_p\}\Pr\{\phi\}}{\Pr\{m\}}\right) \tag{H7c}$$

$$=\frac{\Pr\{\phi\}}{\Pr\{m\}}\prod_{t=1}^{T}(P_D^t)^{\delta_t}(1-P_D^t)^{1-\delta_t} \tag{H7d}$$

where (H7a) comes from Kolmogorov's definition of conditional probability; (H7b) uses Bayes' rule for the term on the right and Kolmogorov's definition of conditional probability for the term on the left; in (H7c), the prior information I_p is assumed to provide information on the prior probability of detection of each of

the stars (assumed independent), where P_D^t is the detection probability of star t for the term on the left, and for the term on the right the substitution is equivalent. Finally, in (H7d), division was performed.

Combining (H7d) with (H6b), one obtains

$$\Pr\{\theta|m,I_p\} = \frac{\phi!}{m!}\frac{\Pr\{\phi\}}{\Pr\{m\}}\prod_{t=1}^{T}\left(P_D^t\right)^{\delta_t}(1-P_D^t)^{1-\delta_t}. \tag{H8}$$

Substituting (H8), (H2), and (H4) into (H1d), one obtains

$$\Pr\{\theta,I_p|Z\} = \frac{\phi!\Pr\{\phi\}}{c_2}\prod_{i=1}^{\phi}p_c\left(\bar{\xi}_i|m,\theta,I_p\right)\prod_{t=1}^{T}\left(P_D^t p_t\left(\xi_t|m,\theta,I_p\right)\right)^{\delta_t}(1-P_D^t)^{1-\delta_t}\Pr\{I_p\} \tag{H9}$$

where the $1/(m!\Pr\{m\})$ term was absorbed into the normalizing constant to get a new normalizing constant c_2. The term $p_t\left(\xi_t|m,\theta,I_p\right)$ was put into the exponent with P_D^t, because from (H3), it can be seen that such a move does not change the result. Eq.(H9) can be rewritten such that the product of the clutter PDFs is over all measurements, dividing out the clutter PDFs for measurements that are assigned to targets. This can be written

$$\Pr\{\theta,I_p|Z\} = \frac{\phi!\Pr\{\phi\}}{c_3}\Pr\{I_p\}\prod_{t=1}^{T}\left(P_D^t\frac{p_t\left(\xi_t|m,\theta,I_p\right)}{p_c\left(\xi_t|m,\theta,I_p\right)}\right)^{\delta_t}(1-P_D^t)^{1-\delta_t} \tag{H10}$$

where the product over all measurements was absorbed into the normalizing constant.

An important step in formulating the problem of finding the optimal θ is getting rid of the $\phi!\Pr\{\phi\}$ term in (H10). These terms can be eliminated by assuming a constant false-alarm rate in the area of interest. If detection is performed using a constant false alarm rate (CFAR) algorithm such as those considered in [104], under the assumption that false alarms are independent of the star locations,[H.1] each false alarm in a particular cell can be considered to be a Bernoulli random variable with some probability of false alarm of P_{FA}. Considering N bins with the same false-alarm probability P_{FA}, the probability of seeing n false alarms (over a particular fixed grid of points) is given by the binomial distribution

$$\Pr\{n\} = \binom{N}{n}P_{FA}^n(1-P_{FA})^{N-n} \tag{H11}$$

with mean

$$\tilde{\lambda} \triangleq NP_{FA}. \tag{H12}$$

To simplify the mathematics of target tracking, and in this case to simplify the cost function of the star-to-catalog association, the binomial distribution is generally replaced with a Poisson approximation as done

---

[H.1]Target state dependent false alarms can be considered part of the target measurement model itself. Such issues arise, for example, when tracking targets with wakes, such as boats or objects reentering the atmosphere. However, such issues are unlikely to arise when observing stars. More on using wake measurements in single-scan tracking algorithms is given in [37, 278].

in [22, Ch. 2.5]. Suppose that the volume under consideration is held constant while the number of bins N is increased by decreasing the size of each of the bins and at the same time the probability of false alarm decreases such that the mean number of false alarms $\tilde{\lambda}$ remains constant (though the maximum possible number of false alarms changes since N changes). As derived in [64, Ch. 5.4], the limit of such a binomial distribution as $N \to \infty$ and $P_{FA} \to 0$ is the Poisson distribution

$$\Pr\{\phi\} = e^{-\tilde{\lambda}} \frac{\tilde{\lambda}^{\phi}}{\phi!}. \tag{H13}$$

The constant $\tilde{\lambda}$ is the mean number of false alarms over the region under consideration. If the size of the region under consideration changes, then $\tilde{\lambda}$ changes. Thus, it makes sense to factor $\tilde{\lambda}$ into a constant times the volume of the detection region, $\tilde{\lambda} = \lambda_c V$. The units of λ_c are the inverse units of the volume in which detections are taken. For example, if detections are taken on a grid of azimuth and elevation points but the measurements also provide additional information, such as the intensity of wavelength of the star, then λ_c will be in units of inverse azimuth-elevation (inverse radians-squared) and V will have units of azimuth-elevation. Substituting (H13) into (H10), one obtains

$$\Pr\{\theta, I_p | Z\} = \frac{1}{c_4} \Pr\{I_p\} \prod_{t=1}^{T} \left(P_D^t \frac{p_t\left(\xi_t | m, \theta, I_p\right)}{(\lambda_c V) p_c\left(\xi_t | m, \theta, I_p\right)} \right)^{\delta_t} (1 - P_D^t)^{1 - \delta_t} \tag{H14}$$

where the constant term $e^{-\tilde{\lambda}}$ was absorbed into the normalizing constant, the $\tilde{\lambda}^{\phi}$ term was expressed as $\tilde{\lambda}^m / \tilde{\lambda}^{m-\phi}$, and the $\tilde{\lambda}^m$ term was absorbed into the normalizing constant as well. Additionally, $\lambda_c V$ has been substituted for $\tilde{\lambda}$.

The 2D-assignment problem seeks to determine the assignment θ with the highest probability for a given hypothesis of prior information I_p. This can be done by maximizing the logarithm of (H14) and discarding constant terms. Let Λ be the cost function. Taking the natural logarithm of (H10) and discarding constant terms, one has

$$\Lambda = \sum_{t=1}^{T} \left(\delta_t \ln\left(P_D^t \frac{p_t\left(\xi_t | m, \theta, I_p\right)}{(\lambda_c V) p_c\left(\xi_t | m, \theta, I_p\right)} \right) + (1 - \delta_t) \ln(1 - P_D^t) \right). \tag{H15}$$

Thus, assuming that the PDF of measurement i assigned to catalogued entry t is independent of the assignments of the other measurements and the number of measurements, the marginal added contribution to the cost function from assigning target t to measurement i, $\Delta\Lambda_{i,j}$, where measurement index 0 is reserved for a missed detection, is

$$\Delta\Lambda_{t,i} = \begin{cases} \ln\left(P_D^t \dfrac{p_t\left(\mathbf{z}_i | I_p\right)}{(\lambda_c V) p_c\left(\mathbf{z}_i | I_p\right)} \right) & \text{if } i \neq 0 \\ \ln(1 - P_D^t) & \text{if } i = 0 \end{cases} \tag{H16}$$

where $\mathbf{z}_i$ is the ith measurement and the conditioning on θ, because the assignment of other measurements does not change the PDF. Thus, the problem of finding the optimal θ becomes the 2D-assignment problem discussed in Section 8.3, where one strives to maximize the sum of the $\Delta\Lambda$ terms.

However, (H16) is not the cost function used in Section 8.3. Rather, a further simplification is performed to eliminate the direct dependence on the viewing region size V. If a CFAR algorithm is used for detection, then a reasonable additional level of simplification to (H16) comes from assuming that the components of the false-alarm measurements within the measurement domain are uniformly distributed. To make use of this information, the clutter measurement $\bar{\xi}_i$ can be split into two halves: the first half $\bar{\xi}_i^d$ consists of the components used for detection; the second half $\bar{\xi}_i^f$ consists of additional components of the measurement. Thus, one can write

$$
p_c\left(\bar{\xi}_i | I_p\right) = \frac{1}{V} p_c^f\left(\bar{\xi}_i^f \Big| I_p\right)
\tag{H17}
$$

where p_c^f is the PDF of the components of the measurement that do not play a role in detection. Incorporating the changes into (H14) and then taking the logarithm, discarding constant terms, and extracting the marginal change due to an assignment to a target, (H16) becomes

$$
\Delta\Lambda_{t,i} =
\begin{cases}
\ln\left(P_D^t \dfrac{p_t\left(\mathbf{z}_i | I_p\right)}{\lambda_c p_c^f\left(\mathbf{z}_i^f | I_p\right)} \right) & \text{if } i \neq 0 \\[2ex]
\ln(1 - P_D^t) & \text{if } i = 0
\end{cases}
\tag{H18}
$$

where $\mathbf{z}_i^f$ is just the components of the measurement that do not play a role in detection. Due to the presence of the p_c^f term, if the false-alarm components are uniformly distributed over a particular parameter space, the volume of that parameter space will appear in (H18). On the other hand, the p_c^f term disappears if detection is performed over the entire parameter space, thus explaining the cost function used in (116) in Section 8.3. Note that if the clutter distribution in the viewing region is truly non-uniform, but one wanted to use (H18), because of its lack of a V term, an *ad hoc* solution is to make λ nonuniform and use the values of λ at the measurement locations.

This page
intentionally
left blank

Appendix I

GETTING A DIRECTION VECTOR FROM THE SPICE TOOLKIT

The National Aeronautics and Space Administration's (NASA's) Spacecraft Planet Instrument C-matrix Events (SPICE) toolkit can read the DE430 ephemerides. However, it does not provide direction vectors for the locations of the planets and moons with respect to an observer on the surface of the Earth, though it does provide direction vectors with respect to the center of the Earth. Additionally, though it can provide a correction for aberration (an angular measurement bias arising due to special relativity), it uses a Newtonian approximation rather than the special relativistic formula. This appendix describes how to obtain a direction vector for an observer at a location offset from the center of the Earth using the SPICE toolkit and the aberration correction function from the International Astronomical Union's (IAU's) Standards of Fundamental Astronomy (SOFA) library, which includes an approximate general relativistic correction for the mass of the Sun.

The SPICE toolkit reads ephemerides at a time in barycentric dynamical time (TDB). In practice, however, an observer's clock will be in terms of terrestrial time (TT) or something similar. The strict conversion from TT to TDB is actually based on the ephemerides themselves. However, the routine for converting from universal coordinated time (UTC) or TT in the SPICE toolkit uses an approximation, as it does not require that an ephemeris kernel be loaded. Thus, for most purposes, the approximate conversion routines in the IAU's SOFA library should be just as accurate. The relevant routines for the conversion are `iauDtdb` and `iauTttdb`. Given the time of the observer, one must consider that (ignoring refraction and aberration) the apparent location of the object is not its current location, but depends on when light left the object (light-time). Strictly speaking, general relativistic raytracing (including atmospheric refraction) must be performed to obtain the correct light-time correction. Raytracing including general relativity and isotropic refraction is considered in [255], but is not used in this report. Rather, the light-time correction here is similar to those described in the references in Table 1.

In Matlab, the code for obtaining the "apparent" location of a celestial body in meters, in this case the Moon, with respect to the center of the Earth, including a light-time correction is

```
LTEst=0;%The estimated light-time delay. Assume that it will converge in three
        %iterations.
for curIter=1:3
    state = cspice_spkezr('MOON',...
                          TDBSec-LTEst,...
                          'J2000', ...
                          'NONE', ...
                          'EARTH');

%Convert the position components to meters and find the position with respect to the
%observer.
    GCRSPos=state(1:3)*1e3-obsPosGeoGCRS;
%Update the light-time estimate with the new position.
    LTEst=norm(GCRSPos)/c;
end
```

where `c` is the speed of light, `TDBSec` is the time in TDB given in seconds past J2000.0 (which has a Julian date of precisely 2451545.0 TDB), and `obsPosGeoGCRS` is a 3×1 position vector of the location of the observer with respect to the center of the Earth in the ICRS. Note that the SPICE toolkit calls axes that are aligned with the International Celestial References System (ICRS) (i.e., the Barycentric Celestial Reference System [BCRS] and the Geocentric Celestial Reference System [GCRS]) the J2000.0 dynamical coordinate system when using DE4xx ephemerides as documented in various data files, such as `http: //naif.jpl.nasa.gov/pub/naif/generic_kernels/fk/satellites/moon_080317.tf`. However, the SPICE toolkit sometimes refers to the actual J2000.0 dynamical coordinate system, which, as seen in Fig. 6, is rotated from the GCRS. The vector `GCRSPos` is the location of the Moon with respect to the center of the Earth aligned with the ICRS/GCRS celestial coordinate axes. The inconsistency in notation used in the library can be very confusing.

Next, a special relativistic aberration correction must be performed. The cause and significance of aberration are described in Appendix J. An aberration correction can be performed using the `iauAb` function from the IAU's SOFA library, which also includes an approximate correction for general relativistic effects due to the mass of the Sun based on the method described in [184]. As documented in the source code of the `iauAb` function, general relativity contributes up to 0.4 microarcseconds of bending to the ray. The function requires the distance from the Sun to the observer, the velocity of the object being observed, and the velocity vector of the observer. The distance from the Sun to the observer can be obtained using the `cspice_spkezr` function and adding in the offset of the observer from the center of the Earth. The velocity vector of the object being observed and of the Earth can also be obtained using the `cspice_spkezr` function. However, the velocity vector of the observer in BCRS coordinates $\mathbf{v}_{\text{obs}}^{\text{BCRS}}$ requires the addition of the observer's velocity with respect to the center of the Earth $\mathbf{v}_{\text{obs}}^{\text{Earth}}$ with the velocity of the Earth $\mathbf{v}_{\text{Earth}}^{\text{BCRS}}$ itself. Ignoring special relativity theory, this addition can be done by just adding the vectors as

$$\mathbf{v}_{\text{obs}}^{\text{BCRS}} = \mathbf{v}_{\text{obs}}^{\text{Earth}} + \mathbf{v}_{\text{Earth}}^{\text{BCRS}}. \tag{I1}$$

However, if one desires the highest theoretical precision, then the addition must occur accounting for special relativity theory. The formula for adding velocities under special relativity theory is derived in vector form in [206, Ch. 1.4]. If $\mathbf{v}$ is the velocity of a reference frame with respect to the global, inertial reference frame, and $\mathbf{u}$ is the velocity of an object in that reference frame, then the velocity of the object in the global frame $\mathbf{u}^{\text{global}}$ is

$$\mathbf{u}^{\text{global}} = \frac{\mathbf{v} + \mathbf{u} + \left(\sqrt{1 - \frac{\|\mathbf{v}\|^2}{c^2}} - 1 \right) \left(\mathbf{u} - \left(\frac{\mathbf{u} \cdot \mathbf{v}}{\|\mathbf{v}\|^2} \right) \mathbf{v} \right)}{1 + \frac{\mathbf{v} \cdot \mathbf{u}}{c^2}}. \tag{I2}$$

In this case, $\mathbf{v}$ is $\mathbf{v}_{\text{Earth}}^{\text{BCRS}}$ and $\mathbf{u}$ is $\mathbf{v}_{\text{obs}}^{\text{Earth}}$.

After accounting for special relativistic aberration, atmospheric refraction must be taken into account. If one desires the highest precision (without resorting to full general relativistic ray tracing), then Fresnel drag should probably also be taken into account. Armand Hippolyte Louis Fizeau observed that the velocity of light passing through a moving container of water is affected by the velocity of the container (the light is dragged along) [94]. The same is true with light passing through the atmosphere, since the Earth is rotating. An explanation of the effect is given in [195]. The effect is named after Fresnel to reflect the fact that Fresnel came up with a low-accuracy approximation based on an outdated theory of substances partially dragging

a hypothesized luminiferous æther along with them in [99]. In the present report, Fresnel drag is ignored. The errors introduced by ignoring Fresnel drag are probably significantly smaller than the errors introduced by using a low-fidelity atmospheric refraction model. For the plots of planets in this report, the low-fidelity numerical ray-tracing algorithm of [138] is used in Fig. 14 and the refraction correction in the IAU's SOFA library (used indirectly through their functions and copied directly out of the source code of `iauAtioq`) the rest of the time.

This page
intentionally
left blank

Appendix J

QUANTIFYING ERRORS DUE TO ABERRATION

Bradley's aberration, which is more commonly known as stellar aberration and which could be termed special relativistic aberration, occurs when relating terrestrial coordinate systems to celestial coordinate systems. It has nothing to do with aberrations that occur in lens design, which are mentioned in [179, Ch. 3]. Bradley's aberration of stars was first described by James Bradley in the 1700s [35]. Bradley's aberration can be explained using the special relativistic velocity addition formula in (I2). Bradley's aberration arises from the fact that the Earth orbits the Sun and the directions of stars are recorded in a heliocentric coordinate system, in modern days, in the Barycentric Celestial Reference System (BCRS). At different times of the year, the Earth moves at a different velocity with respect to the axes of the global celestial coordinate system.

If an observer is moving at a velocity $\mathbf{v}$ with respect to a global coordinate system, and measures an object moving at velocity $\mathbf{v}_p$, then the velocity of the object in the global inertial coordinate system $\mathbf{v}_i$ is given by manipulating (I2) to get

$$\mathbf{v}_i = \frac{\mathbf{v}_p + (\gamma(\|\mathbf{v}\|) - 1)\left(\frac{\mathbf{v}\mathbf{v}^T}{\|\mathbf{v}\|^2}\right)\mathbf{v}_p + \gamma(\|\mathbf{v}\|)\mathbf{v}}{\gamma(\|\mathbf{v}\|)\left(1 + \frac{\mathbf{v}^T\mathbf{v}_p}{c^2}\right)}. \tag{J1}$$

If the moving observer emitted light in direction of the unit vector $\mathbf{u}_p$, then one would use $\mathbf{v}_p = c\mathbf{u}_p$ and $\mathbf{v}_i = c\mathbf{u}_i$ for the velocities in (J1) and find the stationary observer perceiving the emitted light focusing in the direction of motion of the moving observer (the headlight effect). However, for *measured* directions, for light emanating in direction $\mathbf{u}_p$, the light *arrives* with velocity $\mathbf{v}_p = -c\mathbf{u}_p$. Similarly, in the inertial coordinate system, the equivalent to $\mathbf{u}_p$ is $\mathbf{u}_i$, so $\mathbf{v}_i = -c\mathbf{u}_i$. Thus, using (J1), the directions measured in the moving coordinate system map to directions in the stationary coordinate system as illustrated in Fig. J1. The stationary observer would perceive the moving observer's measurements as bunched up *behind* him. The faster the moving observer goes, the more it seems to him that everything bunches up in *front* of him.

Basic corrections for Bradley's aberration based on (J1) are used in the U.S. Navy's astronomical almanac [70, Ch. B]. Note that stellar aberration is only noticeable due to *changes* in velocity of the Earthbound observer with respect to a global inertial coordinate system (otherwise the angular bias is constant) and has nothing to do with the motion of the stars itself (beyond how they might be used to define the coordinate system) [78].

Correcting for Bradley's aberration is important for high-precision tracking of objects in space. The maximum angular bias due to Bradley's aberration of a satellite orbiting in a circular orbit at a particular altitude (the speed of the satellite with respect to the Earth-centered inertial [ECI] coordinate system as a function of altitude is given in (C2) in Appendix C), ignoring refraction and other gravitational effects, when the global coordinate system is an ECI system, such as the Geocentric Celestial Reference System (GCRS), is shown in Fig. J2. The maximum bias in angular measurements occurs when the motion of the satellite in the ECI coordinate system, $\mathbf{v}$, is orthogonal to $\mathbf{v}_p = c\mathbf{u}_p$, where $\mathbf{u}_p$ is the directional of the thing being

137

(a) Stationary Observer   (b) Directions of a Fast Moving Observer Converted into the
   Stationary Coordinate System
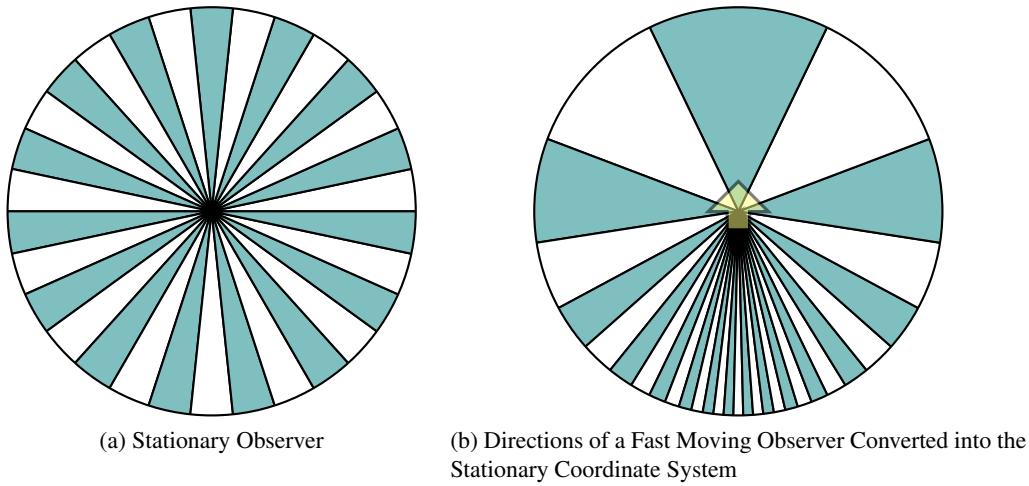
Fig. J1: In (a), 12° angular slices are marked with alternating colors. An inertial observer stationary with respect to a global coordinate system would interpret angles uniformly in all directions, as illustrated. In (b), the stationary observer would find that angles measured by a moving observer traveling at $0.9c$ in the direction of the arrow (as seen by the stationary observer) are biased. The moving observer's measured directions seen in the stationary observer's coordinate system bunch up *behind* the observer, meaning that the moving observer accelerating to a constant velocity would see light bunch up in *front* of him.

observed in the satellite's relativistically warped coordinate system. Thus Bradley's aberration can induce significant angular biases when performing detection from a satellite.
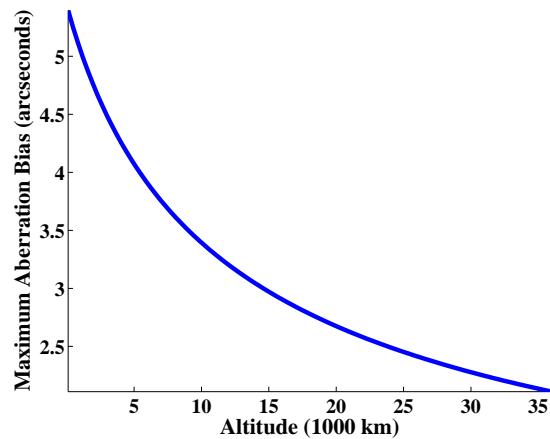
Fig. J2: The maximum angular bias due to special relativistic aberration of measurements in a satellite's local coordinate system with respect to an ECI coordinate system (such as the GCRS) as a function of the altitude of the satellite (beyond the equatorial radius of the Earth) ignoring atmospheric refraction and general relativistic effects. The speed of the satellite, which is the determining factor for the maximum bias magnitude, is determined assuming the satellite is in an ideal circular orbit.

This page
intentionally
left blank

Appendix K

WHY THE FISHER DISTRIBUTION IS BAD FOR HIGH-PRECISION MEASUREMENTS

In Section 8.3, the Fisher distribution is not chosen to represent the uncertainty in direction measurements of stars. This appendix demonstrates the source of numerical precision problems that can arise when using the Fisher distribution as well as many similar distributions of the unit sphere.

If the direction measurement is given in terms of azimuth and elevation, then

$$\mathbf{u}(\mathbf{z}_i) = \begin{bmatrix} \cos(\lambda^i)\cos(\theta_c^i) \\ \sin(\lambda^i)\cos(\theta_c^i) \\ \sin(\theta_c^i) \end{bmatrix}. \tag{K1}$$

To choose a reasonable value of κ in the Fisher distribution (Eq. (117)) in Section 8.3.1, it can be seen that just considering the cut of $\theta_c^i = 0$ and $\theta_c^t = 0$, the Fisher distribution in (117) has the same form as the von Mises probability density function (PDF), which is presented in [211, Ch. 3.5.4], in λ with a von Mises concentration parameter of $\kappa_{vm} = \kappa$ and a different normalization constant. Thus, marginalizing on knowing the elevation is zero, the Fisher PDF reduces to the von Mises PDF. The mean resultant length of the von Mises PDF is [211, Ch. 3.5.4]

$$\rho_{vm} = \frac{I_1(\kappa_{vm})}{I_0(\kappa_{vm})} \tag{K2}$$

where $I_k(x)$ is a modified Bessel function of the first kind. Methods for computing the ratio in (K2) in a numerically stable manner are given in [108].[K.1] The von Mises PDF is a good approximation to a normal distribution wrapped to the unit circle when both have the same mean resultant length. The mean resultant length of the wrapped normal distribution is [211, Ch. 3.5.7]

$$\rho_{normal} = e^{-\frac{\sigma_{normal}^2}{2}} \tag{K3}$$

where σ_{normal} is the standard deviation of the normal distribution prior to wrapping, in radians. Thus, for precise measurements, if it seems that if (ignoring wrapping problems) the mean-squared error of a detection appears to be about σ_{normal}^2 radians, then one can approximate the value of κ in the Fisher distribution as the numeric solution to

$$e^{-\frac{\sigma_{normal}^2}{2}} \approx \frac{I_1(\kappa)}{I_0(\kappa)}. \tag{K4}$$

[K.1]Special techniques are needed to compute the ratio due to the size of the arguments. For example, for $\kappa = 3283$, $I_1(\kappa) \approx 5.81 \times 10^{1423}$, which is too large to fit in a standard double-precision floating-point register [149]. Much larger values of κ are needed for measurement errors less than $1°$.

Here, (K4) is solved using the `FindRoot` command on the difference of both sides of (K4) in Mathematica to get a reasonable value of κ. For $\sigma = 0.2°$ (3.49 mrad), $\kappa = 82070.7$. For $\sigma = 0.02°$ (0.349 mrad), $\kappa = 8.20702 \times 10^6$. Thus, the value of κ increases rapidly. This can lead to numerical stability problems when simulating the distribution and when performing likelihood maximization. For a precision of $20 \,\mu$rad, as considered in Section 8.3, κ cannot be numerically solved in Mathematica using machine-precision routines.

Appendix L

DRAWING THE OUTLINE OF A CELESTIAL OBJECT

To draw the outline of the image of a planet or other celestial object in an observer's field of view, one must find the coordinates of the outer points of the object. The outer points that the observer sees are those that are in planes orthogonal to the line of sight of the observer to the object. Using a spherical object model, all of the outer points are located in a single plane that passes through the sphere and the points are a fixed radius r from the center of the sphere. This appendix tells how to find the points.

Let $\mathbf{u}_o$ be a unit vector from the observer to the object. One can find a rotation matrix $\mathbf{R}$ that rotates the observer's local coordinate axes such that the z-axis points in the direction of $\mathbf{u}_o$. There is no unique solution to the rotation, so the shortest-distance rotation from Appendix C of [52] is used. The rotation matrix is

$$\mathbf{R} = \begin{bmatrix} q_0^2 + q_1^2 - q_2^2 - q_3^2 & 2(q_1 q_2 + q_0 q_3) & 2(q_1 q_3 - q_0 q_2) \\ 2(q_1 q_2 - q_0 q_3) & q_0^2 - q_1^2 + q_2^2 - q_3^2 & 2(q_2 q_3 + q_0 q_1) \\ 2(q_1 q_3 + q_0 q_2) & 2(q_2 q_3 - q_0 q_1) & q_0^2 - q_1^2 - q_2^2 + q_3^2 \end{bmatrix}. \tag{L1}$$

where $\mathbf{q} = [q_0, q_1, q_2, q_3]'$ is given by

$$\mathbf{q} = \left[\sqrt{1-s^2}, -s\frac{\mu_y}{\sqrt{\mu_x^2 + \mu_y^2}}, s\frac{\mu_x}{\sqrt{\mu_x^2 + \mu_y^2}}, 0 \right]' \tag{L2}$$

where $\mu = [\mu_x, \mu_y, \mu_z]'$ and

$$s = -\sqrt{\frac{1}{2}(1 - u_z)}. \tag{L3}$$

The values $[\mathbf{u}_1, \mathbf{u}_2, \mathbf{u}_3] = \mathbf{R}\mathbf{I}_{3,3}$ form an orthogonal basis such that $\mathbf{u}_3 = \mathbf{u}_o$, the direction of the object. The outer points of the spherical object seen by the observer form a circle in the plane defined by $\mathbf{u}_1, \mathbf{u}_2$. If the object is a distance of r away, an expression for a point $\mathbf{r}$ on the outside of the spherical celestial body, whose radius is R is

$$\mathbf{r} = r\mathbf{u}_3 + R\cos(\theta)\mathbf{u}_1 + R\sin(\theta)\mathbf{u}_2 \tag{L4}$$

for some value of θ. Eq.(L4) is just the equation for a circle in the plane. Thus, by varying θ, one can find all of the points on the outside of the object that when plotted form the outline of the object as seen by an observer.

This page
intentionally
left blank

Appendix M

ACRONYMS AND ABBREVIATIONS

General Acronyms and Abbreviations

2D	Two-Dimensional		ECOSOC	UN Economic and Social Council
3D	Three-Dimensional		EGM2008	Earth Gravitation Model
4D	Four-Dimensional		EMM 2010	Enhanced Magnetic Model
ADS-B	Automatic Dependent Surveillance-Broadcast		ENU	East-North-Up
AIS	Automatic Identification System		EOP	Earth Orientation Parameters
API	Application Programming Interface		EPSG	European Petroleum Survey Group
BCRS	Barycentric Celestial Reference System		ET	Ephemeris Time
BDS	BeiDou Satellite Navigation System		ETRF89	European Terrestrial Reference Frame 1989
BDT	BeiDou Time		ETRS	European Terrestrial Reference System
BGGM	British Geological Survey Global Geomagnetic Model		FAA	Federal Aviation Administration
BGI	International Gravimetric Bureau		FAGS	Federation of Astronomical and Geophysical Data Analysis Services
BGS	British Geological Survey			
BIPM	International Bureau of Weights and Measures		FFT	Fast-Fourier Transform
			G8	Group of 8 Nations
CCD	Charge-Coupled Device		GAGAN	GPS Aided GEO Augmented Navigation System (India)
CCIR	International Radio Consultative Committee			
CCTF	Consultative Committee for Time and Frequency		GAST	Greenwich Apparent Sidereal Time
			GCRS	Geocentric Celestial Reference System
CDS	Strasbourg Astronomical Data Center		GDGPS	Global Differential GPS
CFAR	Constant False Alarm Rate		GEO	Group on Earth Observations
CGCS2000	Chinese Geodetic Coordinate System		GEOSS	Global Earth Observation System of Systems
CGPM	General Conference on Weights and Measures			
			GEOTRANS	Geographic Translator
CIO	Celestial Intermediate Origin		GGFC	Global Geophysical Fluids Centre
CIPM	International Committee for Weights and Measures		GGOS	Global Geodetic Observing System
			GIAC	GGOS Inter-Agency Committee
CIRS	Celestial Intermediate Reference Frame		GLONASS	Russian Federation GNSS System
COSPAR	Committee on Space Research		GLOSS	Global Sea Level Observing System
COTS	Commercial-Off-the-Shelf		GMST	Greenwich Mean Sidereal Time
CSTG	Commission on International Coordination of Space Techniques for Geodesy and Geodynamics		GMT	Greenwich Mean Time
			GMTED2010	Global Multi-Resolution Terrain Elevation Data 2010
			GNSS	Global Navigation Satellite System
CTRS	Conventional Terrestrial Reference System		GOOS	Global Ocean Observing System
DARPA	Defense Advanced Research Projects Agency		GPS	Global Positioning System
			GPST	GPS time
DE421	Development Ephemeris 421		GPStk	GPS Toolkit
DE430	Development Ephemeris 430		GSHHG	Global, Self-Consistent, Hierarchical, High-Resolution Geography Database
DMA	Defense Mapping Agency			
DORIS	Doppler Orbitography and Radiopositioning Integrated by Satellite (Stations)		GST	Galileo System Time
			GTRF	Galileo Terrestrial Reference Frame
DTM2006.0	Digital Terrain Model 2006.0		GTRS	Geocentric Terrestrial Reference System
DVD	Digital Versatile Disc			
EAL	échelle atomique libre (free atomic scale)		HCRF	Hipparcos Celestial Reference Frame
ECEF	Earth-Centered Earth-Fixed		HDGM	High-Definition Geomagnetic Model
ECI	Earth-Centered Inertial		IAG	International Association of Geodesy

IAGA	International Association of Geomagnetism and Aeronomy	LOD	Length of Day
IAU	International Astronomical Union	LSB	Least Significant Bit
ICAO	International Civil Aviation Organization	MFR	Modified Forward Row
ICET	International Center for Earth Tides	MJD	Modified Julian Date
ICGEM	International Centre for Global Earth Models	MOD	Mean of Date
		MSL	Mean Sea Level
ICRF	International Celestial Reference Frame	MSP	Mensuration Services Program
ICRS	International Celestial Reference System	NAD 83	North American Datum of 1983 (Current Version NAD 83(2011))
ICSU	International Council for Science	NASA	National Aeronautics and Space Administration
ICSU WDS	ICSU World Data System	NATO	North Atlantic Treaty Organization
IDEMS	International DEM Service	NAVD 88	North American Vertical Datum of 1988
IDS	International DORIS Service	NGA	National Geospatial-Intelligence Agency
IEEE	Institute of Electrical and Electronics Engineers	NGS	National Geodetic Survey
IERS	International Earth Rotation and Reference Systems Service	NIMA	National Imagery and Mapping Agency (now NGA)
IGeS	International Geoid Service (now ISG)	NIST	National Institute of Standards and Technology
IGFS	International Gravity Field Service	NOAA	National Oceanic and Atmospheric Administration
IGRF	International Geomagnetic Reference Field	NOMAD	Naval Observatory Merged Astrometric Dataset
IGS	International GNSS Service	NORAD	North American Aerospace Defense Command
IHO	International Hydrographic Organization	NOVAS	Naval Observatory Vector Astrometry Software
ILRS	International Laser Ranging Service		
IMO	International Maritime Organization	NRLMSISE-00	Naval Research Laboratory Mass Spectrometer and Incoherent Scatter Radar Extended Model 2000
IMU	Inertial Measurement Unit		
INTERMAGNET	International Real-time Magnetic Observatory Network	NTP	Network Time Protocol
IOC	Intergovernmental Oceanographic Commission	NTSC	National Time Service Center of the Chinese Academy of Sciences
IODE	International Oceanographic Data and Information Exchange	OTCCD	Orthogonal Transfer Charge-Coupled Device
IOGP	International Association of Oil and Gas Producers	PDF	Probability Density Function
		PEF	Pseudo-Earth-Fixed
ION	Institute of Navigation	PSMSL	Permanent Service for Mean Sea Level
ISG	International Service for the Geoid	QSST	Quasi-Stationary Sea Surface Topography
ISO	International Organization for Standardization	QUEST	Quaternion Estimator
ITRF	International Terrestrial Reference Frame	QZSS	Quasi-Zenith Satellite System (Japan)
ITRS	International Terrestrial Reference System	RCTA	Radio Technical Commission for Aeronautics
ITU	International Telecommunication Union	RMS	Root Mean Squared
ITU-R	ITU Radiocommunication Sector	RS/PC	Rapid Service/Predictions Centre
IUGG	International Union of Geodesy and Geophysics	SAPOS	Satellitenpositionierungsdienst der deutschen Landesvermessung (Satellite Positioning Service of the German National Survey)
IVS	International VLBI Service for Geodesy and Astrometry		
JCOMM	Joint Technical Commission for Oceanography and Marine Meteorology	SBA	Special Bureau for the Atmosphere
		SBH	Special Bureau for Hydrology
		SBO	Special Bureau for the Oceans
JPL	Jet Propulsion Laboratory	SGP4	Simplified General Perturbations 4
LAGEOS	Laser Geodynamics Satellites	SIMBAD	Set of Identifications, Measurements and Bibliography for Astronomical Data
LAST	Local Apparent Sidereal Time		
LAT	Local Apparent Solar Time	SINEX	Solution Independent Exchange
LMST	Local Mean Sidereal Time	SLA	Sea-Level Anomaly
LMT	Local Mean Solar Time	SLR	Satellite Laser Ranging

SOFA	Standards of Fundamental Astronomy		TT	Terrestrial Time (via TAI or USNO Master Clock)
SOLAS	Safety of Life at Sea			
SPICE	Spacecraft Planet Instrument C-Matrix Events (Toolkit)		UCAC	U.S. Naval Observatory CCD Astrograph Catalog
SPOTL	Some Programs for Ocean-Tide Loading		UN	United Nations
SQUID	Superconducting Quantum Interference Device		UNDG	United Nations Development Group
			UNESCO	United Nations Educational Scientific and Cultural Organization
SRID	Spatial Reference System Identifier			
SSH	Sea-Surface Height		URSI	International Union of Radio Science
SSHA	Sea-Surface Height Anomaly		US DoD	United States Department of Defense
SVD	Singular Value Decomposition		USGS	U.S. Geological Survey
TAI	International Atomic Time		USNO	U.S. Naval Observatory
TCB	Barycentric Coordinate Time		USSTRATCOM	U.S. Strategic Command
TCG	Geocentric Coordinate Time		UT1	Universal Time 1
TDB	Barycentric Dynamical Time		UTC	Coordinated Universal Time
TEME	True Equator Mean Equinox		UTC(k)	UTC at Laboratory k
TIO	Terrestrial Intermediate Origin		VFR	Visual Flight Rules
TIRS	Terrestrial Intermediate Reference System		VLBI	Very Long Baseline Interferometry
TLE	Two-Line Element		WGS 84	World Geodetic System 1984
TOD	True of Date		WMM	World Magnetic Model
TRF	Terrestrial Reference Frame		WMO	World Meteorological Organization
TRS	Terrestrial Reference System			

Acronyms of National Laboratories in Figure 8 Contributing to UTC

AOS	Astrogeodynamical Observatory, Space Research Centre P.A.S. (Poland)		INXE	INMETRO - National Institute for Metrology and Technology - Time and Frequency Laboratory (Brazil)
APL	Applied Physics Laboratory (U.S.)			
AUS	Consortium of Laboratories in Australia		IPQ	Instituto Portugues da Quaidate (Portugal)
BEV	Bundesamt für Eich- und Vermessungswesen (Austria)		IT	Istituto Nazionale di Ricerca Metrologica (Italy)
BIM	Bulgarian Institute of Metrology (Bulgaria)		JATC	Joint Atomic Time Commission (P.R. China)
BIRM	Beijing Institute of Radio Metrology and Measurement (P.R. China)		JV	Justervesenet (Norway)
			KEBS	Kenya Bureau of Standards (Kenya)
BY	Belarussian State Institute of Metrology (Belarus)		KIM	Indonesian Institute of Sciences (Indonesia)
			KRISS	Korea Research Institute of Standards and Science (Rep. of Korea)
CAO	Cagliari Astronomical Observatory (Italy)			
CH	METrology and Accreditation Switzerland		KZ	Kazakh Institute of Metrology (Kazakhstan)
CNM	Centro Nacional de Metrología (Mexico)		LT	Lithuanian National Metrology Institute
CNMP	Centro Nacional de Metrología, de Panamá		MIKES	Mittatekniikan Keskus, Center for Metrology and Accreditation (Finland)
DLR	Deutsche Zentrum für Luft- und Raumfahrt (Germany)			
			MKEH	Hungarian Trade Licensing Office (Hungary)
DMDM	Directorate of Measures and Precious Metals (Serbia)		MSL	Measurement Standards Laboratory of New Zealand (New Zealand)
DTAG	Deutsche Telekom AG (Germany)		MTC	MAKKAH Time Centre - King Abdulah Centre for Crescent Observations and Astronomy (Saudi Arabia)
EIM	Hellenic Institute of Metrology (Greece)			
ESTC	European Space Research and Technology Centre (European Union)			
			NAO	National Astronomical Observatory (Japan)
HKO	Hong Kong Observatory (Hong Kong, P.R. China)		NICT	National Institute of Information and Communications Technology (Japan)
IFAG	Bundesamt für Kartographie und Geodäsie (Germany)		NIM	National Institute of Metrology (P.R. China)
			NIMB	National Institute of Metrology (Bucharest, Romania)
IGNA	Instituto Geográfico Nacional (Argentina)			
INPL	National Physical Laboratory of Israel (Israel)		NIMT	National Institute of Metrology (Thailand)
INTI	Instituto Nacional de Technolgia Industrial (Argentina)		NIS	National Institute for Standards (Egypt)
			NIST	National Institute of Standards and Technology (U.S.)

NMIJ	National Metrology Institute of Japan (Japan)	SIQ	Slovenian Institute of Quality and Metrology (Slovenia)
NMLS	National Metrology Laboratory of SIRIM Berhad (Malaysia)	SMD	Belgium Metrology Service (Metrologische Dienst) (Belgium)
NPL	National Physical Laboratory (UK)	SMU	Slovenský Metrologiċký Ustav (Slovakia)
NPLI	National Physical Laboratory of India (India)	SP	Technical Research Institute of Sweden (Sweden)
NRC	National Research Council (Canada)		
NRL	Naval Research Laboratory (U.S.)	SU	Institute of Metrology for Time and Space, NPO "VNIIFTRI" Mendeleevo (Russia)
NTSC	National Time Service Center of China (P.R. China)	TCC	Transportable Integrated Geodetic Observatory (Chile)
ONBA	Observatorio Naval de Bueno Aires (Argentina)	TL	Telecommunication Laboratories (Taiwan)
ONRJ	Observatório Nacional (Brazil)	TP	Institute of Radio Engineering and Electronics, Academy of Sciences of the Czech Republic
OP	Observatoire de Paris (France)		
ORB	Observatoire Royal de Paris (France)	UA	Scientific-Research Institute for Metrology of Measurement and Control Systems (Ukraine)
PL	Consortium of Laboratories in Poland (Poland)		
PTB	Physikalisch-Technische Bundesanstalt (Germany)	UME	Ulusai Metroloji Enstitüsü, Marmara Research Center (National Metrology Institute) (Turkey)
ROA	Real Instituto y Observatorio de la Armada (Spain)	USNO	U.S. Naval Observatory
		VMI	Vietnam Metrology Institute (Viet Nam)
SCL	Standards and Calibration Laboratory (Hong Kong, P.R. China)	VSL	NMi Van Swinden Laboratorium (Netherlands)
		ZA	National Metrology Institute of South Africa
SG	Standards, Productivity and Innovation Board (Singapore)		

A number of the acronyms used to describe international organizations and timescales are taken from French. Table M1 is a list of the acronyms, the English names and the French names from which the acronyms originate. Though many abbreviations for timescales come from the French, universal coordinated time is called "temps universel coordonné" in French. UTC is an evolution of the old universal time (UT) [226, Ch. 2.7, 2.8, 14], though some use UT to designate UTC. The abbreviation UTC was officially approved by a resolution of the International Astronomical Union for use in French and English, even though it does not directly stand for anything in either language [226, Ch. 14.]. The correct English expression for UTC is "universal coordinated time." Additionally, the abbreviation ICSU for the International Council for Science does not come from French. It comes from the old name of the organization, the International Council of Scientific Unions.

Table M1: Foreign Acronyms

Acronym	English Name	French Name
BGI	International Gravimetric Bureau	Bureau Gravimétrique International
BIPM	International Bureau of Weights and Measures	Bureau International des Poids et Mesures
CIPM	International Committee for Weights and Measures	Comité International des Poids et Mesures
CCIR	International Radio Consultative Committee	Comité Consultatif International Pour la Radio
URSI	International Union of Radio Science	Union Radio-Scientifique Internationale
TAI	International atomic time	Temps atomique international
TCB	Barycentric coordinate time	Temps coordonnée barycentrique
TCG	Geocentric coordinate time	Temps coordonnée géocentrique
TDB	Barycentric dynamical time	Temps dynamique barycentrique

A list of acronyms of international organizations and timescales taken from French used in English that do not match the English words.

REFERENCES

[1] H. Abbas, D. P. Xue, M. Farooq, G. Parkinson, and M. Blanchette, "Track-independent estimation schemes for registration in a network of sensors," in *Proceedings of the 35th Conference on Decision and Control*, Kobe, Japan, 11–13 Dec. 1996, pp. 2563–2568.

[2] E. L. Afraimovich, V. V. Demyanov, and G. Y. Smolkov, "The total failures of GPS functioning caused by the powerful solar radio burst on December 13, 2006," *Earth Planets Space*, vol. 61, no. 5, pp. 637–641, May 2009.

[3] D. Albanee *et al.*, "Laser ranging on space debris with MéO," in *Proceedings of the International Technical Laser Workshop*, Rome, Italy, 5–9 Nov. 2012, slides. [Online]. Available: http://www.lnf.infn.it/conference/laser2012/4thursday/7_4courde/courde_s.pdf

[4] C. O. Alley and T. Van Flandern, "Evidence for the relativity of simultaneity in measured GPS pseudo-ranges," in *Global Positioning System Performance Analysis Working Group*, Falcon Air Force Base, CO, 23–24 Aug. 1995, conference slides. [Online]. Available: http://www.montgomerycollege.edu/Departments/planet/planet/Numerical_Relativity/Relativity_of_Simultaneity_GPS.pdf

[5] R. Alonso and M. Shuster, "Complete linear attitude-independent magnetometer calibration," *The Journal of the Astronautical Sciences*, vol. 50, no. 4, pp. 477–490, Oct. – Dec. 2002.

[6] Z. Altamimi, "Role and importance of the international terrestrial reference frame (ITRF) for science and positioning applications," in *Proceedings of the Second UN High Level Forum on Global Geospatial Information Management*, Doha, Qatar, 4–6 Feb. 2013. [Online]. Available: http://ggim.un.org/docs/meetings/Exchange_Forum_2013/Session%201%20Determining%20Place/Session1_Determining%20Place_IAG_Altamimi.pdf

[7] Z. Altamimi, X. Collilieux, and L. Métivier, "ITRF2008: An improved solution of the international terrestrial reference frame," *Journal of Geodesy*, vol. 85, no. 8, pp. 457–473, Aug. 2011.

[8] "Guide to reference and standard atmosphere models," American Institute of Aeronautics and Astronautics, Reston, VA, Tech. Rep. G-003C-2010e, 2010.

[9] G. Arfken, *Mathematical Models for Physicists*, 2nd ed.   New York: Academic Press, 1970.

[10] E. F. Arias, G. Panfilo, and G. Petit, "Timescales at the BIPM," *Metrologia*, vol. 48, no. 4, pp. S145–S153, Aug. 2011.

[11] ARINC Engineering Services, LLC, "Navstar global positioning system interface specification: Navstar GPS space segment/ navigation user interfaces," Space and Missile Systems Center/ Navstar GPS Joint Program Office, Tech. Rep. IS-GPS-200, 7 Mar. 2006, revision D. [Online]. Available: http://www.gps.gov/technical/icwg/IS-GPS-705A.pdf

[12] K. S. Arun, T. S. Huang, and S. D. Blostein, "Least-squares fitting of two 3-D point sets," *IEEE Transactions on Pattern Analysis and Machine Intelligence*, vol. PAMI-9, no. 5, pp. 698–700, Sep. 1987.

[13] N. Ashby and J. J. Spilker Jr., "Introduction to relativistic effects on the global positioning system," in *Global Positioning System: Theory and Applications*, B. W. Parkinson and J. J. Spilker Jr., Eds. Washington, DC: American Institute of Aeronautics and Astronautics, Inc., 1996, vol. 1, ch. 18.

[14] Associated Press, "Boy genius, 12, wins National Geographic Bee by correctly naming farthest point from Earth's center. . . do YOU know the answer?" *Daily Mail*, 23 May 2013. [Online]. Available: http://www.dailymail.co.uk/news/article-2329331/Sathwik-Karnik-12-wins-2013-National-Geographic-Bee-correctly-naming-farthest-point-Earths-center.html

[15] J. A. Atchison and M. A. Peck, "Length scaling in spacecraft dynamics," *Journal of Guidance, Control and Dynamics*, vol. 34, no. 1, pp. 231–246, Jan. – Feb. 2011.

[16] C. Audoin and B. Guinot, *The Measurement of Time: Time, Frequency and the Atomic Clock*. Cambridge, UK: Cambridge University Press, 2001.

[17] "Mensuration services program (MSP) programmer's guide for MSP geographic translator (GEOTRANS) version 3.3," BAE Systems, Tech. Rep. 5034291, 23 Oct. 2012. [Online]. Available: http://earth-info.nga.mil/GandG/geotrans/geotrans3.3/docs/MSP_Geotrans_Programmers_Guide.pdf

[18] "Mensuration services program (MSP) user's guide for MSP geographic translator (GEOTRANS) version 3.3," BAE Systems, Tech. Rep. 5034289, 23 Oct. 2012. [Online]. Available: http://earth-info.nga.mil/GandG/geotrans/geotrans3.3/docs/MSP_Geotrans_Users_Guide.pdf

[19] R. M. L. Baker Jr. and M. W. Makemson, *An Introduction to Astrodynamics*, 2nd ed. New York: Academic Press, 1967.

[20] Y. Bar-Shalom, H. M. Shertukde, and K. R. Pattipati, "Extraction and optimal use of measurements from an imaging sensor for precision target tracking," in *Proceedings of the IEEE International Conference on Control and Applications*, Jerusalem, Israel, 3–6 Apr. 1989, pp. 305–310.

[21] Y. Bar-Shalom, S. S. Blackman, and R. J. Fitzgerald, "Dimensionless score function for multiple target tracking," *IEEE Transactions on Aerospace and Electronic Systems*, vol. 43, no. 1, pp. 392–400, Jan. 2007.

[22] Y. Bar-Shalom, P. K. Willett, and X. Tian, *Tracking and Data Fusion*. Storrs, CT: YBS Publishing, 2011.

[23] R. L. Beard, "Role of the ITU-R in time scale definition and dissemination," *Metrologia*, vol. 48, no. 4, pp. S125–S131, Aug. 2011.

[24] W. Becker, M. G. Bernhardt, and A. Jessner. (2013, 13 Mar.) Autonomous spacecraft navigation with pulsars. [Online]. Available: http://arxiv.org/abs/1305.4842

[25] M. Belenkii, D. Sandler, D. Bruns, and E. Korevaar, "Daytime stellar imager for attitude determination," U.S. Patent 7,447 591 B2, Nov. 4, 2008.

[26] D. J. Bender, T. R. Parks, and T. F. Brozenec, "Method of attitude determination using earth and star sensors," U.S. Patent 5,412,574, May 2, 1995.

[27] M. S. Bessell, "Standard photometric systems," *Annual Review of Astronomy and Astrophysics*, vol. 43, pp. 293–336, Aug. 2005.

[28] G. Beutler, *Methods of Celestial Mechanics: Application to Planetary System, Geodynamics and Satellite Geodesy*.   Berlin: Springer, 2005, vol. 2.

[29] ——, *Methods of Celestial Mechanics: Physical, Mathematical and Numerical Principles*.   Berlin: Springer, 2005, vol. 1.

[30] C. Bizouard and D. Gambis, "The combined solution C04 for earth orientation parameters consistent with international terrestrial reference frame 2008," International Earth Rotation and Reference Systems Service, Tech. Rep., 2008. [Online]. Available: https://hpiers.obspm.fr/iers/eop/eopc04/C04.guide.pdf

[31] A. Blaauw, C. S. Gum, J. L. Pawsey, and G. Westerhout, "The new I.A.U. system of galactic co-ordinates (1958 revision)," *Monthly Notes of the Royal Astronomical Society*, vol. 121, no. 2, pp. 123–131, 1960.

[32] R. Bondarescu, M. Bondarescu, G. Hetényi, L. Boschi, P. Jetzer, and J. Balakrishna, "Geophysical applicability of atomic clocks: Direct continental geoid mapping," *Geophysical Journal International*, vol. 121, no. 1, pp. 78–82, Oct. 2012.

[33] B. Boxenhorn and B. S. Dew, "A position-modulated alignment test technique in the presence of ship's flexure," *Journal of Guidance, Control, and Dynamics*, vol. 6, no. 4, pp. 246–250, Jul. – Aug. 1983.

[34] T. M. Brace, "Method and system for spectral image celestial navigation," U.S. Patent 8,355,868 B2, Jan. 15, 2013.

[35] J. Bradley, "A letter from the Reverend Mr. James Bradley savilian professor of astronomy at oxford and F.R.S. to Dr. Edmon Halley astronom. reg. &c. giving an account of a new discovered motion of the fix'd stars," *Philosophical Transactions*, vol. 35, pp. 637–661, 1727. [Online]. Available: http://rstl.royalsocietypublishing.org/content/35/399-406.toc

[36] J. B. Breckinridge, *Basic Optics for the Astronomical Sciences*.   Bellingham, WA: SPIE Press, 2012.

[37] E. Brekke, O. Hallingstad, and J. Glattetre, "Improved target tracking in the presence of wakes," *IEEE Transactions on Aerospace and Electronic Systems*, vol. 48, no. 2, pp. 1005–1017, Apr. 2012.

[38] A. Buchanan *et al.*, "Geomagnetic referencing – the real-time compass for directional drillers," *Oilfield Review*, vol. 25, no. 3, pp. 32–47, Autumn 2013. [Online]. Available: https://geomag.usgs.gov/downloads/publications/3_geomagnetic.pdf

[39] *Le Système international d'unités The International System of Units*, Bureau International des Poids et Mesures Std., 2006. [Online]. Available: http://www.bipm.org/en/si/si_brochure/

[40] S. Carlip, "Aberration and the speed of gravity," *Physics Letters A*, vol. 267, no. 2–3, pp. 81–87, 13 Mar. 2000.

[41] S. Casotto and E. Fantino, "Evaluation of methods for spherical harmonic synthesis of the gravitational potential and its gradients," *Advances in Space Research*, vol. 40, no. 1, pp. 69–75, 2007.

[42] Center for Operational Oceanographic Products and Services. (2013, 15 Oct.) FAQ – tide predictions and data. [Online]. Available: http://www.co-ops.nos.noaa.gov/faq2.html#26

[43] (2013, 1 Nov.) The world factbook, appendix G. Central Intelligence Agency. [Online]. Available: https://www.cia.gov/library/publications/the-world-factbook/appendix/appendix-g.html

[44] J. Chen, J. Yuan, C. Guo, Y. Zhang, and P. Zhang, "Progress in technology for the 2005 height determination of Qomolangma Feng (Mt. Everest)," *Science in China Series D*, vol. 49, no. 5, pp. 531–538, May 2006.

[45] M. Cheng, J. C. Ries, and B. D. Tapley, "Variations of the Earth's figure axis from satellite ranging and GRACE," *Journal of Geophysical Research*, vol. 116, no. B1, Jan. 2011.

[46] Y. Cheng, W. D. Banas, and J. L. Crassidis, "Quaternion data fusion," in *Proceedings of the Itzhack Y. Bar-Itzhack Memorial Symposium on Estimation, Navigation, and Spacecraft Control*, Haifa, Israel, Oct. 2012. [Online]. Available: http://ancs.eng.buffalo.edu/pdf/ancs_papers/2012/barsym.pdf

[47] T. Chiba, "The constancy of the constants of nature: Updates," *Progress of Theoretical Physics*, vol. 126, no. 6, pp. 993–1019, Dec. 2011.

[48] China Satellite Navigation Office, "BeiDou navigation satellite system signal in space interface control document," BeiDou Navigation Satellite System, Tech. Rep., Dec. 2012, possibly available from www.beidou.gov.cn but some firewalls block the server. [Online]. Available: http://www.gpsbusinessnews.com/Chinese-GNSS-Constellation-BeiDou-Now-Opened-for-Public-Usage_a4006.html

[49] T. L. Chow, *Classical Mechanics*, 2nd ed.   Boca Raton: CRC Press, 2013.

[50] "Analysis of least-squares attitude determination routine DOAOP," Computer Sciences Corporation, Tech. Rep. CSC/TM-77/6304, 1977, prepared for Goddard Space Flight Center.

[51] J. L. Crassidis, F. L. Markley, and Y. Cheng, "Survey of nonlinear attitude estimation methods," *Journal of Guidance, Control, and Dynamics*, vol. 30, no. 1, pp. 12–28, Jan. – Feb. 2007.

[52] D. F. Crouse, "On measurement-based light-time corrections for bistatic orbital debris tracking," *IEEE Transactions on Aerospace and Electronic Systems*, accepted, 2015.

[53] ——, "Advances in displaying uncertain estimates of multiple targets," in *Proceedings of SPIE: Signal Processing, Sensor Fusion, and Target Recognition XXII*, Baltimore, MD, Apr. 2013.

[54] ——, "Basic tracking using 3D monostatic and bistatic measurements in refractive environments," *IEEE Aerospace and Electronic Systems Magazine*, vol. 29, no. 8, Part II, pp. 54–75, Aug. 2014.

[55] ——, "Basic tracking using nonlinear 3D monostatic and bistatic measurements," *IEEE Aerospace and Electronic Systems Magazine*, vol. 29, no. 8, Part II, pp. 4–53, Aug. 2014.

[56] ——, "On implementing 2D rectangular assignment algorithms," *IEEE Transactions on Signal Processing*, 2014, submitted 2014.

[57] ——, "Basic tracking using nonlinear continuous-time dynamic models," *IEEE Aerospace and Electronic Systems Magazine*, vol. 30, no. 2, Part II, pp. 4–41, Feb. 2015.

[58] ——, "Simulating aerial targets in 3D accounting for the Earth's curvature," *Journal of Advances in Information Fusion*, vol. 10, no. 1, Jun. 2015.

[59] D. F. Crouse, Y. Bar-Shalom, and P. Willett, "Sensor bias estimation in the presence of data association uncertainty," in *Proceedings of SPIE: Signal and Data Processing of Small Targets*, vol. 7445, San Diego, CA, 2 Aug. 2009.

[60] D. F. Crouse, R. W. Osborne III, K. Pattipati, P. Willett, and Y. Bar-Shalom, "Efficient 2D sensor location estimation using targets of opportunity," *Journal of Advances in Information Fusion*, vol. 8, no. 1, pp. 73–89, Jun. 2013.

[61] J. J. Danielson and D. B. Gesch, "Global multi-resolution terrain elevation data 2010 (GMTED2010)," U.S. Department of the Interior, U.S. Geological Survey, Reston, VA, Tech. Rep. 2011-1073, 2011. [Online]. Available: http://pubs.usgs.gov/of/2011/1073/pdf/of2011-1073.pdf

[62] P. B. Davenport, "A vector approach to the algebra of rotations with applications," Goddard Space Flight Center, National Aeronautics and Space Administration, Greenbelt, MD, Tech. Rep. TN D-4696, Aug. 1968.

[63] Defense Advanced Research Projects Agency. (2014, 24 Jul.) Beyond GPS: 5 next-generation technologies for positioning, navigation & timing (PNT). [Online]. Available: http://www.darpa.mil/NewsEvents/Releases/2014/07/24.aspx

[64] M. H. DeGroot and M. J. Schervish, *Probability and Statistics*, 3rd ed.   Boston: Addison Wesley, 2002.

[65] Department of Defense, "DMA technical manual: Datums, ellipsoids, grid, and grid reference systems," Defense Mapping Agency, Tech. Rep. DMA TM 8358.1, Sep. 1990. [Online]. Available: http://earth-info.nga.mil/GandG/publications/tm8358.1/pdf/TM8358_1.pdf

[66] ——, "Addendum to NIMA TR 8350.2: Implementation of the World Geodetic System 1984 (WGS 84) reference frame G1150," National Imagery and Mapping Agency, Tech. Rep., 2003. [Online]. Available: http://earth-info.nga.mil/GandG/publications/tr8350.2/Addendum%20NIMA%20TR8350.2.pdf

[67] ——, "Department of Defense World Geodetic System 1984: Its definition and relationships with local geodetic systems," National Imagery and Mapping Agency, Tech. Rep. NIMA TR8350.2, Jun. 2004, third edition, Amendment 2. [Online]. Available: http://earth-info.nga.mil/GandG/publications/tr8350.2/wgs84fin.pdf

[68] ——, "WGS 84 G1674 geodetic control network upgrade for areas of White Sands Missile Range and Holloman AFB, NM," National Imagery and Mapping Agency, Tech. Rep., 1 Jul. 2012. [Online]. Available: http://www.wsmr.army.mil/pdf/G1674-Upgrade-01Jul2012.pdf

[69] ——, "Department of Defense world geodetic system 1984: Its definition and relationships with local geodetic systems," National Imagery and Mapping Agency, Tech. Rep. NGA.STND.0036_1.0.0_WGS84, 8 Jul. 2014. [Online]. Available: http://earth-info.nga.mil/GandG/publications/NGA_STND_0036_1_0_0_WGS84/NGA.STND.0036_1.0.0_WGS84.pdf

[70] Department of Defense, Navy, Nautical Almanac Office, *The Astronomical Almanac for the Year 2014*.   Department of the Navy, 2013.

[71] K. Dismukes. (2011, 23 Sep.) Definition of two-line element set coordinate system. National Aeronautics and Space Administration. [Online]. Available: http://spaceflight.nasa.gov/realdata/sightings/SSapplications/Post/JavaSSOP/SSOP_Help/tle_def.html

[72] A. T. Doodson, "The harmonic development of the tide-generating potential," *Proceedings of the Royal Society A: Mathematical, Physical & Engineering Sciences*, vol. 100, no. 701, pp. 305–329, 1 Dec. 1921.

[73] T. D. Downs, "Orientation statistics," *Biometrika*, vol. 59, no. 3, pp. 665–676, Dec. 1972.

[74] D. P. Drob, "The NRLMSISE-00 and HWM-93 users guide," United States Naval Research Laboratory, Tech. Rep., Nov. 2003, documented included with NRLMSISE-00 code.

[75] N. H. Durland, "Defining mean sea level in military simulations with DTED," in *Proceedings of the 2009 Spring Simulation Multiconference*, San Diego, CA, 22–27 Mar. 2009.

[76] D. W. Eggert, A. Lorousso, and R. B. Fisher, "Estimating 3-D rigid body transformations: A compairson of four major algorithms," *Machine Vision and Applications*, vol. 9, no. 5–6, pp. 272–290, Mar. 1997.

[77] M. Ekman, "Impacts of geodynamic phenomena on systems for height and gravity," *Bulletin Géodésique*, vol. 63, no. 3, pp. 281–296, 1996.

[78] R. Emden, "Aberration und Relativitätstheorie," *Naturwissenschaften*, vol. 14, no. 16, pp. 329–335, 16 Apr. 1926.

[79] "ESRI shapefile technical description," Environmental Systems Research Institute, Inc., Tech. Rep., Jul. 1998. [Online]. Available: http://www.esri.com/library/whitepapers/pdfs/shapefile.pdf

[80] Escapist Games. (2014, 22 Aug.) Star chart for smart phones & tablets. [Online]. Available: http://www.escapistgames.com/sc.html

[81] European Commission, "Commission implementing European regulation no 1207/2011 of 22 November 2011 laying down requirements for the performance and interoperability of surveillance for the single European airspace," Official Journal of the European Union, 23 Nov. 2011. [Online]. Available: http://eur-lex.europa.eu/LexUriServ/LexUriServ.do?uri=OJ:L:2011:305:0035:0052:EN:PDF

[82] "The Hipparcos and Tycho catalogues: Astrometric and photometric catalogues derived from the ESA Hipparcos space astrometry mission," European Space Agency, Tech. Rep. SP-1200, Jun. 1997, volumes 1–17. [Online]. Available: http://www.rssd.esa.int/index.php?project=HIPPARCOS&page=Overview

[83] "European GNSS (Galileo) open service signal in space interface control document," European Union, Tech. Rep. OS SIS ICD, Issue 1.1, Sep. 2010. [Online]. Available: http://ec.europa.eu/enterprise/policies/satnav/galileo/files/galileo-os-sis-icd-issue1-revision1_en.pdf

[84] L. Fairhead and P. Bretagnon, "An analytical formula for the time transformation TB-TT," *Astronomy and Astrophysics*, vol. 22, no. 1, pp. 240–247, Mar. 1990.

[85] E. Fantino and S. Casotto, "Methods of harmonic synthesis for global geopotential models and their first-, second- and third-order gradients," *Journal of Geodesy*, vol. 83, no. 7, pp. 595–619, Jul. 2009.

[86] J. L. Farrell and J. C. Stuelpnagel, "Problem 65-1: A least squares estimate of satellite attitude, solution," *SIAM Review*, vol. 8, no. 3, pp. 384–386, Jul. 1966, other authors' solutions are listed in the article.

[87] W. E. Featherstone, "The use and abuse of vertical deflections," in *Proceedings of the 6th South East Asian Surveyors Congress*, Fremantle, WA, Australia, 1–6 Nov. 1999, pp. 85–97.

[88] W. E. Featherstone and S. J. Claessens, "Closed-form transformation between geodetic and ellipsoidal coordinates," *Studia Geophysica et Geodaetica*, vol. 52, no. 1, pp. 1–18, Jan. 2008.

[89] "Automatic Dependent Surveillance— Broadcast (ADS–B) out performance requirements to support air traffic control (ATC) service; final rule," Federal Register Part III, Department of Transportation, Federal Aviation Administration, pp. 30 160–30 195, May 2010. [Online]. Available: http://edocket.access.gpo.gov/2010/pdf/2010-12645.pdf

[90] J. P. Ferry, "Exact association probability for data with bias and features," *Journal of Advances in Information Fusion*, vol. 5, no. 1, pp. 41–67, Jun. 2010.

[91] C. C. Finlay *et al.*, "International geomagnetic reference field: The eleventh generation," *Geophysical Journal International*, vol. 183, no. 1, pp. 1216–1230, Dec. 2010.

[92] N. Fisher, *Statistical Analysis of Circular Data*. Cambridge, UK: Cambridge University Press, 1993.

[93] N. Fisher, T. Lewis, and B. Embleton, *Statistical Analysis of Spherical Data*. Cambridge, UK: Cambridge University Press, 1987.

[94] M. H. Fitzeau, "Sur les hypothèses relatives à l'éther lumineux, et sur une expérience qui paraît démontrer que le mouvement des corps change la vitesse avec laquelle la lumière se propage dans leur intérieur," *Comptes rendus hebdomadaires des séances de l'Académie des sciences*, vol. 33, pp. 349–355, Jul. – Dec. 1851. [Online]. Available: http://www.academie-sciences.fr/activite/archive/dossiers/Fizeau/Fizeau_pdf/CR1851_p349.pdf

[95] W. M. Folkner, J. G. Williams, D. H. Boggs, R. S. Park, and P. Kuchynka, "The planetary and lunar ephemerides DE430 and DE431," *Interplanetary Network Progress Report*, vol. 42-196, 15 Feb. 2014. [Online]. Available: http://naif.jpl.nasa.gov/pub/naif/generic_kernels/spk/planets/DE430%20and%20DE431.pdf

[96] T. J. Ford, "Apparatus and method for determining pitch and azimuth from satellite signals," U.S. Patent 6,211,821 B1, Apr. 3, 2001.

[97] A. M. Fosbury, "Estimation with multitemporal measurements," *Journal of Guidance, Control, and Dynamics*, vol. 33, no. 5, pp. 1518–1526, Sep. – Oct. 2010.

[98] P. Foukal, *Solar Astrophysics*, 3rd ed. Weinheim, Germany: WILEY-VCH Verlag GmbH & Co. KGaA, 2013.

[99] A. Fresnel, "Lettre d'Augustin Fresnel à François Arago sur l'influence du mouvement terrestre dans quelques phénomènes d'optique," in *Œuvres complètes d'Augustin Fresnel*, H. de Senarmont, E. Verdet, and L. Fresnel, Eds. Imprimerie Impériale, 1868, vol. 2, pp. 627–636.

[100] T. Fukushima, "Numerical computation of spherical harmonics of arbitrary degree and order by extending exponent of floating point numbers," *Journal of Geodesy*, vol. 86, no. 4, pp. 271–285, Apr. 2012.

[101] T. Furumura, S. Takemura, S. Noguchi, T. Takemoto, T. Maeda, K. Iwai, and S. Padhy, "Strong ground motions from the 2011 off-the Pacific-coast-of-Tohoku, Japan (Mw=9.0) earthquake obtained from a dense nationwide seismic network," *Landslides*, vol. 8, no. 3, pp. 333–338, Sep. 2011.

[102] C. Förste *et al.*, "EIGEN-6C4 the latest combined global gravity field model including GOCE data up to degree and order 2190 of GFZ Potsdam and GRGS Toulouse," in *The 5th GOCE User Workshop*, Paris, France, Nov. 2014, pp. 25–28, slides. [Online]. Available: http://icgem.gfz-potsdam.de/ICGEM/documents/Foerste-et-al-EIGEN-6C4.pdf

[103] E. Gai, K. Daly, J. Harrison, and L. Lemos, "Star-sensor-based satellite attitude/attitude rate estimator," *Journal of Guidance, Control, and Dynamics*, vol. 8, no. 5, pp. 560–565, Sep. – Oct. 1985.

[104] P. P. Gandhi and S. A. Kassam, "Analysis of CFAR processors in nonhomogeneous background," *IEEE Transactions on Aerospace and Electronic Systems*, vol. 24, no. 4, pp. 427–445, Jul. 1988.

[105] J. W. Gangestad, G. E. Pollock, and J. M. Longuski, "Propellantless stationkeeping at Enceladus via the electromagnetic Lorentz force," *Journal of Guidance, Control and Dynamics*, vol. 32, no. 5, pp. 1466–1475, Sep. – Oct. 2009.

[106] ——, "Analytical expressions that characterize propellantless capture with electrostatically charged spacecraft," *Journal of Guidance, Control, and Dynamics*, vol. 34, no. 1, pp. 247–258, Jan. – Feb. 2011.

[107] E. García-Berro, J. Isern, and Y. A. Kubyshin, "Astronomical measurements and constraints on the variability of fundamental constants," *The Astronomy and Astrophysics Review*, vol. 14, no. 2, pp. 113–170, Mar. 2007.

[108] W. Gautschi and J. Slavik, "On the computation of modified Bessel function ratios," *Mathematics of Computation*, vol. 32, no. 143, pp. 865–875, Jul. 1978.

[109] F. Gini and M. Rangaswamy, Eds., *Knowledge Based Radar Detection, Tracking and Classification*. Hoboken, NJ: Wiley-Interscience, 2008.

[110] D. R. Glandorf, "Gravity gradient torque for an arbitrary potential function," *Journal of Guidance, Control, and Dynamics*, vol. 9, no. 1, pp. 122–124, Jan. – Feb. 1986.

[111] G. H. Golub and C. F. Van Loan, *Matrix Computations*, 4th ed. Baltimore, MD: The Johns Hopkins University Press, 2013.

[112] R. Gounley, R. White, and E. Gai, "Autonomous satellite navigation by stellar refraction," *Journal of Guidance, Control, and Dynamics*, vol. 7, no. 2, pp. 129–134, Mar. 1984.

[113] T. Grinter and C. Roberts, "Real time precise point positioning: Are we there yet?" in *Proceedings of the International Global Navigation Satellite Systems Society Symposium*, Outrigger Gold Coast, Queensland, Australia, 16–18 Jul. 2013.

[114] R. S. Gross and B. F. Chao, "The rotation and gravitational signature of the December 26, 2004 Sumatran earthquake," *Surveys in Geophysics*, vol. 27, no. 6, pp. 615–632, Nov. 2006.

[115] G. Gustafsson, N. E. Papitashvili, and V. O. Papitashvili, "A revised corrected geomagnetic coordinate system for epochs 1985 and 1990," *Journal of Atmospheric and Terrestrial Physics*, vol. 54, no. 11/12, pp. 1609–1631, Nov. – Dec. 1992.

[116] J. Gómez-Enri, P. Villares, M. Bruno, and M. Catalán, "Evidence of different ocean responses to atmospheric pressure variations in the Atlantic, Indian, and Pacific basins as deduced from ERS-2 altimetric data," *Annales Geophysicae*, vol. 22, no. 2, pp. 331–345, 2004.

[117] B. Görres and M. Mayer, "Referenzsysteme und -rahmen für GNSS-Vermessungen (DVW-Merkblatt)," in *Beiträge zum 124. DVW-Seminar, GNSS 2013 Schneller. Genauer. Effizienter*, Karlsruhe, Germany, 14–15 Mar. 2013. [Online]. Available: http://www.gib.uni-bonn.de/mitarbeiter/wm/bgoerres/papers/2013ka_dvw.pdf

[118] A.-R. Hakimi and S. Setayeshi, "A novel approach to delta-*t* from 1620 to 2010," *Monthly Notices of the Royal Astronomical Society*, vol. 417, no. 4, pp. 2714–2720, Nov. 2011.

[119] D. Hambrick and W. D. Blair, "Multisensor track association in the presence of bias," in *Proceedings of the IEEE Aerospace Conference*, Big Sky, MT, 1–8 Mar. 2014.

[120] R. B. Harris and R. G. Mach, "The GPSTk: an open source GPS toolkit," *GPS Solutions*, no. 2, pp. 145–150, Mar. 2007.

[121] R. Hartley, J. Trumpf, Y. Dai, and H. Li, "Rotation averaging," *International Journal of Computer Vision*, vol. 103, no. 3, pp. 267–305, Jul. 2013.

[122] J. Haverinen, "Applying indoor magnetic field for acquiring movement information," U.S. Patent 2013/0 295 957 A1, Nov. 7, 2013.

[123] ——, "Generating magnetic field map for indoor positioning," U.S. Patent 2013/0 177 208 A1, Jul. 11, 2013.

[124] ——, "Indoor magnetic fields based location discovery," U.S. Patent 2013/0 179 075 A1, Jul. 11, 2013.

[125] ——, "Utilizing magnetic field based navigation," U.S. Patent 2013/0 179 074 A1, Jul. 11, 2013.

[126] ——, "Utilizing magnetic field based navigation," U.S. Patent 2013/0 310 069 A1, Nov. 21, 2013.

[127] J. Haverinen and A. Kemppainen, "Global indoor self-localization based on the ambient magnetic field," *Robotics and Autonomous Systems*, vol. 57, no. 10, pp. 1028–1035, 31 Oct. 2009.

[128] R. E. Helmick and T. R. Rice, "Alignment of a 2-D sensor and a 3-D radar," in *Proceedings of SPIE: Acquisition, Tracking and Pointing VI*, vol. 1697, Orlando, FL, 20 Apr. 1992, pp. 142–157.

[129] ——, "Removal of alignment errors in an integrated system of two 3-D sensors," *IEEE Transactions on Aerospace and Electronic Systems*, vol. 29, no. 4, pp. 1333–1343, Oct. 1993.

[130] R. R. Helmick, J. E. Conte, and T. R. Rice, "Absolute alignment of sensors," Naval Surface Warfare Center, Dahlgren Division, Dahlgren, VA, Tech. Rep. NSWCDD/TR-96/46, May 1996.

[131] W. Heres and N. A. Bonito, "An alternative method of computing altitude adjustment corrected geomagnetic coordinates as applied to IGRF epoch 2005," Air Force Research Laboratory, Space Vehicles Directorate, Hanscom AFB, MA, Tech. Rep. AFRL-RV-HA-TR-2007-1190, 20 Jul. 2007.

[132] S. M. Herman and A. B. Poore, "Nonlinear least squares estimation for sensor and navigation biases," in *Proceedings of SPIE: Signal and Data Processing of Small Targets*, vol. 6236, Orlando, FL, 17 Apr. 2006.

[133] A. Hirshfeld, R. W. Sinnott, and F. Ochsenbein, *Sky Catalog 2000.0: Stars to Magnitude 8.0*, 2nd ed. Cambridge, MA: Sky Publishing Corporation and Cambridge University Press, 1991, vol. 1.

[134] C. Hirt, "Prediction of vertical deflections from high-degree spherical harmonic synthesis and residual terrain model data," *Journal of Geodesy*, vol. 84, no. 3, pp. 179–190, Mar. 2010.

[135] C. Hirt, M. Kuhn, W. E. Featherstone, and F. Göttl, "Topographic/isostatic evaluation of new-generation GOCE gravity-field models," *Journal of Geophysical Research*, vol. 11, no. B5, May 2012.

[136] B. Hofmann-Wellenhof and H. Moritz, *Physical Geodesy*, 2nd ed.   SpringerWienNewYork, 2006.

[137] C. Y. Hohenkerk, "SOFA and the algorithms for transformations between time scales & between reference systems," in *Proceedings of the Journées 2011 "Systèmes de référence spatio-temporels"*, Vienna, Austria, 19–21 Sep. 2011, pp. 21–24. [Online]. Available: http://syrte.obspm.fr/jsr/journees2011/pdf/hohenkerk.pdf

[138] C. Y. Hohenkerk and A. T. Sinclair, "The computation of angular atmospheric refraction at large zenith angles," United Kingdom Hydrographic Office, HM Nautical Almanac, Tech. Rep. 63, Apr. 1985.

[139] I. Holleman, A. Huuskonen, M. Kurri, and H. Beekhuis, "Monitoring of weather radar receivers using solar signals detected in operational scan data," in *Proceedings of the WMO Technical Conference*, St. Petersburg, Russia, 27–29 Nov. 2008.

[140] S. A. Holmes and W. E. Featherstone, "A unified approach to the Clenshaw summation and the recursive computation of very high degree and order normalized associated Legendre functions," *Journal of Geodesy*, vol. 76, no. 5, pp. 279–299, May 2002.

[141] Honeywell, Aeronautical Division, "Analysis of the application of image-forming photosensors to wide-field-of-view star trackers," Air Force Systems Command, Research and Technology Division, Wright-Patterson Air Force Base, OH, Tech. Rep. AL TDR 64-190, 20 Aug. 1964.

[142] F. R. Hoots and R. L. Roehrich, "Spacetrack report no. 3: Models for propagation of NORAD element sets," Aerospace Defense Command, U.S. Air Force, Tech. Rep., Dec. 1980. [Online]. Available: https://celestrak.com/NORAD/documentation/spacetrk.pdf

[143] D. D. Howard, "Radar target angular scintillation in tracking and guidance systems," Naval Research Laboratory, Washington, DC, Tech. Rep. 5430, 23 Dec. 1959.

[144] D. Y. Hsu, "Comparison of four gravity models," in *Proceedings of the IEEE Position, Location and Navigation Symposium*, Atlanta, GA, 22–26 Aug. 1996, pp. 631–635.

[145] E. R. Huggins, "On teaching the lack of simultaneity," *American Journal of Physics*, vol. 43, no. 7, pp. 599–601, Jul. 1975.

[146] IAU SOFA Board, "IAU SOFA software collection." [Online]. Available: http://www.iausofa.org

[147] IERS/IVS Working Group, "The second realization of the international celestial reference frame by very long baseline interferometry," International Earth Rotation and Reference Systems Service, Frankfurt am Main, Germany, Tech. Rep. 35, 2009.

[148] N. Inaba, A. Matsumoto, H. Hase, S. Kogure, M. Sawabe, and K. Terada, "Design concept of quasi zenith satellite system," *Acta Astronautica*, vol. 65, no. 7–8, pp. 1068–1075, Oct. – Nov. 2009.

[149] *IEEE Standard for Floating Point Arithmetic*, Institute for Electrical and Electronics Engineers Std. IEEE Std 754-2008, 29 Aug. 2008.

[150] *Annex 10 to the Convention on International Civil Aviation, Aeronautical Telecommunications*, International Civil Aviation Organization Std., Jul. 2007.

[151] International Maritime Organization, *International Conference on Tonnage Measurement of Ships, 1969: Final Act of the Conference, with attachments, including the International Convention on Tonnage Measurement of Ships*. London: International Maritime Organization, 1983. [Online]. Available: http://www.uscg.mil/hq/msc/tonnage/docs/TM_Convention_Draft_Text_Version_With_Figures.pdf

[152] *SOLAS Consolidated Edition 2009*, International Maritime Organization Std., Dec. 2009, the URL goes the the relevant chapter (V) of the 2002 edition.; the full, up-to date document is not online for free. [Online]. Available: http://www.imo.org/ourwork/facilitation/documents/solas%20v%20on%20safety%20of%20navigation.pdf

[153] International Telecommunication Union. (2012, 26 Nov.) Space network list online. [Online]. Available: http://www.itu.int/snl/freqtab_snl.html

[154] ——. (2013, 18 Jun.) Status of coordinated universal time (UTC) study in ITU-R. [Online]. Available: http://www.itu.int/net/newsroom/wrc/2012/reports/atomic_time.aspx

[155] *Technical Characteristic for an Automatic Identification System Using Time-Division Multiple Access in the VHF Maritime Mobile Band*, International Telecommunication Union, Radiocommunication Sector Std. M.1371-4, Apr. 2010. [Online]. Available: http://www.itu.int/rec/R-REC-M.1371-4-201004-I/

[156] S. Islam, M. Sadiq, and M. S. Qureshi, "Assessing polynomial approximation for δt," *Journal of Basic and Applied Sciences*, vol. 4, no. 1, 2008.

[157] ——, "Error minimization of polynomial approximation of delta T," *Journal of Astrophysics and Astronomy*, vol. 29, no. 3–4, pp. 363–366, Dec. 2008.

[158] M.-T. Jaekel and S. Reynaud, "Radar ranging and Doppler tracking in post-Einsteinian metric theories of gravity," *Classical and Quantum Gravity*, vol. 23, no. 24, pp. 7561–7579, 21 Dec. 2006.

[159] C. Jekeli, "An analysis of vertical deflections derived from high-degree spherical harmonic models," *Journal of Geodesy*, vol. 73, no. 1, pp. 10–22, Feb. 1999.

[160] ——, "Heights, the geopotential, and vertical datums," The Ohio State University, Columbus, OH, Tech. Rep. OSHU-TB-054, 2001.

[161] S. C. Johnson and N. G. Fitz-Coy, "Minimal attitude parameterizations for data fusion," *Journal of Guidance, Control, and Dynamics*, vol. 37, no. 4, pp. 1356–1361, Jul. – Aug. 2014.

[162] Joint Range Instrumentation Accuracy Group Range Commanders Council, "Using satellites for radar performance monitoring and calibration," Secretariat Range Commanders Council, U.S. Army White Sands Missile Range, NM, Tech. Rep. 753-95, Mar. 1995.

[163] L. Joon and L. You-Chol, "Transfer alignment considering measurement time delay and ship body flexure," *Journal of Mechanical Science and Technology*, vol. 23, no. 1, pp. 195–203, Jan. 2009.

[164] T. Jorgensen and R. Rothrock, "Correcting for bias in Mahalanobis and log-likelihood estimates," *IEEE Transactions on Aerospace and Electronic Systems*, vol. 46, no. 4, pp. 2078–2089, Oct. 2010.

[165] P. E. Jupp and K. V. Mardia, "Maximum likelihood estimators for the matrix von Mises-Fisher and Bingham distributions," *The Annals of Statistics*, vol. 7, no. 3, pp. 599–606, 1979.

[166] N. Kaiser, J. L. Tonry, and G. A. Luppino, "A new strategy for deep wide-field high-resolution optical imaging," *Publications of the Astronomical Society of the Pacific*, vol. 112, no. 772, pp. 768–800, Jun. 2000.

[167] A. Kamel, "Precise spacecraft camera image navigation and registration," U.S. Patent 5,963,166, Oct. 5, 1999.

[168] A. A. Kamel, D. E. Ekman, J. Savides, and G. J. Zwirn, "Star sightings by satellite for image navigation," U.S. Patent 4,746,976, May 24, 1988.

[169] P. Kammeyer, "A UT1-like quantity from analysis of GPS orbit planes," *Celestial Mechanics and Dynamical Astronomy*, vol. 77, no. 4, pp. 241–272, Aug. 2000.

[170] K. Kanatani, "Analysis of 3-D rotation fitting," *IEEE Transactions on Pattern Analysis and Machine Intelligence*, vol. 16, no. 5, pp. 543–549, May 1994.

[171] L. H. Kantha and C. A. Clayson, *Numerical Models of Oceans and Oceanic Processes*. Academic Press, 2000.

[172] G. H. Kaplan, "Determining the position and motion of a vessel from celestial observations," *Navigation*, vol. 42, no. 4, pp. 633–650, 1995. [Online]. Available: http://aa.usno.navy.mil/publications/reports/GK_posmo.pdf

[173] ——, "A navigation solution involving changes to course and speed," *Navigation*, vol. 43, no. 4, pp. 469–482, 1996. [Online]. Available: http://oai.dtic.mil/oai/oai?verb=getRecord&metadataPrefix=html&identifier=ADA434100

[174] ——, "New technology for celestial navigation," in *Proceedings, Nautical Almanac Office Sesquicentennial Symposium*, U.S. Naval Observatory, 3–9 Mar. 1999, pp. 239–254, slides available. [Online]. Available: http://gkaplan.us/content/NewTech.html

[175] ——, "Celestial pole offsets: Conversion from (dx,dy) to (dψ,dε)," U.S. Naval Observatory, Tech. Rep., May 2005. [Online]. Available: http://aa.usno.navy.mil/publications/reports/dXdY_to_dpsideps.pdf

[176] ——, "The IAU resolutions on astronomical reference systems, time scales, and Earth rotation models: Explanation and implementation," U.S. Naval Observatory, Tech. Rep. 179, 20 Oct. 2005. [Online]. Available: http://aa.usno.navy.mil/publications/docs/Circular_179.pdf

[177] ——, "Angle-only navigation: Position and velocity solution from absolute triangulation," *Navigation*, vol. 58, no. 3, pp. 187–201, Fall 2011.

[178] S. M. Karsenti, "A study of IMU alignment transfer," Master's thesis, Massachusetts Institute of Technology, Cambridge, MA, Feb. 1989.

[179] K. J. Kasunic, *Optical Systems Engineering*. New York: McGraw Hill, 2011.

[180] S. V. Kibe, "Indian plan for satellite-based navigation systems for civil aviation," *Current Science*, vol. 84, no. 11, pp. 1405–1411, 10 Jun. 2003.

[181] Y. Kinashi and D. Salazar, "Attitude determination and alignment using electro-optical sensors and global navigation satellites," U.S. Patent 6,463,366 B2, Oct. 8, 2002.

[182] G. Kirchner and F. Koidl, "SLR Graz: Laser ranging to space debris objects," in *Proceedings of the International Technical Laser Workshop*, Rome, Italy, 5–9 Nov. 2012, slides. [Online]. Available: http://www.lnf.infn.it/conference/laser2012/4thursday/7_5georg/georg_s.pdf

[183] G. Kirchner, F. Koidl, F. Friederich, I. Buske, U. Völkner, and W. Riede, "Laser measurements to space debris from Graz SLR station," *Advances in Space Research*, vol. 51, no. 1, pp. 21–24, Jan. 2013.

[184] S. A. Klioner, "A practical relativistic model for microarcsecond astrometry in space," *The Astronomical Journal*, vol. 125, no. 3, pp. 1580–1597, Mar. 2003.

[185] W. Koch, *Tracking and Sensor Data Fusion: Methodological Framework and Selected Applications*. Heidelberg: Springer, 2014.

[186] A. S. Konopliv *et al.*, "The JPL lunar gravity field to spherical harmonic degree 660 from the GRAIL primary mission," *Journal of Geophysical Research: Planets*, vol. 118, no. 7, pp. 1415–1434, Jul. 2013.

[187] S. Kopeikin, M. Efroimsky, and G. Kaplan, *Relativistic Celestial Mechanics of the Solar System*. Weinheim, Germany: WILEY-VCH Verlag GmbH & Co. KGaA, 2011.

[188] S. M. Kopeikin and E. B. Fomalont, "On the speed of gravity and relativistic v/c corrections to the Shapiro time delay," *Physics Letters A*, vol. 355, no. 3, pp. 163–166, 3 Jul. 2006.

[189] B. D. Kragel, S. Danford, S. M. Herman, and A. B. Poore, "Bias estimation using targets of opportunity," in *Proceedings of SPIE: Signal and Data Processing of Small Targets*, vol. 6699, San Diego, CA, 26 Aug. 2007.

[190] B. D. Kragel, S. Danford, and A. B. Poore, "Concurrent MAP data association and absolute bias estimation with an arbitrary number of sensors," in *Proceedings of SPIE: Signal and Data Processing of Small Targets*, vol. 6969, Orlando, FL, 16 Mar. 2008.

[191] B. A. Kriegsman and K. B. Mahar, "Gravity-model errors in mobile inertial-navigation systems," *Journal of Guidance, Control, and Dynamics*, vol. 9, no. 3, pp. 312–318, May – Jun. 1986.

[192] J. Kuhn, "Relevant information about using a mobile phone acceleration sensor in physics experiments," *American Journal of Physics*, vol. 82, no. 2, p. 94, Feb. 2014.

[193] J. H. Kwon and C. Jekeli, "Gravity requirements for compensation of ultra-precise inertial naviga-tion," *The Journal of Navigation*, vol. 58, no. 3, pp. 479–492, Sep. 2005.

[194] D. Last, "GNSS: The present imperfect," *InsideGNSS*, pp. 60–64, May 2010.

[195] M. Laue, "Die Mitführung des Lichtes durch bewegte Körper nach dem Relativitätsprinzip," *Annalen der Physik*, vol. 328, no. 10, pp. 989–990, 1907.

[196] P. Y. Le Traon, P. Schaeffer, S. Guinehut, M. H. Rio, F. Hernandez, G. Larnicol, and J. M. Lemoine, "Mean ocean dynamic topography from GOCE and altimetry," in *International GOCE User Workshop*, ESTEC, Noordwijk, The Netherlands, 2001, pp. 135–139. [Online]. Available: http://earth.esa.int/goce04/first_igw/papers/Letraon_etal.pdf

[197] E. J. Lefferts, F. L. Markley, and M. D. Shuster, "Kalman filtering for spacecraft attitude estimation," *Journal of Guidance, Control and Dynamics*, vol. 5, no. 5, pp. 417–429, Sep. – Oct. 1982.

[198] F. G. Lemoine *et al.*, "The development of the joint NASA GSFC and the National Imagery and Mapping Agency (NIMA) geopotential model EGM96," National Aeronautics and Space Administration, Goddard Space Flight Center, Greenbelt, MD, Tech. Rep. NASA/TP-1998-206861, Jul. 1998. [Online]. Available: http://bowie.gsfc.nasa.gov/697/staff/lemoine/EGM96_NASA-TP-1998-206861.pdf

[199] M. Levedahl, "An explicit pattern matching assignment algorithm," in *Proceedings of SPIE: Signal and Data Processing of Small Targets*, vol. 4728, Orlando, FL, 1 Apr. 2002, pp. 461–469.

[200] M. D. Levedahl, "Method and system for assigning observations," U.S. Patent 7,092,924 B1, Aug. 15, 2006.

[201] A. Levin, M. Adams, and B. Marrison, "Part I: Terror attacks brought drastic decision: Clear the skies," *USA Today*, 12 Aug. 2002.

[202] X. R. Li and V. P. Jilkov, "Survey of maneuvering target tracking part II: Motion models of ballistic and space targets," *IEEE Transactions on Aerospace and Electronic Systems*, vol. 46, no. 1, pp. 96–119, Jan. 2010.

[203] C. C. Liebe, "Accuracy performance of star trackers – a tutorial," *IEEE Transactions on Aerospace and Electronic Systems*, vol. 38, no. 2, pp. 587–599, Apr. 2002.

[204] X. Lin, Y. Bar-Shalom, and T. Kirubarajan, "Multisensor-multitarget bias estimation for general asyn-chronous sensors," *IEEE Transactions on Aerospace and Electronic Systems*, vol. 41, no. 3, pp. 899–921, Jul. 2005.

[205] T. E. LLC. (2014, 18 Feb.) Skyview® free - explore the universe. [Online]. Available: https://itunes.apple.com/us/app/skyview-free-explore-universe/id413936865?mt=8

[206] G. Ludyk, *Einstein in Matrix Form: Exact Derivation of the Theory of Special and General Relativity without Tensors*.   Heidelberg: Springer, 2013.

[207] J. B. Lundberg and B. E. Schutz, "Recursion formulas of Legendre functions for use with nonsingular geopotential models," *Journal of Guidance, Control, and Dynamics*, vol. 11, no. 1, pp. 31–38, Jan. – Feb. 1988.

[208] B. Luzum and D. Gambis, "Earth rotation monitoring, UT1 determination and prediction," *Metrologia*, vol. 48, no. 4, pp. S165–S170, 2011.

[209] F. Lyard, F. Lefevre, T. Letellier, and O. Francis, "Modelling the global ocean tides: Modern insights from FES2004," *Ocean Dynamics*, vol. 56, no. 5–6, pp. 394–415, Dec. 2006.

[210] S. Macmillan and S. Grindrod, "Confidence limits associated with values of the Earth's magnetic field used for directional drilling," *SPE Drilling & Completion*, no. 2, pp. 230–238, 2010.

[211] K. V. Mardia and P. E. Jupp, *Directional Statistics*. Chichester, England: John Wiley & Sons, 2000.

[212] F. L. Markley, "Attitude determination using vector observations and the singular value decomposition," *The Journal of the Astronautical Sciences*, vol. 31, no. 3, pp. 245–258, Jul. – Sep. 1988.

[213] ——, "Attitude determination using vector observations: A fast optimal matrix algorithm," *The Journal of the Astronautical Sciences*, vol. 41, no. 2, pp. 261–280, Apr. – Jun. 1993.

[214] ——, "Attitude determination using two vector measurements," in *Proceedings of the Flight Mechanics Symposium*, NASA Goddard Space Flight Center, Greenbelt, MD, May 1999, pp. 39–52.

[215] F. L. Markley, Y. Cheng, J. L. Crassidis, and Y. Oshman, "Averaging quaternions," *Journal of Guidance, Control, and Dynamics*, vol. 30, no. 4, pp. 1193–1196, Jul. – Aug. 2007.

[216] G. E. Marsh and C. Nissim-Sabat, "Comment on 'The speed of gravity'," *Physics Letters A*, vol. 262, no. 2–3, pp. 257–260, 1 Nov. 1999.

[217] E. L. Mathers and P. L. Woodworth, "A study of departures from the inverse-barometer response of sea level to air-pressure forcing at a period of 5 days," *Quarterly Journal of the Royal Meteorological Society*, vol. 130, no. 597, pp. 725–738, Jan. 2004.

[218] J. D. Mathews, D. D. Meisel, K. P. Hunter, V. S. Getman, and Q. Zhou, "Very high resolution studies of micrometeors using the Arecibo MHz radar," *Icarus*, vol. 126, no. 1, pp. 157–169, Mar. 1997.

[219] S. Maus, "An ellipsoidal harmonic representation of Earth's lithospheric magnetic field to degree and order 720," *Geochemistry, Geophysics, Geosystems*, vol. 11, no. 6, Jun. 2010.

[220] S. Maus *et al.*, "EMAG2: A 2-arc min resolution Earth magnetic anomaly grid compiled from satellite, airborne, and marine magnetic measurements," *Geochemistry, Geophysics, Geosystems*, vol. 10, no. 8, 7 Aug. 2009. [Online]. Available: http://geomag.org/info/Smaus/Doc/emag2.pdf

[221] S. Maus, T. Sazonova, K. Hemant, J. D. Fairhear, and D. Ravat, "National geophysical data center candidate for the world digital magnetic anomaly map," *Geochemistry, Geophysics, Geosystems*, vol. 8, no. 6, 29 Jun. 2007. [Online]. Available: http://geomag.org/info/Smaus/Doc/wdmam.pdf

[222] S. Maus *et al.*, "High definition geomagnetic models: A new perspective for wellbore positioning," in *IADC/SPE Drilling Conference and Exhibition*, San Diego, CA, 6–8 Mar. 2012.

[223] S. Maus, S. McLean, M. Nair, C. Rollings, S. Macmillan, B. Hamilton, and A. Thomson, "The US/UK world magnetic model for 2010-2015," National Oceanic and Atmospheric Administration, National Geophysical Data Center, Tech. Rep., 2010. [Online]. Available: http://www.ngdc.noaa.gov/geomag/WMM/data/WMM2010/WMM2010_Report.pdf

[224] D. D. McCarthy, "Evolution of timescales from astronomy to physical metrology," *Metrologia*, vol. 48, no. 4, pp. S132–S144, Aug. 2011.

[225] D. D. McCarthy and G. Petit, *IERS Conventions (2003)*, International Earth Rotation and Reference Systems Service Std. 32, 2004.

[226] D. D. McCarthy and P. K. Seidelmann, *Time from Earth Rotation to Atomic Physics*. Weinheim, Germany: Wiley-VCH, 2009.

[227] K. M. Merrill and S. T. Ridgway, "Infrared spectroscopy of stars," *Annual Review of Astronomy and Astrophysics*, vol. 17, pp. 9–41, 1979.

[228] D. J. Miller, "Giant waves in Lituya Bay, Alaska," in *Shorter Contributions to General Geology 1959: Geological Survey Professional Paper 354*. Washington, DC: United States Government Printing Office, 1961, no. 354-C, pp. 51–83.

[229] N. Miller and Z. Malkin, "Joint analysis of the polar motion and celestial pole offset time series," in *Proceedings of the 7th IVS General Meeting*, Madrid, Spain, 4–9 Mar. 2012, pp. 385–389.

[230] MIT Game Lab. (2013) OpenRelativity. Massachusetts Institute of Technology. [Online]. Available: http://gamelab.mit.edu/research/openrelativity/

[231] S. Mohiuddin and M. L. Psiaki, "Continuous-time Kalman filtering with implicit discrete measurement times," *Journal of Guidance, Control, and Dynamics*, vol. 34, no. 1, pp. 148–163, Jan. – Feb. 2011.

[232] P. J. Mohr, B. N. Taylor, and D. B. Newell, "CODATA recommended values of the fundamental physical constants: 2010," *Journal of Physical and Chemical Reference Data*, vol. 41, no. 4, Dec. 2012.

[233] A. Monet, G. Kaplan, and W. Harris, "Testing coordinate frame transformations NOVAS vs SOFA," U.S. Naval Observatory, Washington, DC, Tech. Rep. 2014-04, 14 Jul. 2010.

[234] O. Montenbruck and E. Gill, *Satellite Orbits: Models, Methods, Applications*. Berlin: Springer, 2000.

[235] J. R. Moore and W. D. Blair, "Practical aspects of multitarget tracking," in *Multitarget-Multisensor Tracking: Applications and Advances*, Y. Bar-Shalom and W. D. Blair, Eds. Boston: Artech House, 2000, vol. 3, ch. 1.

[236] H. Moritz, "Geodetic reference system 1980," *Bulletin géodésique*, vol. 54, no. 3, pp. 395–405, 1980.

[237] ——, *Advanced Physical Geodesy*. Columbus, OH: Ohio State University, 2008.

[238] L. V. Morrison and F. R. Stephenson, "Historical values of the Earth's clock error δt and the calculation of eclipses," *Journal for the History of Astronomy*, vol. 35, no. 2, pp. 327–336, 2004.

[239] J. J. Mueller and T. D. Syrett, "The smartphone royalty stack: Surveying royalty demands for the components within modern smartphones," WilmerHale, Tech. Rep., 29 May 2014. [Online]. Available: http://www.wilmerhale.com/pages/publicationsandnewsdetail.aspx?NewsPubId=17179872441

[240] National Geospatial Intelligence Agency. (2013, 30 Apr.) NGA: Office of Geomatics. [Online]. Available: http://earth-info.nga.mil/GandG/

[241] *U.S. Standard Atmosphere, 1976*, National Oceanic and Atmospheric Administration Std., Oct. 1976.

[242] R. A. Nelson, "Generalized Lorentz transformation for an accelerated, rotating frame of reference," *Journal of Mathematical Physics*, vol. 28, no. 10, pp. 2379–2383, Oct. 1987.

[243] NGA Office of Geomatics. (2014, 16 May) WGS 84 and the web mercator projection. National Geospatial Intelligence Agency. A slide presentation on the linked page. [Online]. Available: http://earth-info.nga.mil/GandG/wgs84/web_mercator/index.html

[244] R. N. Nof, A. Ziv, M. P. Doin, G. Baer, Y. Fialko, S. Wdowinski, Y. Eyal, and Y. Bock, "Rising of the lowest place on Earth due to Dead Sea water-level drop: Evidence from SAR interferometry and GPS," *Journal of Geophysical Research*, vol. 117, no. B5, May 2012.

[245] "Ln-120g stellar-inertial-GPS navigation," Northrop Grumman, Tech. Rep., Mar. 2010. [Online]. Available: http://www.northropgrumman.com/Capabilities/LN120GStellarInertialNavigationSystem/Documents/ln120g.pdf

[246] Office of the NGA Historian, "The advent of the National Geospatial-Intelligence Agency," National Geospatial-Intelligence Agency, Tech. Rep., Sep. 2011. [Online]. Available: https://www1.nga.mil/About/Documents/04a_History.pdf

[247] H.-T. Ong, B. Ristic, and M. G. Oxenham, "Sensor registration using airlanes," in *Proceedings of the Fifth International Conference on Information Fusion*, vol. 1, Annapolis, MD, 8–11 Jul. 2002, pp. 354–360.

[248] C. Padgett, K. Kreutz-Delgado, and S. Udomkesmalee, "Evaluation of star identification techniques," *Journal of Guidance, Control, and Dynamics*, vol. 20, no. 2, pp. 259–267, Mar. – Apr. 1997.

[249] D. J. Papageorgiou and M. Holender, "Track-to-track association and ambiguity management in the presence of sensor bias," *Journal of Advances in Information Fusion*, vol. 6, no. 2, pp. 77–100, Dec. 2011.

[250] G. C. Parkinson, D. P. Xue, and M. Farooq, "Registration in a distributed multi-sensor environment," in *Proceedings of the 40th Midwest Symposium on Circuits and Systems*, vol. 2, Sacramento, CA, 3–6 1997, pp. 993–996.

[251] N. K. Pavlis, J. K. Factor, and S. A. Holmes, "Terrain-related gravimetric quantities computed for the next EGM," in *Gravity Field of the Earth: Proceedings of the 1st International Symposium of the International Gravity Field Service*, vol. 18, Istanbul, Turkey, 28 Aug. – 1 Sep. 2006, pp. 318–323.

[252] N. K. Pavlis, S. A. Holmes, S. C. Kenyon, and J. K. Factor, "The development and evaluation of the Earth gravitational model 2008 (EGM2008)," *Journal of Geophysical Research*, vol. 117, no. B4, Apr. 2012.

[253] N. K. Pavlis, S. A. Holmes, S. C. Kenyon, and F. J. K., "Correction to 'The development and evaluation of the Earth gravitational model 2008 (EGM2008)'," *Journal of Geophysical Research*, vol. 118, 2013.

[254] N. T. Penna, M. S. Bos, T. F. Baker, and H. G. Scherneck, "Assessing the accuracy of predicted ocean tide loading displacement values," *Journal of Geodesy*, vol. 82, no. 12, pp. 893–907, Dec. 2008.

[255] V. Perlick, *Ray Optics, Fermat's Principle, and Applications to General Relativity*. Berlin, Germany: Springer-Verlag, 2000.

[256] G. Petit, "A new realization of terrestrial time," in *Proceedings of the 35th Annual Precise Time and Time Interval Meeting*, San Diego, CA, 2–4 Dec. 2003.

[257] G. Petit and B. Luzum, *IERS Conventions (2010)*, International Earth Rotation and Reference Systems Service Std. 36, 2010.

[258] G. Petit and P. Wolf, "Relativistic theory for time comparisons: A review," *Metrologia*, vol. 42, no. 3, pp. S138–S144, Jun. 2005.

[259] W. F. Phillips, C. E. Hailey, and G. A. Gebert, "Review of attitude representations used for aircraft kinematics," *Journal of Aircraft*, vol. 38, no. 4, pp. 718–737, Jul. – Aug. 2001.

[260] ——, "Errata: Review of attitude representations used for aircraft kinematics," *Journal of Aircraft*, vol. 40, no. 1, p. 223, Jan. – Feb. 2003.

[261] J. M. Picone, A. E. Hedin, D. P. Drob, and A. C. Aikin, "NRLMSISE-00 empirical model of the atmosphere: Statistical comparisons and scientific issues," *Journal of Geophysical Research*, vol. 107, no. A12, Dec. 2002. [Online]. Available: http://ntrs.nasa.gov/archive/nasa/casi.ntrs.nasa.gov/20020038771.pdf

[262] S. Pines, "Uniform representation of the gravitational potential and its derivatives," *AIAA Journal*, vol. 11, no. 11, pp. 1508–1511, Nov. 1973.

[263] V. A. Popovkin and A. N. Perminov, "Global navigation satellite system GLONASS interface control document," Russian Institute of Space Device Engineering, Tech. Rep., 2008. [Online]. Available: http://facility.unavco.org/data/docs/ICD_GLONASS_5.1_(2008)_en.pdf

[264] M. Poutanen, M. Vermeer, and J. Mäkinen, "The permanent tide in GPS positioning," *Journal of Geodesy*, vol. 70, no. 8, pp. 499–504, May 1996.

[265] T. Quinn, "Time, the SI and the metre convention," *Metrologia*, vol. 48, no. 4, pp. S121–S124, Aug. 2011.

[266] A. M. Rad, J. H. Nobari, and A. A. Nikkhah, "Optimal attitude and position determination by integration of INS, star tracker, and horizon sensor," *IEEE Aerospace and Electronic Systems Magazine*, vol. 29, no. 4, pp. 20–33, Apr. 2014.

[267] S. A. Radhakrishnan, "GAGAN system ready for operations," *The Hindu*, 11 Jan. 2014. [Online]. Available: http://www.thehindu.com/news/national/kerala/gagan-system-ready-for-operations/article5565700.ece

[268] S. K. Range, "Gravity Probe B examining Einstein's spacetime with gyroscopes: An educator's guide," National Aeronautics and Space Administration, Tech. Rep., Oct. 2004. [Online]. Available: http://einstein.stanford.edu/content/education/GP-B_T-Guide4-2008.pdf

[269] R. H. Rapp, "Use of potential coefficient models for geoid undulation determinations using a spherical harmonic representation of the height anomaly/geoid undulation difference," *Journal of Geodesy*, vol. 71, no. 5, pp. 282–289, Apr. 1997.

[270] ——, "Geometric geodesy, part I," Ohio State University Department of Geodetic Science and Surveying, Tech. Rep., Apr. 1991. [Online]. Available: http://hdl.handle.net/1811/24333

[271] ——, "Geometric geodesy, part II," Ohio State University Department of Geodetic Science and Surveying, Tech. Rep., Mar. 1993. [Online]. Available: http://hdl.handle.net/1811/24409

[272] "Standard 22: Anschütz gyro compass system," Raytheon Anschütz, Kiel, Germany, Tech. Rep., 2014. [Online]. Available: http://www.raytheon-anschuetz.com/data/media/products_downloads/39/file_0/standard22-gyro-compass.pdf

[273] O. Razumovskaya, "iPhone 4S supports Russia's GLONASS navigation system," *The Wall Street Journal*, 20 Oct. 2011. [Online]. Available: http://blogs.wsj.com/tech-europe/2011/10/20/iphone-4s-supports-russias-glonass-navigation-system/

[274] R. B. Roncoli, "Lunar constants and models document," Jet Propulsion Laboratory, California Institute of Technology, Tech. Rep. JPL D-32296, 23 Sep. 2005. [Online]. Available: http://www.hq.nasa.gov/alsj/lunar_cmd_2005_jpl_d32296.pdf

[275] A. M. Rosenwinkel, "Geoposition determination by starlight refraction measurement," U.S. Patent 8,767,072 B1, Jul. 1, 2014.

[276] A. M. Rosenwinkel and C. V. Jannetti, "Geoposition determination from star and satellite observations," U.S. Patent 8,676,490 B1, Mar. 18, 2014.

[277] P. Rouger, "Guidance and control of artillery projectiles with magnetic sensors," in *Proceedings of the 45th AIAA Aerospace Sciences Meeting and Exhibit*, Reno, NV, 8–11 Jan. 2007.

[278] A. Rødningsby, Y. Bar-Shalom, O. Hallingstad, and J. Glattetre, "Multitarget multisensor tracking in the presence of wakes," *Journal of Advances in Information Fusion*, vol. 4, no. 2, pp. 117–145, Dec. 2009.

[279] Y. V. Savenko, P. O. Bemayenenko, and Y. F. Zinkovskiy, "High sensitive precise 3D accelerometer for solar system exploration with unmanned spacecrafts," in *Proceedings of the 35th COSPAR Scientific Assembly*, Paris, France, 18–25 Jul. 2004, extended abstract and citation available; full article/ proceedings could not be found. [Online]. Available: http://adsabs.harvard.edu/abs/2004cosp.meet.4575S

[280] B. E. Schaefer, "The origin of the Greek constellations," *Scientific American*, vol. 295, no. 5, pp. 96–101, Nov. 2006.

[281] E. W. Schwiderski, "On charting global ocean tides," *Reviews of Geophysics and Space Physics*, vol. 18, no. 1, pp. 243–268, Feb. 1980.

[282] P. D. D. Schwindt, S. Knappe, V. Shah, L. Hollberg, J. Kitching, L.-A. Liew, and J. Moreland, "Chip-scale atomic magnetometer," *Applied Physics Letters*, vol. 85, no. 26, pp. 6409–6411, 27 Dec. 2004.

[283] P. H. Schönemann, "A generalized solution of the orthogonal Procrustes problem," *Psychometrika*, vol. 31, no. 1, pp. 1–10, Mar. 1966.

[284] L. J. Sczaniecki, "Gridlock processing method," U.S. Patent 7,672,801 B1, Mar. 2, 2010.

[285] K. P. Seidelmann, Ed., *Explanatory Supplement to the Astronomical Almanac*, 2nd ed.   Mill Valley, CA: University Science Books, 1992.

[286] P. K. Seidelmann, R. Gaume, N. Zacharias, K. J. Johnston, and B. Dorland, "Optical reference stars for space surveillance: Future plans: Latest developments," U.S. Naval Observatory, Washington, DC, Tech. Rep., 2010. [Online]. Available: http://www.dtic.mil/docs/citations/ADA520456

[287] A. Seryi and P. A. Moore, "Accelerator on the move, but scientists compensate for tidal effects," *Stanford Report*, 29 Mar. 2000. [Online]. Available: http://news.stanford.edu/news/2000/march29/linac-329.html

[288] M. D. Shuster, "Approximate algorithms for fast optimal attitude computation," in *Proceedings of the AIAA Guidance and Control Conference*, Palo Alto, CA, 7–9 Aug. 1978.

[289] ——, "Maximum likelihood estimation of spacecraft attitude estimation," *The Journal of the Astronautical Sciences*, vol. 37, no. 1, pp. 79–88, Jan. – Mar. 1989.

[290] ——, "A survey of attitude representations," *The Journal of the Astronautical Sciences*, vol. 41, no. 4, pp. 439–517, Oct. – Dec. 1993.

[291] ——, "Uniform attitude probability distributions," *The Journal of the Astronautical Sciences*, vol. 51, no. 4, pp. 451–475, Oct. – Dec. 2003.

[292] ——, "The generalized Wahba problem," *The Journal of the Astronautical Sciences*, vol. 54, no. 2, pp. 245–259, Apr. – Jun. 2006.

[293] M. D. Shuster and S. D. Oh, "Three-axis attitude determination from vector observations," *Journal of Guidance, Control, and Dynamics*, vol. 4, no. 1, pp. 70–77, Jan. 1981.

[294] K. Silver, "An intuitive approach to the Coriolis effect," Master's thesis, Uppsala Universitet, Uppsala, Sweden, 2011. [Online]. Available: http://urn.kb.se/resolve?urn=urn:nbn:se:uu:diva-168017

[295] A. T. Sinclair, "The effect of atmospheric refraction on laser ranging data," United Kingdom Hydrographic Office, HM Nautical Almanac, Tech. Rep. 59, 1982.

[296] L. E. Sjöberg, "Closed-form and iterative weighted least squares solutions to Helmert transformation parameters," *Journal of Geodetic Science*, vol. 3, no. 1, pp. 7–11, Mar. 2013.

[297] ——, "New solutions for the geoid potential w_0 and the mean Earth ellipsoid dimensions," *Journal of Geodetic Science*, vol. 3, no. 4, pp. 258–265, Dec. 2013.

[298] A. J. E. Smith, "Application of satellite altimetry for ocean global tide modeling," Ph.D. dissertation, Technische Universiteit Delft, Delft, The Netherlands, 1999.

[299] D. Smith. (1997, 12 May) Permanent tide systems. National Geodetic Survey. [Online]. Available: http://www.ngs.noaa.gov/GEOID/tidepot.html

[300] D. A. Smith, "There is no such thing as 'the' EGM96 geoid: Subtle points on the use of a global geopotential model," *IGeS Bulletin*, no. 8, pp. 17–28, 1998. [Online]. Available: http://www.ngs.noaa.gov/PUBS_LIB/EGM96_GEOID_PAPER/egm96_geoid_paper.html

[301] R. Snay, "NGS geodetic toolkit, part 5: Horizontal time-dependent positioning," *Professional Surveyor Magazine*, vol. 23, no. 11, Nov. 2003. [Online]. Available: https://www.ngs.noaa.gov/TOOLS/ Professional_Surveyor_Articles/Professional_Surveyor_Magazine-Geodetic_Toolkit_Pt5-Nov03.pdf

[302] J. P. Snyder, *Map Projections: A Working Manual*. Washington, DC: United States Government Printing Office, 1987, no. 1532. [Online]. Available: http://pubs.er.usgs.gov/publication/pp1395

[303] D. Sobel, *Longitude: The True Story of a Lone Genius Who Solved the Greatest Scientific Problem of His Time*. New York: Walker & Company, 2007.

[304] I. Sofair, "Improved method for calculating exact geodetic latitude and altitude," *Journal of Guidance, Control, and Dynamics*, vol. 20, no. 4, pp. 824–826, Jul.–Aug. 1997.

[305] ——, "Improved method for calculating exact geodetic latitude and altitude revisited," *Journal of Guidance, Control, and Dynamics*, vol. 23, no. 2, p. 369, Mar. 2000.

[306] T. Soler. (2006, 5 Dec.) Transformations between NAD83 and WGS84. GPS World – Discussion Forums. [Online]. Available: www.ngs.noaa.gov/CORS/Articles/WGS84NAD83.pdf

[307] K. Sośnica, D. Thaller, A. Jäggi, R. Dach, and G. Beutler, "Sensitivity of LAGEOS orbits to global gravity field models," *Artificial Satellites*, vol. 47, no. 2, pp. 47–65, Jun. 2012.

[308] J. L. Spencer, "Pines' nonsingular gravitational potential derivation, description and implementation," National Aeronautics and Space Administration, Lyndon B. Johnson Space Center, Tech. Rep. MDC-W0013, 9 Feb. 1976.

[309] B. B. Spratling IV and D. Mortari, "A survey on star identification algorithms," *Algorithms*, vol. 2, no. 1, pp. 93–107, Mar. 2009.

[310] T. Springer and F. Dilssner, "SVN49 and other GPS anomalies: Elevation-dependent pseudorange errors in blocks IIRs and IIR-Ms," *InsideGNSS*, pp. 32–36, Jul./Aug. 2009.

[311] S. Sra, "A short note on parameter approximation for von Mises-Fisher distributions and a fast implementation of $i_s(x)$," *Computational Statistics*, vol. 27, no. 1, pp. 177–190, Mar. 2012.

[312] B. St-Louis, "INTERMAGNET technical reference manual," INTERMAGNET, United Kingdom, Tech. Rep., 2011. [Online]. Available: http://www.intermagnet.org/publications/im_manual.pdf

[313] E. M. Standish, "Time scales in JPL and CfA ephemerides," *Bulletin of the American Astronomical Society*, vol. 30, Sep. 1998. [Online]. Available: http://iau-comm4.jpl.nasa.gov/timescales.pdf

[314] B. Stanfill, "Statistical methods for random rotations," Ph.D. dissertation, Iowa State University, Ames, IA, 2014. [Online]. Available: http://lib.dr.iastate.edu/cgi/viewcontent.cgi?article= 4767&context=etd

[315] "Ultra-compact high-performance ecompass module: 3D accelerometer and 3D magnetometer," STMicroelectronics, Tech. Rep. LSM303D, Nov. 2013. [Online]. Available: http://www.st.com/ web/en/resource/technical/document/datasheet/DM00057547.pdf

[316] L. D. Stone, M. L. Williams, and T. M. Tran, "Track-to-track association and bias removal," in *Proceedings of SPIE: Signal and Data Processing of Small Targets*, vol. 4728, Orlando, FL, 1 Apr. 2002, pp. 315–329.

[317] W. Storms, J. Shockley, and J. Raquet, "Magnetic field navigation in an indoor environment," in *Proceedings of Ubiquitous Positioning Indoor Navigation and Location Based Services*, Kirkkonummi, Finland, 14–15 Oct. 2010.

[318] B. Streetman and M. A. Peck, "New synchronous orbits using the geomagnetic Lorentz force," *Journal of Guidance, Control, and Dynamics*, vol. 30, no. 6, pp. 1677–1690, Nov. – Dec. 2007.

[319] J. Stuelpnagel, "On the parameterization of the three-dimensional rotation group," *SIAM Review*, vol. 6, no. 4, pp. 422–430, Oct. 1964.

[320] J. S. Subirana, J. M. J. Zornoza, and M. Hernándes-Pajarez, "GNSS data processing: Volume I: Fundamentals and algorithms," European Space Agency, Tech. Rep., May 2013. [Online]. Available: www.navipedia.net/GNSS_Book/ESA_GNSS-Book_TM-23_Vol_I.pdf

[321] E. Sviestins, "Bias estimation method for a target tracking system," U.S. Patent 6,359,586 B1, Mar. 19, 2002.

[322] K. R. Symon, *Mechanics*, 3rd ed. Reading, MA: Addison-Wesley, 1971.

[323] L. G. Taff, "Relativity and radars," Lincoln Laboratory, Tech. Rep. 660, 11 Jun. 1983.

[324] E. Taghavi, R. Tharmarasa, T. Kirubarajan, and Y. Bar-Shalom, "Bias estimation for practical distributed multiradar-multitarget tracking systems," in *Proceedings of the 16th International Conference on Information Fuson*, Istanbul, Turkey, 9–12 Jul. 2013.

[325] D. Teagle and B. Ildefonse, "Journey to the mantle of the earth," *Nature*, vol. 471, pp. 437–439, 24 Mar. 2011.

[326] "The world's smallest digital marine gyrocompass," Teledyne TSS, Tech. Rep., Feb. 2008. [Online]. Available: http://www.seatronics-group.com/assets/uploads/resources/2010/3/2f204527-a10b-4bb6-b39c-5ab1058e2550.pdf

[327] R. Tenzer, P. Vaníček, M. Santos, W. E. Featherstone, and M. Kuhn, "The rigorous determination of orthometric heights," *Journal of Geodesy*, vol. 79, no. 1–3, pp. 82–92, Jun. 2005.

[328] W. Tian, Y. Wang, X. Shan, and J. Yang, "Track-to-track association for biased data based on the reference topology feature," *IEEE Signal Processing Letters*, vol. 21, no. 4, pp. 449–453, Apr. 2014.

[329] P. Tregoning and R. Jackson, "The need for dynamic datums," *Geomatics Research Australasia*, vol. 71, pp. 87–102, Dec. 1999.

[330] S. Tsujii, M. Bando, and H. Yamakawa, "Spacecraft formation flying dynamics and control using geomagnetic Lorentz force," *Journal of Guidance, Control, and Dynamics*, vol. 36, no. 1, pp. 136–148, Jan. – Feb. 2013.

[331] S. Umeyama, "Least-squares estimation of transformation parameters between two point patterns," *IEEE Transactions on Pattern Analysis and Machine Intelligence*, vol. 13, no. 4, pp. 376–380, Apr. 1991.

[332] S. E. Urban and K. P. Seidelmann, Eds., *Explanatory Supplement to the Astronomical Almanac*, 3rd ed. Mill Valley, CA: University Science Books, 2013.

[333] U.S. Department of Transportation, "Standard for aeronautical surveys and related products," Federal Aviation Administration, Tech. Rep. 405, Sep. 1996. [Online]. Available: http://www.ngs.noaa.gov/AERO/aerospecs.htm#FAA405

[334] ——, "Advisory circular: Altitude reporting equipment and transponder system maintenance and inspection practice," Federal Aviation Administration, Tech. Rep. 43-6C, 17 Sep. 2012. [Online]. Available: http://www.faa.gov/documentLibrary/media/Advisory_Circular/AC%2043-6C.pdf

[335] ——, "Aeronautical information manual: Official guide to basic flight information and ATC procedures," Federal Aviation Administration, Tech. Rep., 3 Apr. 2014. [Online]. Available: https://www.faa.gov/air_traffic/publications/atpubs/aim/Index.htm

[336] ——. (2014, Feb.) Digital products. Washington, DC. [Online]. Available: http://www.faa.gov/air_traffic/flight_info/aeronav/digital_products/

[337] U.S. Naval Observatory. (2011, 13 Sep.) Naval Observatory Vector Astrometry Software (NOVAS). [Online]. Available: http://aa.usno.navy.mil/software/novas/novas_info.php

[338] ——. (2013, Jun.) International time scales and the B.I.P.M. [Online]. Available: http://www.usno.navy.mil/USNO/time/master-clock/international-time-scales-and-the-b.i.p.m

[339] D. A. Vallado, P. Crawford, R. Hujsak, and T. S. Kelso, "Revisiting spacetrack report #3: Rev 2," in *Proceedings of the AIAA/AAS Astrodynamics Specialist Conference*, Keystone, CO, 21–24 Aug. 2006. [Online]. Available: http://celestrak.com/publications/AIAA/2006-6753/AIAA-2006-6753-Rev2.pdf

[340] D. A. Vallado, P. Crawford, R. Hujsak, and T. Kelso, "Implementing the revised SGP4 in STK," in *Proceedings of the AGI User Exchange*, Washington, DC, 17–18 Oct. 2006, slides. [Online]. Available: http://www.agi.com/downloads/events/2006-agi-user-exchange/8_revised_sgp4_vallado2.pdf

[341] D. A. Vallado, J. H. Seago, and P. K. Seidelmann, "Implementation issues surrounding the new IAU reference systems for astrodynamics," in *Proceedings of the 16th AAS/AIAA Space Flight Mechanics Conference*, Tampa, FL, 22–26 Jan. 2006. [Online]. Available: http://www.centerforspace.com/downloads/files/pubs/AAS-06-134.pdf

[342] J. C. Van der Ha and M. D. Shuster, "A tutorial on vectors and attitude," *IEEE Control Systems Magazine*, vol. 29, no. 2, pp. 94–107, Apr. 2009.

[343] T. C. Van Flandern, "Is the gravitational constant changing?" *The Astrophysical Journal*, vol. 218, pp. 813–816, 1 Sep. 1981.

[344] T. Van Flandern, "The speed of gravity – what the experiments say," *Physics Letters A*, vol. 250, no. 1–3, pp. 1–11, 21 Dec. 1998.

[345] ——, "Reply to comment on 'the speed of gravity'," *Physics Letters A*, vol. 262, no. 2–3, pp. 261–263, 1 Nov. 1999.

[346] F. van Leeuwen and E. Fantino, "A new reduction of the raw Hipparcos data," *Astronomy and Astrophysics*, vol. 439, no. 2, pp. 791–803, Aug. 2005. [Online]. Available: http://arxiv.org/abs/astro-ph/0505432

[347] F. van Leeuwen, "Validation of the new Hipparcos reduction," *Astronomy and Astrophysics*, vol. 474, no. 2, pp. 653–664, Nov. 2007. [Online]. Available: http://arxiv.org/abs/0708.1752

[348] V. Vdovin, "Global geocentric coordinate system of the Russian Federation," in *Proceedings of the 7th Meeting of the International Committee on Global Navigation Satellite Systems*, Beijing, China, 7 Nov. 2012. [Online]. Available: http://www.oosa.unvienna.org/pdf/icg/2012/template/ PZ90-02_v2.pdf

[349] ——, "National reference systems of the Russian Federation used in GLONASS including the user and fundamental segments," in *Proceedings of the 8th Meeting of the International Committee on Global Navigation Satellite Systems*, Dubai, United Arab Emirates, 11–15 Nov. 2013. [Online]. Available: http://www.oosa.unvienna.org/pdf/icg/2013/icg-8/wgD/D3_3_2.pdf

[350] H. Vermeille, "Direct transformation from geocentric coordinates to geodetic coordinates," *Journal of Geodesy*, vol. 76, no. 8, pp. 451–454, Nov. 2002.

[351] ——, "Computing geodetic coordinates from geocentric coordinates," *Journal of Geodesy*, vol. 78, no. 1–2, pp. 94–95, Sep. 2004.

[352] A.-D. Vîlcu, "An analytical expression for the angular velocity of rotation of the Earth," *Applied Mathematical Sciences*, vol. 5, no. 13–16, pp. 707–716, 2011.

[353] G. Wahba, "Problem 65-1: A least squares estimate of satellite attitude," *SIAM Review*, vol. 7, no. 3, p. 409, Jul. 1965.

[354] P. Wallace, "IAU 2000 resolutions for the general user," in *Twenty Sixth General Assembly of the International Astronomical Union*, Prague, Czech Republic, 21 Aug. 2006. [Online]. Available: http://syrte.obspm.fr/iau/iauWGnfa/wallace_com8_ga06.pdf

[355] P. W. Ward, H. L. Scott, J. D. Holmes, and L. J. LaPadula, "GPS system and method for deriving pointing or attitude from a single GPS receiver," U.S. Patent 5,185,610, Feb. 9, 1993.

[356] J. T. Weaver, "Magnetic variations associated with ocean waves and swell," *Journal of Geophysical Research*, vol. 70, no. 8, pp. 1921–1929, 15 Apr. 1965.

[357] E. W. Weisstein. (2013) Associated Legendre polynomial. From MathWorld–A Wolfram Web Resource. [Online]. Available: http://mathworld.wolfram.com/AssociatedLegendrePolynomial.html

[358] M. Wenger *et al.*, "The SIMBAD astronomical database: The CDS reference database for astronomical objects," *Astronomy and Astrophysics*, vol. 143, no. 1, pp. 9–22, Apr. 2000.

[359] P. Wessel and W. H. F. Smith, "A global, self-consistent, hierarchical, high-resolution shoreline database," *Journal of Geophysical Research*, vol. 101, no. B4, pp. 8741–8743, 10 Apr. 1996.

[360] R. P. Whitemarsh, "Great sea waves," *United States Naval Institute Proceedings*, vol. 60, no. 8, pp. 1097–1103, Aug. 1934.

[361] G. A. Wilkins, "The IAU style manual (1989): The preparation of astronomical papers and reports," International Astronomical Union, Tech. Rep., 1989. [Online]. Available: http://www.iau.org/static/publications/stylemanual1989.pdf

[362] World Meteorological Organization, "Manual on codes: International codes, part A–alphanumeric codes," World Meteorological Organization, Tech. Rep. 306, 2011, updated in 2013. [Online]. Available: http://www.wmo.int/pages/prog/www/WMOCodes/WMO306_vI1/VolumeI.1.html

[363] X. Wu, J. Ray, and T. van Dam, "Geocenter motion and its geodetic and geophysical implications," *Journal of Geodynamics*, vol. 58, pp. 44–61, Jul. 2012.

[364] G. Xu, *GPS: Theory, Algorithms and Applications*, 2nd ed.   Springer, 2007.

[365] Y. Yang, "Chinese geodetic coordinate system 2000," *Chinese Science Bulletin*, vol. 54, no. 15, pp. 2714–2721, Aug. 2009.

[366] C. F. Yoder, J. G. Williams, J. O. Dickey, B. E. Schutz, R. J. Eanes, and B. D. Tapley, "Secular variation of Earth's gravitational harmonic J2 coefficient from Lageos and nontidal acceleration of earth rotation," *Nature*, vol. 303, no. 5920, pp. 757–762, 30 Jun. 1983.

[367] A. T. Young, "Sunset science. IV. Low-altitude refraction," *The Astronomical Journal*, vol. 127, no. 6, pp. 3622–3637, Jun. 2004.

[368] G. M. Young, "NGS geodetic tool kit, part I," *Professional Surveyor*, vol. 23, no. 4, Apr. 2003. [Online]. Available: http://www.profsurv.com/magazine/article.aspx?i=1056

[369] X. Yun, E. R. Bachmann, and R. B. McGhee, "A simplified quaternion-based algorithm for orientation estimation from Earth gravity and magnetic field measurements," *IEEE Transactions on Instrumentation and Measurement*, vol. 57, no. 3, pp. 638–650, Mar. 2008.

[370] N. Zacharias, "Dense optical reference frames: UCAC and URAT," in *Proceedings IAU, Symposium S248*, vol. 3, 2007, pp. 310–315.

[371] Z.-W. Zheng and Y.-S. Zhu, "New least squares registration algorithm for data fusion," *IEEE Transactions on Aerospace and Electronic Systems*, vol. 40, no. 4, pp. 1410–1416, Oct. 2004.

[372] Y. Zhou, H. Leung, and M. Blanchette, "Sensor alignment with Earth-centered Earth-fixed (ECEF) coordinate system," *IEEE Transactions on Aerospace and Electronic Systems*, vol. 35, no. 2, pp. 410–418, Apr. 1999.

[373] Y. Zhou, H. Leung, and P. C. Yip, "An exact maximum likelihood registration algorithm for data fusion," *IEEE Transactions on Signal Processing*, vol. 45, no. 6, pp. 1560–1573, Jun. 1997.

[374] H. Zhu and S. Han, "Track-to-track association based on structural similarity in the presence of sensor biases," *Journal of Applied Mathematics*, no. 294657, 25 Mar. 2014.